LBNL-46421

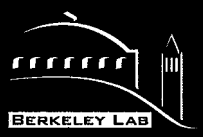

ERNEST ORLANDO LAWRENCE
BERKELEY NATIONAL LABORATORY

Development of Techniques in Magnetic Resonance and Structural Studies of the Prion Protein

Hans-Marcus L. Bitter

Materials Sciences Division

July 2000

Ph.D. Thesis

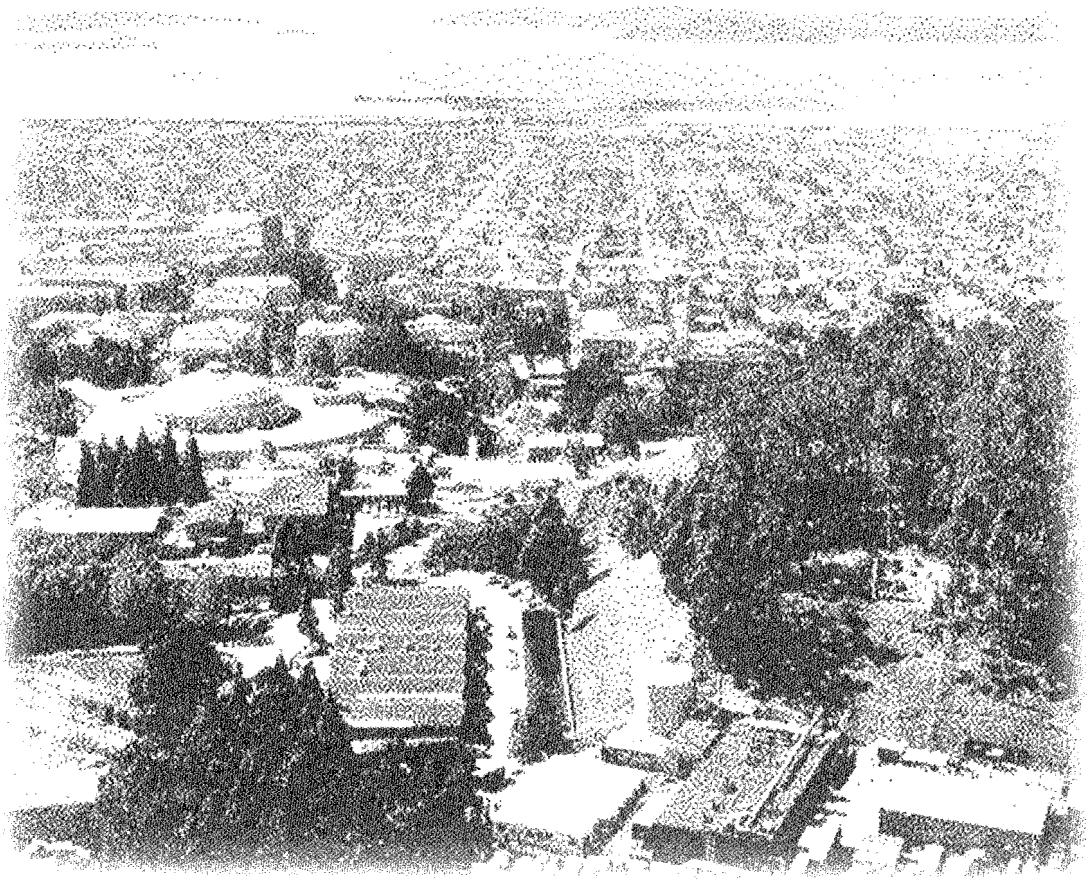

Development of Techniques in Magnetic Resonance and Structural Studies of the Prion Protein

Hans-Marcus Ludwig Bitter
Ph.D. Thesis

Department of Chemistry
University of California, Berkeley

and

Materials Sciences Division
Ernest Orlando Lawrence Berkeley National Laboratory
University of California
Berkeley, Calfornia 94720

July 2000

This work was supported by the Director, Office of Science, Office of Basic Energy Sciences, Materials Sciences, Division, of the U.S. Department of Energy under Contract No. DE-AC03-76SF00098.

Development of Techniques in Magnetic Resonance and Structural Studies of the Prion Protein

by

Hans-Marcus Ludwig Bitter

A.B. (Princeton University) 1995

a dissertation submitted in partial satisfaction of the
requirements for the degree of
Doctor of Philosophy
in
Chemistry
in the
GRADUATE DIVISION
of the

UNIVERSITY OF CALIFORNIA, BERKELEY

Committee in charge:
Professor Alexander Pines, Chair
Professor Ignacio Tinoco Jr.
Professor Corey Goodman

SUMMER 2000

Development of Techniques in Magnetic Resonance and Structural Studies of the Prion Protein

by

Hans-Marcus Ludwig Bitter

To Cathie and my family

Table of Contents

List of Figures

List of Tables

Acknowledgements

The past four years have been truly challenging, exciting, and enjoyable. I have many people to thank for this. First, I wish to thank Cathie and my family, who have supported me every step of the way. Second, I wish to thank the friends I made outside the Pines group. It was fun getting to know them and it was always nice to get away from work and think about and do other things. Third, I wish to thank Alex Pines for giving me the opportunity to work in his group. His inspiration and constant flow of ideas certainly instilled excitement in me about science. Fourth, I wish to thank Dione Carmichael. Without her, I know for a fact I would have left graduate school. She is caring, refreshingly cynical, and always there for you in a pinch. Fifth, I have to thank David King and Haydn Ball for making all of the peptides used in our experiments. Needless to say, without them this research would not have been possible. Sixth, I have to thank one Pinenut in particular, Dave Laws. Especially over the past half year, and also throughout my time here, Dave has been a joy to work with: always efficient, always opinionated, and always full of ideas, he has certainly helped make our research exciting, fun, and ultimately successful.

Lastly, I wish to thank the other pinenuts and especially those I had the pleasure of working with (Jonathan Heller, Marco Tomaselli, Sunil Saxena, Annjoe Wong-Foy, Bob Havlin, Jamie Walls, Kai Liu, Seth Bush, Tuan Nguyen, Adam Moule, Julie Seeley, Alexej Jerschow, and Hun Lim). It is impossible to thank them all specifically, however I would like to mention a few in particular that helped me tremendously. Jonathan Heller introduced me to the prion project and was kind enough to explain a lot of the basics of

NMR and biology. In the past few years, he, Connie, and Isaak have become close friends and neighbors! Marco Tomaselli was also very kind and generous with his time. Aside from being an extremely competent scientist, he is also a very good teacher. Lastly, I wish to mention Sunil Saxena and Annjoe Wong-Foy, who were wonderful collaborators on the SQUID imaging project. Whether it was having interesting discussions about science, food, or politics, it was a real pleasure to work with them.

Abstract

Development of Techniques in Magnetic Resonance
and Structural Studies of the Prion Protein

by

Hans-Marcus L. Bitter
Doctor of Philosophy in Chemistry
University of California, Berkeley
Professor Alexander Pines, Chair

Magnetic resonance is the most powerful analytical tool used by chemists today. Its applications range from determining structures of large biomolecules to imaging of human brains. Nevertheless, magnetic resonance remains a relatively young field, in which many techniques are currently being developed that have broad applications. In this dissertation, two new techniques are presented, one that enables the determination of torsion angles in solid-state peptides and proteins, and another that involves imaging of heterogenous materials at ultra-low magnetic fields. In addition, structural studies of the prion protein via solid-state NMR are described.

More specifically, work is presented in which the dependence of chemical shifts on local molecular structure is used to predict chemical shift tensors in solid-state peptides with theoretical *ab initio* surfaces. These predictions are then used to determine the backbone dihedral angles in peptides. This method utilizes the theoretical chemical-shift tensors and experimentally determined chemical-shift anisotropies (CSAs) to predict the backbone and side chain torsion angles in alanine, leucine, and valine residues.

Additionally, structural studies of prion protein fragments are described in which conformationally-dependent chemical-shift measurements were made to gain insight into the structural differences between the various conformational states of the prion protein. These studies are of biological and pathological interest since conformational changes in the prion protein are believed to cause prion diseases.

Finally, an ultra-low field magnetic resonance imaging technique is described that enables imaging and characterization of heterogeneous and porous media. The notion of imaging gases at ultra-low fields would appear to be very difficult due to the prohibitively low polarization and spin densities as well as the low sensitivities of conventional Faraday coil detectors. However, Chapter 5 describes how gas imaging at ultra-low fields is realized by incorporating the high sensitivities of a dc superconducting quantum interference device (SQUID) with the high polarizations attainable through optically pumping ^{129}Xe gas.

Chapter One

An Overview of Modern Solid-State NMR Techniques

1.1 Introduction

Over the past two decades, solid-state NMR (SSNMR) has increasingly been used to study structure and dynamics in a variety of solid systems such as polymers, glasses, and even proteins. Much of the success of SSNMR is due to the development of a vast number of techniques for studying internuclear distances, torsion angles, spin diffusion, molecular dynamics, and exchange processes—while maintaining the high-resolution and sensitivity that is necessary for any practical NMR experiment.

The purpose of this introductory chapter is to demonstrate the utility of solid-state NMR not only for detailed studies of molecular structure and dynamics in solids, but also as a tool for everyday chemical analysis of solid-state materials. The interactions between nuclear spins and magnetic fields that give rise to the notoriously broad SSNMR lineshapes will be discussed, as well as the common (and not-so-common) tools for eliminating this broadening. The concepts underlying techniques, such as REDOR[1, 2] and rotational resonance[3], which are routinely used to measure internuclear distances in solids, will also be described. Furthermore, in section 1.5 of this chapter, a description of solid-state NMR of quadrupolar nuclei such as ^{2}H and ^{23}Na, and how they can be used to probe orientation, dynamics, and structure will be provided. Since the intent of this chapter is to provide an overview of SSNMR and to discuss how it can be used to address interesting molecular questions, a detailed mathematical description of SSNMR will not be provided in the ensuing sections. However, where appropriate, I will provide references to books and reviews that explain in greater detail the topics presented.

1.2 Solid-State NMR of Low Abundance Spin-½ Nuclei

Unlike liquid-state NMR, where the observation of nuclei other than protons is rare, the most common NMR experiments performed in the solid-state are those involving the observation of spin $I = \frac{1}{2}$ nuclei with low magnetogyric ratios, like ^{13}C, ^{15}N, and ^{31}P. Thus, this chapter will begin with an introduction to the spin interactions that play a role in solid-state NMR spectra of spin $I = \frac{1}{2}$ nuclei and discuss common spectroscopic methods that eliminate and manipulate the effects these interactions have on solid-state NMR spectra.

To aid in this discussion, consider a sample of 10% 1-^{13}C labeled glycine. If one were to dissolve the labeled glycine in water and apply a single $\frac{\pi}{2}-$pulse at the appropriate NMR frequency for ^{13}C nuclei, the familiar spectrum shown in Figure (1.2.1) would result. The two well-resolved lines in the spectrum correspond to the 10% ^{13}C-labeled carbonyl carbon and the natural abundance (~1% for ^{13}C) α-carbon in the glycine sample. The familiar 1:2:1 splitting pattern of the carbonyl carbon resonance provides information about its coupling to the two α-protons. The splittings of the isotopically dilute α-carbon resonance are a result of J-couplings to both the α-protons and the carbonyl carbon. In contrast, Figure (1.2.2) shows the result of a comparable experiment performed on 10% 1-^{13}C labeled glycine in the solid-state. As one can see, the two spectra are quite different; the carbonyl ^{13}C lineshape, which was extremely sharp in the liquid-state spectrum, is now masked by an extremely broad and generally uninterpretable blob, and the α-carbon line is so broad that it is not even resolvable.

These extremely broad solid-state lineshapes are primarily the result of three interactions that are always present, but are rarely observed in liquid-state spectra. These interactions are the heteronuclear dipolar coupling, the chemical shift anisotropy, and the homonuclear dipolar coupling. In the ensuing sections, the origin of each of these interactions will be examined as well as how their effects on a solid-state NMR spectrum can be minimized to produce a "liquid-like" spectrum.

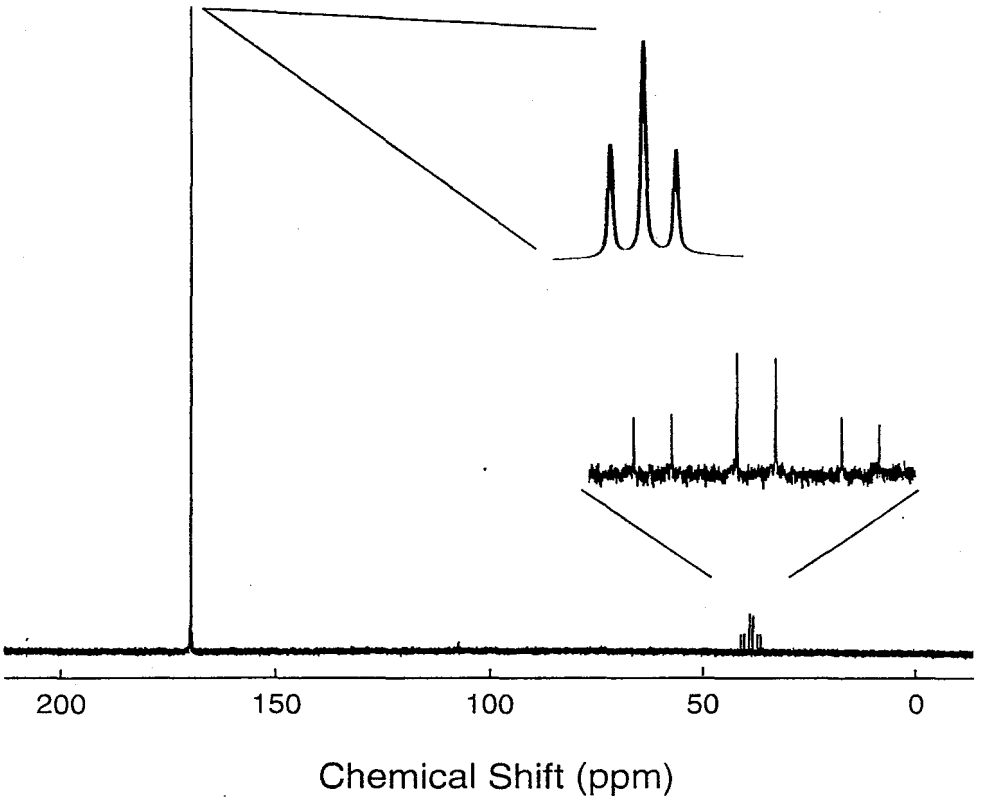

Figure 1.2.1. 75 MHz liquid-state ^{13}C NMR spectrum of 10% 1-^{13}C labeled glycine dissolved in H_2O to a concentration of ~10 mM.

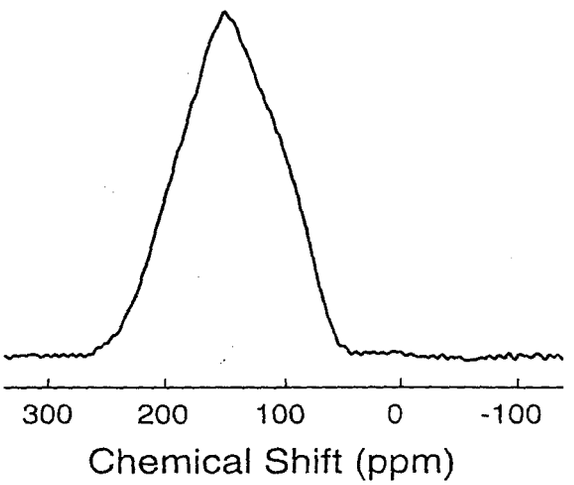

Figure 1.2.2. 125 MHz solid-state ^{13}C NMR spectrum of a 10% 1-^{13}C labeled glycine powder. A one pulse sequence without decoupling was used.

1.2.1 - Heteronuclear Dipolar Coupling

The analysis of the solid-state ^{13}C glycine spectrum will begin with the examination of the heteronuclear dipolar coupling. The heteronuclear dipolar coupling arises from an interaction between the nuclear magnetic moments of two different nuclei, which for simplicity are designated I and S. Recall that in an external magnetic field, the Zeeman Hamiltonian describes the energy of spin-I based on its orientation, either parallel ("spin-up") or antiparallel ("spin-down"), with respect to the external field,

$$E_{Zeeman} = -\hbar\gamma B_0 m_I, \tag{1.2.1}$$

where γ is the magnetogyric ratio, B_0 is the external magnetic field, and m_I is the nuclear spin quantum number, which is either $\pm\frac{1}{2}$ for a spin $I = \frac{1}{2}$ nucleus. Similarly, spin S will align itself either parallel or antiparallel to B_0. Since each spin is a nuclear magnetic moment that produces a small magnetic field, when the two spins I and S are within a reasonable proximity (<10Å), the S spin will feel the magnetic field produced by the I spin and vice versa. This magnetic field produced by the I-spin will either add to or

subtract from the external field felt by the S-spin (depending on the orientation of the I-spin), thus increasing or decreasing the effective magnetic field and changing the resonance frequency of spin S. The degree to which spin-I affects the magnetic field felt by spin-S is characterized by the strength of the heteronuclear dipolar coupling Hamiltonian:

$$H_{IS} = \frac{\hbar \gamma_I \gamma_S}{r_{IS}^3} \left(1 - 3\cos^2 \theta\right) I_z S_z, \tag{1.2.2}$$

where r_{IS} is the internuclear distance, γ_I and γ_S are the magnetogyric ratios of the I and S spins, and I_z and S_z are the z-components of the nuclear angular momentum operators $\boldsymbol{I}$ and $\boldsymbol{S}$, respectively. The angle θ describes the orientation of the internuclear vector with respect to the direction of the external magnetic field (Figure 1.2.3). Because the strength of the coupling between two nuclei is distance dependent, the dipolar coupling is considered a *through-space* interaction; e.g., whereas J-couplings are typically observed only between nuclei that are less than three bonds apart, dipolar couplings can often be observed between nuclei in different *molecules*.

There are three important things to notice about the heteronuclear dipolar coupling Hamiltonian. First, the strength of the dipolar coupling is directly proportional to the product of the magnetogyric ratios. This stands to reason since the magnetic moment of a nucleus is proportional to γ, and nuclei with larger magnetic moments produce stronger magnetic fields, which in turn increase the strength of the dipolar coupling interaction. Second, the dipolar coupling is inversely proportional to the cube of the internuclear distance, so the strength of the interaction falls off rapidly as the nuclei are farther apart.

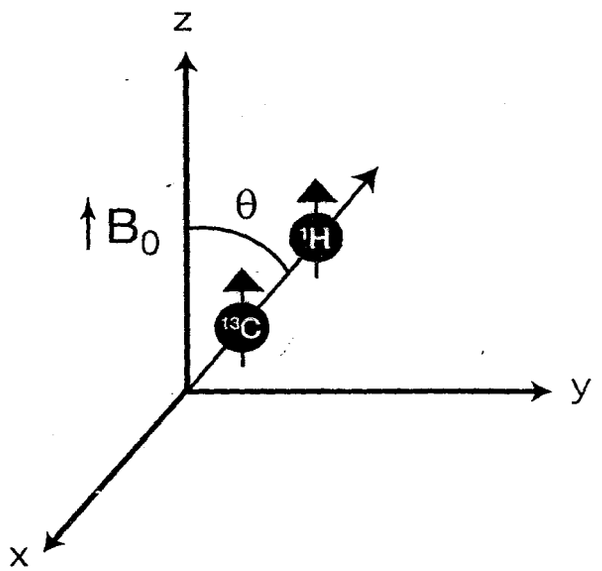

Figure 1.2.3. Definition of the Euler angle θ. For the ^{13}C-^{1}H heteronuclear dipolar coupling, θ represents the angle between the ^{13}C-^{1}H bond vector and direction of the external magnetic field, B_0.

Finally, *the dipolar coupling is orientationally dependent*, as evidenced by the $\left(1-3\cos^2\theta\right)$ term in the dipolar Hamiltonian. This means that for a pair of spins, I and S, separated by a fixed distance, the magnitude of the dipolar interaction will be greater for certain orientations of the I-S internuclear vector than for others. It is the orientational dependence of the dipolar coupling that limits its role in liquid-state NMR. The rapid reorientation of a molecule in solution on a timescale much faster than the dipolar coupling evolves causes the $\left(1-3\cos^2\theta\right)$ term of the heteronuclear dipolar coupling Hamiltonian to average to zero. However, in a static solid comprised of randomly oriented crystallites, the direction of the internuclear vector remains fixed and the resonant frequency produced by each crystallite will depend on its orientation with respect to the external field. In a powder, where crystallites are oriented in all possible directions, the presence of a heteronuclear dipolar coupling will result in an S-spin spectrum like the one shown in Figure (1.2.4). The two opposing patterns, known as a

"Pake doublet"[4], arise from differences in the sign of H_{IS} depending on the alignment, either parallel or antiparallel, of the I-spin with the S-spin. The intensity of the pattern at

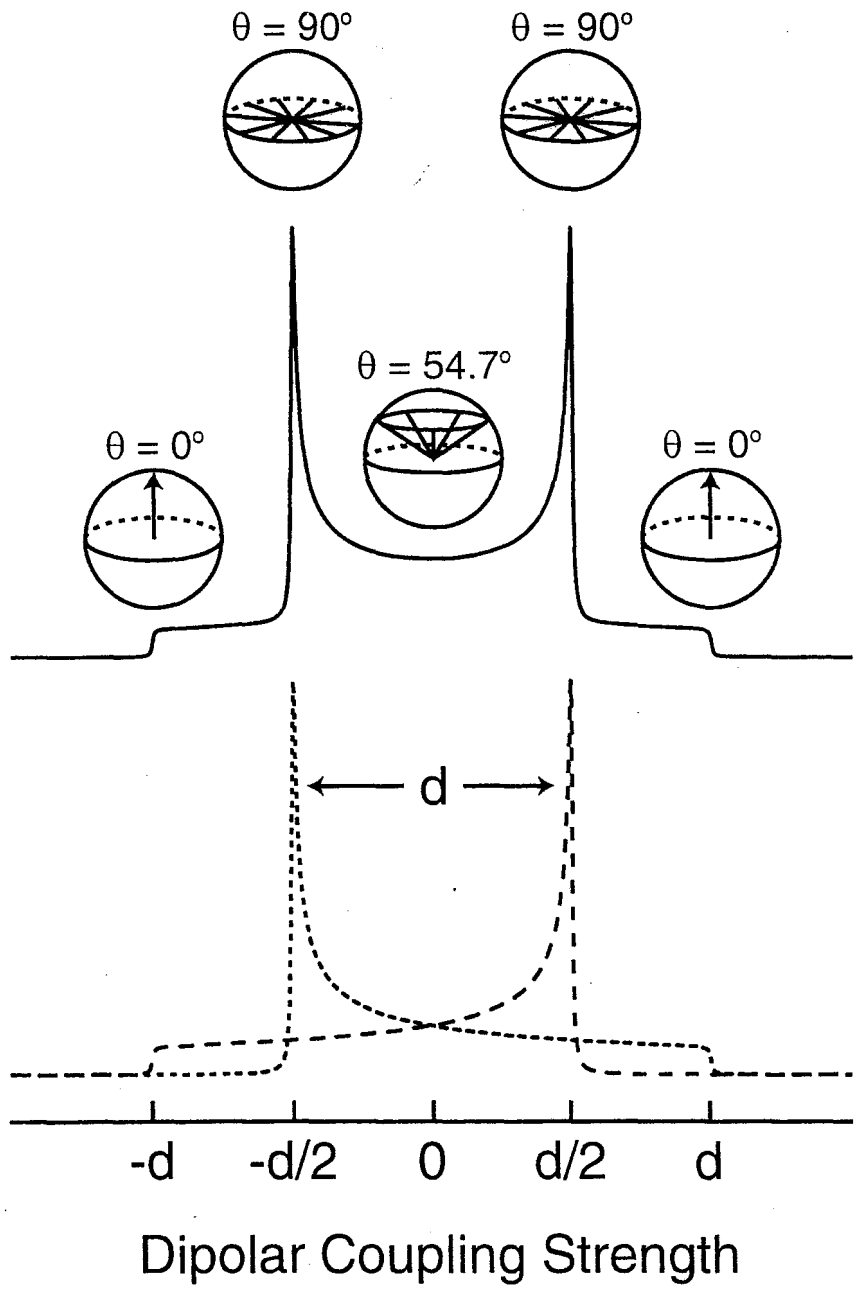

Figure 1.2.4. A representation of the dipolar Pake pattern or "Pake doublet". A typical Pake pattern would look very similar to the top spectrum. The highest points of the spectrum are due to the geometrically abundant internuclear vectors that point perpendicular to B_0. The lowest points of the spectrum are due to the relatively few internuclear vectors that point along B_0. The trace on the bottom shows the two components of a Pake doublet that arise from the two possible S-spin orientations.

a particular frequency reflects the abundance of crystallites that resonate at that frequency. If the possible crystallite orientations in a powdered solid were considered to lie on a globe with the external magnetic field pointing through the poles, the highest points of the Pake pattern would correspond to the large number of crystallites whose I-S internuclear vectors point toward the equator (perpendicular to the external field). The two lowest points of the Pake pattern would correspond to the relatively few crystallites whose I-S internuclear vectors point toward the poles (parallel to the external field). Note that there is also an orientation of the I-S vector relative to B_0 where the resonant frequency of the crystallites is not altered by heteronuclear dipolar coupling. This occurs when $\left(1-3\cos^2\theta\right)$ is equal to zero, which holds for the angle $\theta = 54.74°$, appropriately referred to as the "magic angle".

1.2.2 - Heteronuclear Dipolar Decoupling

Returning to the solid-state glycine spectrum in Figure (1.2.2), the heteronuclear coupling that is responsible for much of the broadening in our spectrum involves ^{1}H nuclei coupled to the detected ^{13}C nuclei. This is due to the fact that the ^{1}H-^{13}C dipolar coupling is typically very large; the magnitude of the coupling between a bonded ^{1}H-^{13}C pair is ~30 kHz. However, close inspection of the Hamiltonian in Equation (1.2.2) suggests two possible means of eliminating the interaction to give narrower lines. One way is to take advantage of the fact that the dipolar coupling is zero for crystallites oriented at the magic angle. This technique, known as magic angle spinning, will be discussed in subsection 1.2.4. Another way to eliminate the effect of the ^{1}H nuclei on our

^{13}C spectrum is to manipulate the proton spins such that their effect on the ^{13}C nucleus, when averaged over time, is equal to zero.

As one may recall from the two opposing lineshapes shown in Figure (1.2.4), a proton whose spin is parallel to the external field ("spin-up") will produce a shift in the resonant frequency of a ^{13}C nucleus that is equal and opposite the shift produced by a proton whose spin is antiparallel to the external field ("spin-down"). By constantly applying radio-frequency (RF) pulses that rotate the proton nuclear spins between their "spin-up" and "spin-down" states, the orientation of the ^{1}H magnetic moments, when averaged over time, becomes zero. As a result, the dipolar coupling is averaged to zero. This technique, known as continuous-wave (CW) spin decoupling[5, 6] can be very effective, and is widely used to eliminate heteronuclear couplings in solid-state NMR. As can been seen in Figure (1.2.5), under CW irradiation at the ^{1}H Larmor frequency, the ^{13}C linewidths are dramatically reduced, leaving a spectrum that is dominated by the chemical shift anisotropy of the ^{13}C nuclei, which will be discussed in the next subsection. It is worth noting that the ^{1}H decoupling has a much more dramatic effect in Figure (1.2.5) on the α-carbon (which is now visible in the spectrum) than it does on the carbonyl carbon. This is a result of the distance dependence of the dipolar coupling—with two α-protons ~1 Å away, the α-carbon experiences a much stronger ^{1}H-^{13}C coupling than the unprotonated carbonyl carbon.

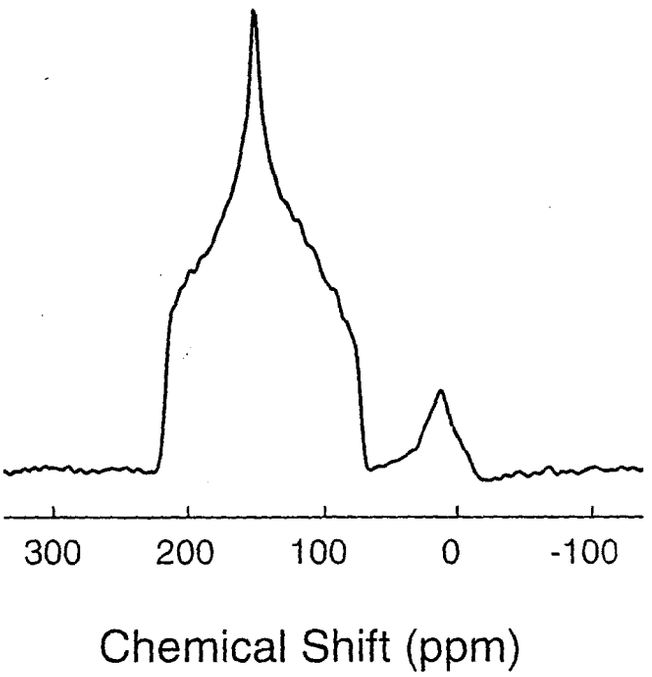

Figure 1.2.5. 125 MHz solid-state ^{13}C NMR spectrum of a 10% 1-^{13}C labeled glycine powder acquired under continuous-wave ^{1}H decoupling.

1.2.3 - Chemical Shift Anisotropy

The origin of the chemical shift can be understood by examining the effect of B_0 on the electrons around a nucleus. When an external magnetic field is applied to an atom, not only are the nuclear spins perturbed, but the surrounding electrons are also affected since they too have magnetic moments. The external field induces circulating currents of electrons that in turn produce small magnetic fields (typically ~$1x10^6$ times smaller than B_0) that either add to or subtract from the external field felt by the nucleus. Therefore, the effective magnetic field felt by the nucleus is altered, as is its resonance frequency.

For individuals familiar with chemical shifts in liquid-state NMR, it can be quite difficult to imagine the chemical shift as an orientationally-dependent interaction. However, in a solid, the orientational dependence or *anisotropy* of the chemical shift can

be quite dramatic; for a non-sp^3-hybridized ^{13}C atom, the chemical shift anisotropy can be upwards of 120 ppm, as shown for the carbonyl carbon in the spectrum in Figure (1.2.5). The chemical shift anisotropy (CSA) results from the fact that atoms in molecules rarely possess spherical electron distributions—rather the electron density can be thought of as an ellipsoid, typically elongated along bonds or non-bonding *p*-orbitals. The degree to which the electron density affects the resonance frequency of a nucleus depends on the orientation of the molecule (and hence the electron cloud) with respect to B_0. For example, the resonance frequency of a carbonyl carbon can differ by more than 120 ppm, depending on the orientation of C=O moiety to the external field, as can be seen in Figure (1.2.6). The smallest shift in the resonance frequency of the ^{13}C nucleus occurs when the narrowest part of the electron cloud is oriented along the B_0 axis (Figure 1.2.6A), whereas the largest shift occurs when the widest part of the electron cloud is oriented along B_0 (Figure 1.2.6C). These two chemical shifts, referred to as δ_{11} and δ_{33}, respectively, are two of the three "principal values" of the CSA. Together with δ_{22}, which is the shift produced by the molecular orientation perpendicular to both δ_{11} and δ_{33} (Figure 1.2.6B), the three principal values provide all the information necessary to describe the CSA of a nucleus. In a powdered sample, where the vast number of randomly oriented crystallites means that all of the possible molecular orientations are sampled, a "powder pattern" such as those shown in Figure (1.2.5) results. The left and right extremes of the powder pattern correspond to the chemical shifts δ_{11} and δ_{33}, respectively, and the highest point of the CSA corresponds to δ_{22}.

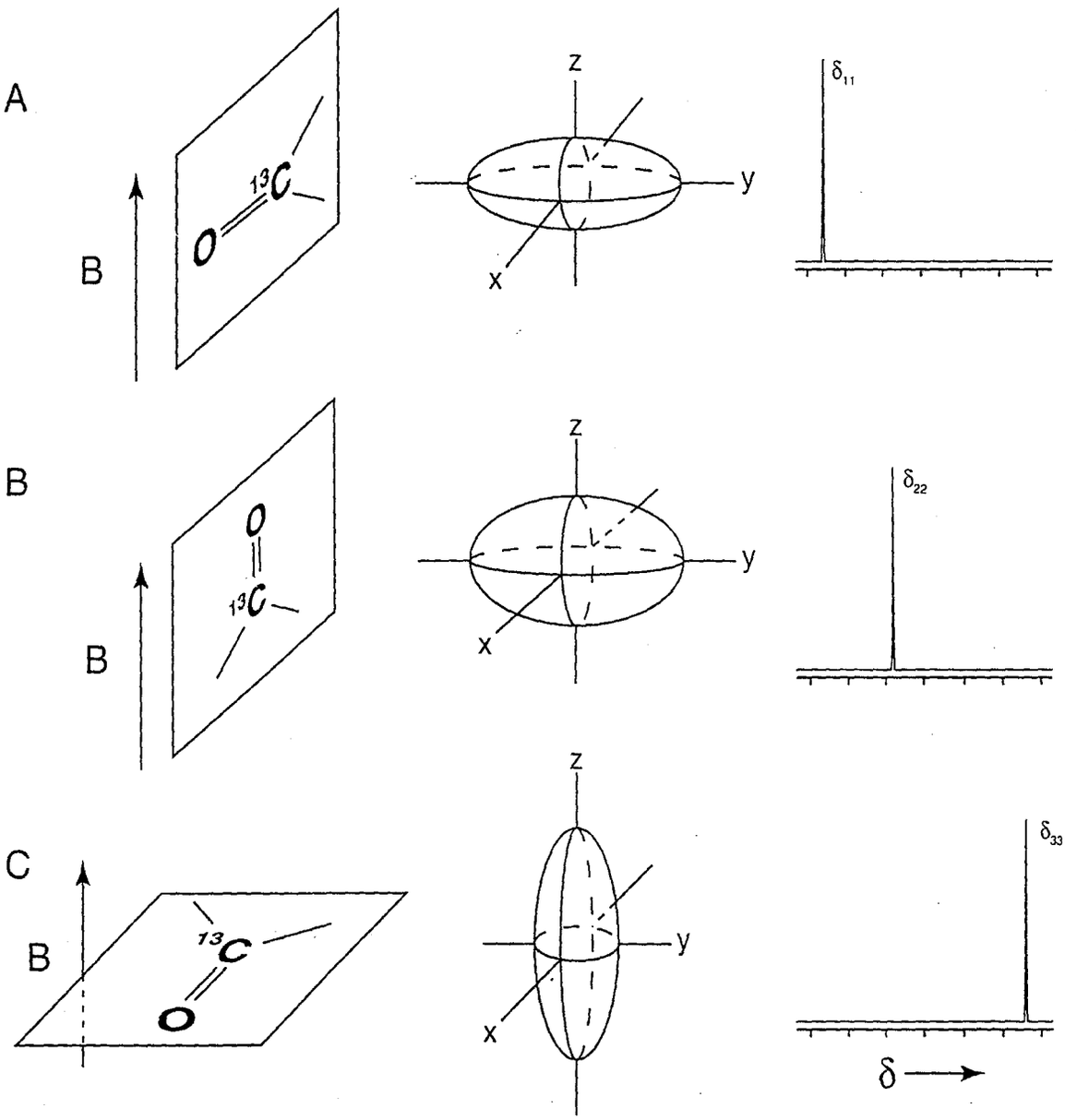

Figure 1.2.6. A schematic representation of the principal values of chemical shift anisotropy, δ_{11} (A), δ_{22} (B), and δ_{33} (C). The position of each resonance depends on the relative orientation of the magnetic field with respect to the principal axes of the chemical shift tensor. (Adapted from reference [7], with permission).

Eliminating the chemical shift anisotropy in solid samples is by no means a trivial undertaking. The broad CSA lineshape is the result of an interaction between the detected spins and the external field, and so there is no simple way to pulse the anisotropy away (as was shown with the heteronuclear dipolar coupling) without

affecting the free precession of the spins required for signal detection. However, liquid-state NMR provides a subtle clue as to how the chemical shift anisotropy can be eliminated.

In liquids, molecules rapidly and randomly sample a plethora of orientations, and so even the most asymmetric electron distribution will appear spherical if viewed on the NMR timescale. Mathematically, this can be described by the chemical shift Hamiltonian, which is typically divided into an isotropic term and an anisotropic term. For the special case where $\delta_{11} = \delta_{22}$ (so that the ellipsoids in Figure (1.2.6) would be symmetric, like a cigar), the chemical shift Hamiltonian can be written as:

$$H_{cs} = \delta_{iso}\gamma B_0 I_z + \tfrac{1}{2}\delta_{csa}\left(1-3\cos^2\theta\right)B_0 I_z, \tag{1.2.3}$$

where δ_{iso} is the chemical shielding factor (typically on the order of $1\text{x}10^{-6}$),

$$\delta_{iso} = \frac{\delta_{11}+\delta_{22}+\delta_{33}}{3}, \tag{1.2.4}$$

θ relates the orientation of the cigar-like ellipsoid with respect to B_0, and δ_{csa} dictates the magnitude of the chemical shift anisotropy,

$$\delta_{csa} = \delta_{33} - \delta_{iso}. \tag{1.2.5}$$

In a rapidly tumbling molecule, all possible orientations of the ellipsoid are sampled, causing the orientationally dependent term to average to zero and leaving only the isotropic component of the chemical shift, $\delta_{iso}\gamma B_0 I_z$. This is what is commonly observed in liquid-state NMR spectra. Unfortunately, imposing a random, liquid-like motion on a solid-state sample is a mechanical impossibility since it would require motion around multiple axes at speeds that are currently unattainable. However, as will

be discussed in the next subsection, magic angle spinning (MAS) is a simpler way of eliminating the anisotropic term of the chemical shift Hamiltonian.

1.2.4 - Magic Angle Spinning

Previously it was pointed out that at $\theta = 54.74°$ (the magic angle), the value of the $\left(1-3\cos^2\theta\right)$ term in the heteronuclear dipolar coupling, as well as the chemical shift anisotropy (for $\delta_{11} = \delta_{22}$), is zero. Thus, one way to remove the CSA in a solid and leave only the isotropic chemical shift is to use a single crystal that is oriented so that $\theta = 54.74°$. However, this is not a very elegant solution since it would require first forming a single crystal and then orienting the crystal such that $\theta = 54.74°$ (which is not trivial). Fortunately, one can achieve the same effect in a powdered sample by simply *spinning* around an axis of 54.74° via a technique known as magic angle spinning[8, 9].

The mathematical description of the evolution of an NMR Hamiltonian under sample spinning is quite complex[7, 10], and so will not be treated here. However, a qualitative description of why spinning a sample around the magic angle results in the removal of the CSA can be given. For a static sample, the value of the chemical shift is fixed for a given crystallite orientation. When the sample is spun, the chemical shift of the crystallite becomes time dependent, since the crystallite's orientation changes as it is spun in the rotor. Figure (1.2.7) shows, for two crystallite orientations, the evolution of their orientation under MAS. Over a single rotor period, each crystallite sweeps out a cone around the magic angle, and at each orientation of the cone, the crystallite experiences a different effective chemical shift. At the magic angle, the average of all of the chemical shifts that a crystallite experiences in one rotor cycle is just the isotropic

chemical shift. Therefore, by spinning the sample in a rotor oriented at 54.74°, the chemical shift anisotropy is removed.

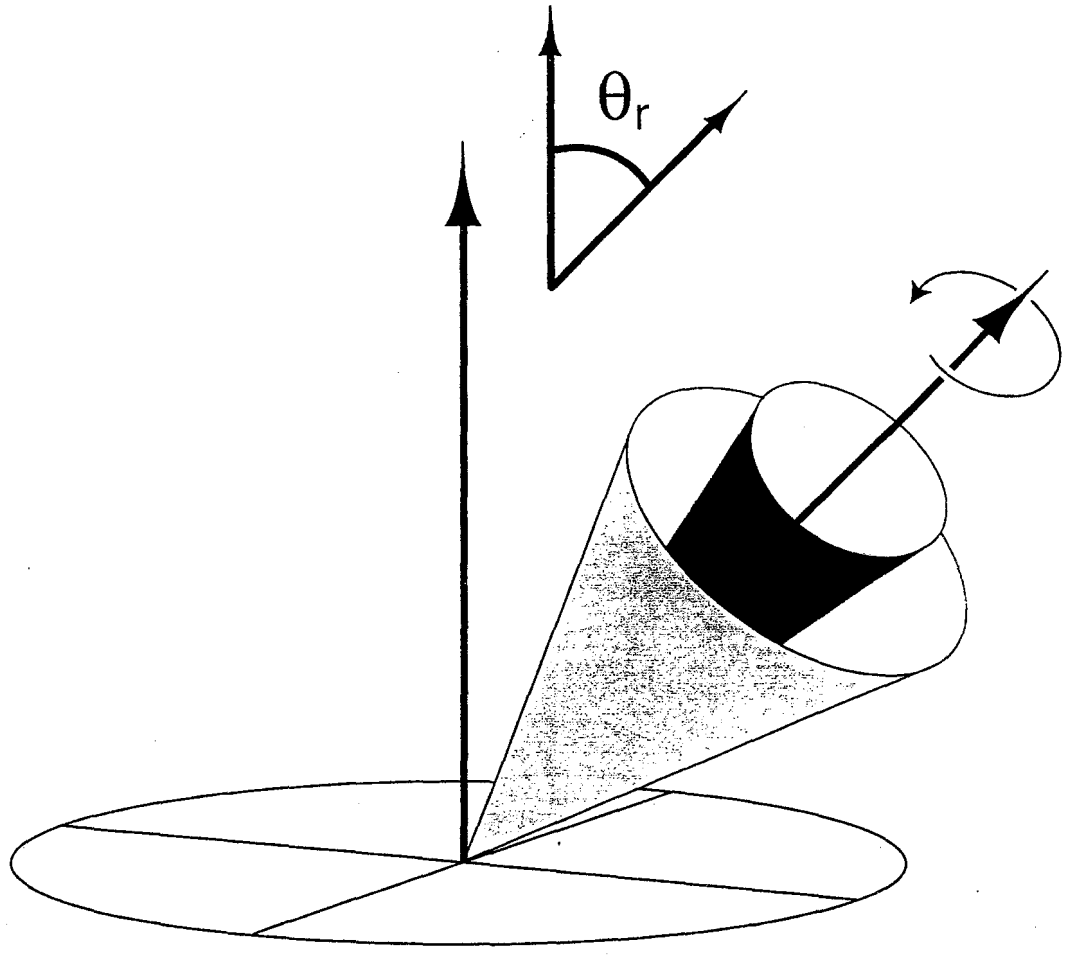

Figure 1.2.7. A graphic representation of the evolution of two crystallites under magic angle spinning. Depending on the initial orientation of the crystallite, its evolution in one rotor cycle sweeps out a cone centered around the rotor axis, which is inclined at an angle of θ_r.

Figure (1.2.8) shows a series of ^{13}C MAS spectra for 10% uniformly ^{13}C labeled glycine at a variety of spinning speeds. Note that as the spinning speed decreases, numerous peaks begin to appear at integer multiples of the spinning speed. These peaks, known as spinning sidebands, result from an inability to remove resonances that evolve in step with the spinning rotor[8, 9]. Although sidebands are typically a nuisance (which

can be minimized by spinning at a frequency larger than the width of the CSA), there are instances where the presence of spinning sidebands provides additional information about a particular sample, as will be discussed further in subsection 1.4.4.

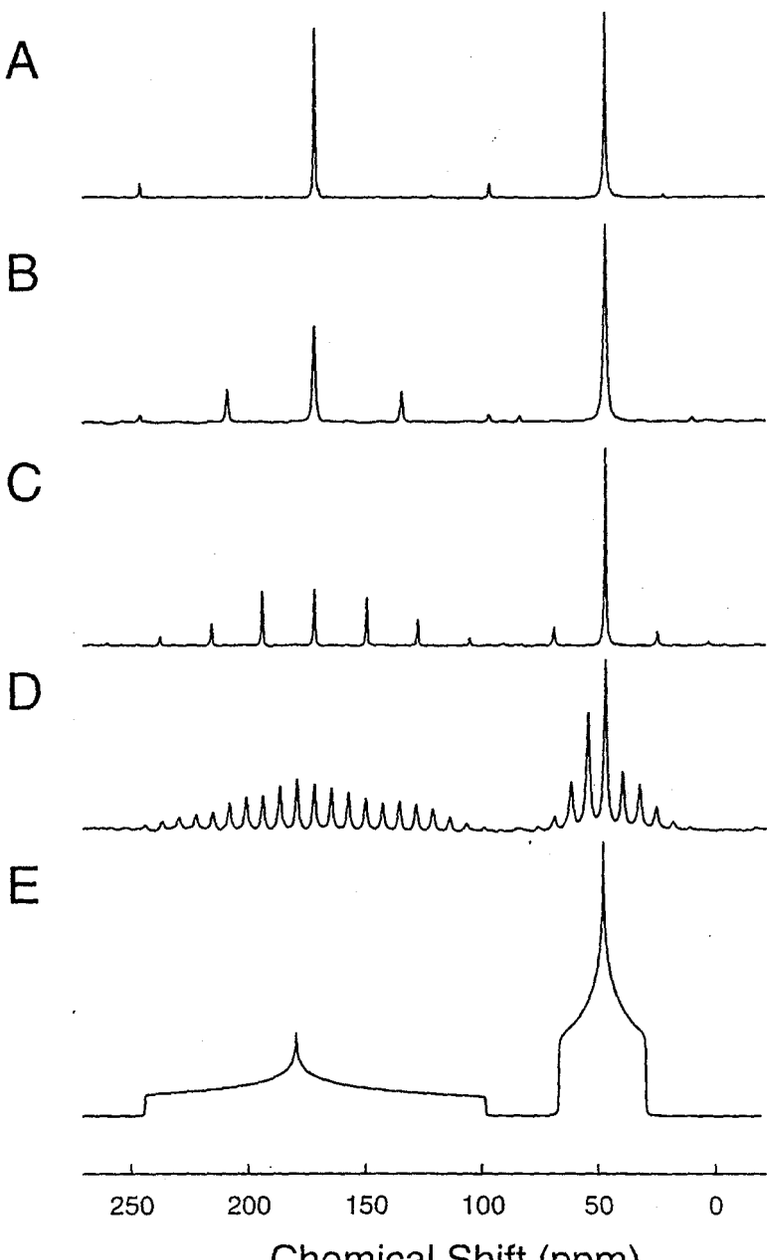

Figure 1.2.8. 125 MHz solid-state ^{13}C NMR spectra of 10% uniformly ^{13}C labeled glycine powder acquired under continuous-wave ^{1}H decoupling and magic angle spinning. The top four spectra correspond to spinning speeds of 10 kHz (A), 5 kHz (B), 2 kHz (C), and 1 kHz (D). As the spinning speed decreases the envelope of spinning sidebands begins to resemble the simulated static NMR spectrum shown in (E).

1.2.5 - Homonuclear Dipolar Coupling

As described in subsection 1.2.1, the *heteronuclear* dipolar coupling is the result of an interaction between the magnetic fields produced by neighboring nuclear spins. The same form of coupling exists between like spins, such as two ^{13}C nuclei. However, unlike two heteronuclei that have vastly different resonance frequencies (e.g. when ^{1}H nuclei resonate at 500 MHz, ^{13}C nuclei resonate at 125 MHz), two like nuclei possess the ability to undergo an energy conserving "flip-flop" interaction in which one spin flips up while the other spin flips down (Figure 1.2.9). To take into account the "flip-flop" interaction, an additional term is added to the heteronuclear dipolar Hamiltonian to give the homonuclear dipolar Hamiltonian,

$$H_{IS} = \frac{\hbar\gamma_I^2}{r_{I_1I_2}^3}\frac{1}{2}\left(1-3\cos^2\theta\right)\left(3I_{1z}I_{2z}-(\boldsymbol{I}_1\cdot\boldsymbol{I}_2)\right), \tag{1.2.6}$$

where $\boldsymbol{I}_1\cdot\boldsymbol{I}_2 = I_{1x}I_{2x}+I_{1y}I_{2y}+I_{1z}I_{2z}$. The origin of the $\boldsymbol{I}_1\cdot\boldsymbol{I}_2$ term can be better understood by rewriting Equation (1.2.6) in terms of raising and lowering operators, where

$$I^+ = \frac{I_x+\mathrm{i}I_y}{2} \text{ and } I^- = \frac{I_x-\mathrm{i}I_y}{2}, \tag{1.2.7}$$

such that

$$H_{IS} = \frac{\hbar\gamma_I^2}{r_{IS}^3}\frac{1}{2}\left(1-3\cos^2\theta\right)\left(3I_{1z}I_{2z}-\frac{1}{2}(I_1^+I_2^- + I_1^-I_2^+)\right). \tag{1.2.8}$$

The raising operator, I^+, increases the spin angular momentum of a spin by $\hbar$, which amounts to flipping a spin from the "down" orientation to the "up" orientation (Figure 1.2.9). Conversely, the lowering operator, I^-, lowers a spin's angular momentum by $\hbar$,

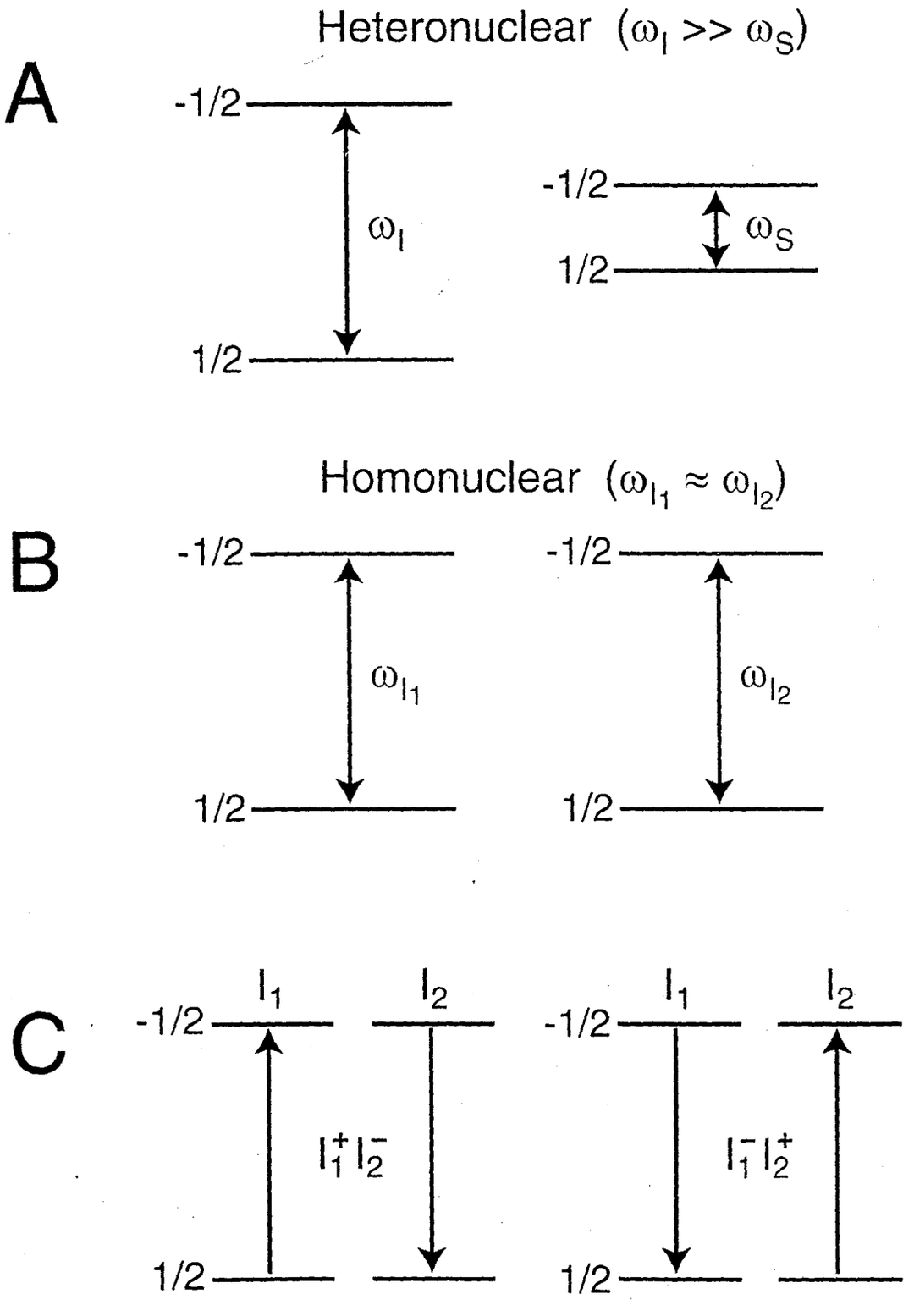

Figure 1.2.9. A diagram depicting the "flip-flop" term of the homonuclear dipolar coupling. When the transition frequencies of two spins, ω_I and ω_S differ (A), no energy conserving transition can occur. When ω_I and ω_S are the same (B), the spins can exchange magnetization via an energy conserving "flip-flop" interaction (C).

causing an "up" spin to flip "down". Together, the $I_1^+ I_2^-$ and $I_1^- I_2^+$ provide for an energy conserving exchange of angular momentum between any two coupled spins whose resonance frequencies even partially overlap. When two like spins have very different chemical shifts, so that there is no overlap between their resonance frequencies, there can be no energy conserving transition, in which case the homonuclear dipolar Hamiltonian reverts to the same form as the heteronuclear dipolar Hamiltonian shown in Equation (1.2.2).

For low-γ nuclei like ^{13}C and ^{15}N, the homonuclear dipolar coupling is typically not an issue, since even for directly bonded ^{13}C nuclei, the dipolar coupling strength, $\frac{\hbar\gamma_I^2}{r_{IS}^3}$, does not exceed 5 kHz, and so it is eliminated at even moderate MAS speeds. The homonuclear dipolar interaction has perhaps the largest impact on ^1H solid-state NMR, since the strength of the homonuclear dipolar coupling between two protons, because of their large magnetogyric ratio, can routinely exceed 100 kHz. The problem of strong ^1H-^1H dipolar couplings is exacerbated by the high abundance of protons in most organic systems, which results in a network of strongly coupled spins that are very difficult to decouple from each other. As a result, proton spectra in the solid-state typically consist of a single broad peak, often greater than 50 kHz wide, depending on the conditions. Figure (1.2.10A) shows a static ^1H spectrum of glycine, where the sea of protons combines to give a spectrum that is completely uninterpretable. Although magic angle spinning does help reduce the ^1H linewidth, as seen in Figure (1.2.10B), the line is still far too broad to be of general use without some form of homonuclear dipolar decoupling, which will be discussed in section 1.3.

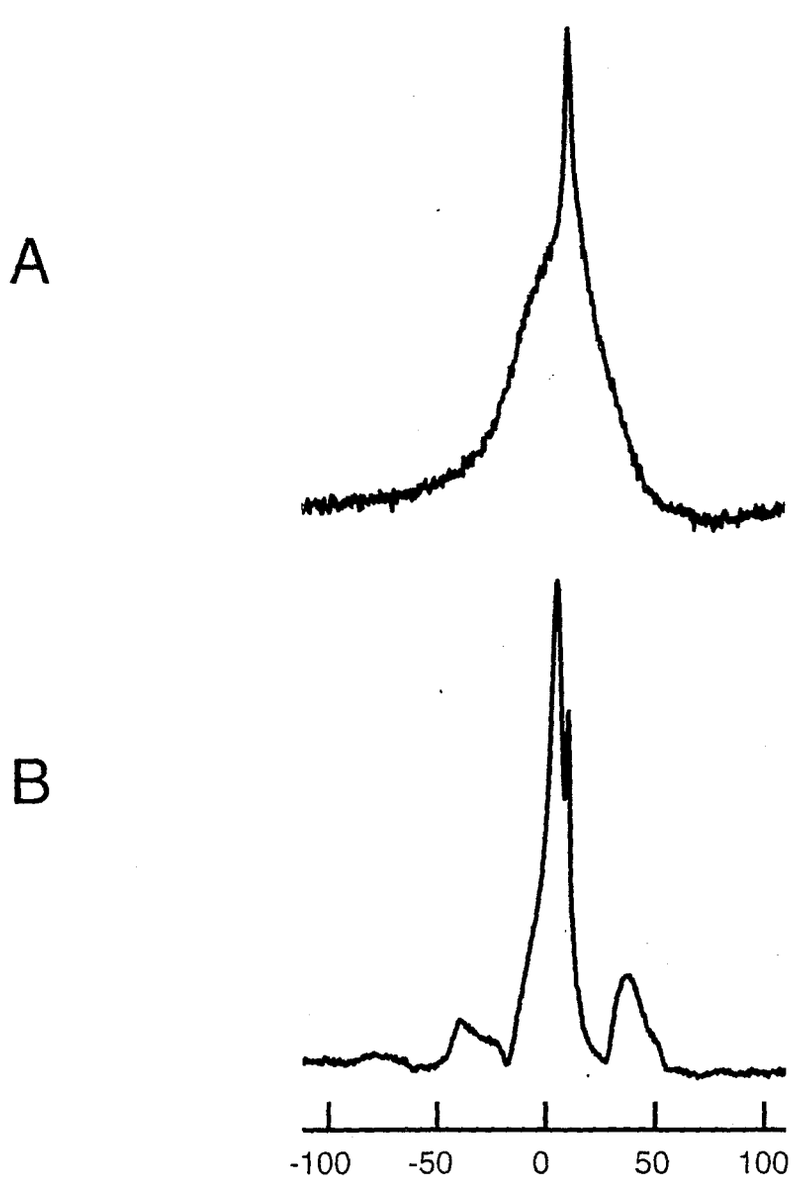

Figure 1.2.10. 500 MHz solid-state ^{1}H NMR spectrum of glycine powder acquired without any sample spinning (A) and while spinning at 10 kHz about the magic angle (B).

1.2.6 - Cross Polarization

Thus far, the differences between solid- and liquid-state Hamiltonians, and how these differences can be overcome by utilizing techniques such as spin decoupling and magic angle spinning have been discussed. To finish this section, a more fundamental

difference between liquid-state and solid-state NMR experiments will be mentioned. In liquid-state NMR, most experiments performed involve detection of protons, since their higher sensitivity and faster relaxation times help minimize acquisition times. Even in liquid-state experiments that measure ^{13}C or ^{15}N chemical shifts or couplings, the magnetization often originates from and is returned to neighboring protons for detection. Due to the difficulties involved in obtaining high-resolution ^{1}H NMR spectra in the solid state, the vast majority of solid-state NMR experiments detect the magnetization of other nuclei, such as ^{13}C, ^{31}P, and ^{15}N. However, even the detection of some of these nuclei has its drawbacks. Compared to protons, nuclei such as ^{13}C and ^{15}N have inherently low sensitivities, polarizations, and isotopic abundances. In addition, the relaxation times of low-γ spin $I = \frac{1}{2}$ nuclei are typically many orders of magnitude longer than ^{1}H relaxation times, resulting in longer overall experiment times. Fortunately, there exists a technique in solid-state NMR that gives the best of all worlds—the high polarizations and short relaxation times typical in ^{1}H NMR, with high-resolution in the solid state through the detection of nuclei other than protons.

To enhance the signal of rare spins, such as ^{13}C and ^{15}N nuclei, many solid-state NMR experiments involve the transfer of polarization from abundant spins (usually ^{1}H nuclei) to rare spins using technique called Cross-Polarization or CP[11]. CP occurs through the natural entropic tendency for magnetization from highly-polarized nuclei to flow to nuclei with lower polarizations when the two are coupled in some manner. This flow of magnetization is analogous to the flow of heat from a hot object to a cold object when the two are in thermal contact. Unfortunately, magnetization is exchanged between nuclei through mutual, energy conserving spin flips, and for heteronuclei such as ^{1}H and

^{13}C, such spin flips are only energy conserving at very low fields[12]. Therefore, the exchange of magnetization must be driven externally by the application of RF fields. Although there are many techniques for establishing a dipolar connection between two different spin systems, I and S, perhaps the most effective method was developed by Erwin Hahn and Sven Hartmann in 1962[13].

The Hartmann-Hahn method for cross-polarization requires the simultaneous application of two continuous RF fields, one at the I-spin Larmor frequency and one at the S-spin Larmor frequency. The effect of any RF field is to rotate the magnetization about the axis of the applied field. The rotation or "nutation" rate depends on two factors: the strength and the frequency of the RF field. The nutation rate increases with increasing field strength, and decreases as the frequency of the field moves further from the Larmor frequency. Therefore, an RF field oscillating at the I-spin frequency, say 500 MHz, would have almost no affect on S-spins with a frequency of 125 MHz. Likewise, an RF field tuned to the S-spin resonance frequency would have almost no affect on the I-spins. By applying two RF fields, one tuned to the I-spins the other to the S-spins, both the I-spins and S-spins can be rotated independently around a particular axis at rates dependent on the strengths of the two applied fields. Hartmann and Hahn found that when the nutation frequencies of the I and S spins were equal, an artificial, energy-conserving dipolar connection between the two spin systems is created with the differences in energy being supplied by the RF fields. It is through this dipolar connection that polarization is transferred between the I- and S-spins.

The experimental implementation of this concept is shown in Figure (1.2.11A). First, the proton magnetization is pulsed down along the x-axis. RF fields are then

applied to the I- and S-spins for a time τ_{mix}, causing the magnetization to be exchanged from the I-spins to the S-spins. Finally, the S-spins are detected while the I-spins are decoupled. The growth of S-spin magnetization during the CP mixing period, τ_{mix}, is dependent on the strength of the I-S dipolar coupling, as shown in Figure (1.2.11B). The

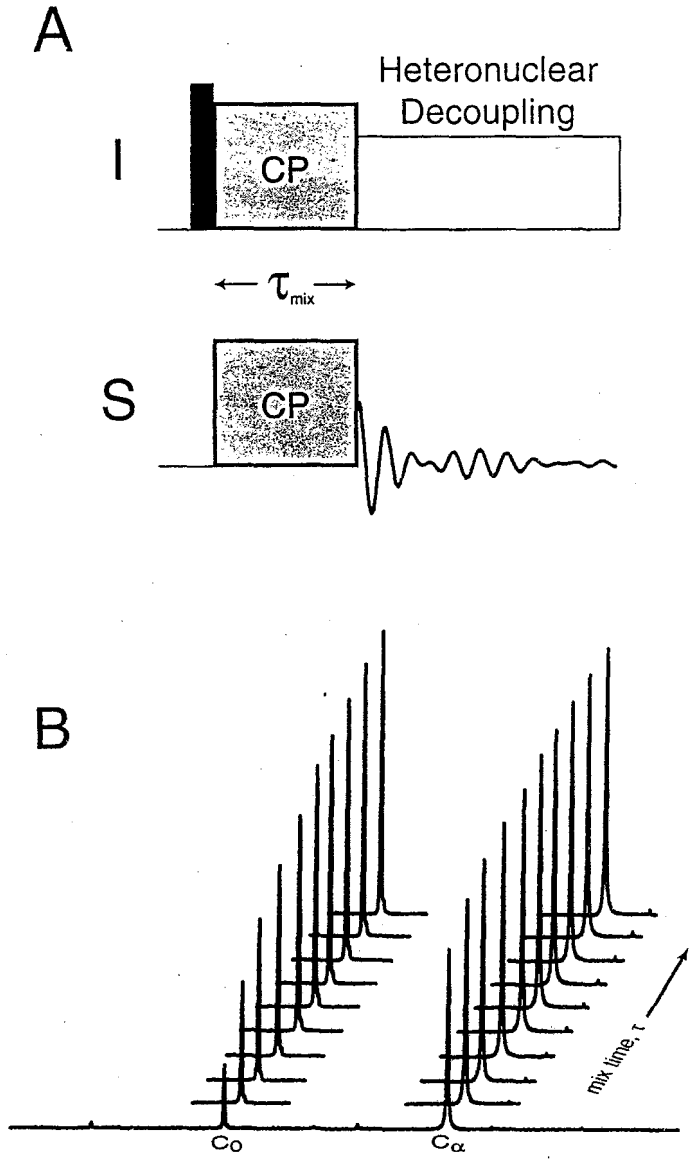

Figure 1.2.11. Hartmann-Hahn cross polarization. (A) Pulse sequence for the cross-polarization of ^{13}C nuclei from ^{1}H nuclei with detection of the ^{13}C magnetization. (B) 125 MHz solid-state ^{13}C NMR spectra of 10% uniformly labeled ^{13}C labeled glycine powder acquired using the pulse sequence in (A). In each experiment, the cross polarization time τ_{mix} is varied. Due to the directly bonded H_α protons, the $^{13}C_\alpha$ nuclei are polarized faster than the $^{13}C_0$ nuclei.

build-up of polarization in the unprotonated carbonyl carbon requires a longer mixing time than the α-carbon, which is quickly polarized by the directly bonded protons. Typical mixing times range from between 100 μs to 10 ms. The maximum theoretical enhancement using the Hartmann-Hahn method of cross-polarization is $\frac{1}{2}\frac{\gamma_I}{\gamma_S}$ (where γ_I and γ_S are the magnetogyric rations of spins I and S), although this degree of enhancement is rarely attainable. However, this theoretical enhancement is merely a thermodynamic argument, and does not account for the practical advantages of using cross-polarization. In most NMR experiments, the acquisition or sampling rate is dictated by relaxation time (T_1) of the detected nuclei. In CP, the sampling rate depends on the relaxation time of the nuclei from which the magnetization is transferred. Since protons in the solid state have a far shorter relaxation time than most other spin $I = \frac{1}{2}$ nuclei, experimental times are usually far shorter than would be used in a simple one-pulse experiment. To illustrate this point, Figure (1.2.12) shows a natural abundance solid-state ^{13}C spectrum of alanyl-histidine both with and without CP from the protons. Although signal to noise ratios of the two spectra in Figures (1.2.12A-B) are comparable (~17:1) the acquisition time of the non-CP spectrum was 45 times longer than the CP spectrum, due to the ~18 s T_1 of the carbon nuclei.

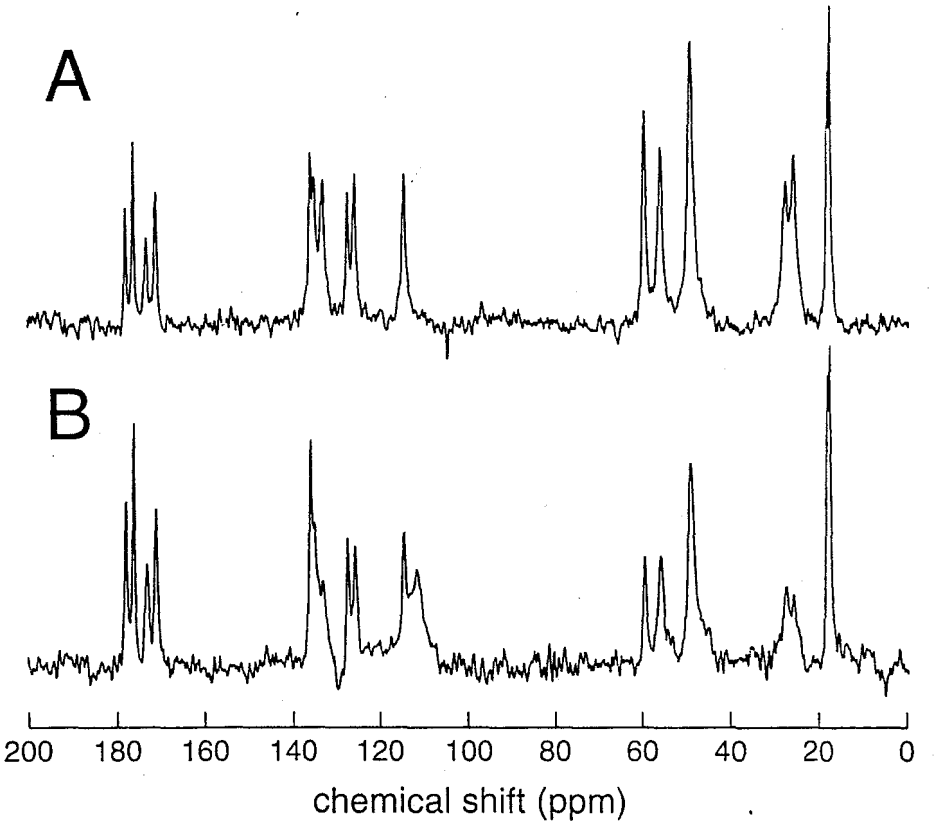

Figure 1.2.12. 125 MHz solid-state ^{13}C NMR spectra of unlabeled alanyl-histidine powder acquired using cross-polarization from protons (A), and using a standard one-pulse experiment (B). Both spectra were recorded under MAS at a speed of 12 kHz and using c.w. ^{1}H decoupling. The recycle delay for the spectrum in (A) was 2 s. The recycle delay for the spectrum in (B) was 90 s, owing to the long ^{13}C T_1 relaxation time (~18 s for this sample).

1.2.7 - Summary

As shown in Figure (1.2.12A), a combination of high-speed MAS, high-power CW decoupling, and cross-polarization can quickly and easily generate one-dimensional solid-state spectra of natural abundance ^{13}C, ^{15}N, and ^{31}P compounds with reasonably good resolution. However, as in liquid-state NMR, to perform a more detailed analysis of the structure and dynamics of a sample, techniques that are more complex must be

utilized. In the next three sections, an overview of commonly used techniques in solid-state NMR is provided, with primary emphasis on those methods that are easy to understand and implement.

1.3 Multi-pulse Decoupling and Multi-dimensional NMR

The majority of solid-state NMR experiments performed on organic or biological systems involve the detection of low abundance nuclei, such as ^{15}N or ^{13}C. One reason for this is the fact that the homonuclear dipolar coupling between these nuclei is typically very small, even when the nuclei are directly bonded—so small that it is almost entirely removed when the spinning speed is greater than 5 kHz. In contrast, the homonuclear dipolar coupling between neighboring protons is very large (as high as 100 kHz), and so magic angle spinning does little to narrow the lineshape, as was shown in Figure (1.2.10B). Fortunately, there are methods that permit the acquisition of ^{1}H NMR spectra with reasonable resolution through the active pulse decoupling of the ^{1}H spins during signal detection. Although the thought of detecting an NMR signal while simultaneously pulsing on the nucleus that is being detected may seem absurd, the practice is quite common. The trick that must be employed is to detect the magnetization *indirectly*, using multi-dimensional NMR.

1.3.1 - Two-dimensional NMR: the WISE Experiment

Although two-dimensional NMR has many different applications in solid-state NMR[14, 15], the basic form of all 2D NMR experiments is essentially the same, as shown in Figure (1.3.1A). First, the magnetization is prepared in a state appropriate to whatever properties are to be detected in the indirect dimension. For instance, to detect a standard chemical shift spectrum in the indirect dimension, the preparation period could be a

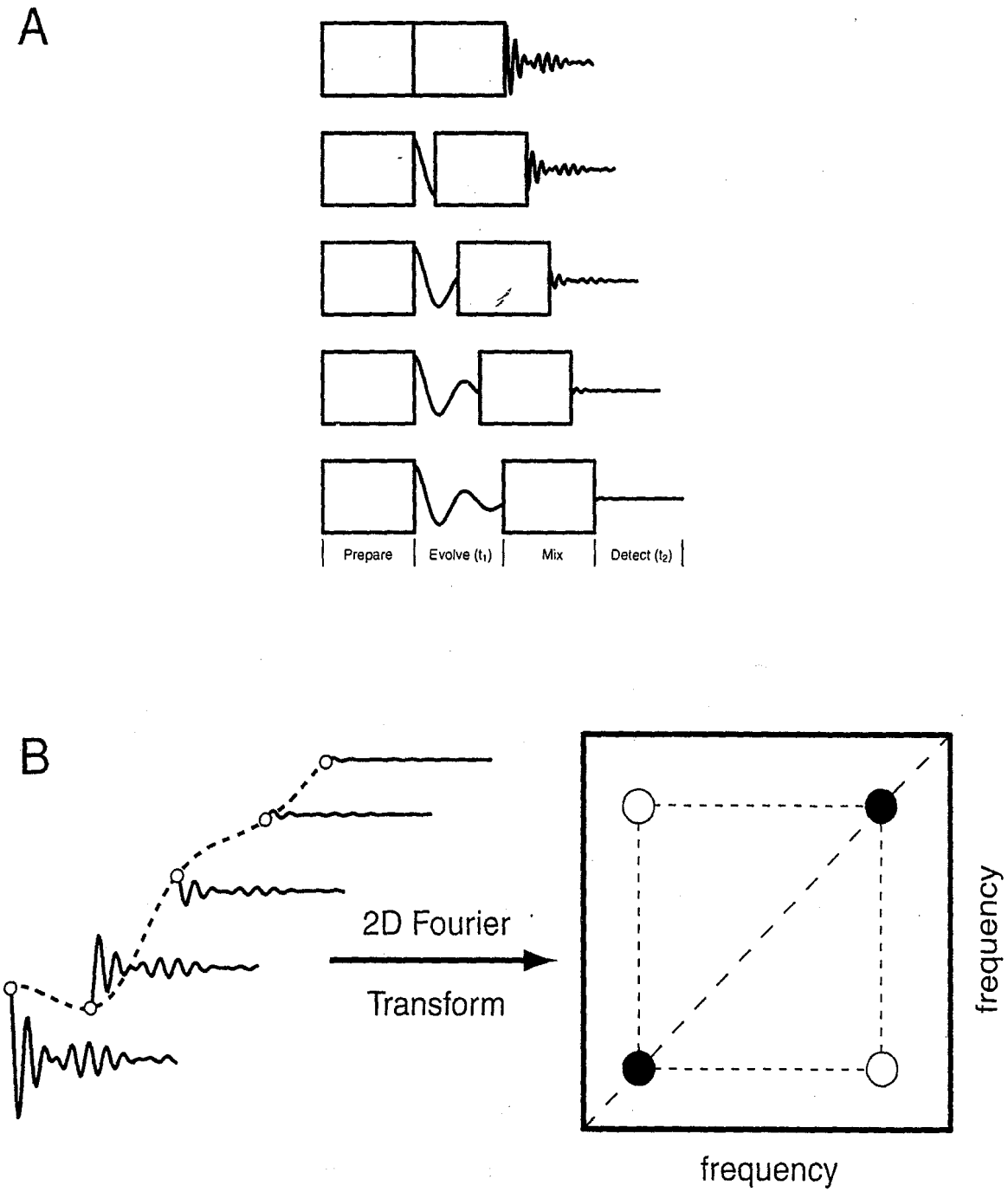

Figure 1.3.1. (A) Diagram of a pulse sequence for two-dimensional NMR experiments. Magnetization is detected in the indirect dimension by repeating the experiment numerous times while varying the time period t_1 in such a way as to stroboscopically detect the evolution of the magnetization under the prepared Hamiltonian. (B) Diagram depicting a two-dimensional Fourier transform. First each directly detected (t_2) spectrum is Fourier transformed, followed by a Fourier transform in the t_1 dimension. Since the evolution of the magnetization during t_1 is embedded in the phase of the detected t_2 spectra, the double Fourier transform produces a spectrum in which the indirectly detected spectrum is correlated with the directly detected spectrum. (Reproduced from reference [16], with permission.)

$\frac{\pi}{2}$-pulse, or possibly a cross-polarization sequence. Next, the magnetization is allowed to evolve for a period t_1, which corresponds to the indirect dimension. It is during this period that the magnetization is allowed to evolve under a specific set of NMR Hamiltonians. For instance, if one wishes the I-spins in an I-S spin system to evolve only under H_{II} and H_{cs}, then the S-spins should be decoupled to remove H_{IS}. To evolve only under H_{II}, a π-pulse can be applied in the middle of t_1 to create an echo that refocuses H_{cs}.

After t_1, an optional mixing pulse (or series of pulses) is used to prepare the magnetization for the final detection period t_2. As with the initial preparation period, the nature of the mixing period depends largely on the spectrum desired. In many homonuclear experiments, no mixing pulse is needed at all. In heteronuclear experiments, it is often necessary to transfer the magnetization from one set of spins to another. For instance, in an experiment correlating ^{1}H and ^{13}C chemical shifts, the mixing period might involve cross-polarization from the ^{1}H spins to the ^{13}C spins. Once the mixing period is complete, the resulting magnetization is detected in the direct dimension, t_2.

The free-induction decay (the signal that is acquired in a Fourier transform NMR experiment) of the indirect dimension is produced by varying the time period t_1 so that the magnetization is detected stroboscopically based on how much it has evolved during t_1 (Figure 1.3.1A). By performing a Fourier transform in both dimensions, a 2D spectrum is produced which correlates the interactions detected in the indirect dimension with the interactions detected in the direct dimension, as shown in Figure (1.3.1B).

A simple example of a typical 2D solid-state NMR experiment is WISE, which stands for WIdeline SEparation[17]. In the WISE experiment, shown in Figure (1.3.2A), ^{1}H nuclei are initially prepared using a $\frac{\pi}{2}$-pulse, which rotates the magnetization into the

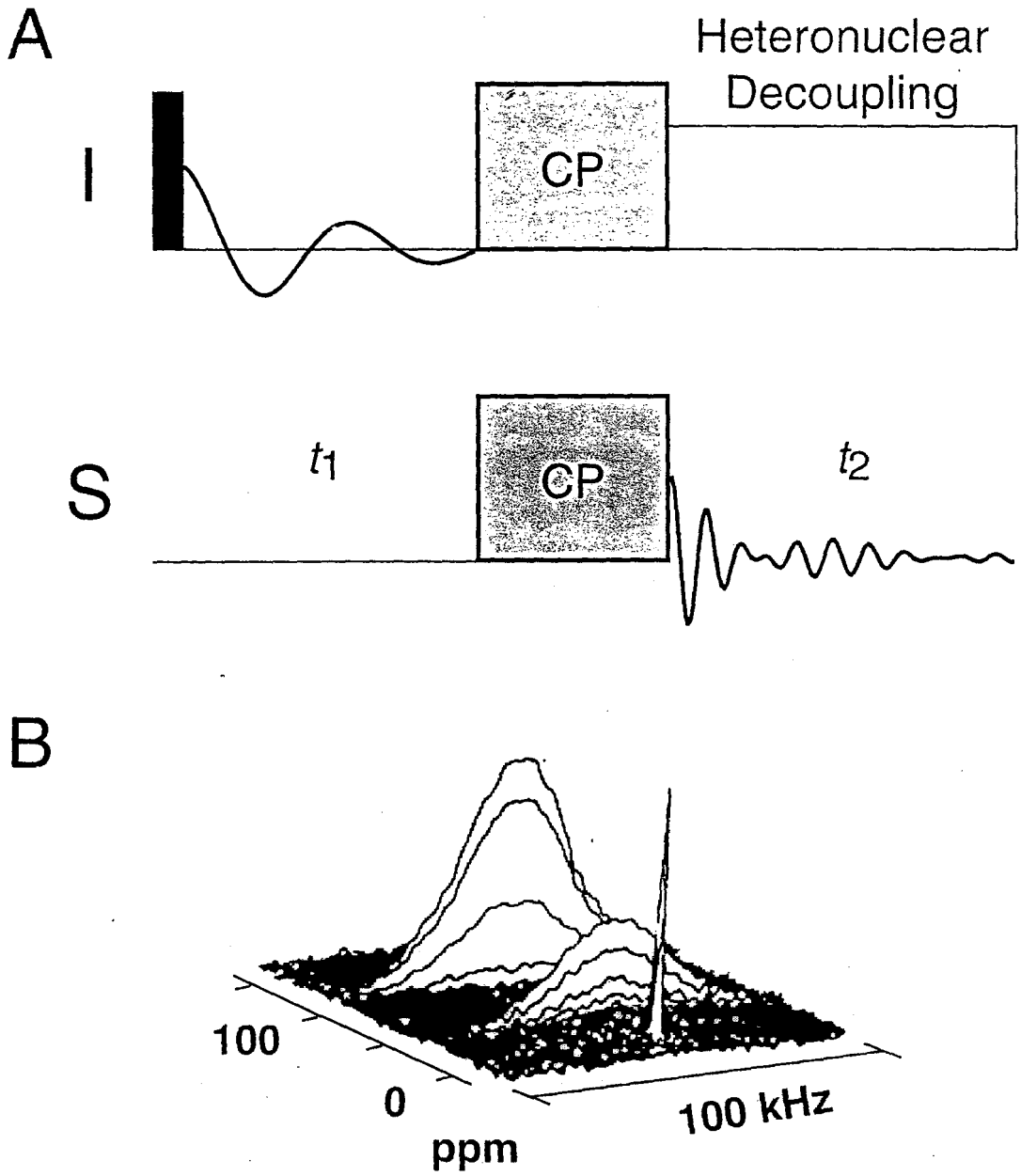

Figure 1.3.2. The WISE experiment. (A) Pulse sequence for the correlation of ^{1}H and ^{13}C resonances via WISE. (B) Two-dimensional ^{1}H-^{13}C WISE spectrum of PS-*b*-PDMS (50:50 mol %). The broad ^{1}H linewidths correspond to protons that are rigid, while narrow ^{1}H linewidths are due to protons that are mobile, thus averaging away H_{II}. (Reproduced from reference [17], with permission.)

x-y plane. During t_1, the magnetization then evolves under the ^{1}H NMR Hamiltonian ($H_{cs} + H_{II} + H_{IS}$), after which magnetization is transferred via cross polarization to neighboring ^{13}C nuclei. Finally, the ^{13}C magnetization is detected in t_2. Because in the WISE experiment the magnetization of a particular ^{13}C nucleus originates only from nearby ^{1}H nuclei, a two-dimensional WISE spectrum correlates broad ^{1}H resonances with the relatively narrow resonances of the neighboring ^{13}C nuclei under MAS, as shown in Figure (1.3.2B). In this manner, a normally unresolvable one-dimensional ^{1}H spectrum is separated into the contributions of various ^{1}H sites. The WISE experiment is commonly used to study dynamics in polymer systems, since the greater the mobility of a ^{1}H nucleus, the narrower its ^{1}H NMR lineshape will be. The spectrum in Figure (1.3.2B) is of a 50:50 weight percent polymer blend of polystyrene and polydimethylsiloxane. The linewidths of various ^{1}H sites in the polymer blend provide information about the mobility of the different polymer components.

Although WISE does allow the separation and study of broad ^{1}H resonances based on their coupling to nearby ^{13}C nuclei, this experiment does not achieve the original goal set forth in this subsection, which was to remove the ^{1}H homonuclear coupling and obtain a resolved ^{1}H chemical shift spectrum. However, 2D NMR does provide the framework necessary to achieve this goal. Since the magnetization evolving in the period t_1 is not directly detected, there is no harm in applying RF pulses to the magnetization so long as the natural evolutions of the Zeeman and chemical shift Hamiltonians are not interrupted. Therefore, as will be shown in the next section, by using the appropriate *homonuclear* decoupling sequence, the ^{1}H-^{1}H dipolar coupling can be removed.

1.3.2 - Homonuclear Dipolar Decoupling

Thus far, the discussion of dipolar decoupling has been limited to the heteronuclear case, where the dipolar coupling between two sets of spins, I and S, is removed by applying a strong RF field to the I spins while the S spins evolve. The success of CW decoupling depends strongly on the form of H_{IS}, which is proportional to I_zS_z. By constantly rotating the I-spins around one axis with a continuous RF field, the sign of I_zS_z oscillates between positive and negative, producing a time average of zero. Unfortunately, the homonuclear dipolar coupling is related to $I_{1z}I_{2z}$, and so continuous wave irradiation of the I-spins around one axis will have no effect on the sign of H_{II}. Therefore, to eliminate the homonuclear dipolar coupling, a multiple-pulse technique must be employed that toggles the I-spin magnetization between *all three* axes. One such technique is WAHUHA or WHH-4[18].

1.3.2.1 WAHUHA

To understand how the WAHUHA sequence works, consider the form of the homonuclear dipolar Hamiltonian. Depending on the direction of the I-spin magnetization, the homonuclear dipolar Hamiltonian can be written as H_{xx}, H_{yy}, or H_{zz}, where

$$H_{xx} = \frac{\hbar\gamma_I^2}{r_{I_1I_2}^3}\frac{1}{2}\left(1-3\cos^2\theta\right)\left(3I_{1x}I_{2x}-(\boldsymbol{I}_1\cdot\boldsymbol{I}_2)\right), \tag{1.3.1}$$

$$H_{yy} = \frac{\hbar\gamma_I^2}{r_{I_1I_2}^3}\frac{1}{2}\left(1-3\cos^2\theta\right)\left(3I_{1y}I_{2y}-(\boldsymbol{I}_1\cdot\boldsymbol{I}_2)\right), \tag{1.3.2}$$

and

$$H_{zz} = \frac{\hbar\gamma_I^2}{r_{I_1I_2}^3}\frac{1}{2}\left(1-3\cos^2\theta\right)\left(3I_{1z}I_{2z}-(I_1\cdot I_2)\right). \tag{1.3.3}$$

Since the dot product of the two angular momentum operators, $I_1 \cdot I_2$, can be written as

$$I_1 \cdot I_2 = I_{1x}I_{2x} + I_{1y}I_{2y} + I_{1z}I_{2z}, \tag{1.3.4}$$

the sum of $H_{xx} + H_{yy} + H_{zz} = 0$. Therefore, any pulse sequence that places the I-spin magnetization along the x-, y-, and z-axes for equal periods of time should successfully eliminate the homonuclear dipolar coupling. As can be seen in Figure (1.3.3), the WAHUHA sequence utilizes a series of $\frac{\pi}{2}$-pulses to toggle the magnetization between the three axes, so that over a single period, τ, the homonuclear decoupling is removed. On the other hand, the chemical shift is proportional to I_z alone, and thus the sum of the chemical shift evolution at each axis is not zero, although it is scaled by a factor of $\frac{1}{\sqrt{3}}$ [18]. Thus, the WHH-4 sequence accomplishes the goal of eliminating the ^{1}H-^{1}H homonuclear dipolar coupling while still allowing the magnetization to evolve under H_{cs}.

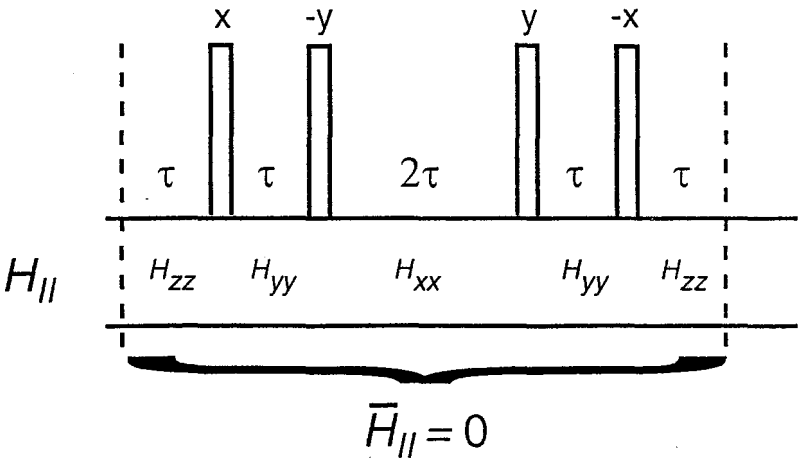

Figure 1.3.3. Pulse sequence for one cycle of the 4-pulse WAHUHA decoupling sequence.

1.3.2.2 Decoupling Supercycles

Although under ideal conditions the WAHUHA sequence is very effective at removing the homonuclear dipolar interaction, solid-state NMR is very rarely performed under ideal conditions. Pulse imperfections and chemical shifts can often interfere with ^{1}H decoupling using WHH-4[19, 20]. Fortunately, these problems can be obviated to a large extent by the use of decoupling *supercycles*, which are repetitive implementations of simple sequences like WHH-4, with specific phase shifts at the start of each new cycle[19-21]. For instance, the supercycle MREV-8[21, 22] is a composite sequence of two WHH-4 pulse trains, with a 180° phase shift in three of the last four pulses (Figure 1.3.4). Since in the last 4 pulses the magnetization retraces the path generated by the first 4 pulses, the MREV-8 sequence eliminates problems with pulse imperfection and, to an extent, problems with nuclei that have large chemical shifts. In addition to MREV-8, there exist many more complex decoupling supercycles, including BLEW-12[23], BR-24[24].

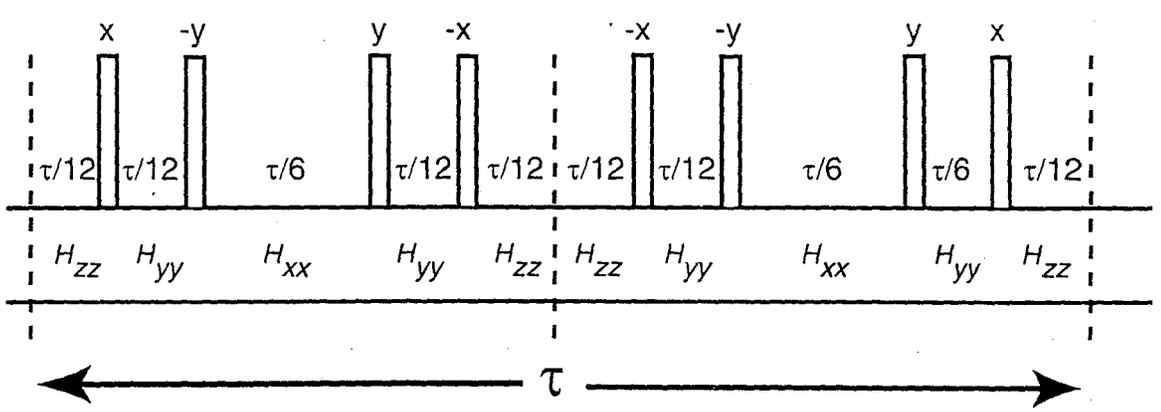

Figure 1.3.4. Pulse sequence for one cycle of the MREV-8 decoupling sequence.

There is one complication that must be considered when using a homonuclear decoupling sequence under MAS. Both magic angle spinning and multi-pulse

decoupling affect the time-average of H_{II} in different ways. However, the two can interfere with each other when the spinning speed is very high (so that the rotor period is very short)[25]. Since this interference can often degrade the effectiveness of multi-pulse decoupling sequences, it is advantageous to optimize the multiple-pulse sequence to improve their performance under MAS. First, the pulse cycles should be rotor synchronized; that is, an integer number of pulse trains should be applied per rotor cycle. Second, as many pulse cycles should be applied per rotor period as possible. Unfortunately, these two ideas make implementation of long sequences (especially the 24 pulse BR-24 sequence) difficult under fast MAS, where the rotor cycle can be as short as 30 μs. One alternative is to use an off-resonance decoupling technique such as Frequency-Switched Lee-Goldberg decoupling (FS-LG)[26, 27]. The full cycle time for FS-LG is typically between ~10-20 μs, which is short compared to the rotor period even when spinning at a frequency 30-50 kHz. However, in spite of its very short cycle time, FS-LG is a very effective decoupling sequence that has been used with great success at all spinning speeds.

1.3.3 - Solid-State Heteronuclear Correlation Spectroscopy: HETCOR

Like HSQC and HMQC in liquid-state NMR, the HETCOR experiment[28, 29] in solids correlates ^{1}H chemical shifts with the chemical shifts of another nucleus, such as ^{13}C or ^{15}N. One possible HETCOR sequence for ^{1}H-^{13}C correlations is shown in Figure (1.3.5). Like the WISE sequence, the ^{1}H magnetization is first excited with a $\frac{\pi}{2}$-pulse.

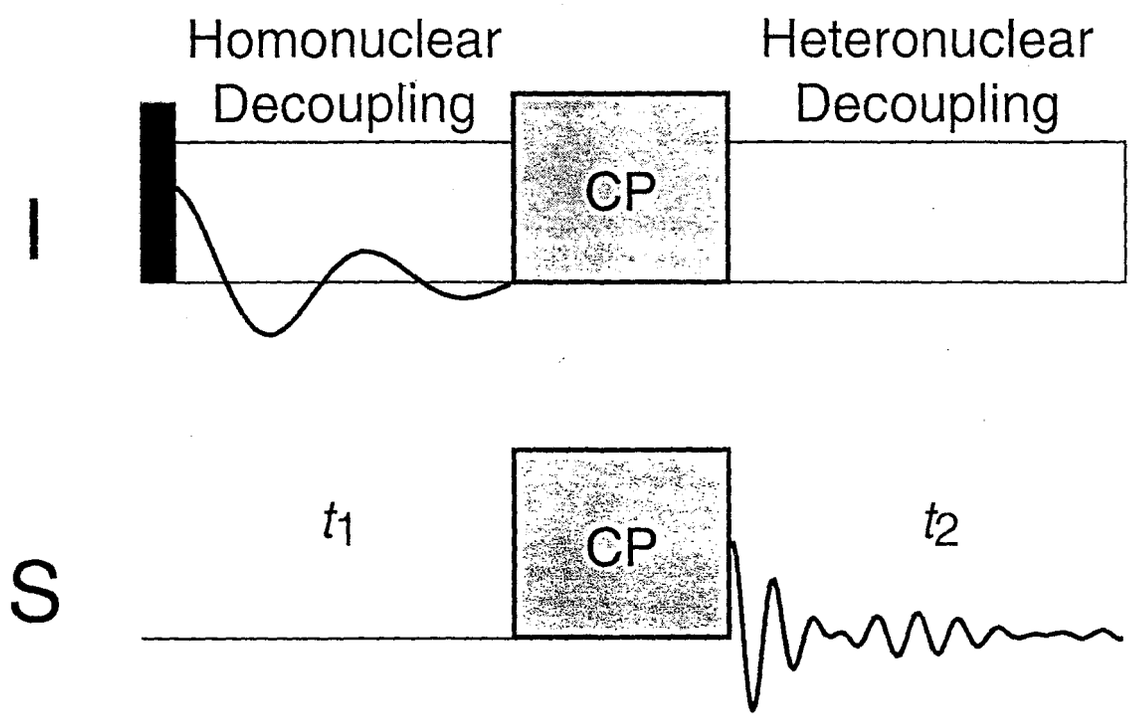

Figure 1.3.5. A possible implementation of the HETCOR experiment. The pulse sequence is identical to that of the WISE experiment, except for the incorporation of homonuclear dipolar decoupling pulses during the indirect dimension. Heteronuclear decoupling of the S-spins can also be incorporated into the indirect dimension.

During the t_1 period, protons are decoupled from each other using one of the decoupling techniques mentioned in the previous subsection. An optional CW decoupling field can be applied to the ^{13}C nuclei so that H_{IS} is also removed and the protons will evolve only under H_{cs}. After t_1, magnetization is transferred to the ^{13}C nuclei via CP, and is then detected in t_2. Figure (1.3.6) shows a ^{1}H-^{13}C HETCOR spectrum of uniformly ^{13}C-labeled chlorophyll α aggregates obtained using FS-LG homonuclear dipolar decoupling during t_1. Although the ^{1}H resonances are still somewhat broad (~1-2 ppm), they are sufficiently narrow to observe and measure the variety of ^{1}H chemical shifts in the sample.

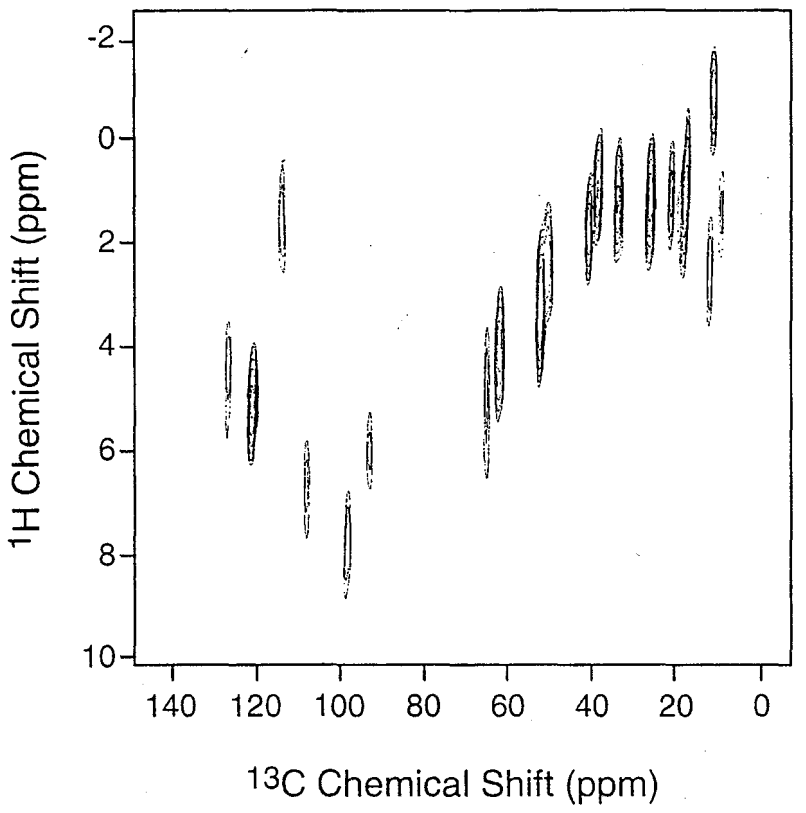

Figure 1.3.6. ^{1}H-^{13}C HETCOR spectrum of uniformly ^{13}C labeled chlorophyll α aggregates obtained at a field strength of 14.1 T and with a spinning speed of 13 kHz. FS-LG decoupling was used to remove the homonuclear dipolar coupling. (Reproduced from reference [25], with permission.)

Unlike HSQC or HMQC in liquids, which both utilize through-bond J-couplings to transfer polarization, HETCOR is a strictly dipolar technique, and thus correlates both through-space and through-bond interactions. As was shown in Figure (1.2.11B), strongly coupled spins transfer polarization quicker than weakly coupled spins. For this reason, the distance the magnetization travels during CP can be controlled to some extent by varying the CP mixing time. For long mixing times, the magnetization will travel much farther, producing correlations to carbons many angstroms away. Short CP mixing times will limit the distance the magnetization travels. By comparing HETCOR spectra

taken at a variety of mixing times, it is possible to gain insight into the structure of the system that is being examined.

1.3.4 - Multi-pulse Heteronuclear Dipolar Decoupling

Before leaving the topic of multi-pulse NMR, let us once again return to the topic of heteronuclear dipolar decoupling. Thus far, the discussion of heteronuclear decoupling has been limited to brute-force CW irradiation. However, the beauty and efficiency of multiple-pulse decoupling in the homonuclear case begs the question, "Can a multiple-pulse sequence be employed for heteronuclear decoupling?" Indeed, the answer is yes; a wealth of multiple-pulse sequences exists for removing the heteronuclear dipolar coupling, such as WALTZ-16[30], COMARO-2[31], and MLEV-16[32]. Unfortunately, because of the same interference effects that arise under MAS that were discussed in the previous subsection, multiple-pulse sequences are rarely more efficient than high-power CW decoupling in high-speed MAS experiments. However, there is a heteronuclear decoupling technique called two-pulse phase modulation (TPPM)[33] that incorporates some degree of multi-pulse phase shifting into a continuous-wave irradiation. As shown in Figure (1.3.7), the TPPM sequence divides the CW irradiation into phase alternating sections, which are between $(\theta + \phi)$ and $(\theta - \phi)$. For instance, if θ is 90° and ϕ is 15°, then the phase is alternated between 75° and 105°. Typically, the

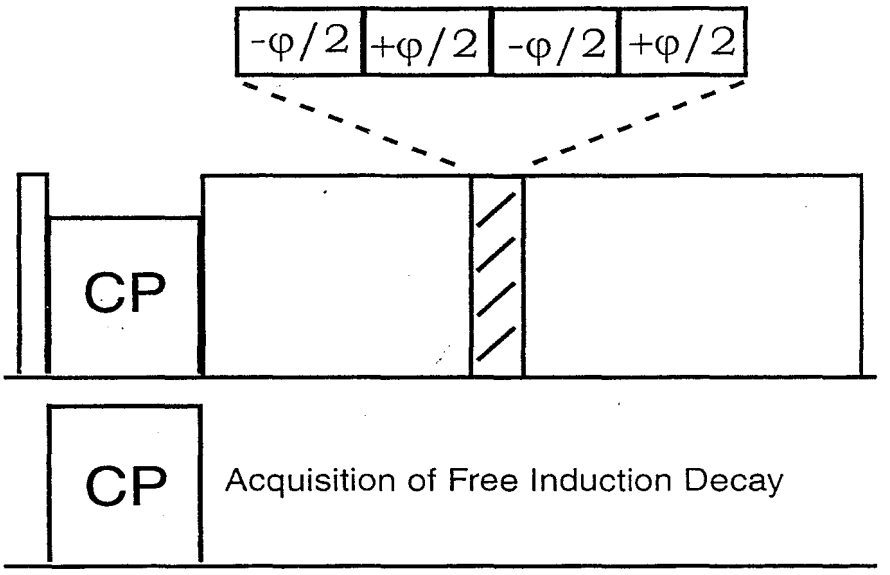

Figure 1.3.7. A diagram of the two-pulse phase modulation (TPPM) heteronuclear decoupling sequence. RF is continuously applied, with an alternating phase-shift of $+\varphi$ and $-\varphi$ from some angle θ (typically 90°) for a pulse length of τ. The values of θ, φ, and τ are optimized to achieve maximum decoupling efficiency.

series of discrete time periods are on the order of 5-20 μs. The values of θ, ϕ, and τ must be optimized in order to produce the smallest possible linewidths in the acquired spectrum[34]. Figure (1.3.8) shows a spectrum of ^{13}C labeled calcium formate acquired under TPPM decoupling (Figure 1.3.8A) and under CW decoupling (Figure 1.3.8B). With the improved resolution resulting from the use of TPPM decoupling, the 80 Hz chemical shift difference between the two ^{13}C sites in calcium formate is resolved, whereas with standard CW decoupling it is not. When coupled with high-speed MAS, the effects of TPPM decoupling can be quite stunning, as can be seen in the cyclosporin-A spectrum shown in Figure (1.3.9). Although the linewidths in this natural abundance ^{13}C spectrum are still larger than would typically be seen in a liquid-state NMR spectrum, at 10 to 50 Hz, they are sufficiently small to resolve the vast majority of the resonances in the spectrum.

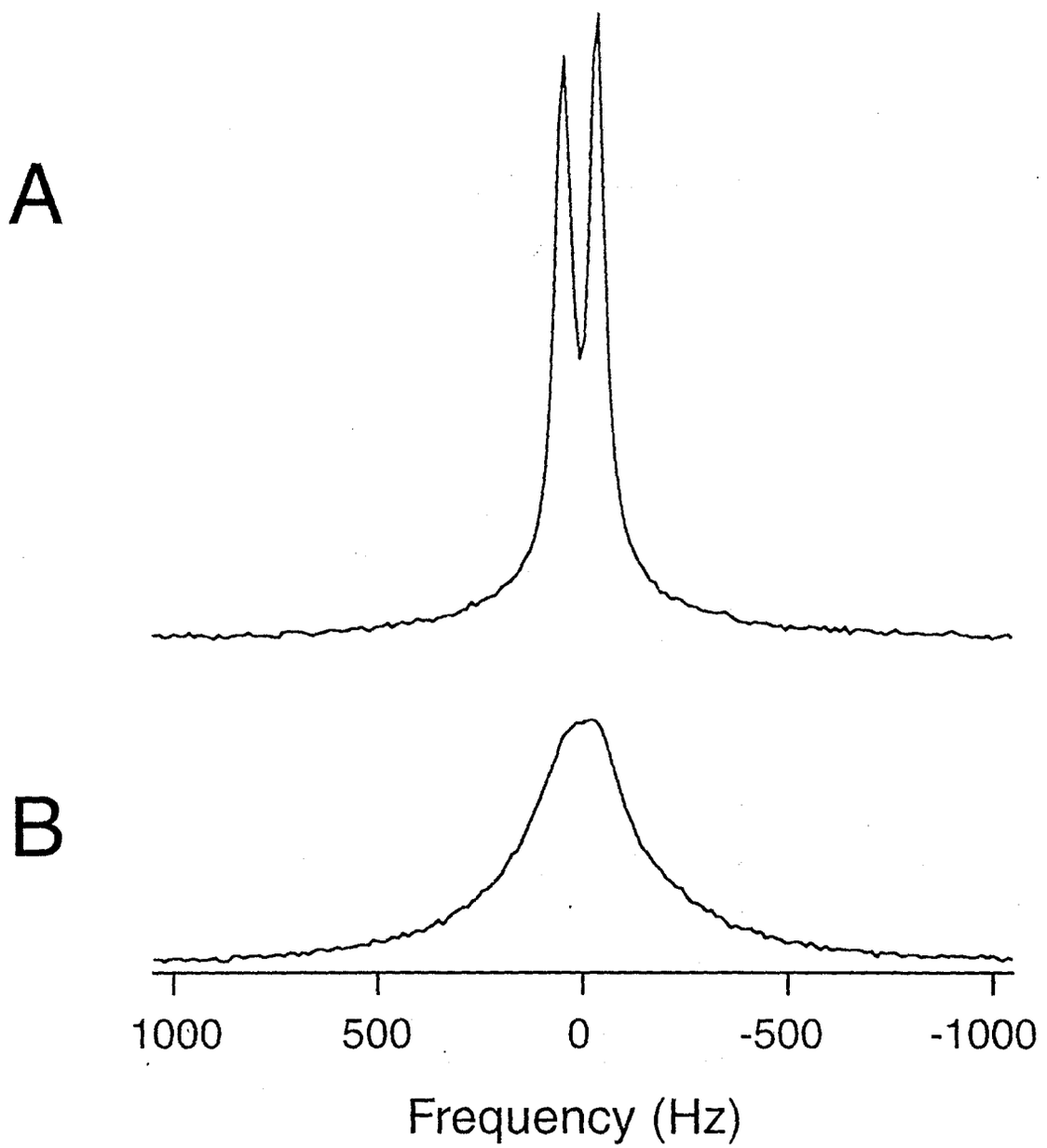

Figure 1.3.8. ^{13}C CPMAS spectra of calcium formate obtained using TPPM decoupling (A) and using continuous-wave decoupling (B). In both cases, the spinning speed was 10.7 kHz. The splitting observed in is due to the 80 Hz chemical shift difference between the two ^{13}C sites in calcium formate. (Reproduced from reference [33], with permission).

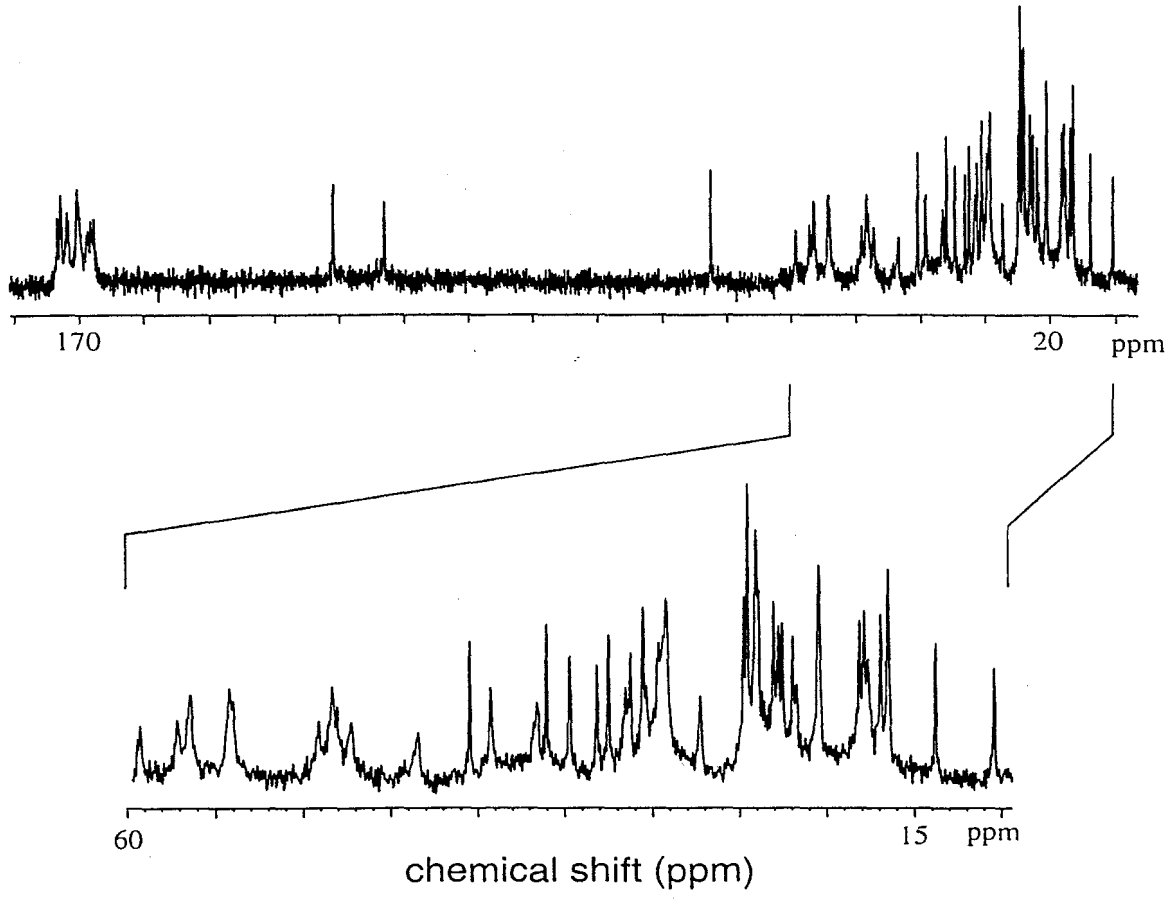

Figure 1.3.9. 125 MHz ^{13}C CPMAS spectrum of cyclosporin-A, a cyclic decapeptide, obtained at a spinning frequency of 33.3 kHz using TPPM decoupling ($\theta = 170°$ and $\varphi = 20°$). With the combination of high spinning speeds and TPPM decoupling ^{13}C linewidths are ~10-50 Hz are obtained. (Reproduced from reference [16], with permission.)

1.3.5 - Summary

In this section, it was demonstrated that it is possible, through a combination of multi-pulse decoupling and two-dimensional NMR, to obtain ^{1}H NMR spectra with reasonably high resolution. Although multi-pulse homonuclear decoupling of protons can often be more trouble than it is worth, the concept of using a series of pulses to manipulate a Hamiltonian has applications far beyond homonuclear decoupling. As will be seen in the next section, through the use of clever pulse sequences and two-dimensional NMR, it is possible to derive information from interactions that are removed

under MAS, such as the CSA or dipolar couplings, without sacrificing the high resolution that was obtained with the techniques described in section 1.2.

1.4 Reintroducing Lost Hamiltonians

Section 1.2 addressed the question of how to remove some of the unwanted interactions that are found in solid-state NMR, such as dipolar couplings and the CSA. It was shown that by utilizing techniques like magic angle spinning and high-power spin decoupling it is possible to remove these anisotropic interactions and leave only a high-resolution "liquid-like" spectrum like the one shown in Figure (1.2.12A). There is, however, an important issue to consider: the lineshapes produced by dipolar couplings and the CSA can provide information about the sample, and by removing these interactions through spinning and decoupling, this information is lost. In this section, techniques that selectively reintroduce dipolar couplings and the chemical shift anisotropy under magic angle spinning and how the information obtained by these approaches can be used to study molecular structure will be discussed. Although there exists a vast number of ways to reintroduce the dipolar coupling and the CSA, only a limited number of these techniques that are both simple to understand and easy to implement will be described.

1.4.1 - Distance Measurements in Solids

An integral part of structure determination in molecular systems is the measurement of distances between atoms. In liquid-state NMR, this is usually accomplished through the measurement of cross-relaxation rates using Nuclear Overhauser Effect SpectroscopY or NOESY. Unfortunately, such techniques usually cannot be used in solids since cross relaxation is short-circuited by more efficient dipole-

dipole relaxation processes. However, there is a way to measure distances in solids using heteronuclear and homonuclear dipolar couplings.

As shown in Equation (1.2.2), the strength of the dipolar coupling between two nuclei is proportional to the inverse cube of the internuclear distance. Therefore, if one could measure the magnitude of the dipolar coupling between two nuclei, their internuclear distance can be determined. However, with the exception of couplings involving protons (e.g., ^{1}H-^{1}H or ^{1}H-^{13}C), homonuclear and heteronuclear dipolar couplings are usually removed under magic angle spinning, since the magnitude of the coupling is less than the spinning speed. Thus, to measure dipolar couplings while retaining the high-resolution afforded by MAS, the couplings must be selectively reintroduced.

1.4.1.1 Heteronuclear Recoupling: REDOR

Hamiltonians in NMR can be separated into two components, one dependent on the spatial orientation of the nucleus or nuclei with respect to B_0, and the other dependent on the orientation of the spin. For instance, the heteronuclear dipolar Hamiltonian introduced in section 1.2,

$$H_{IS} = \frac{\hbar\gamma_I\gamma_S}{r_{IS}^3}\left(1-3\cos^2\theta\right)I_zS_z, \tag{4.1}$$

can be separated into the magnitude of the dipolar coupling, d

$$d = \frac{\hbar\gamma_I\gamma_S}{r_{IS}^3}, \tag{4.2}$$

multiplied by a spatial component that depends on θ,

$$A_{IS} = \left(1-3\cos^2\theta\right), \tag{4.3}$$

and a spin component involving the nuclear spin operators, I and S,

(4.4) $$T_{IS} = I_z S_z .$$

In previous sections, it was shown how it is possible to manipulate both the spin and the spatial components of an NMR Hamiltonian. For instance, in CW spin decoupling, either the I- or S-spin is rotated by constant RF irradiation, so that the time average of the spin component of the heteronuclear dipolar coupling is zero. For spin decoupling, recoupling is quite simple: turn on the RF irradiation and the interaction is removed, turn off the RF irradiation and the dipolar coupling returns. Unfortunately, recoupling a dipolar interaction removed by magic angle spinning is more complicated, for it is no simple task to turn the spinning on and off quickly[35]. However, by properly manipulating the *spin* component of the dipolar Hamiltonian, it is possible to counteract the effect of MAS on the heteronuclear dipolar coupling.

As a single crystallite moves in its conical path under MAS, the value of the heteronuclear dipolar coupling, H_{IS}, changes both intensity and sign, as shown in Figure (1.4.1A). Over a single rotor period, the integrated value of H_{IS} is zero, so the dipolar coupling is effectively removed under MAS. However, by applying pulses at the proper intervals, it is possible to interfere with the trajectory of H_{IS} so that over one rotor period the value of H_{IS} is non-zero. One simple way to alter the trajectory of H_{IS} under MAS is to apply π-pulses, because every time a π-pulse is applied to say the S-spin, the spin is flipped ($S_z \rightarrow -S_z$) and the sign of H_{IS} changes. Indeed, by applying two π-pulses per rotor period as shown in Figure (1.4.1B), the evolution of H_{IS} can be altered in such a way as to recouple 70% of the heteronuclear dipolar coupling (i.e. the integrated value of H_{IS} is 70% of its static value).

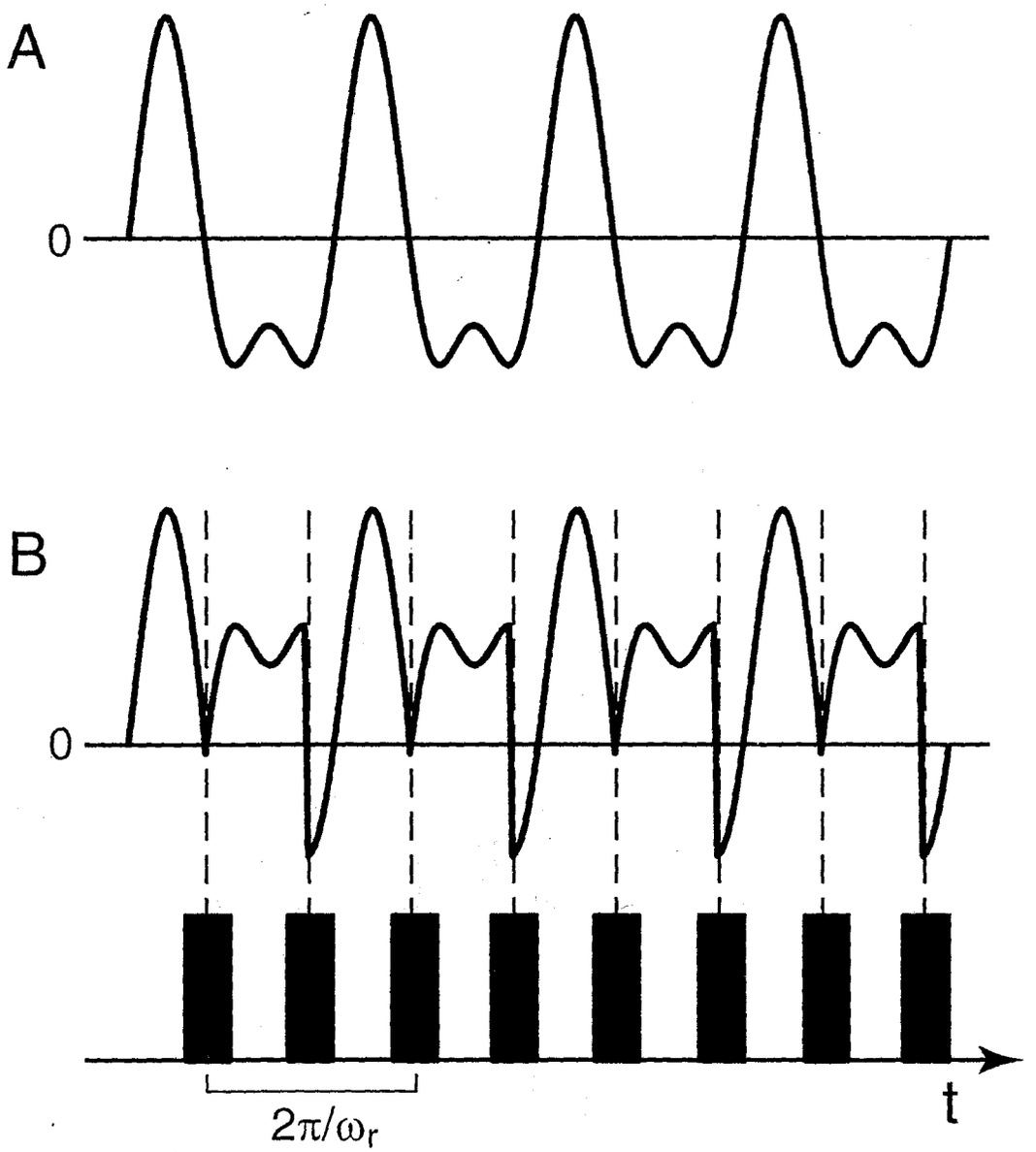

Figure 1.4.1. Time-dependent behavior of the heteronuclear dipolar coupling. (A) The time-dependent evolution of the heteronuclear dipolar Hamiltonian, H_{IS}, under MAS. Since the integral of the dipolar coupling over a single rotor cycle is zero, the dipolar coupling is effectively removed if the spinning speed is sufficiently high. (B) The time-dependent of H_{IS} under MAS with two 180° pulses on the S-spin per rotor cycle. Each 180° pulse reverses the sign of the dipolar coupling Hamiltonian, creating a time evolution which no longer averages to zero. (Reproduced from reference [16], with permission.)

This two π-pulse technique, known as Rotational Echo DOuble Resonance or REDOR[1, 2], is a powerful tool for determining dipolar couplings between two

heteronuclei, like ^{13}C and ^{15}N. The pulse sequence for REDOR is shown in Figure (1.4.2). The ^{13}C nuclei are first polarized via CP from the protons, and are then allowed to evolve for a period τ_m before detection. During τ_m, two ^{15}N π-pulses are applied every rotor period, so that the ^{13}C-^{15}N

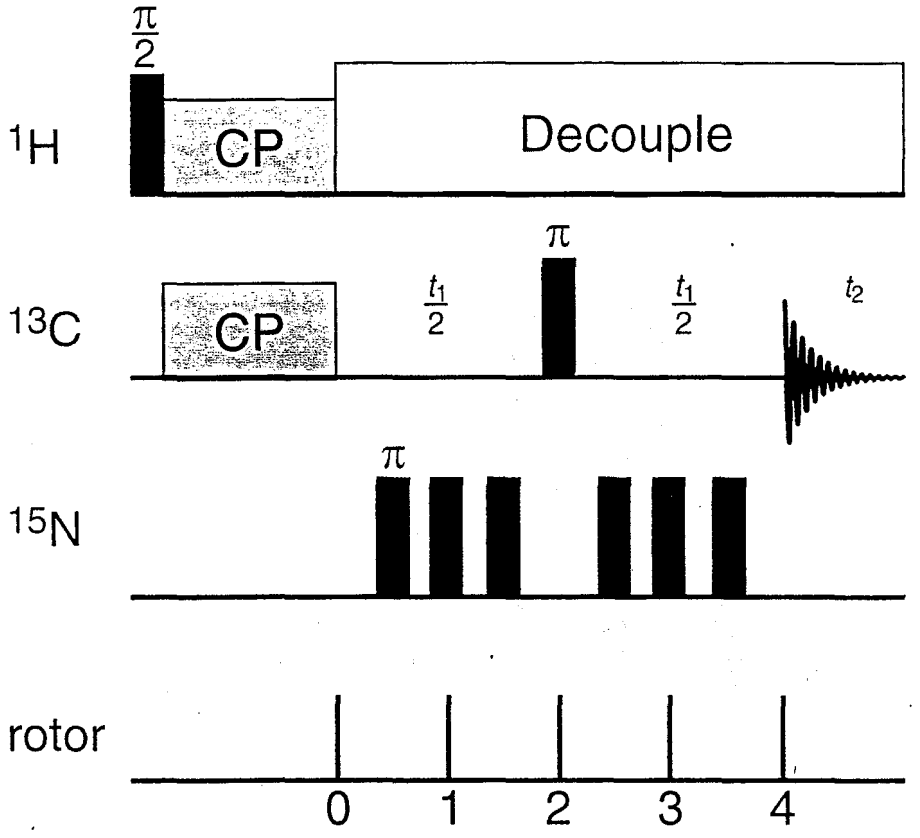

Figure 1.4.2. The REDOR pulse sequence. Cross-polarization of the ^{13}C nuclei is followed by a period t_1 in which the ^{13}C magnetization is dephased by the application of a series of pulses on the ^{15}N magnetization, which recouple the ^{13}C-^{15}N dipolar coupling[16].

heteronuclear dipolar coupling is reintroduced. The experiment is then repeated without the ^{15}N pulses and the spectra are compared. With the ^{13}C-^{15}N dipolar coupling reintroduced, the ^{13}C magnetization will decay due to the dephasing effect of the heteronuclear dipolar coupling. By adjusting the value of τ_m and measuring the

normalized decay of the magnetization, a REDOR decay curve can be created, such as the one for 10% 1-^{13}C,^{15}N glycine shown in Figure (1.4.3). From the fitted line, it is

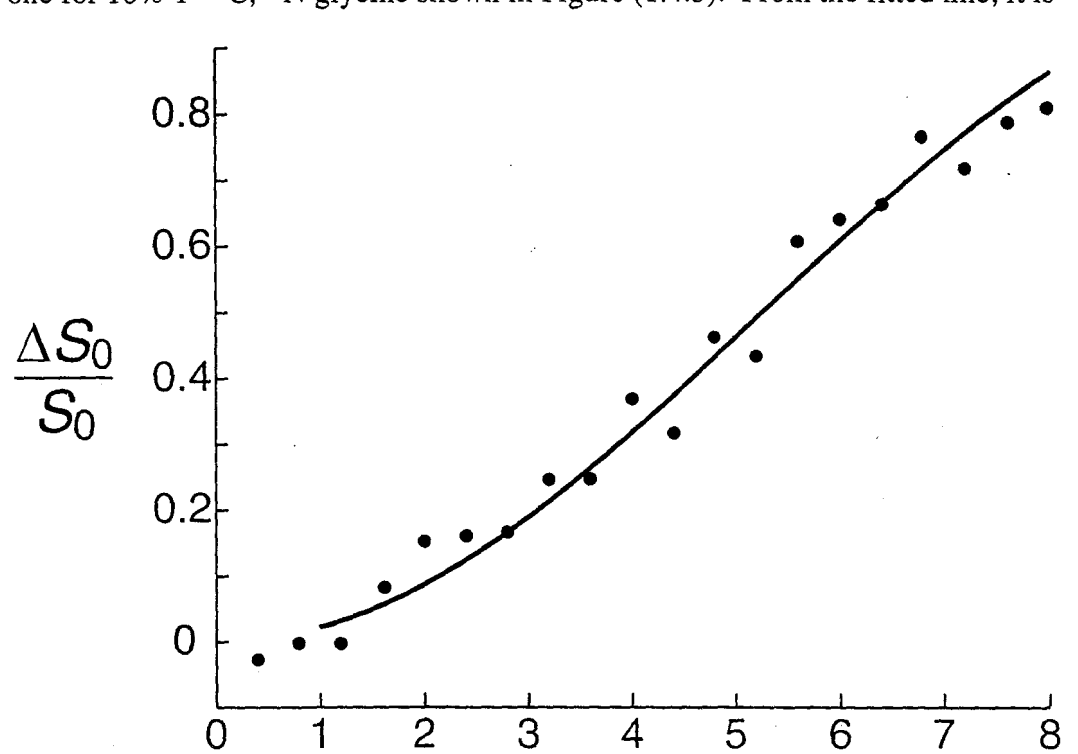

Figure 1.4.3. Decay of the ^{13}C magnetization in 1-^{13}C and ^{15}N labeled glycine as a function of the length of the dephasing period, t_1. The quantity ΔS/S (known as the REDOR difference) is the normalized difference between the ^{13}C signal with and without pulsing the ^{15}N nuclei. By fitting the decay of the ^{13}C magnetization, the ^{13}C-^{15}N dipolar coupling was determined to be 767 Hz. (Courtesy of David D. Laws.)

possible to determine the magnitude of the ^{13}C-^{15}N dipolar coupling, *d*, which for 1-^{13}C,^{15}N glycine was found to be 767 Hz. The ^{15}N-^{13}C internuclear distance was then found to be 2.45 Å using Equation (1.4.2). As the strength of the heteronuclear dipolar coupling approaches ~50 Hz, it can be difficult to determine distances using REDOR. This corresponds to a ^{15}N-^{13}C distance of ~5 Å and a ^{13}C-^{31}P distance of ~7.5 Å. It should be noted however, that these distances are much further than is possible using liquid-state NMR.

1.4.1.2 Homonuclear Recoupling: DRAMA and R2

Homonuclear dipolar recoupling can be accomplished in much the same way as heteronuclear dipolar recoupling—by manipulating the spin component of the dipolar Hamiltonian, one can interfere with the motional averaging produced by the spinning rotor. The principle difference between heteronuclear and homonuclear dipolar recoupling lies in the impossibility of individually addressing different homonuclear spins. In REDOR, one can repeatedly alternate the sign of H_{IS} by applying pulses to either the I- or the S-spin. Unfortunately, for a homonuclear I_1I_2-spin system, the I_1- and I_2-spins have very similar (and some times even the same) resonant frequencies, and so any π-pulse intended to change the sign of I_{1z}, will also result in changing the sign of I_{2z}. Thus, the value of H_{II} is unaffected by the application of a π-pulse.

One alternative to using π-pulses is to use $\frac{\pi}{2}$-pulses, which instead change the *direction* of the dipolar coupling. As was shown in Figure (1.4.1A), the spatial evolution of the dipolar Hamiltonian is such that its value is zero over a single rotor period. This is true regardless of the whether the spin component of the dipolar Hamiltonian, T_{II}, is equal to T_{xx}, T_{yy}, or T_{zz}, where

$$\begin{aligned} T_{xx} &= 3I_{1x}I_{2x} - \boldsymbol{I}_1 \cdot \boldsymbol{I}_2 \\ T_{yy} &= 3I_{1y}I_{2y} - \boldsymbol{I}_1 \cdot \boldsymbol{I}_2 \\ T_{zz} &= 3I_{1z}I_{2z} - \boldsymbol{I}_1 \cdot \boldsymbol{I}_2. \end{aligned} \tag{1.4.5}$$

However, by toggling between one or more of these spin states during the rotor period by the application of $\frac{\pi}{2}$-pulses, the averaging produced by the MAS rotor can be interrupted.

One technique that makes use of $\frac{\pi}{2}$-pulses to toggle between different spin states is DRAMA, which stands for Dipolar Recovery At the Magic Angle[36]. During the DRAMA pulse sequence, shown in Figure (1.4.4A), two $\frac{\pi}{2}$-pulses per rotor period toggle

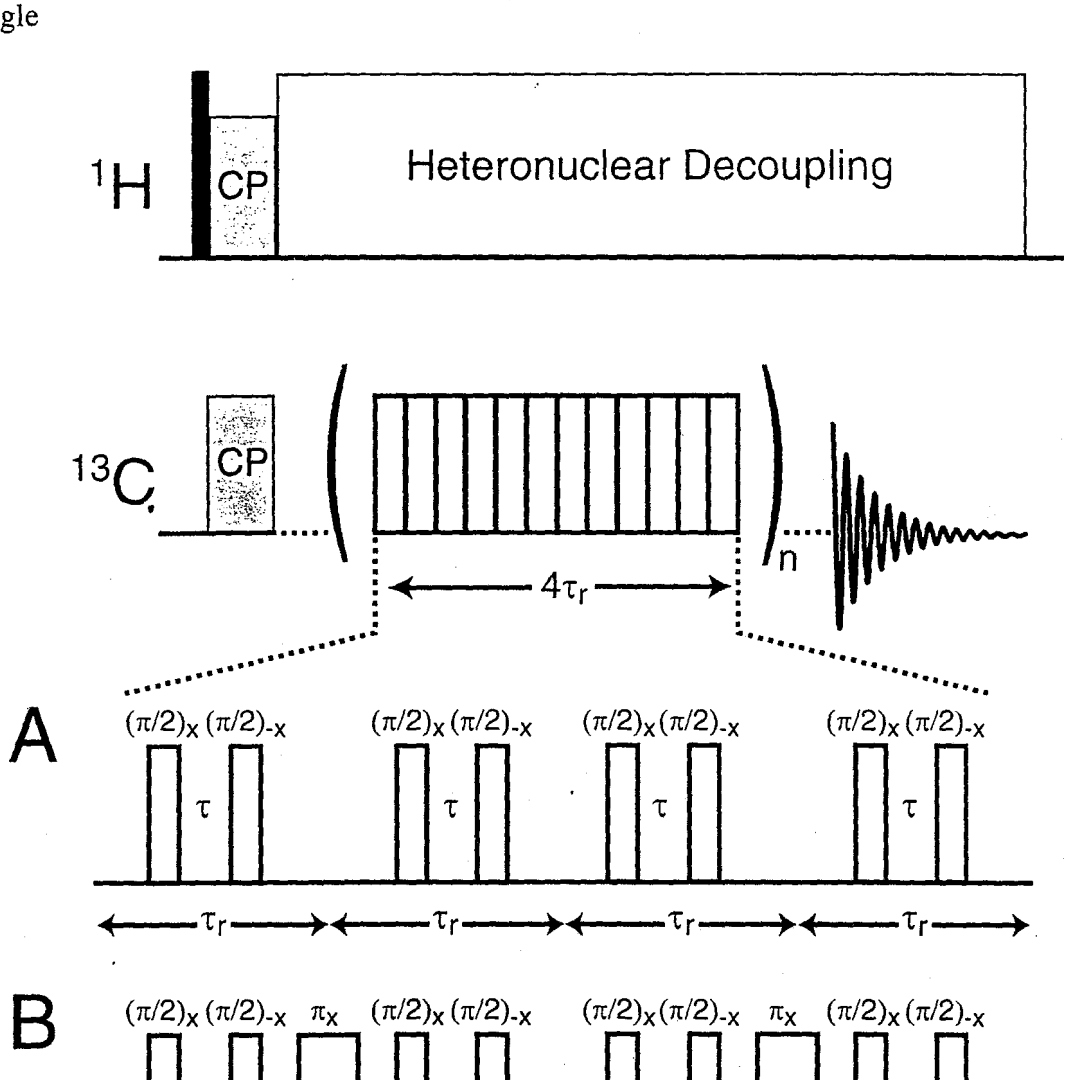

Figure 1.4.4. (A) Pulse sequence for one cycle of the DRAMA homonuclear dipolar recoupling sequence. The partial recoupling of the CSA that occurs under the sequence in (A) can be removed by applying a π-pulse at the end of each rotor cycle, as shown in (B).

the magnetization from the z-axis to the y-axis and back again. When optimized such that the magnetization spends half of the rotor period along the z-axis and half of the rotor period along the y-axis (i.e. $\tau = \frac{\tau_r}{2}$), DRAMA is capable of recoupling up to 45% of the homonuclear dipolar coupling. Unfortunately, the two-pulse per rotor period sequence also interrupts the averaging of the chemical shift anisotropy under MAS, so the best implementation of the DRAMA sequence also includes an occasional π-pulse, as shown in Figure (1.4.4B), to remove the CSA.

Distance determination via DRAMA is carried out in generally the same way as REDOR. During the mixing period, τ_m, the magnetization of the recoupled nuclei will decay due to the dephasing effects of the homonuclear dipolar coupling. For example, Figure (1.4.5) shows solid-state NMR spectra of [carbonyl-^{13}C]-polycarbonate obtained using the pulse sequence in Figure (1.4.4B) both with (Figure 1.4.5A) and without (Figure 1.4.5B) the recoupling pulses. As the mixing time increases, the intensities of all of the ^{13}C resonances decrease because of the presence of recoupled ^{13}C-^{13}C dipolar couplings (Figure 1.4.5A). This decay is substantially larger than the natural decay of the magnetization when the DRAMA recoupling pulses are removed (Figure 1.4.5B). By measuring the decay of the ^{13}C magnetization as a function of τ_m, it is possible to determine ^{13}C-^{13}C dipolar couplings and internuclear distances. For the polycarbonate sample, ^{13}C-^{13}C internuclear distances were used to help determine a model for polycarbonate chain packing in the solid state.

Another commonly used method for recoupling homonuclear dipolar couplings under MAS is rotational resonance or R2[3]. Unlike DRAMA, rotational resonance does

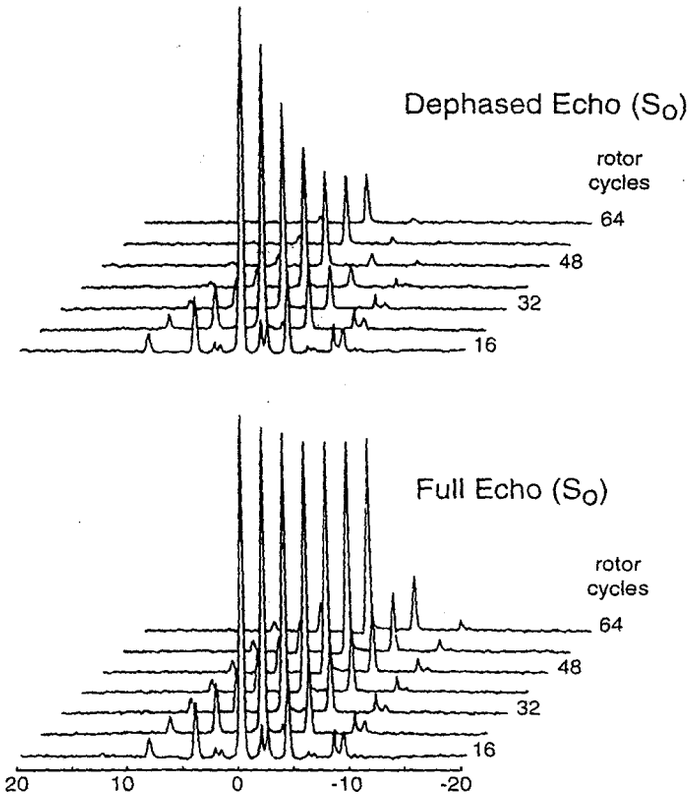

Figure 1.4.5. Solid-state ^{13}C NMR spectra of [^{13}C-carbonyl]polycarbonate obtained using the DRAMA sequence in Figure (1.4.4B). (A) Decay of the ^{13}C carbonyl resonance as a function of the mixing, τ_m. As τ_m is increased, the ^{13}C magnetization decays due to the reintroduction of the homonuclear dipolar coupling. (B) As in (A), except with the DRAMA 90°-pulses removed. The observed decay is due to the natural relaxation of the magnetization. (Reproduced from reference [37], with permission.)

not require the application of pulses to interrupt the effect of the spinning rotor—in fact, rotational resonance utilizes the spinning rotor to recouple two spins. Recall from section 1.2.5 that the $I_1 \cdot I_2$ component of the homonuclear dipolar coupling can be rewritten in terms of the "flip-flop" interaction, $(I_1^+ I_2^- + I_1^- I_2^+)$. When the chemical shifts of two nuclei differ enough that their resonance frequencies do not overlap, the "flip-flop" term disappears since it is no longer possible for the spins to undergo an energy conserving transfer of angular momentum. However, when the frequency of the MAS rotor, ω_r, is

set such that it is equal to an integer multiple of the difference in isotropic chemical shifts of the two nuclei to be recoupled,

(1.4.6) $$\Delta\omega_{iso} = n\omega_r ,$$

then the homonuclear dipolar coupling is effectively recoupled. Although the origin of this recoupling is complex, it can generally be understood by considering the rotor to be an additional source of energy for the system to bridge the energy gap between the nuclear transitions. Only when the rotor spins at one of the rotational resonance conditions dictated by Equation (1.4.6) are the nuclei recoupled. Figure (1.4.6) shows a ^{13}C CPMAS spectrum of glycine taken while spinning at 8.3 kHz, which corresponds to the $n = 1$ rotational resonance condition for glycine. The splitting is a result of the interaction between the nuclei, and is indicative of the coupling strength.

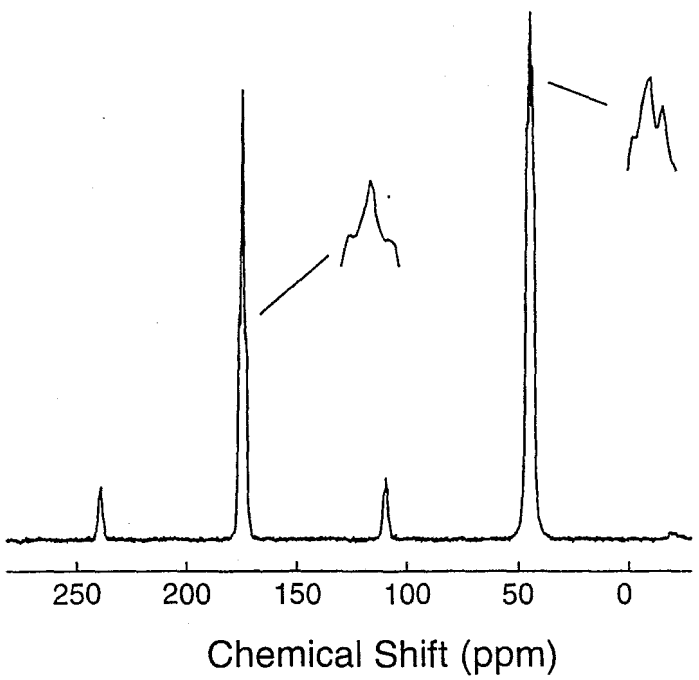

Figure 1.4.6. 125 MHz CPMAS spectra of 10% uniformly ^{13}C labeled glycine powder acquired while spinning such that the rotational resonance condition is satisfied. The 8.3 kHz spinning speed corresponds to the $n = 1$ rotational resonance condition of Equation (1.4.6). The distorted lineshapes are the result of the recoupling of H_{II}.

Distance measurement using rotational resonance is accomplished in a somewhat different manner than the recoupling techniques discussed so far. Figure (1.4.7A) shows a general pulse sequence for measuring ^{13}C-^{13}C homonuclear dipolar couplings by R^2. The first step in R^2 is to set the spectrometer frequency to the resonance frequency of one of the two nuclei to be recoupled, and set the spinning speed so that it complies with the rotational

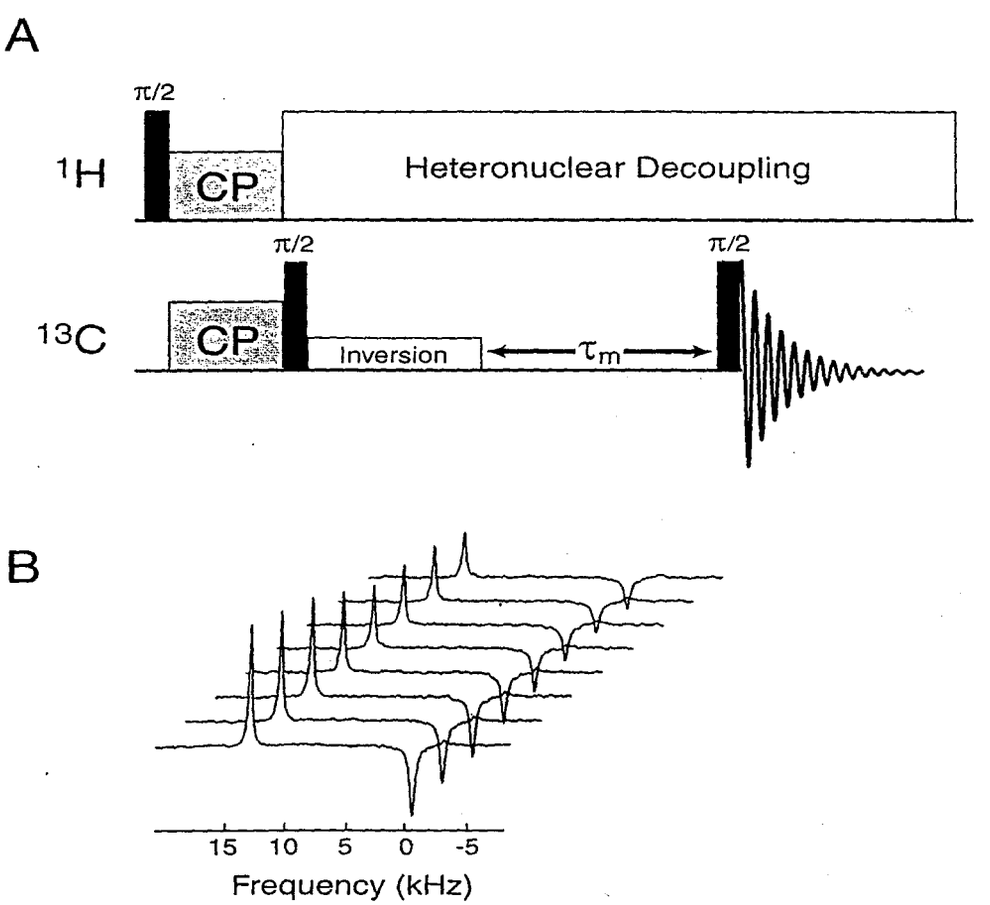

Figure 1.4.7. The rotational resonance experiment. (A) Pulse sequence for rotational resonance. Following CP from protons, the ^{13}C magnetization is stored along the z-axis and one of the resonances is inverted. The magnetization then decays for a period, τ_m, before the magnetization is returned to the x-y plane for detection. (B) Rotational resonance spectra of doubly-^{13}C labeled peptide obtained by incrementing the mixing period, τ_m. As τ_m increases, the ^{13}C nuclei have more time to exchange magnetization, and so the intensity of both resonances decreases. (Reproduced from reference [38], with permission.)

resonance condition of Equation (1.4.6). Following the initial cross-polarization step, the ^{13}C magnetization is returned to the z-axis, at which point the magnetization of the on-resonance ^{13}C nuclei is inverted using a long, low-power pulse. Absent any dipolar recoupling, the inverted ^{13}C nuclei would slowly relax back to equilibrium. However, when the ^{13}C-^{13}C nuclei are recoupled by satisfying Equation (1.4.6), they will undergo energy conserving flip-flop transitions, in which the inverted spins will "flip-up" and the uninverted spins will "flop-down". This effect is manifest in a decrease in the intensity of both resonances when the magnetization is detected after a $\frac{\pi}{2}$–pulse. In Figure (1.4.7B) a series of ^{13}C R^2 spectra of a doubly ^{13}C-labeled peptide as a function of the mixing time, τ_m is shown. By observing the decay in the intensity of both peaks, it is possible to determine the size of the dipolar coupling between the two ^{13}C sites and thus the internuclear distance.

In addition to DRAMA and rotational resonance, a plethora of homonuclear recoupling sequences have been developed, including HORROR[39], DRAWS[40], MELODRAMA[37], RFDR[41], and C7[42]. Aside from the potential for more robust recoupling, each of these sequences possess certain advantages and disadvantages when compared to DRAMA or rotational resonance. Although a comparison of these techniques will not be given in this chapter, a detailed evaluation of homonuclear recoupling techniques can be found elsewhere[43].

1.4.2 - Correlation Spectroscopy in Solid-State NMR

Thus far, techniques that allow the reintroduction of the dipolar coupling between both homo- and heteronuclei and how these techniques can be used to measure internuclear distances have been discussed. However, the reintroduction of the dipolar coupling provides a means of doing much more than simply measuring distances. Since the exchange of magnetization is most efficient between strongly coupled spins and the strength of the dipolar coupling is distance dependent, recoupled nuclei will primarily exchange magnetization with neighboring spins. Thus, dipolar recoupling in solids can be used to correlate the resonances of neighboring spins in much the same way as liquid-state techniques, such as COSY, NOESY or HMQC.

1.4.2.1 Heteronuclear Correlation Spectroscopy in Solids

The concept of heteronuclear correlation in solid-state NMR has already been introduced in section 1.3, with the discussion of the ^{1}H-^{13}C HETCOR experiment. The relative simplicity of the HETCOR experiment is largely due to the ability to transfer polarization between nuclei using cross-polarization. Unfortunately, CP is far less useful when transferring polarization between low-γ nuclei such as ^{13}C and ^{15}N because the ^{13}C-^{15}N dipolar coupling is effectively removed under MAS. Although it is possible to modify the Hartmann-Hahn condition to recouple these spins under MAS[44, 45], the practice can often be difficult.

A far more robust means of creating heteronuclear dipolar correlation spectra is to utilize a REDOR-like recoupling scheme to exchange magnetization between the ^{13}C and ^{15}N spins. Figure (1.4.8A) shows one possible pulse sequence for obtaining a ^{13}C-^{15}N

correlation spectrum in the solid-state. The ^{13}C nuclei are first polarized using CP from the protons, after which a REDOR sequence is used to recouple the ^{13}C and ^{15}N nuclei. Following the REDOR sequence, the ^{15}N spins are allowed to evolve for a period t_1 (the indirect dimension), before a second REDOR sequence is used to return magnetization to the ^{13}C spins for detection. Figures (1.4.8B-C) show two-dimensional ^{13}C-^{15}N correlation

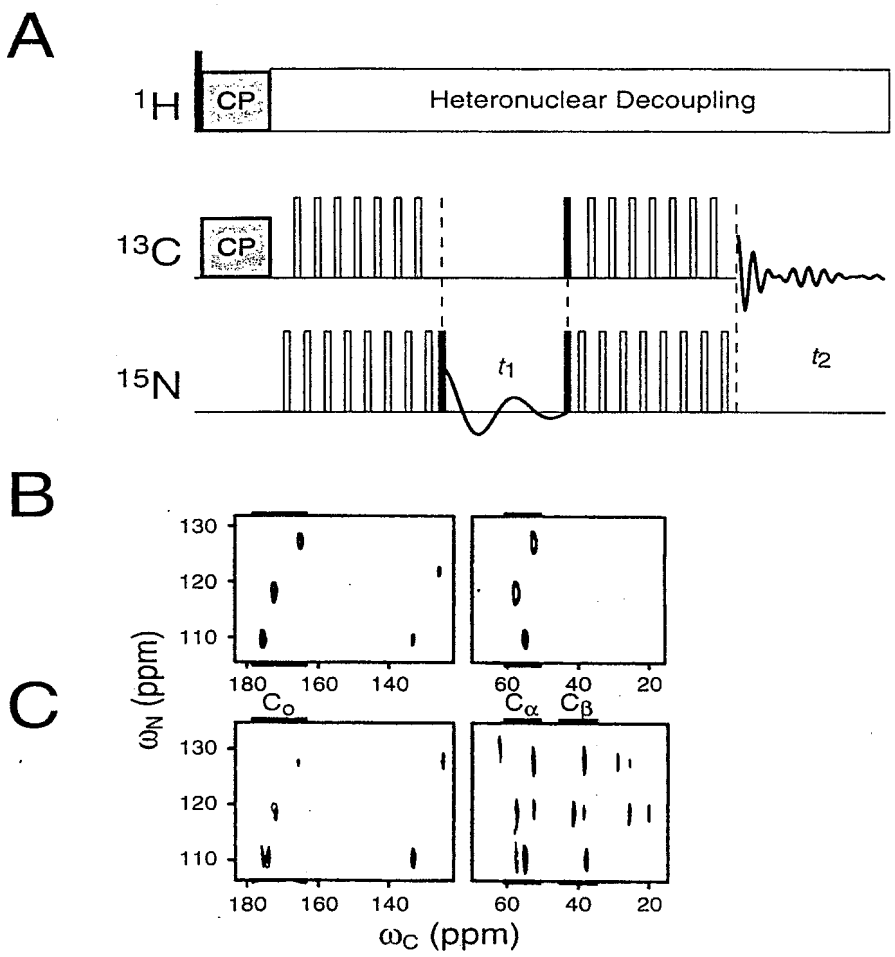

Figure 1.4.8. Heteronuclear correlation by dipolar recoupling. (A) One possible sequence for obtaining heteronuclear correlations between ^{13}C and ^{15}N nuclei. The recoupling sequence is a modified REDOR sequence that incorporates pulses on the ^{13}C nuclei in addition to the standard train of pulses on ^{15}N nuclei. (B) 2D ^{13}C-^{15}N correlation spectrum of the tripeptide Formyl-Met-Leu-Phe obtained using the pulse sequence in (A). Due to the short mixing time of 614.4 μs, the ^{13}C magnetization does not spread much further than one bond, giving rise only to N-C' and N-C_α correlations. With a mixing time of 2.46 ms (C), the magnetization travels much further, permitting the observation of N-C_β and N-C_γ correlations. (Reproduced from reference [46], with permission.)

spectra of Formyl-Met-Leu-Phe obtained with the sequence in Figure (1.4.8A) using different REDOR mixing times. With a short mixing time, τ_m, the magnetization has very little time to diffuse, and so correlations are limited to neighboring atoms, such as N-C' and N-C_α (Figure 1.4.8B). However, when the nuclei are recoupled for longer times (Figure 1.4.8C), the magnetization has more time to diffuse through the sample, leading to chemical shift correlations of non-bonded atoms, such as N-C_β and N-C_γ.

1.4.2.2 Homonuclear Correlation Spectroscopy in Solids

Two-dimensional homonuclear correlation spectra can be obtained in solids in a manner very similar to that used for heteronuclear correlations. Figure (1.4.9) shows a general scheme for ^{13}C-^{13}C homonuclear correlation spectroscopy in the solid state. The sequence begins with the cross polarization of the ^{13}C nuclei from protons. Following CP, the ^{13}C magnetization is detected indirectly during t_1. Next, a homonuclear

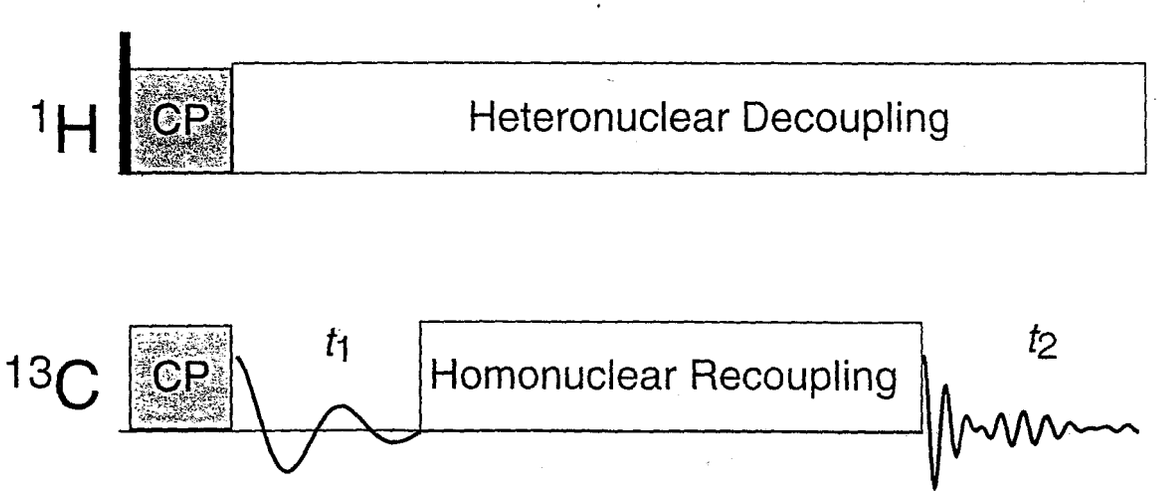

Figure 1.4.9. Generalized pulse sequence for homonuclear correlation spectroscopy using dipolar recoupling. Once the ^{13}C magnetization has evolved in the indirect dimension, a homonuclear recoupling sequence is used to exchange magnetization between neighboring ^{13}C nuclei. The ^{13}C magnetization is then detected a second time in the direct dimension.

recoupling sequence is utilized to recouple H_{II}, allowing the transfer of magnetization between neighboring ^{13}C atoms. Finally, the ^{13}C magnetization is detected in the direct dimension, t_2. Figure (1.4.10) shows a 150 MHz ^{13}C-^{13}C correlation spectrum of uniformly ^{13}C labeled chlorosomes obtained using the sequence shown in Figure (1.4.9), with an RFDR sequence[47] used to recouple the ^{13}C-^{13}C dipolar coupling. As was the case for the heteronuclear correlation spectra in Figures (1.4.8B-C) , the number of cross-peaks in a homonuclear correlation spectrum can be controlled to some degree by the length of the recoupling period. As the recoupling time increases, the magnetization

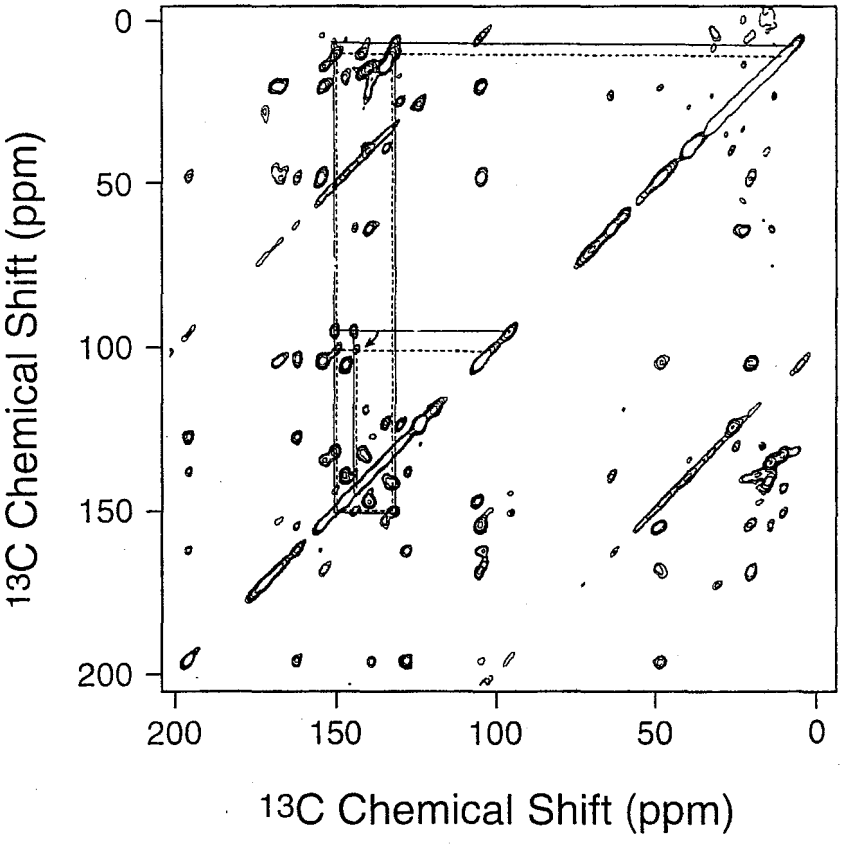

Figure 1.4.10. Two-dimensional ^{13}C-^{13}C correlation spectrum of uniformly-^{13}C enriched chlorosomes obtained at a field of 14.1 T with a spinning speed of 15 kHz. A RFDR sequence was used to recouple the ^{13}C-^{13}C homonuclear dipolar coupling and create the ^{13}C-^{13}C correlations shown in the spectrum. (Reproduced from reference [25], with permission.)

diffuses farther through the sample, leading to chemical shift correlations between more nuclei.

1.4.3 - Recoupling Away from the Magic Angle

Previously it was stated that it was impossible to spatially recouple the dipolar coupling under MAS because one could not stop and restart the spinning fast enough. However, there is another solution: the dipolar coupling is fully removed only at the magic angle, so if the spinning rotor were to be hopped from the magic angle rotor axis to another axis (for instance 0°), the dipolar coupling would return. The sample can then be returned to the magic angle for detection. This technique, known as Switched-Angle Spinning or SAS[48], has been utilized to recouple ^{13}C-^{13}C homonuclear dipolar couplings in ^{13}C zinc acetate, as shown in Figure (1.4.11). Although the recoupling at $\theta = 0°$ is 100%, the mechanical difficulty of hopping a spinning sample between two angles make recoupling via SAS less attractive than some of the pulsed techniques discussed above. However, as will be shown in section 1.5, there are instances where it is advantageous to use multi-angle spinning techniques like SAS.

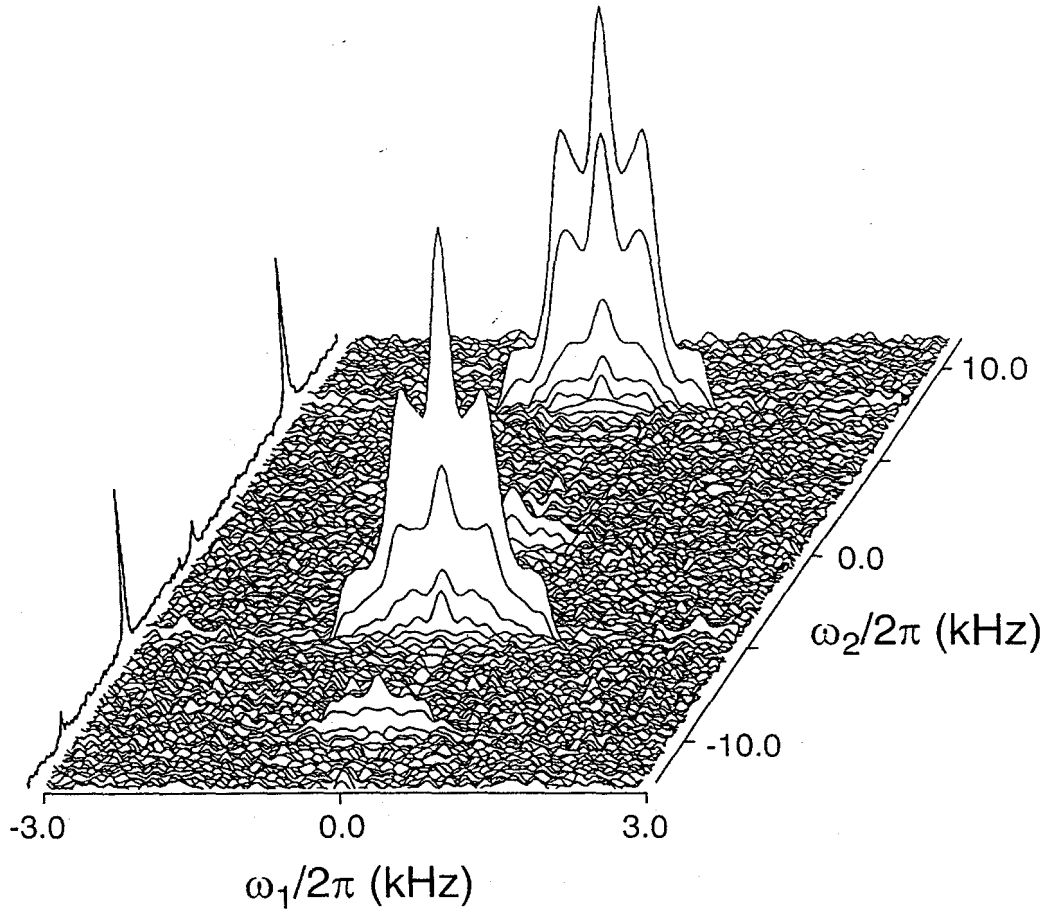

Figure 1.4.11. Two-dimensional Switched-Angle Spinning (SAS) spectrum of uniformly-^{13}C labeled zinc acetate. The ^{13}C-^{13}C homonuclear dipolar coupling is recoupled by hopping the rotor axis to 0°, after which the rotor is returned to the magic angle for detection of the ^{13}C magnetization. (Reproduced with permission from reference [48].)

1.4.4 - Reintroduction of the CSA

Figure (1.2.5) showed a ^{13}C static carbon spectrum of glycine obtained with heteronuclear decoupling. The spectrum has two broad lines corresponding to the chemical shift anisotropy of the α– and carbonyl carbons. The two lineshapes are the direct result of the electronic structure around the nuclei, and thus contain a wealth of localized information about the structure, dynamics, and orientation of the nucleus with respect to its surrounding atoms. For example, the chemical shift anisotropy for the α-

carbon of most amino acids in proteins and peptides is heavily dependent on the secondary structure (α-helix versus β-sheet) within which the amino acid resides[49, 50], as shown in Figure (1.4.12) for valine.

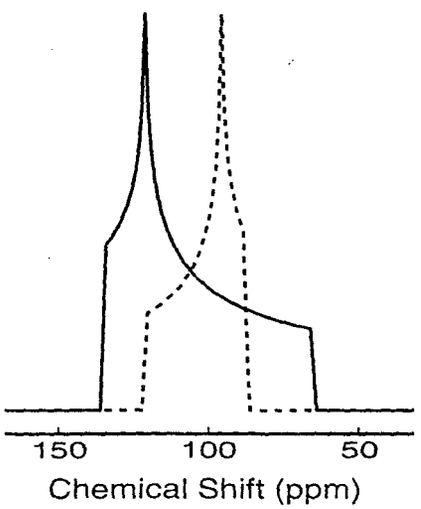

Figure 1.4.12. Simulated static spectra of the α-carbon chemical shift anisotropies for a L-valine residue in a peptide or protein. The shape of the α-carbon CSA depends strongly on whether the residue is located within an α-helix (dashed line) or a β-sheet (solid line).

Although measurement of CSA lineshapes from static solid-state NMR spectra is possible in many singly and even doubly labeled samples, it is generally not feasible in many-spin systems, where the CSA powder patterns could overlap. Furthermore, static spectra typically require extensive signal averaging in order to obtain the signal intensity and resolution required to determine the CSA lineshape. Thus, what is often required is an experiment that combines the speed and resolution of a MAS experiment with the information content available from a static NMR experiment. In this subsection, two such techniques will be presented.

1.4.4.1 The Herzfeld-Berger Method

Figure (1.2.8) showed a series of MAS spectra taken at different spinning speeds. One may recall that as the spinning speed decreased, more and more "spinning sidebands" appeared in the spectrum, due to the inability of the rotor to fully average the CSA. More importantly, as the spinning speed approached zero, the envelope of spinning sidebands began to strongly resemble the shape of the static powder pattern shown in Figure (1.2.8E). The intensity of the spinning sidebands contains information about the CSA, and, through proper analysis of spinning sideband intensities, one can determine the three CSA parameters, δ_{11}, δ_{22}, and δ_{33}. The Herzfeld-Berger[51] method uses a series of pre-calculated surfaces to determine δ_{11}, δ_{22}, and δ_{33} from integrated intensity (or even peak height) of the spinning sidebands. The advantage to the Herzfeld-Berger method is that it is not technically demanding, since it only requires the acquisition of a one-dimensional MAS spectrum. By taking spectra at numerous spinning speeds and averaging the values of δ_{11}, δ_{22}, and δ_{33} determined from the Herzfeld-Berger surfaces, the accuracy of the method can be further enhanced. Figure (1.4.13) shows a spectrum of ^{15}N labeled AMP (which has five ^{15}N sites) taken at a MAS speed of 1105 Hz. The spinning speed for the spectrum in Figure (1.4.13) was chosen specifically to minimize sideband overlap, allowing the determination of the CSAs of all five ^{15}N AMP sites using the Herzfeld-Berger method. However, had the spectrum been much more crowded, it would have been difficult to obtain enough non-overlapping sidebands to perform a rigorous Herzfeld-Berger analysis of the sideband intensities. When spectra are too crowded with sidebands to resolve the CSAs using the Herzfeld-Berger method, it

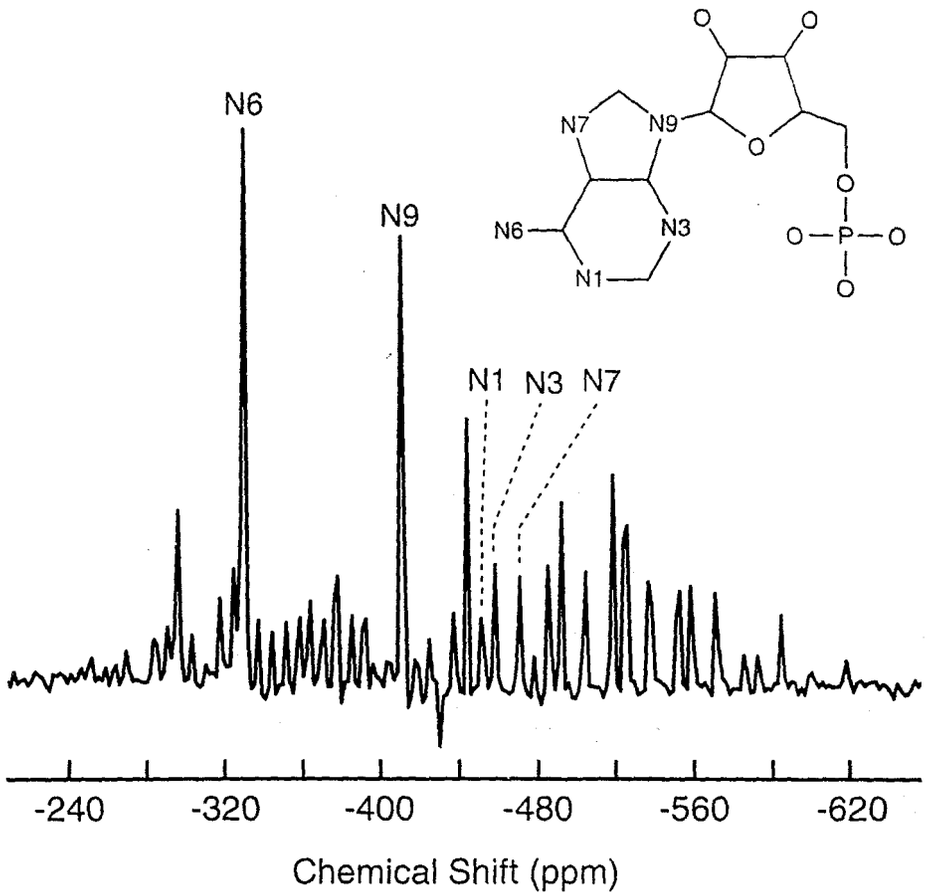

Figure 1.4.13. Slow-spinning CPMAS spectrum of uniformly-^{15}N labeled adenosine monophosphate (AMP) obtained at a spinning speed of 1105 Hz. Because sidebands are spaced at integer multiples of the spinning speed the identity of each sideband can be ascertained based on its distance from any one of the five isotropic peaks (which are found by spinning much faster). By fitting all of the sidebands, the principal values of the CSA for each ^{15}N site were determined.

becomes necessary to utilize two-dimensional NMR techniques to spread the overlapping chemical shift anisotropies across a second dimension.

1.4.4.2 Anisotropic/Isotropic Chemical Shift Correlation

Although slow-spinning MAS is an excellent way to determine the chemical shift anisotropy of a nucleus in the solid-state, the method does not *really* reintroduce the CSA. Instead, the Herzfeld-Berger method takes advantage of the incomplete averaging of the CSA that occurs when the rotor frequency is less than the width of the CSA. The

only way to truly observe a "static-like" powder pattern under fast MAS is to recouple the CSA in a manner analogous to dipolar recoupling.

The evolution of the CSA under MAS is very similar to that of the heteronuclear dipolar coupling—not surprising since the spatial component of the anisotropic chemical shift Hamiltonian is proportional to $\left(1-3\cos^2\theta\right)$ and the spin component is proportional to I_z. Therefore, a technique analogous to REDOR, which applies two π-pulses per rotor period should effectively reintroduce the CSA under MAS leaving only the spatially-independent isotropic chemical shift. Although a two-pulse technique does work[52], the resulting powder pattern tends to be a bit distorted due to reasons that will not be discussed here. An improved technique was developed by Tycko and co-workers[53] that utilizes four π pulses per rotor period (Figure 1.4.14) to reintroduce the CSA with very

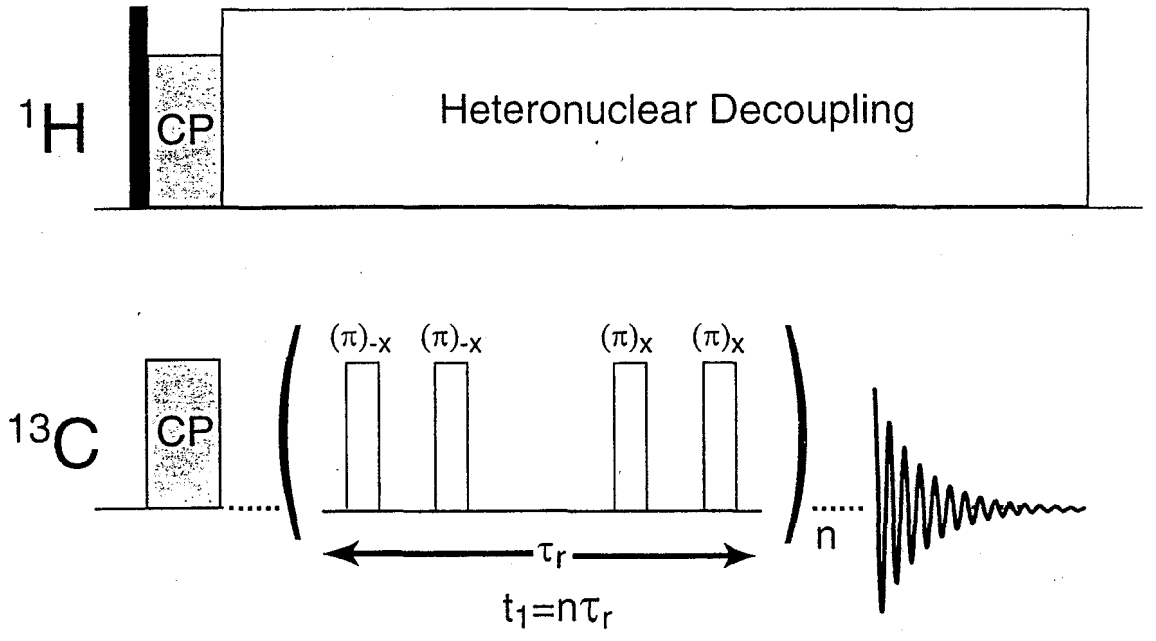

Figure 1.4.14. Pulse sequence for the 4-π-pulse experiment for recoupling the chemical shift anisotropy.

little distortion of the CSA lineshape. By incorporating the 4-π-pulse sequence into the indirect detection period of a two-dimensional experiment, it is possible to produce a two-dimensional spectrum that correlates the broad CSA lineshape in one dimension with the isotropic MAS lineshape in the other dimension. Figure (1.4.15) shows a series of CSA patterns from six of the seven ^{13}C sites in methyl-α-D-glucopyranoside obtained using the 4-π-pulse technique to reintroduce the CSA under MAS. Below each experimentally obtained spectrum is a simulated CSA lineshape based on lineshapes obtained in a static experiment. It is readily apparent from Figure (1.4.15) that the 4-π-pulse technique faithfully reproduces the static lineshape with reasonable resolution.

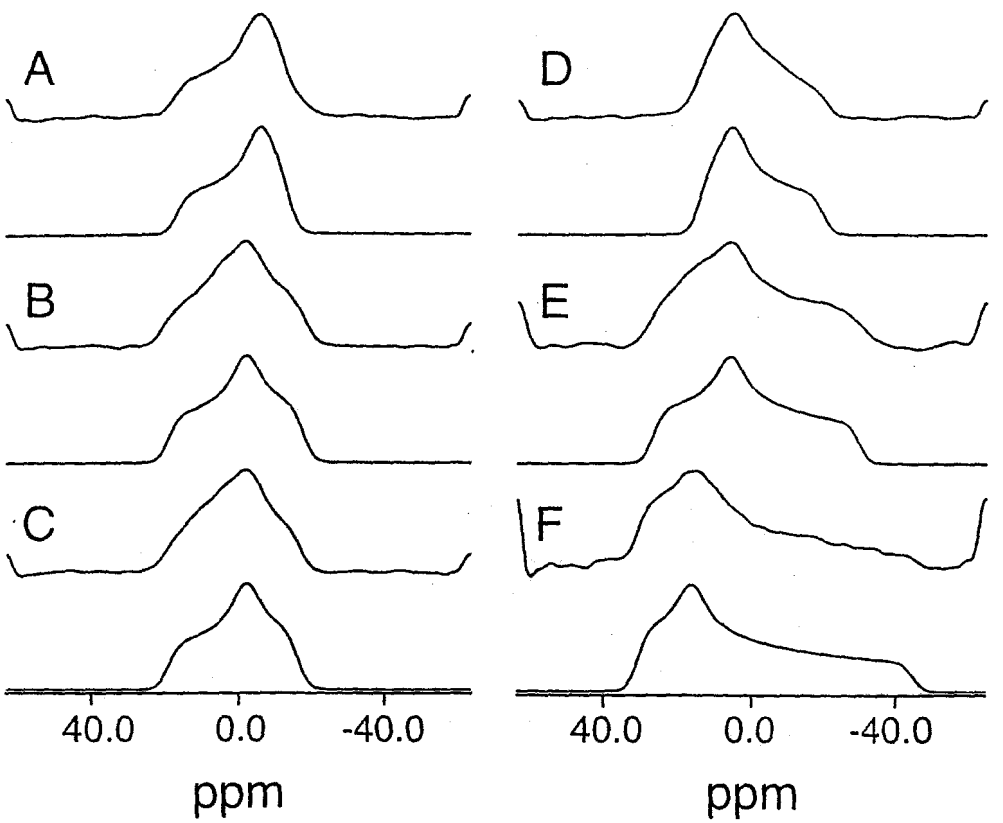

Figure 1.4.15. ^{13}C CSA lineshapes of six carbons (A-F) in methyl-α-D-glucopyranoside obtained using the 4-π-pulse technique. Below each experimentally obtained lineshape is a corresponding simulated lineshape based on the static lineshape. (Reproduced from reference [53], with permission.)

In addition to the 4-π-pulse method, a variety of other techniques have been developed that can correlate the anisotropic and isotropic components of the chemical shift which do not involve traditional pulsed recoupling. Among these techniques are magic angle hopping[54-56], Magic Angle Turning or MAT[57, 58], and Variable-Angle Correlation SpectroscopY or VACSY[59]. Figure (1.4.16) shows a two-dimensional isotropic/anisotropic correlation spectrum of L-tyrosine produced using VACSY. It should be noted that although magic angle hopping, MAT and VACSY all have definite advantages over slow-spinning MAS or the 4-π-pulse sequence, they are technologically more difficult to implement, and can not be performed using a standard MAS probe.

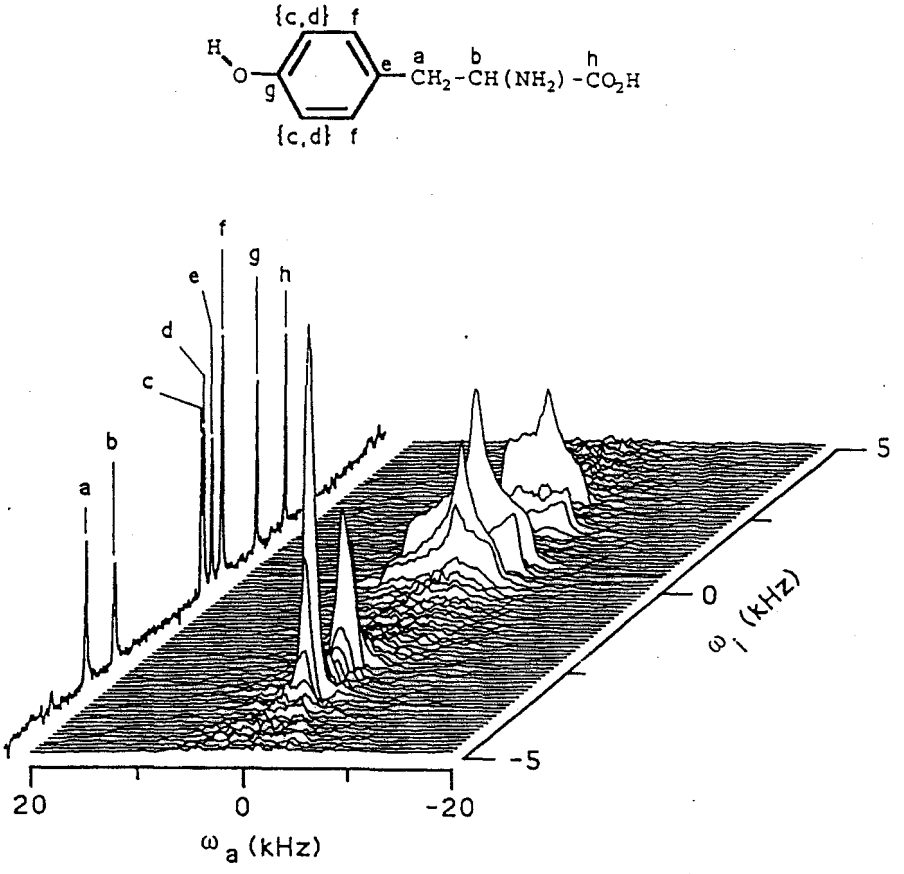

Figure 1.4.16. Two-dimensional isotropic-anisotropic NMR chemical shift correlation spectrum of L-tyrosine, showing the isotropic projection and the assignment of the peaks to each site in the molecule. (Reproduced from reference [59], with permission.)

1.4.5 - J-couplings in Solid-State NMR

As a final note in this section, I would briefly like to reintroduce a Hamiltonian that has so far been missing in this chapter, the J-coupling Hamiltonian. In solid-state NMR, the J-coupling is almost never observed, because solid-state NMR linewidths are typically larger than the 1-200 Hz J-couplings between nuclei. However, this does not mean that J-couplings do not exist—rather their effects on the spectrum are usually too small to see. Only recently has the technology become available, through high-speed (>30 kHz) MAS and high-power (up to 1000 Watts) CW ^{1}H decoupling, to observe J-couplings in polycrystalline samples[60]. This can be done without recoupling because the J-coupling has no spatial dependence, and so is not averaged away under MAS. Recently, a number of groups have shown that although J-couplings are not always observable in solids, they can still be used to perform typical liquid-state NMR experiments in the solid-state, such as INADEQUATE[60].

1.4.6 - Summary

In sections 1.2 and 1.3, the interactions in solid-state NMR that prevent the acquisition of high-resolution NMR spectra as well as ways to counteract the effects of these interactions were discussed. However, interactions like the dipolar coupling, chemical shift anisotropy, and quadrupolar coupling (which will be covered in the next section) are more than just a barrier to high-resolution and sensitivity. The sizes and orientational dependencies of these interactions provide more information about the environment surrounding a nucleus than could ever be extracted in a liquid-state NMR experiment—and by using some of the techniques that were presented in this section and

the next, these interactions can be used to further our understanding of the structure and dynamics of solid-state materials.

1.5 Solid-State NMR of Quadrupolar Nuclei

Thus far, the discussion of solid-state NMR has only involved spin $I = \frac{1}{2}$ nuclei, such as ^{1}H, ^{13}C, and ^{15}N. However, this has somewhat limited the survey of solid-state NMR methodology, since the majority of nuclei found in the periodic table have spin $I > \frac{1}{2}$. Although these "quadrupolar nuclei" possess the same set of basic interactions that were introduced in section 1.2 (e.g. the chemical shift anisotropy, dipolar couplings, etc.), there are two principle differences between spin $I = \frac{1}{2}$ and spin $I > \frac{1}{2}$ nuclei. First, for quadrupolar nuclei, the allowed values for the nuclear spin quantum number, m_I, are no longer simply $+\frac{1}{2}$ and $-\frac{1}{2}$. For a spin $I = 1$ nucleus, such as ^{2}H and ^{14}N, the allowed values for m_I are –1, 0, and +1, and so in the presence of an external magnetic field, spin $I = 1$ nuclei have three energy levels. Likewise, a spin $I = \frac{3}{2}$ nucleus like ^{23}Na or ^{87}Rb has four spins states, since the allowed values for m_I are $-\frac{3}{2}$, $-\frac{1}{2}$, $\frac{1}{2}$, and $\frac{3}{2}$. In general, the number of possible spin states goes as $2I+1$, and the number of possible transitions between those spin states goes as $2I$. The other difference between spin $I = \frac{1}{2}$ and spin $I > \frac{1}{2}$ nuclei is that quadrupolar nuclei possess a non-spherical charge distribution (i.e., some areas of the nucleus are more positively charged than others) that can couple to electric field gradients that are present in almost all solid-state materials[61]. This coupling, known as quadrupolar coupling, can have an enormous effect on the observed NMR spectrum, as will be shown in the ensuing section.

1.5.1 - Solid-State NMR of Spin I = 1 Nuclei

When compared to the number of half-integer quadrupolar nuclei ($I > 1$), the occurrence of spin $I = 1$ nuclei in the periodic table is extremely rare. Nevertheless, the solid-state NMR literature on spin $I = 1$ nuclei is quite vast, due almost entirely to the popularity of deuterium (^{2}H) NMR[62-65]. Based on its small electron cloud and relatively low magnetogyric ratio ($\sim\frac{1}{7}$ that of ^{1}H), which together lead to a chemical shift range of ~3-4 ppm and relatively weak dipolar couplings, one might expect static ^{2}H NMR linewidths to be narrow. Thus, it may be somewhat surprising to learn that static ^{2}H NMR linewidths routinely exceed 100 kHz, as seen in Figure (1.5.1) for CDI_3. The origin of this very broad line is the quadrupolar interaction.

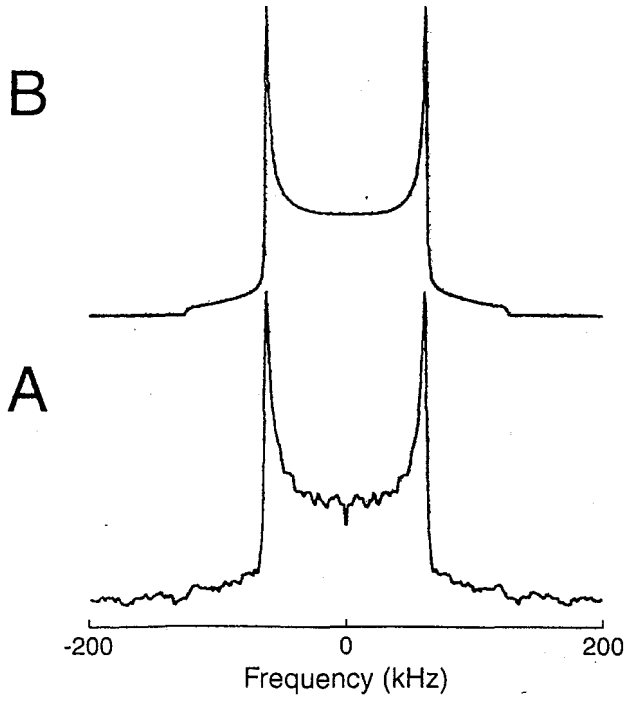

Figure 1.5.1. Static ^{2}H NMR spectrum of CDI_3. (A) Experimentally obtained spectrum. (B) A simulated spectrum based on the quadrupolar coupling derived from the spectrum in (A). (Reproduced from reference [66], with permission.)

To understand the ^2H quadrupolar lineshape displayed in Figure (1.5.1), it is helpful to examine the effect of the quadrupolar coupling on the ^2H Zeeman energy levels. In Figure (1.5.2A), the energy levels of a spin $I = 1$ nucleus are shown in an external magnetic field with no quadrupolar coupling present. Note that both the $m_I = -1$ to 0 and $m_I = 0$ to +1 transitions have the same resonance frequency since the energy differences between the states are identical. Figure (1.5.2B) shows the same three energy levels under the influence of the 1st-order quadrupolar Hamiltonian, $H_Q^{(1)}$ and the Zeeman Hamiltonian. Note that whereas the $m_I = -1$ and the $m_I = +1$ spin states decrease

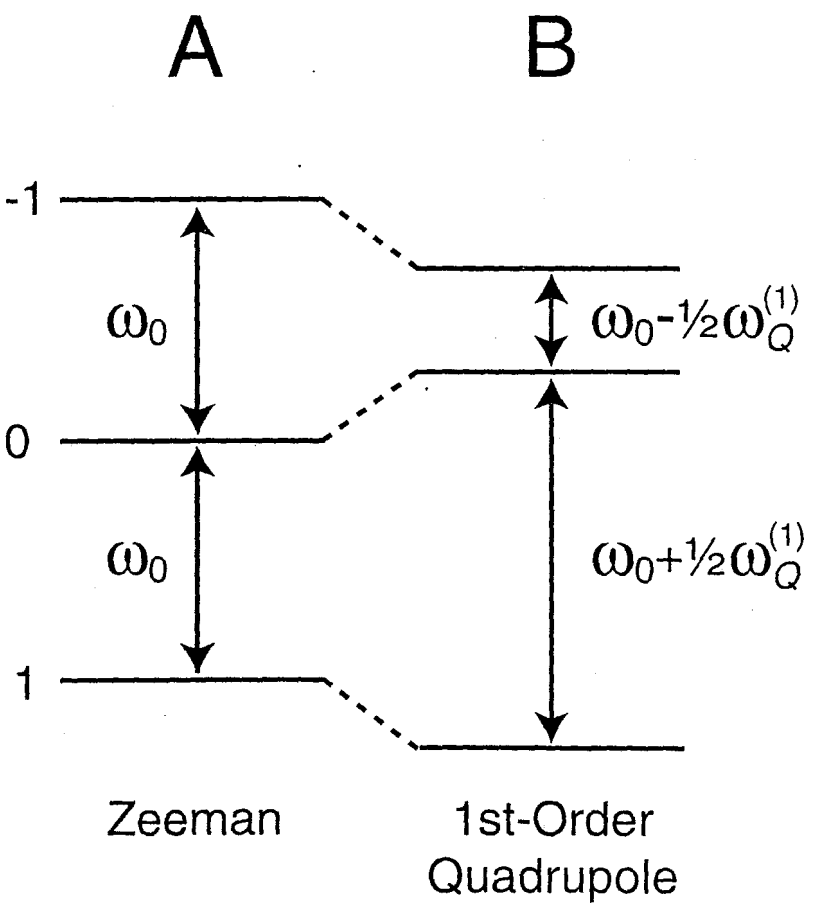

Figure 1.5.2. Spin $I = 1$ energy level diagram for spins subject to the Zeeman Hamiltonian (A) and to both the Zeeman Hamiltonian and 1st-order Quadrupolar Hamiltonian (B). The splitting shown in (B) is a result of the 1st-order Quadrupolar coupling at one particular crystalline orientation.

in energy upon the addition of $H_Q^{(1)}$, the $m_I = 0$ spin state increases in energy. As a result, the $m_I = -1$ to 0 and the $m_I = 0$ to +1 transitions are no longer equivalent, and thus have different resonance frequencies. The difference in the resonance frequencies of the two transitions is proportional to $\omega_Q^{(1)}$, the 1st-order quadrupolar coupling constant. This constant can be expressed mathematically as,

$$\omega_Q^{(1)} = \frac{3eq \cdot eQ}{2I(2I-1)\hbar}, \tag{1.5.1}$$

where e is the electron charge, eq is the z-component of the electric field gradient felt at the nucleus, and Q is the nuclear electric quadrupole moment. The constant Q is a nuclear property (like γ) that describes the strength with which a quadrupolar nucleus couples to an electric field gradient at the nucleus. For instance, deuterium has a relatively small nuclear electric quadrupole moment ($Q = 3\times10^{-31}$ m^2), and so typically experiences quadrupolar couplings on the order of 100-300 kHz[62]. On the other hand, $Q = 2\times10^{-30}$ m^2 for ^{14}N, another spin $I = 1$ nucleus, and so ^{14}N nuclei typically experience quadrupolar couplings that are ~10 times higher (1-5 MHz).

As seen in Figure (1.5.2B), the effect of the 1st-order quadrupolar coupling is to produce a quadrupolar splitting, whose magnitude is dictated by $\omega_Q^{(1)}$. However, in Figure (1.5.1), one saw more than just a splitting, but rather a lineshape that strongly resembles the dipolar Pake pattern shown in Figure (1.2.4). This is because, like other Hamiltonians that have been discussed in this chapter, the 1st-order quadrupolar Hamiltonian possesses an orientational dependence that is proportional to $\left(1-3\cos^2\theta\right)$. Thus, for different molecular orientations, the splitting caused by the 1st-order

quadrupolar Hamiltonian will change. Furthermore, just as the width of the Pake pattern of Figure (1.2.4) was an exact measure of the dipolar coupling constant, d, the width of the ^{2}H Pake pattern is a measure of the 1st-order quadrupolar coupling constant, $\omega_Q^{(1)}$.

Since the orientational dependence of the 1st-order quadrupolar coupling is proportional to $(1-3\cos^2\theta)$, this coupling can be eliminated under MAS. Figure

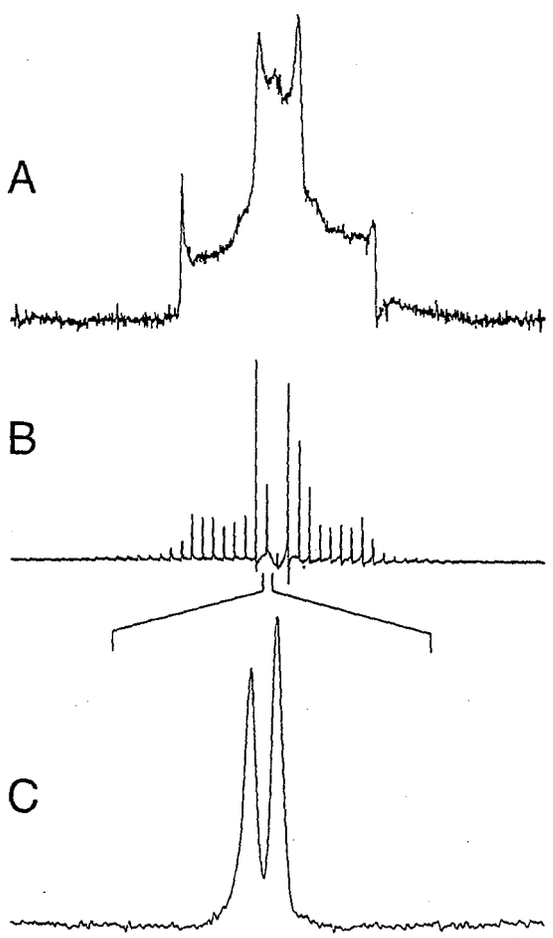

Figure 1.5.3. ^{2}H NMR spectra of a solid mixture of deuterated ferrocene and deuterated hexmethylbenzene both static (A) and under magic angle spinning (B). The two resonances in (C) are expansions of the centerband in (B) and correspond to the isotropic chemical shifts of the two deuterated species. (Adapted from reference [67], with permission.)

(1.5.3A) shows a static ^{2}H NMR spectrum of a mixture of deuterated hexamethylbenzene and deuterated ferrocene, which consists of two overlapping Pake patterns, corresponding to the two deuterium environments. Under magic angle spinning (Figure 1.5.3B) the quadrupolar linewidth is reduced to a series of spinning sidebands, and upon closer inspection of the residual isotropic line (Figure 1.5.3C), it is possible to discern the chemical shifts of the two ^{2}H sites.

Although MAS can be quite effective in reducing the deuterium quadrupolar linewidth, ^{2}H NMR is most often performed on static samples. The reasons for this choice are three fold. First, in contrast to the vast amount of time necessary to acquire a static spectrum of a spin $I = \frac{1}{2}$ nucleus, a static quadrupolar spectrum can be obtained quickly. This is because the quadrupolar coupling greatly facilitates the relaxation of quadrupolar nuclei, obviating the need to wait long periods of time before the magnetization relaxes back to thermal equilibrium. Second, the ^{2}H quadrupolar coupling is a sensitive measure of internal molecular motion[63, 66]. Since the quadrupolar coupling of a species is reduced by fast molecular motion, the width of the static ^{2}H lineshape can be used to measure of the degree of molecular motion. Figure (1.5.4) shows a series of ^{2}H NMR spectra of deuterated DMPC in a lipid bilayer. By adding different species to the bilayer (such as cholesterol or cytochrome *c* oxidase) it is possible to alter the mobility of the deuterated hydrophobic lipid tails. The narrow quadrupolar lineshapes in Figure (1.5.4B-D) indicate that the added compounds increases the mobility of the lipid tails, whereas adding cholesterol to the bilayer (Figure 1.5.4E) decreases the lipid mobility.

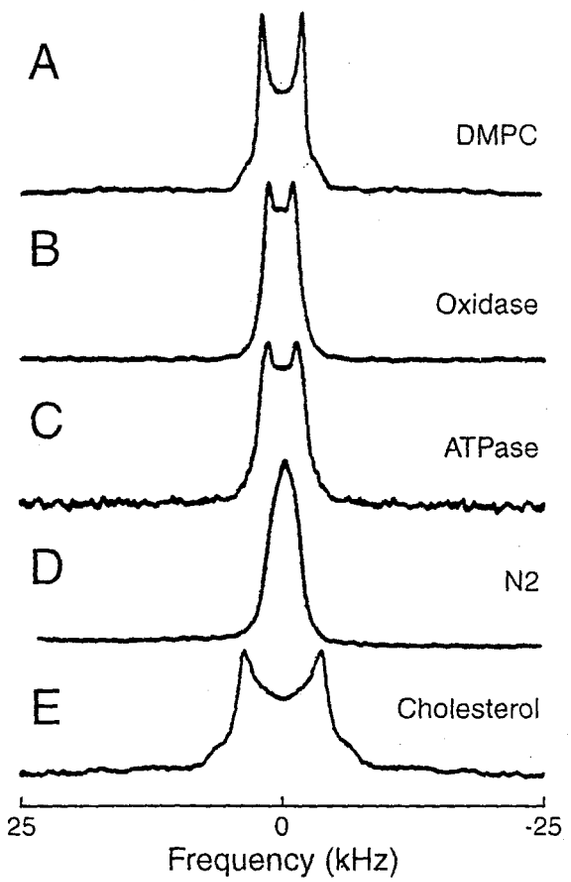

Figure 1.5.4. ^{2}H NMR spectra of deuterated lipids (1-myristoyl-2(14,14,14-trideutero)myristoyl-*sn*-glycero-3-phosphocholine or DMPC-d_3) in a lipid bilayer as a function of the additional molecules present. (A) DMPC-d_3 in excess water at 30°C. (B) as in (A), but the lipid contains 67 weight % cytochrome *c* oxidase. (C) as in (A), but the lipid contains 67 weight % sarcoplasmic reticulum adenosinetriphosphatase. (D) as in (A), but the lipid contains 67 weight % beef brain myelin proteolipid apoprotein (N2). (E) as in (A), but the lipid contains 33 weight % chlosterol. (Reproduced from reference [66], with permission.)

Finally, static ^{2}H NMR is a powerful tool for studying molecular orientation[62, 68, 69]. For example, in Figure (1.5.5) a series of ^{2}H spectra of -CD_2-S-CD_2-bridged perinaphthalene dissolved in Phase V liquid crystals are shown as a function of temperature. As the temperature is increased, the liquid crystalline solvent causes the perinaphthalene molecules to align, and the ^{2}H powder linewidth narrows, giving way to

a pair of sharp lines that correspond to the quadrupolar splitting for the molecules' adopted orientation. Since the quadrupolar spitting changes for different orientations, it is possible to discern in which direction the molecules are aligned, based on the quadrupolar splitting in the NMR spectrum.

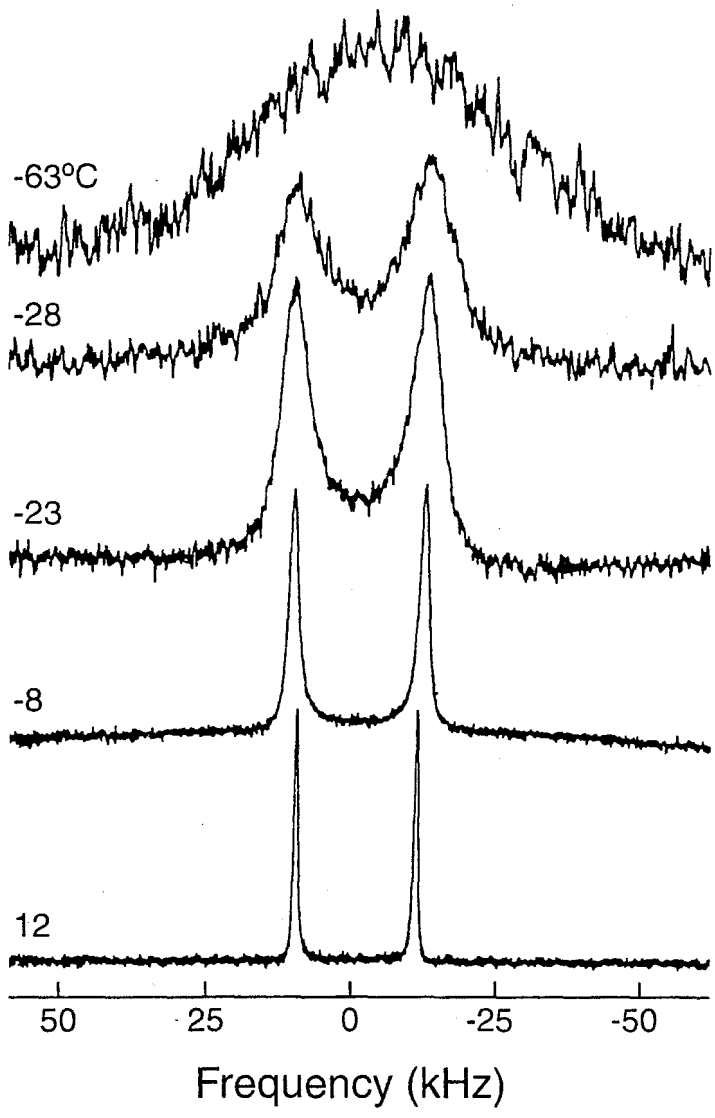

Figure 1.5.5. ^2H NMR spectra of a 3 weight % solution of $-CD_2-S-CD_2-$bridged perinaphthalene in a Phase V liquid crystal solvent. As the temperature is increased, the degree of orientational heterogeneity decreases. Above a temperature of 0°C, the bridged perinaphthalene orients in the liquid crystal and a single doublet is observed since all the deuterons are equivalent, and the orientation of the liquid crystal can be determined as a function of the splitting. (Reproduced from reference [70], with permission.)

Thus far, the discussion has been limited to ^{2}H NMR, where, compared to other quadrupolar nuclei, the value of Q is small. For this reason, there has not been the need to point out the existence of a second, more insidious quadrupolar term—the 2nd-order quadrupolar coupling. However, in every ^{2}H spectrum that was shown in this subsection, the 2nd-order quadrupolar coupling was present, although masked by its relatively small size. When the quadrupolar coupling is very large, as it is for ^{14}N, the 2nd-order quadrupolar coupling can have a significant effect on the observed lineshape. Figure (1.5.6) shows the effect of the 2nd-order quadrupolar coupling on the energy levels of a

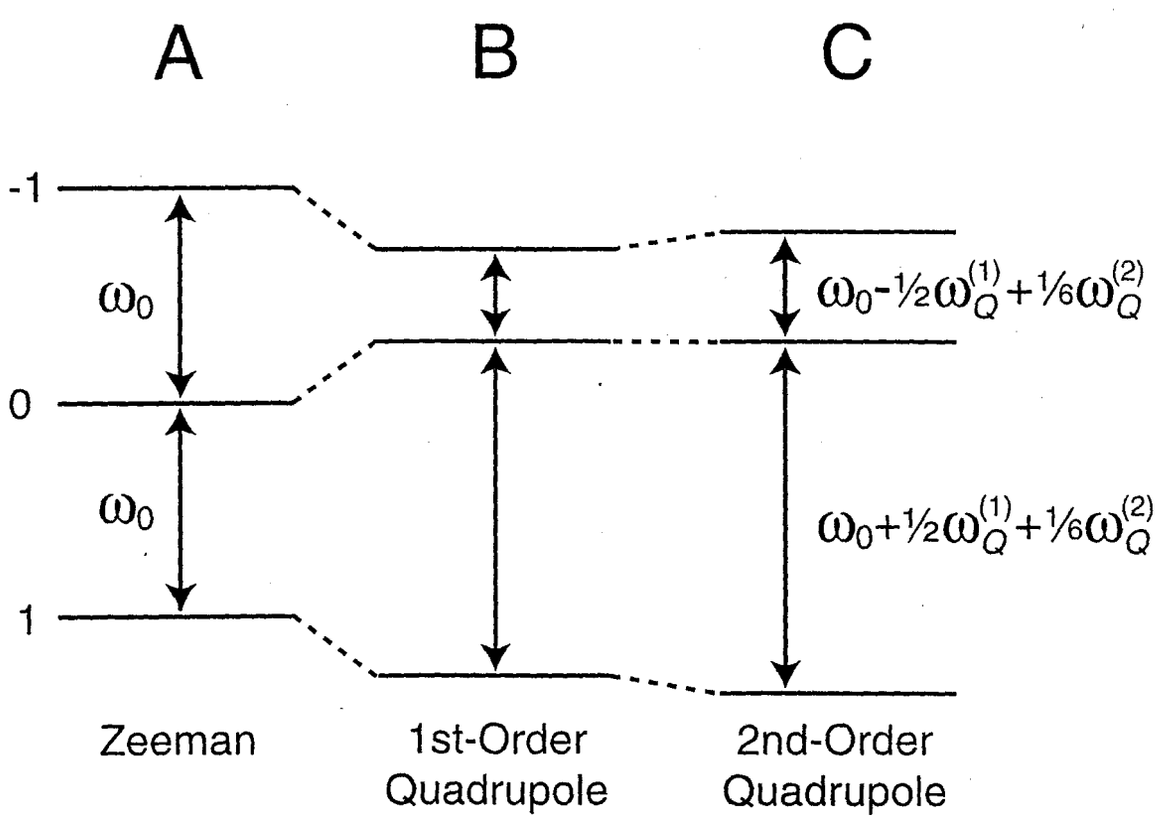

Figure 1.5.6. Spin I = 1 energy level diagram for spins subject to the Zeeman Hamiltonian (A), to both the Zeeman Hamiltonian and 1st-order Quadrupolar Hamiltonian (B), and to the Zeeman, 1st-order quadrupolar, and 2nd-order quadrupolar Hamiltonians (C).

spin I = 1 nucleus. Since the m_I = 1 and -1 spin states are now shifted in opposite directions by an amount $\omega_Q^{(2)}$, it is no longer reasonable to expect the same symmetric lineshapes that were shown previously. Indeed, even when the 1st-order quadrupolar coupling is completely removed, the 2nd-order quadrupolar Hamiltonian can still be large enough to make a spectrum completely uninterpretable.

1.5.2 - Solid-State NMR of Spin I > 1 Nuclei

Although subject to the same quadrupolar Hamiltonian as was discussed in the previous subsection, spin $I > 1$ nuclei, also known as half-integer quadrupolar nuclei, behave quite differently than spin $I = 1$ nuclei. The reason for this difference is made clear by examining the effect that the quadrupolar Hamiltonian has on the energy levels of a half-integer quadrupolar nucleus. Figure (1.5.7) shows the energy levels for a spin $I = \frac{3}{2}$ nucleus without any quadrupolar coupling (Figure 1.5.7A), under the influence of the 1st-order quadrupolar coupling (Figure 1.5.7B), and including the 2nd-order quadrupolar coupling (Figure 1.5.7C). Notice that the 1st-order quadrupolar Hamiltonian shifts the $m_I = -\frac{1}{2}$ and the $m_I = \frac{1}{2}$ energy levels by the same amount and in the same direction. Thus, the resonant frequency of the $m_I = -\frac{1}{2}$ to $+\frac{1}{2}$ transition, known as the central transition, is unchanged by the 1st-order quadrupolar Hamiltonian. In contrast, the resonance frequencies of the $m_I = -\frac{3}{2}$ to $-\frac{1}{2}$ and $m_I = +\frac{1}{2}$ to $+\frac{3}{2}$ transitions, known as the satellite transitions, are each shifted by an amount proportional to $\omega_Q^{(1)}$. The net

result of $H_Q^{(1)}$ on a half-integer quadrupolar nucleus is to substantially shift and broaden the resonances

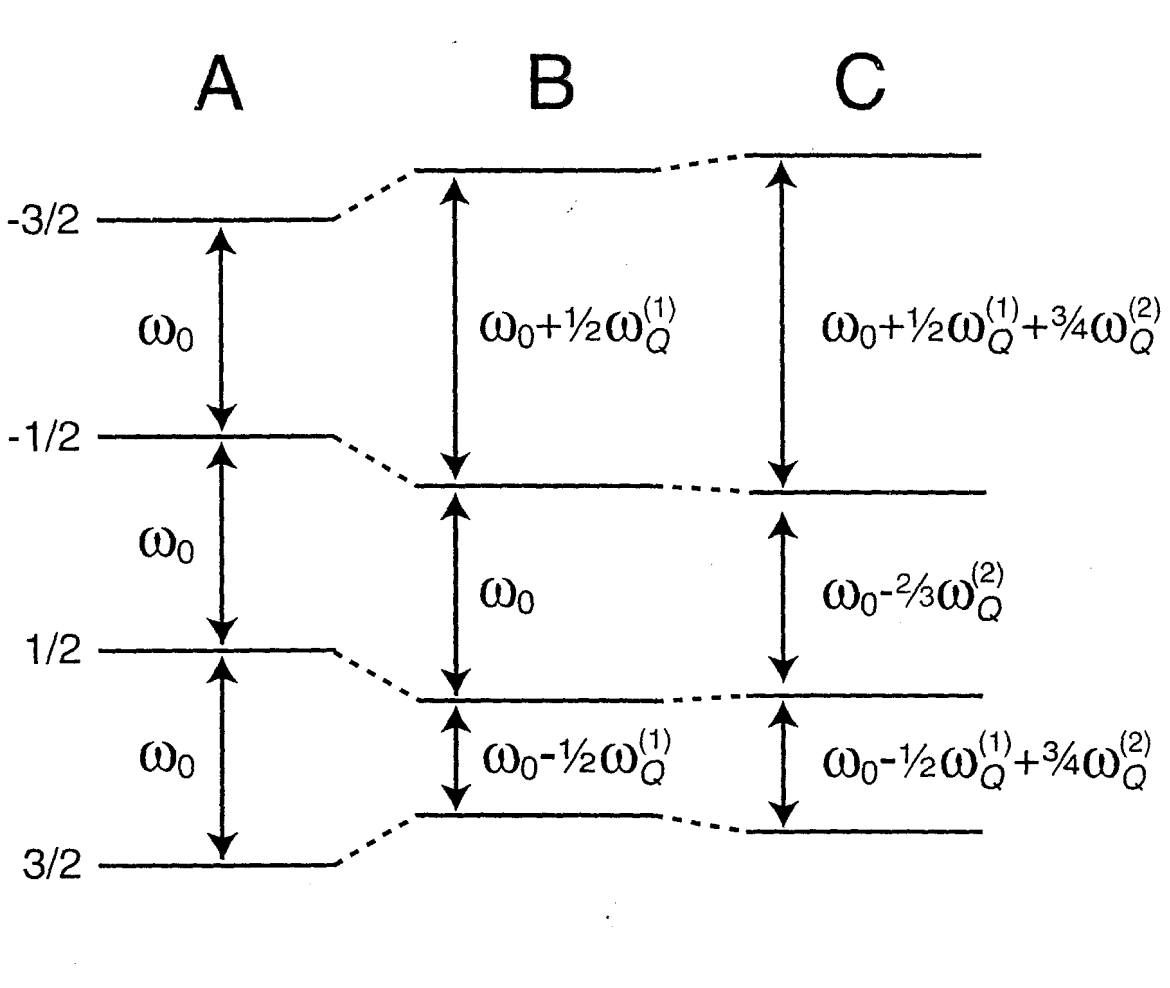

Figure 1.5.7. Spin $I = 3/2$ energy level diagram for spins subject to the Zeeman Hamiltonian (A), to both the Zeeman Hamiltonian and 1st-order Quadrupolar Hamiltonian (B), and to the Zeeman, 1st-order quadrupolar, and 2nd-order quadrupolar Hamiltonians (C).

resulting from the satellite transitions. Therefore, in a standard solid-state NMR experiment performed at the frequency of the central transition, the satellite transitions are usually not observed[71]. Yet, because the central transition is still broadened by the

2nd-order quadrupolar coupling, the resulting linewidth can still be quite large, as seen in the solid-state ^{23}Na NMR spectrum of sodium oxalate (Figure 1.5.8A).

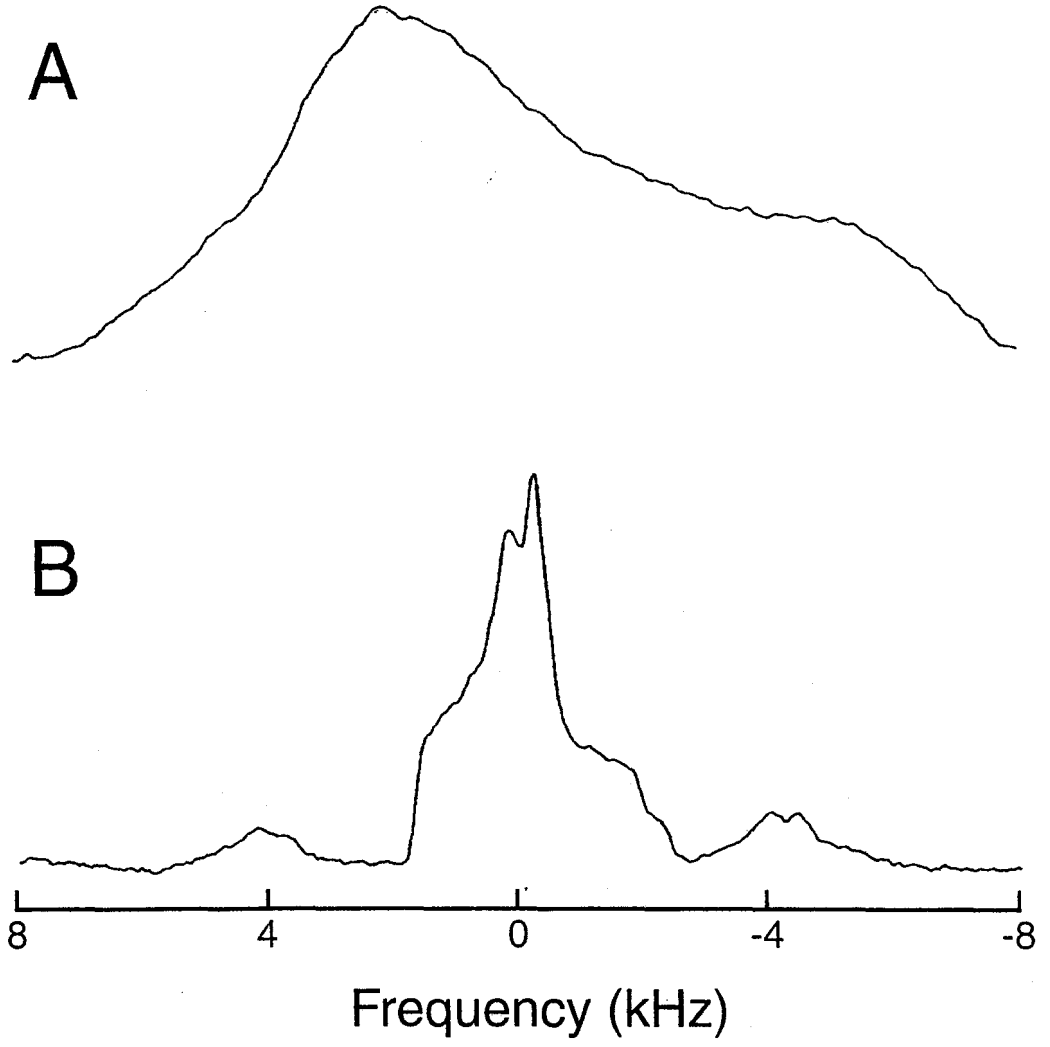

Figure 1.5.8. ^{23}Na NMR spectra of sodium oxalate acquired without any sample spinning (A), and while spinning at 10 kHz around the magic angle (B). (Reproduced from reference [72], with permission.)

For reasons of simplicity, a full mathematical description of the 2nd-order quadrupolar Hamiltonian, $H_Q^{(2)}$ will not be provided, although it can be found elsewhere[71, 73]. Instead, two important features will be mentioned that are relevant to

the study of half-integer quadrupolar nuclei via solid-state NMR. First, $H_Q^{(2)}$ has associated with it, a coupling constant, $\omega_Q^{(2)}$, that can be expressed as,

$$\omega_Q^{(2)} = \frac{\left(\omega_Q^{(1)}\right)^2}{2\omega_0} = \frac{\left(\omega_Q^{(1)}\right)^2}{2\gamma B_0} \tag{1.5.2}$$

where $\omega_Q^{(1)}$ is the 1st-order quadrupolar coupling and ω_0 is the Larmor frequency. From Equation (1.5.2), it is clear why the effects of the 2nd-order quadrupolar coupling are rarely observed in ^{2}H NMR. Even if $\omega_Q^{(1)}$ is as large as 300 kHz, the value of $\omega_Q^{(2)}$ in a 2.3 T magnet is only ~3 kHz. Equation (1.5.2) also provides a major motivation for studying quadrupolar nuclei at high field, since the size of $\omega_Q^{(2)}$ is decreased by increasing the strength of B_0.

The second important feature of the 2nd-order quadrupolar Hamiltonian is its orientational dependence, which is far more complicated than any Hamiltonian that has been addressed thus far. In fact, there are three orientational terms associated with $H_Q^{(2)}$, that correspond mathematically to the 0th, 2nd, and 4th-order Legendre polynomials[10]:

$$P_0(\cos\theta) = 1, \tag{1.5.3}$$

$$P_2(\cos\theta) = \tfrac{1}{2}\left(1 - 3\cos^2\theta\right), \tag{1.5.4}$$

and

$$P_4(\cos\theta) = \tfrac{1}{8}\left(3 - 30\cos^2\theta + 35\cos^4\theta\right). \tag{1.5.5}$$

Just like the isotropic component of the chemical shift, Equation (1.5.3) has no dependence on θ. Indeed, one of the effects of the 2nd-order quadrupolar coupling is to

produce an isotropic *quadrupolar* shift that cannot be removed, even in liquids. Moreover, $H_Q^{(2)}$ has a $(1-3\cos^2\theta)$ dependence, and so can be partially removed under magic angle spinning. Figure (1.5.8) shows a ^{23}Na spectrum of sodium oxalate obtained both with and without MAS. Although there is some narrowing, the effect is not nearly as impressive as for other spectra shown in this chapter. This is due to the existence of an additional θ dependence, as shown in Equation (1.5.5). Unfortunately, the values of θ that make $P_2(\cos\theta)$ and $P_4(\cos\theta)$ zero do not coincide (Figure 1.5.9). Therefore, to remove the 2nd-order quadrupolar coupling and produce a narrow line, a technique other than magic angle spinning must be employed.

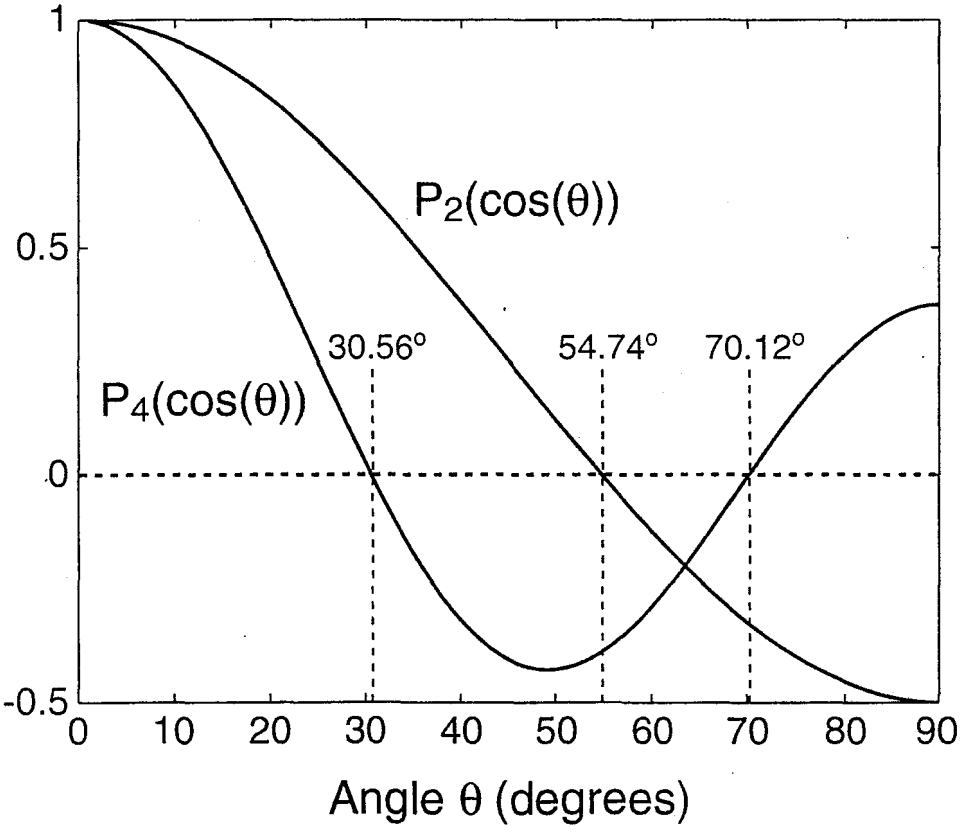

Figure 1.5.9. Plot of the 2nd- and 4th-order Legendre polynomials, $P_2(\cos\theta)$ and $P_4(\cos\theta)$, as a function of θ. The value of $P_2(\cos\theta)$ is zero when $\theta = 54.74°$ (the magic angle), whereas the value of $P_4(\cos\theta)$ is zero when $\theta = 30.56°$ or $70.12°$.

1.5.2.1 Double Rotation (DOR)

A variety of techniques have been developed that seek to counter the effects of the 2nd-order quadrupolar Hamiltonian in order to produce sharp NMR spectra of quadrupolar nuclei. The first technique that will be discussed is by far the simplest to understand although it is perhaps the most difficult to implement experimentally. When faced with a chemical shift anisotropy in a powdered sample, it is common practice to spin the sample at an angle of 54.74° to average to zero the $P_2(\cos\theta)$ spatial term of the CSA Hamiltonian. Similarly, DOuble Rotation or DOR[72, 74] eliminates the 2nd-order quadrupolar coupling by spinning at angles of 54.74° and 30.56° *simultaneously*, to remove the $P_2(\cos\theta)$ and $P_4(\cos\theta)$ spatial terms of $H_Q^{(2)}$, respectively. This is accomplished using the "rotor in a rotor" design shown in Figure (1.5.10), which allows

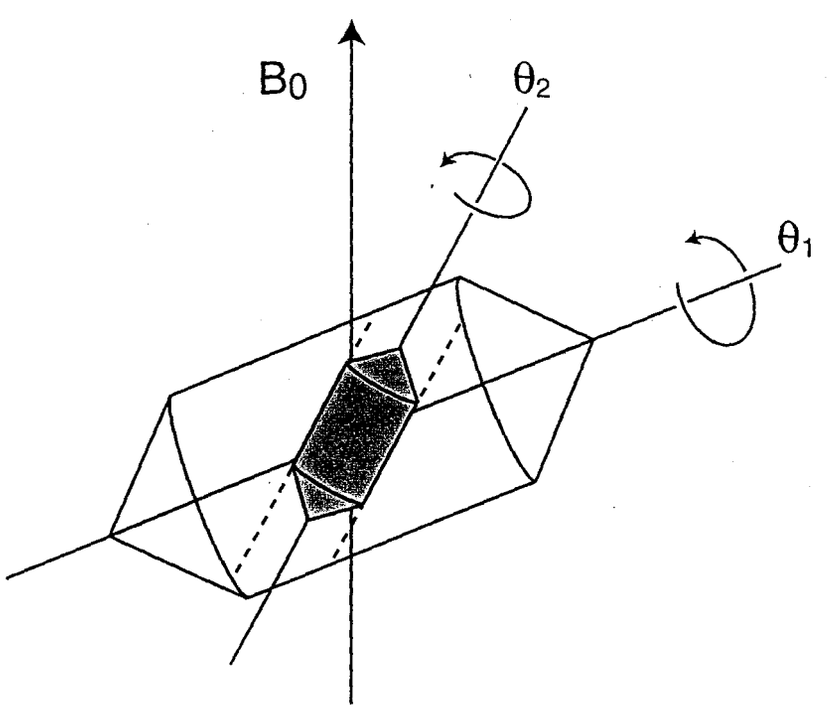

Figure 1.5.10. A schematic of the "rotor-in-a-rotor" design of an NMR probe for DOR experiments. The outer rotor spins around an axis oriented at 30.56° relative to B_0, while the inner rotor spins around an axis oriented at 54.74° relative to B_0. (Adapted from reference [72], with permission.)

the simultaneous rotation of the sample about two different axes. Under DOR, all of the 2nd-order quadrupolar coupling is removed except for its isotropic component, leaving a sharp isotropic peak flanked by a series of sidebands spaced at integer multiples of the outer rotor frequency. Figure (1.5.11) shows a ^{23}Na DOR spectrum of sodium oxalate obtained at a variety of outer rotor speeds. When compared to the ^{23}Na spectra of sodium oxalate in Figures (1.5.8A-B), the high-resolution possible through DOR is quite stunning. Although a technique as straightforward as the Herzfeld-Berger method is not available to analyze DOR sidebands, it is possible to fit the sidebands from a DOR spectrum to obtain information about the strength of the quadrupolar coupling[75].

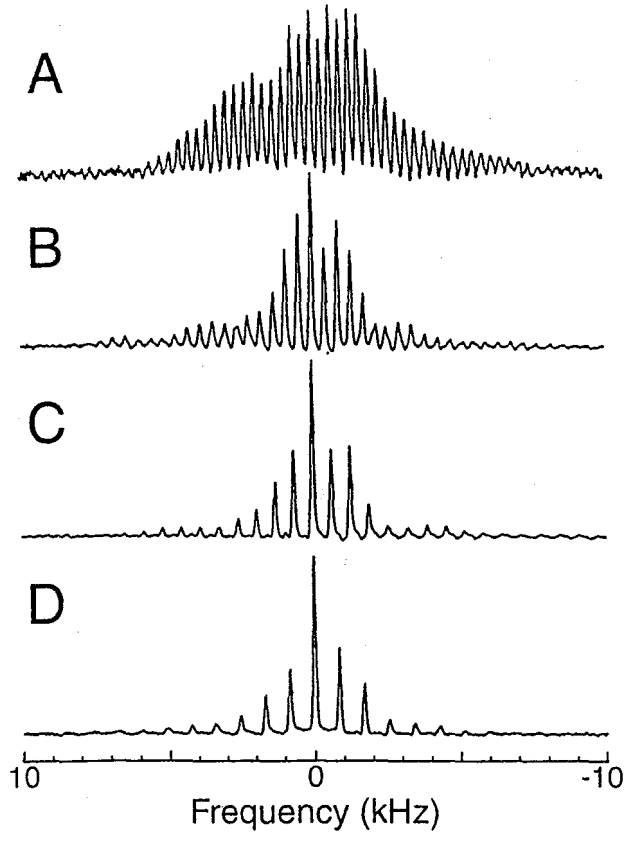

Figure 1.5.11. ^{23}Na DOR spectra of sodium oxalate acquired at outer-rotor spinning speeds of 250 Hz (A), 500 Hz (B), 750 Hz (C), and 1000 Hz (D). (Reproduced from reference [72], with permission.)

1.5.2.2 Dynamic Angle Spinning (DAS)

Dynamic-angle spinning, or DAS, is another technique for removing the 2nd-order quadrupolar coupling[76, 77]. Like DOR, DAS seeks to remove the 2nd-order quadrupolar coupling by spinning the sample at multiple angles. However, DAS does not spin at both angles simultaneously; rather, DAS averages away $H_Q^{(2)}$ by spinning at two different angles *sequentially*.

Suppose a powdered sample of a sodium salt were to be spun around an angle of 37.38°. As the magnetization of the ^{23}Na nuclei evolves following a $\frac{\pi}{2}$-pulse, nuclei in different crystallites will precess at different frequencies depending on the value of $H_Q^{(2)}$ for each crystallite orientation. As a result, one might expect to obtain any one of the five simulated 2nd-order quadrupolar lineshapes shown in Figure (1.5.12A), depending on the nature of the

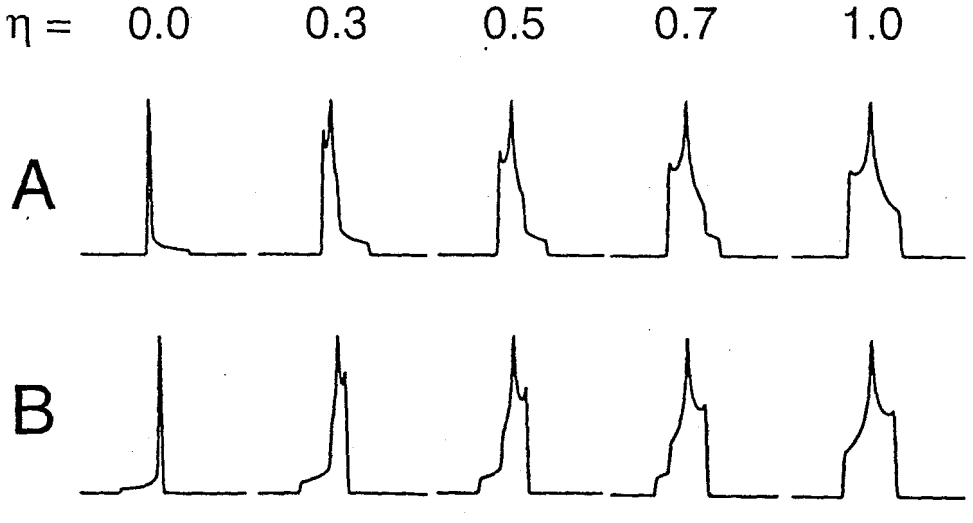

Figure 1.5.12. Simulated 2nd-order quadrupolar powder patterns for the central transition of a spin I = 3/2 nucleus spinning at an angle of 37.38° (A) and 79.19° (B). The parameter η is used to describe the overall anisotropy of the lineshape. (Reproduced from reference [75], with permission.)

sodium salt. Now suppose that the same sample were to be spun at the same speed around an angle of 79.19°. The 2nd-order quadrupolar lineshapes for spinning at this angle are shown in Figure (1.5.12A). The key thing to notice about these two sets of simulated spectra is that the lineshapes for these two angles are exact mirror images of each other. This means that a crystallite spinning at an angle of 37.38° has the opposite sign of $H_Q^{(2)}$ as a crystallite spinning at an angle of 79.19°. This is analogous to the heteronuclear dipolar coupling, where two parallel spins (↑↑) have the opposite sign of H_{IS} as two antiparallel spins (↑↓), leading to the Pake doublet in Figure (1.2.4). In section 1.2 it was shown that by flipping the I-spin with CW irradiation, it was possible to remove H_{IS} by creating an average of $+H_{IS}$ and $-H_{IS}$. In DAS, the 2nd-order quadrupolar coupling is removed by flipping the *angle*, thus creating an average of $+H_Q^{(2)}$ and $-H_Q^{(2)}$.

Figure (1.5.13A) shows two possible pulse sequences for the implementation of DAS. For magnetization to evolve at two different angles, one must use an NMR probe that hops the spinning rotor from one axis to another. Since it is impractical to hop a spinning rotor while actively acquiring a signal, DAS must be incorporated into a two-dimensional experiment, where the 2nd-order quadrupolar coupling is removed in the indirect dimension, t_1, but not in the direct dimension, t_2. First, magnetization is excited with a $\frac{\pi}{2}$-pulse and is allowed to evolve for half of t_1 while spinning at 37.38°. The magnetization is then pulsed back along the z-axis (so that evolution is halted) and the rotor is hopped to an angle of 79.19°. Once the hop is complete, the magnetization is returned to the x-y plane with another $\frac{\pi}{2}$-pulse, and evolves for the second half of t_1.

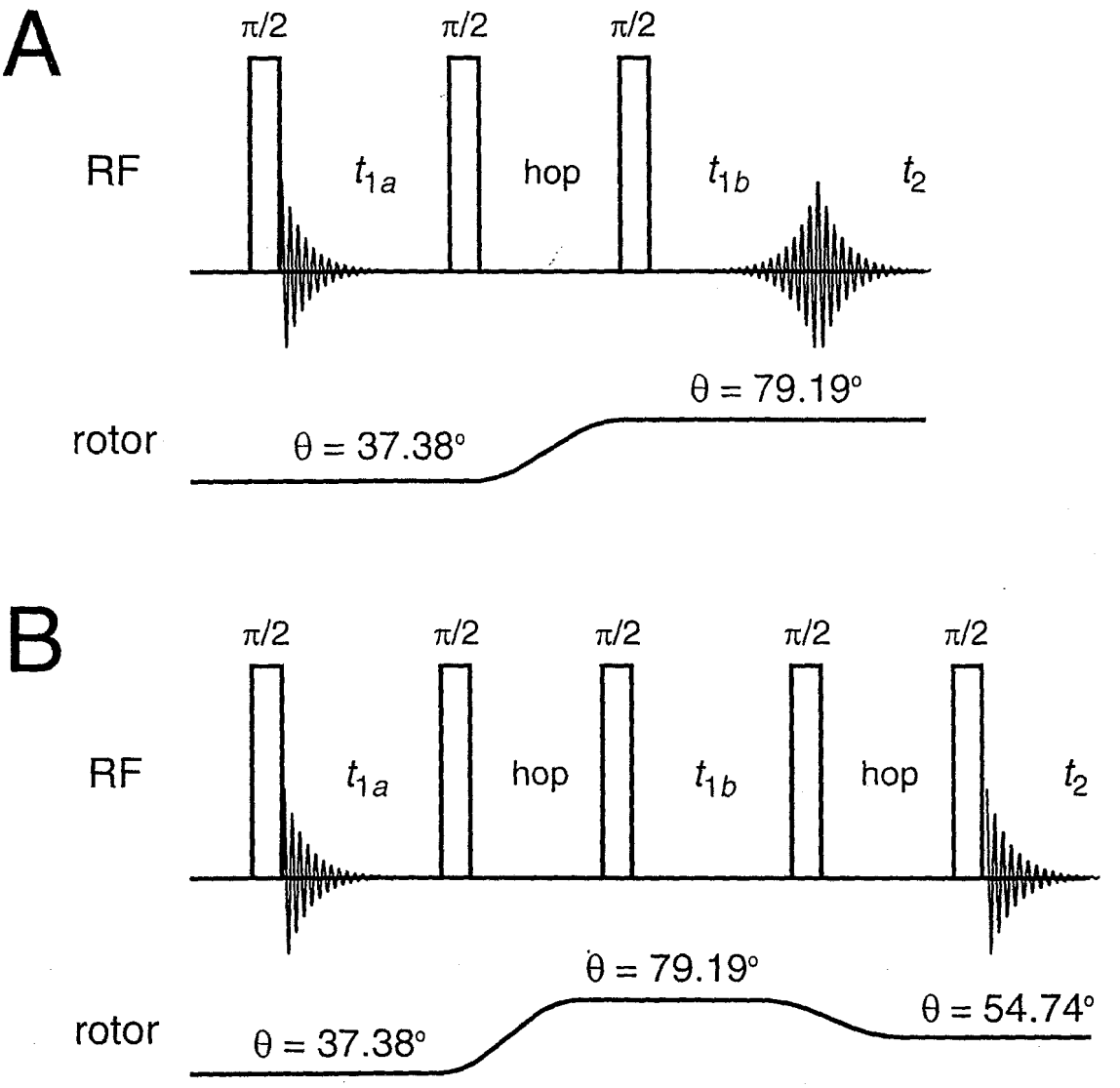

Figure 1.5.13. Pulse sequences for two-dimensional DAS experiments. (A) Conventional sequence to obtain an isotropic-anisotropic correlation, with powder patterns in the direct dimension characteristic of the second spinning angle. (B) Sequence including a second hop to allow detection at the magic angle.

After t_1, the magnetization is detected in the direct dimension, t_2. By varying the total time of the indirect dimension, it is possible to produce a two-dimensional spectrum that correlates the narrow isotropic quadrupolar lineshape with the broad 2nd-order quadrupolar lineshape (which is attenuated to some extent by spinning the sample during

acquisition). In Figure (1.5.14) a two-dimensional ^{87}Rb DAS spectrum of $RbNO_3$ is shown, which has three different rubidium sites. Although none of the Rb sites are resolvable in the projection of the anisotropic dimension, they are resolved in the isotropic dimension. By fitting the 2nd-order quadrupolar lineshapes obtained by taking slices through the three isotropic peaks, it is possible to determine the strength of the quadrupolar coupling at each site.

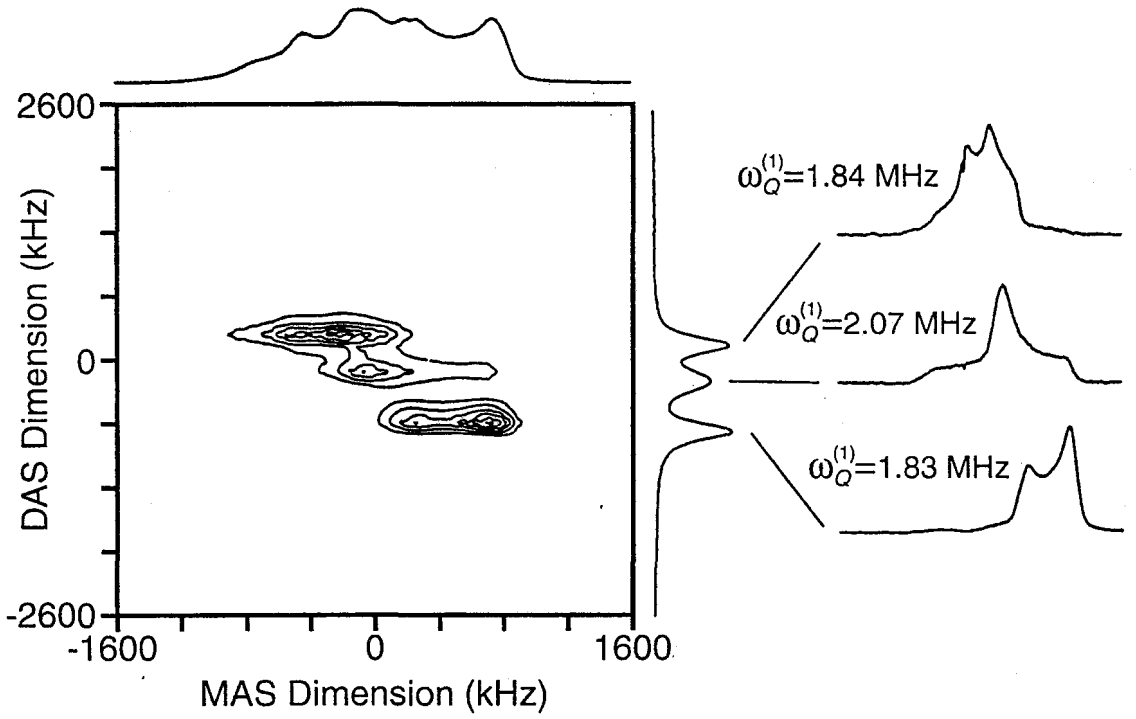

Figure 1.5.14. A two-dimensional DAS spectrum of the central transitions of ^{87}Rb in $RbNO_3$ obtained using the pulse sequence in Figure (1.5.12B). By taking slices in the isotropic (indirect) dimension at the different isotropic frequencies, powder patterns can be obtained which are characteristic of the different sites and yield the quadrupolar coupling constants and anisotropy parameters. (Reproduced from reference [16], with permission.)

1.5.2.3 Multiple-quantum MAS

Both DAS and DOR are very good techniques for removing the effects of the 2nd-order quadrupolar coupling in half-integer quadrupolar nuclei. However, they do suffer from one major drawback: each requires the use of a specialized NMR probe that is not readily available in most solid-state NMR facilities. Fortunately, a recently developed technique has eliminated the need for such specialized equipment. This technique, known as multiple-quantum MAS or MQMAS[78, 79], instead uses a standard MAS probe along with a clever pulse sequence to remove $H_Q^{(2)}$.

Recall that for the spin $I = \frac{3}{2}$ energy level diagram shown in Figure (1.5.7), the frequency of the central transition was *decreased* by a quantity proportional to $\omega_Q^{(2)}$, whereas the frequency of the triple-quantum (3-Q) transition ($m_I = -\frac{3}{2}$ to $\frac{3}{2}$) was *increased* by a quantity proportional to $\omega_Q^{(2)}$. Thus, if one were to first excite the 3-Q transition and let the magnetization evolve for a period t_{1a}, and then transfer the magnetization into the central transition and evolve for a period t_{1b}, at the end of the two periods, $t_1 = t_{1a} + t_{1b}$, the effects of the 2nd-order quadrupolar coupling would be removed. This is completely analogous to canceling $H_Q^{(2)}$ by evolving at two angles, as is done in DAS. The only difference is that in MQMAS, the rotor angle remains fixed and the magnetization evolves under two *coherences* that together remove $H_Q^{(2)}$ instead of two *angles*.

The similarity between MQMAS and DAS can be seen by examining the MQMAS pulse sequence in Figure (1.5.15). First, the 3-Q transition is excited using

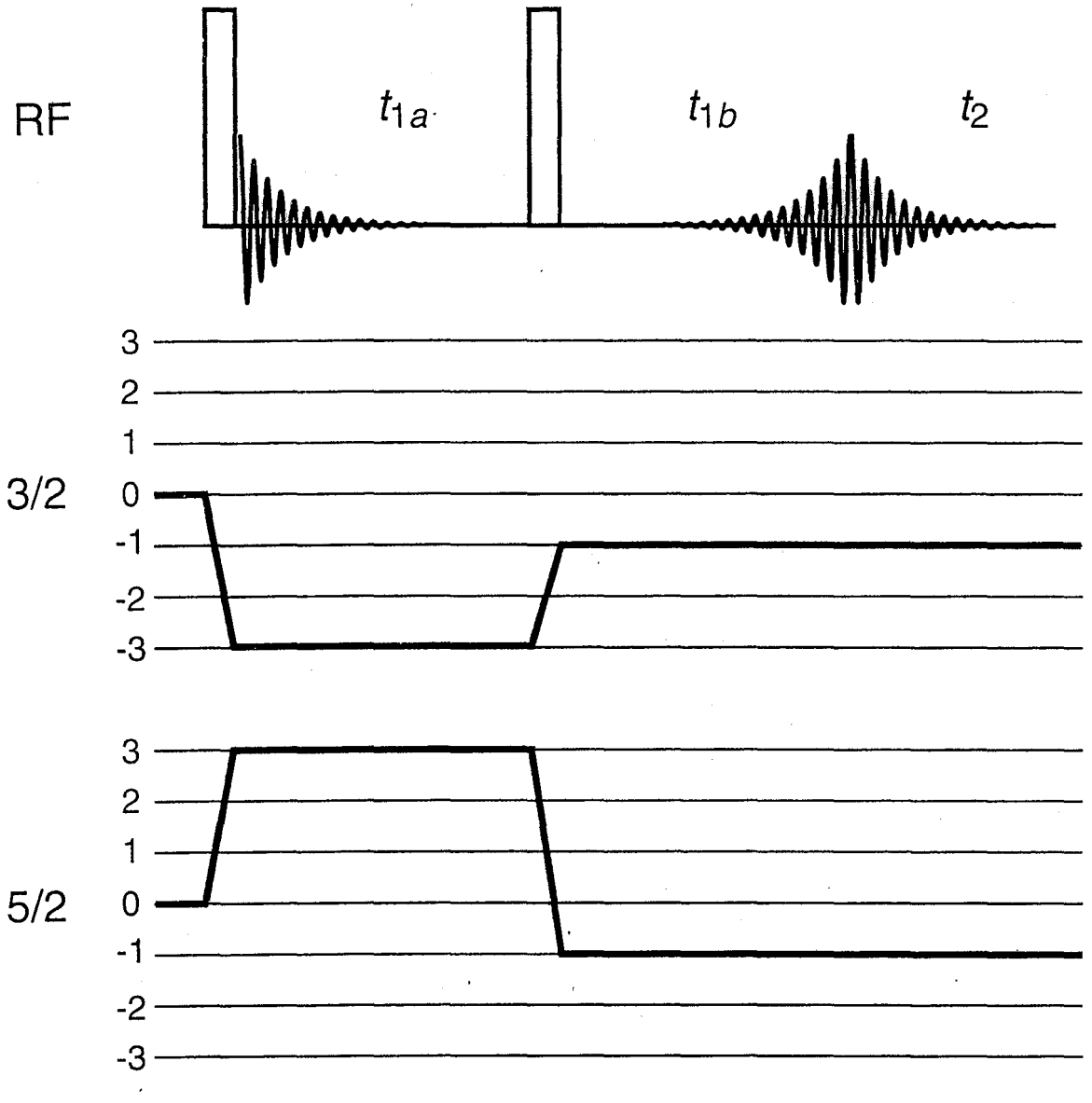

Figure 1.5.15. MQMAS pulse sequence and coherence pathways. In the period ($t_{1a} + t_{1b}$) the 1st and 2nd-order quadrupolar coupling is averaged to zero leaving a scaled isotropic spectrum in the indirect dimension. For spin I = 3/2 nuclei, the 0 → -3 → -1 coherence pathway is selected. For spin I = 5/2 nuclei, the 0 → 3 → -1 coherence pathway is selected. (Courtesy of S.H. Wang.)

some sort of pulse or train of pulses[80-82]. The magnetization then evolves for a period t_{1a}, at which point the magnetization is transferred into the single-quantum (1-Q) $m_I = -\frac{1}{2}$ to $\frac{1}{2}$ transition by way of a second pulse or series of pulses. The magnetization then

evolves for a period t_{1b}, after which it is detected during t_2. Just as with DAS, a two-dimensional spectrum is obtained by varying the time, $t_1 = t_{1a} + t_{1b}$, of the indirect dimension. Figure (1.5.16) shows an ^{23}Na MQMAS spectrum of Na_2HPO_4 obtained while spinning at a rate of 10 kHz. With the high resolution obtained in the isotropic (ω_1) dimension, it is possible to resolve all three sodium sites in the sample. By fitting the 2nd-order quadrupolar lineshapes obtained by taking slices through the three isotropic peaks, the quadrupolar couplings of all three sodium sites were determined. From this information, it is possible to back out the strength and orientation of the electric field gradients present at each site.

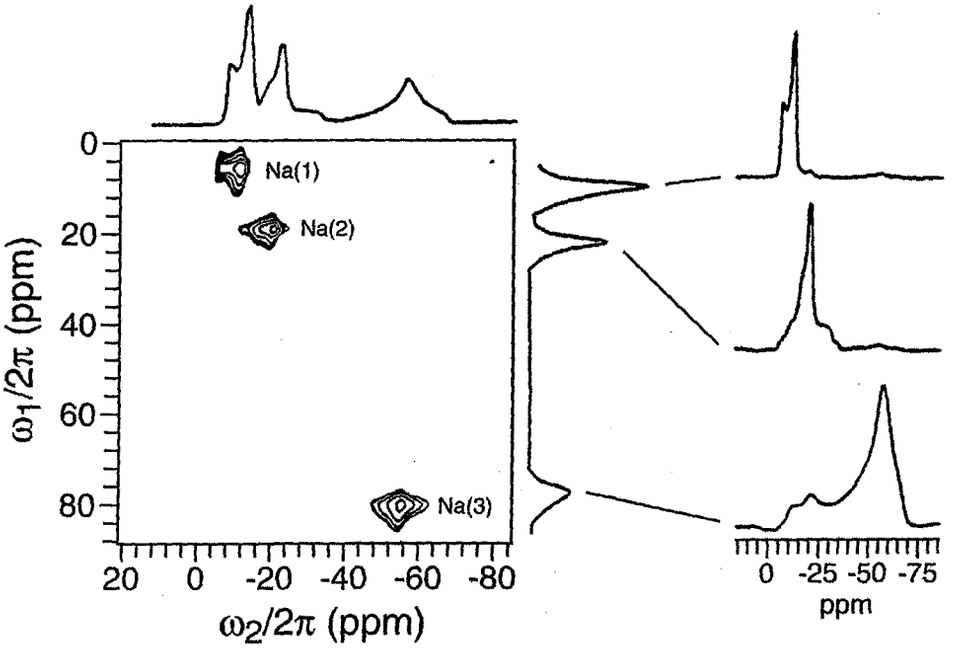

Figure 1.5.16. ^{23}Na MQMAS spectrum of $NaHPO_4$ obtained at a spinning speed of 10 kHz. The one-dimensional spectra to the right were obtained by taking slices through the peaks in the isotropic (ω_1) dimension. (Courtesy of K.H. Lim.)

1.5.3 - Summary

When compared to other solid-state NMR interactions, the complexity of the quadrupolar coupling is readily apparent. Nevertheless, the goal of this section was to provide some insight into the behavior and spectroscopy of quadrupolar nuclei. For nuclei with small quadrupolar couplings, like ^{2}H, information on dynamics and orientation is both simple to acquire and relatively easy to interpret. For nuclei such as ^{3}Li and ^{23}Na, high resolution spectra require more complex experiments like DAS or MQMAS. However, the recent boom in the study of quadrupolar nuclei in the solid state has made quadrupolar techniques like MQMAS far more commonplace in everyday research.

Chapter Two

Predicting α-Carbon Chemical Shift Tensors in Alanine, Valine, and Leucine using Theoretical Surfaces

2.1 Introduction

In this chapter and the next, studies on the dependence of the chemical shift anisotropy on local structure will be presented. As was pointed out in Chapter 1, chemical shifts depend strongly on the local environment surrounding the nucleus (see, for example, Figure 1.4.12). Previously, this was shown both experimentally[83, 84] and theoretically[85, 86] for isotropic chemical shifts of α- and β-carbons of amino acid residues. More recently, the chemical-shift anisotropies (CSAs) of α-carbons in alanine residues in peptides have been shown to be strongly dependent on the local secondary structure—so much so that it was possible to accurately predict the ϕ and ψ dihedral angles of alanine in a peptide from the CSA alone[50]. With the advent of new techniques for measuring chemical-shift tensors in liquids[87] and the existence of numerous techniques for measuring CSAs in solids[51, 58, 88, 89] as described in Chapter 1, there now exists the potential for using chemical-shift tensors to predict secondary structure in proteins and peptides. However, for such techniques to be possible, the complex dependence of chemical shift tensors on their local environment must first be understood.

There are two possible ways in which the CSAs of amino acids can be correlated with local structure. First, one can experimentally measure the chemical shift anisotropies of a group of proteins that have known structures and create empirical surfaces that describe each chemical shift tensor (δ_{11}, δ_{22}, and δ_{33}) as a function of the dihedral angles ϕ, ψ, and where appropriate χ_1 and χ_2. Indeed, this approach has already been used to produce empirical ϕ/ψ surfaces for isotropic C_α and C_β chemical shifts in

proteins[83]. The second way to correlate C_α chemical shift tensors with local structure is to use theoretical surfaces obtained by *ab initio* quantum chemical calculations on small amino acid fragments[49, 90-92]. The main advantage to using theoretical surfaces for structure prediction and refinement is that they are not confined to allowed regions of Ramachandran ϕ/ψ space, and thus these surfaces are valid for awkward conformations that may be forced on an amino acid to lower the overall energy of a protein. Indeed, simulated annealing programs often stray into unallowed regions of Ramachandran space on a path determining an overall fold. However, there is one major problem with using theoretical surfaces to predict chemical shifts.

Although it has been definitively shown that chemical shift surfaces can reproduce the relative C_α and C_β chemical shifts in proteins[85, 86], they are not scaled properly, and as a result, they often do not predict the full *range* of chemical shifts—especially surfaces created using Hartree-Fock methods[93]. This can easily be overcome by scaling the chemical shift surfaces based on comparisons between measured and predicted chemical shift values[50]. However, scaling surfaces for each amino acid could prove problematic. With 20 naturally occurring amino acids, most with a variety of rotomer conformations, scaling each surface based on experimentally measured chemical shifts could potentially be very time consuming. Furthermore, given the relatively small ~8 to 10 ppm ranges of most C_α and C_β isotropic chemical shifts in proteins, it is often difficult to define a correlation between theory and experiment accurate enough to properly scale the theoretical surfaces. One possible way to remedy this situation is to use comparisons between experimentally determined and theoretically predicted C_α chemical shift *tensors* in peptides. Whereas the isotropic C_α chemical shift range in

proteins may be only 8-18 ppm, anisotropic C_α chemical shifts in solid-state peptides can exceed 60 ppm, thereby providing a larger chemical shift range with which to correlate theory and experiment.

In this chapter, the first predictions of valine and leucine C_α chemical shift tensors using theoretical chemical shift surfaces based on local structure and produced from *ab initio* calculations are presented. The chemical shift anisotropies (CSAs) of alanine, valine, and leucine C_α nuclei from four peptides were determined using cross-polarization magic angle spinning (CPMAS) NMR. Dihedral angles taken from the x-ray structures of each of these peptides were then used in conjunction with theoretical chemical shift surfaces for alanine, valine, and leucine to obtain theoretical predictions of the C_α chemical shift tensors. The predicted and experimental CSAs agreed to within an rmsd of 2.4 ppm (slope = −0.77). The "best-fit" line for this data was then used to scale isotropic chemical shift calculations from *Drosophila* calmodulin and *Staphylococcal* nuclease[94-96]. Unscaled, the calculations predicted only 77% of the full chemical shift range, whereas the scaled chemical shift calculations predicted 101% of the total range. This suggests that small model peptides are a reasonable means for calibrating theoretical chemical shift surfaces for use in dihedral angle prediction and structure refinement in peptides and proteins.

2.2 Experimental

2.2.1 - Peptide Synthesis and Crystallization

All of the solid-state NMR experiments described in this chapter involve the measurement of $^{13}C\alpha$ chemical shift tensors in small peptides containing alanine, leucine, and valine residues. In all, six peptides were synthesized: A*AA and G*AV, which were done previously[50], and L*LVY-OMe, LL*VY-OMe, Boc-V*AL-Aib-*VAL-OMe, and Boc-VA*L-Aib-VAL-OMe. The asterik placed before an amino acid indicates that the α-carbon in this amino acid is ^{13}C labeled. The "Aib" in the Boc peptides refers to aminoisobutyric acid. Of the six peptides, two could be crystallized in multiple conformations based on the crystallization solvent used. The different peptides used, along with the references that describe their x-ray crystal structures and how to crystallize the peptides, are listed in Table (2.1). For a more thorough description of their synthesis and crystallization, please see Chapter 3.

Compound	Reference
GAV	[97]
AAA I[a]	[98, 99]
AAA II[a]	[98, 99]
Boc-VAL-Aib-VAL-OMe I[b]	[100]
Boc-VAL-Aib-VAL-OMe II[b]	[101]
L*LVY-OMe	[102]

[a]AAA I refers to the crystal form grown from 60% *N,N'*-dimethylformamide:water, whereas AAA II refers to AAA-hemihydrate crystals grown from 20% DMF:water.

[b]Boc-VAL-Aib-VAL-OMe I refers to the crystal form grown from 50% methanol:water, whereas Boc-VAL-Aib-VAL-OMe II refers to crystals grown from 50% isopropanol:water.

Table 2.1. Crystal structure references for the peptides discussed in this chapter.

2.2.2 - Solid-State NMR

The chemical shift tensors of all the labeled C_α nuclei were determined via CPMAS NMR. The Herzfeld-Berger method[51] was employed to measure the $^{13}C_\alpha$ CSAs of valine in two peptides, Leu-Leu-Val*-Tyr-OMe (LL*VY)[102] and Boc-Val-Ala-Leu-Aib-*Val-Ala-Leu-OMe (Boc-V-A-L-Aib-*V-A-L-OMe)[100, 101] and $^{13}C_\alpha$ CSAs of leucine in the same two peptides (LL*VY-OMe) and (Boc-V-A-*L-Aib-V-A-L-OMe). The alanine $^{13}C_\alpha$ CSA was measured in Boc-V*A-L-Aib-V-A-L-OMe. Since Boc-V-A-*L-Aib-V-A-L-OMe peptide can be crystallized into two forms (depending on the crystallization solvents used), and hence the CSAs were determined for two valines, three leucines, and one alanine. For a more detailed description of solid-state NMR experiments, please see Chapter 3.

2.2.3 - Theoretical Calculations

The alanine chemical shift surface was calcualted using the TEXAS-90 program[103], which utilizes the gauge-including-atomic-orbital (GIAO) method[104, 105]. The leucine and valine calculations were calculated using the GIAO package in Gaussian-98 (Gaussian, Inc., Carnegie, PA). All calculations were done on N-formyl-L-[amino acid] amide fragments extensively minimized at the helical geometry. For a more thorough description of the computations, please see Chapter 3.

2.3 Results and Discussion

The chemical shift anisotropies of alanine, valine, and leucine were determined in a series of small $^{13}C_\alpha$ labeled peptides using CPMAS NMR. Since the x-ray crystal structures of these compounds are known, it was possible to predict the chemical shift tensors for each of these residues by using the alanine, valine, and leucine chemical shift tensor surfaces. In Figure (2.1) plots of the experimentally determined $^{13}C_\alpha$ chemical shift tensors versus the predicted values for the alanine (Figure 2.1A), leucine (Figure 2.1B), and valine (Figure 2.1C) residues in the peptides listed in Table (2.1) are shown. The slopes and intercepts for all three amino acid residues are comparable, as are the rmsd's. Figure (2.1D) shows a compilation of the data for all three amino acids. With a total of 27 data points and an overall rmsd of 2.4 ppm, Figure (2.1D) clearly demonstrates the ability of theoretical *ab initio* chemical shift surfaces to predict C_α CSA values in both β-branched (leucine) and non-β-branched (valine) amino acids alike. Furthermore, the fact that all three data sets lie along the same line suggests that there may be a global scaling factor for all chemical shift surfaces, negating the need to do experimental scalings for all amino acid C_α chemical shift surfaces.

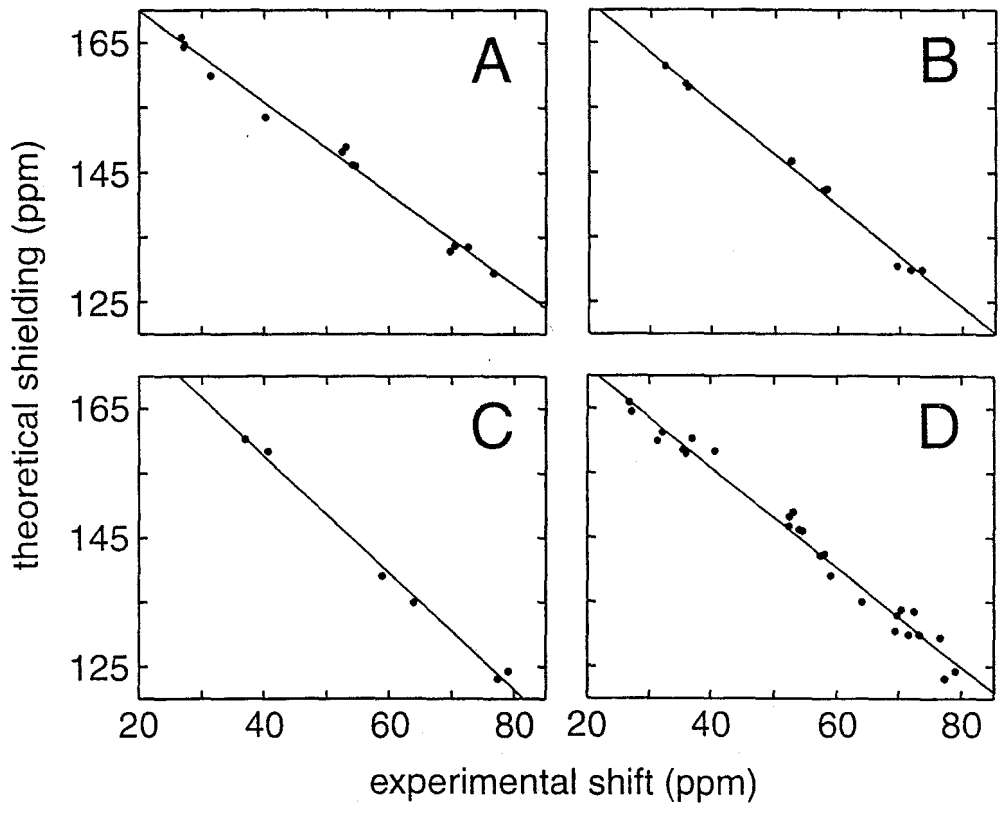

Figure 2.1. Theoretical $^{13}C_{\alpha}$ chemical shift tensor values for alanine (A), leucine (B), valine (C), and all three amino acids together (D) calculated using GIAO method and dihedral angles taken from the crystal structures versus the experimentally measured tensors.

One issue that remains to be address regarding theoretical chemical shift tensor surfaces is their ability to predict local structure in proteins and peptides based on measured chemical shift anisotropies. Although this work will be presented in Chapter 3, it is possible to test whether the overall scaling factor determined in Figure (2.1D) applies to proteins as well as peptides. Figure (2.2A) shows a plot of experimentally measured

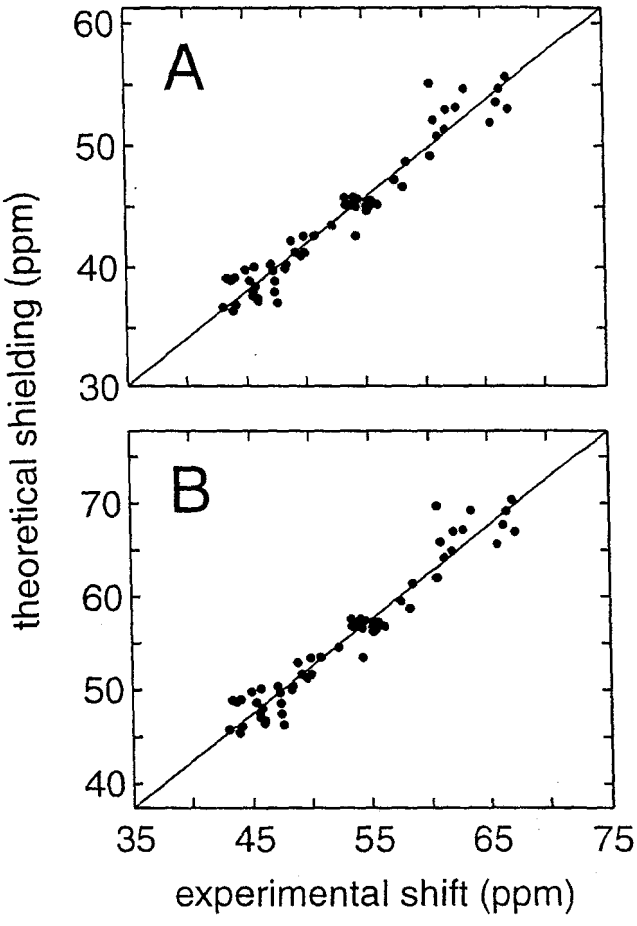

Figure 2.2. (A) Theoretical $^{13}C_\alpha$ chemical shielding for alanine, glycine, and valine in *Drosophila* calmodulin[106] and *Staphylococcal* nuclease[107] versus theoretically calculated chemical shifts[86]. (B) The same chemical shift values as in (A) except scaled with the slope and intercept from Figure (2.1D).

C_α chemical shifts for alanine, glycine, and valine *Drosophila* calmodulin[106] and *Staphylococcal* nuclease[107] versus theoretically calculated chemical shifts[86]. Figure (2.2B) shows the same 57 data points with the theoretically predicted chemical shifts scaled using the slope and intercept from Figure (2.1D). With the scaling, 101% of the chemical shift range is now predicted, as opposed to 77% in Figure (2.2A). Furthermore, the y-intercept of the best-fit line (which would correspond to the ^{13}C chemical shift of TMS) in Figure (2.2B) decreases from 3 ppm to 2 ppm, which is closer to the ideal value of 0.0 ppm.

3.1 Introduction

As was noted in Chapter 1, numerous solid-state NMR techniques for molecular structure determination have been developed in the last two decades. These methods have been used widely to measure internuclear distances[108] via dipole-dipole couplings in the case of REDOR[1], DRAMA[36], or Rotational Resonance[3], as well as to map out connectivities in small biomolecules[109, 110] via J-couplings. Moreover, other approaches, which were not mentioned in Chapter 1, have been developed to determine torsion angles[17, 111]. For example, several techniques[112-115] have used 2D-exchange or correlation spectroscopies to measure the relative orientation of dipolar coupling tensors to determine the torsion angles. Meanwhile, Levitt and co-workers[116] have used double quantum heteronuclear local field spectroscopy (2D-HLF) to measure the torsion angles in an H-C-C-H moiety to within ±10° or ±20°, depending on whether the molecule is *cis* or *trans*, respectively.

These techniques for structure determination have greatly advanced the capabilities of solid-state NMR. Its use as a tool to study structures of biomolecules remains limited, however, due to the inherent lack of resolution that results from the strong dipolar couplings (predominantly between ^{1}H nuclei) and chemical shift anisotropies present in solids. The resulting broad lines, which are rarely less than ~1-2 ppm, effectively eliminate the possibility of performing experiments on fully ^{13}C and ^{15}N labeled protein samples (as is routinely done in liquids) unless they are either polycrystalline or relatively small (<30 residues)[117]. Thus, in solid-state NMR, selective labeling schemes are required to avoid spectral overlap, and techniques for structure

determination must be employed that maximize the information derived from each labeled site.

Currently, the vast majority of existing techniques require two or more labels for the determination of a single distance or pair of dihedral angles. However, one possible alternative requires only one labeled site and uses *ab initio* chemical shift calculations to gain insight into the backbone and side chain torsion angles of amino acids. These *ab initio* chemical shift calculations have been used to correlate experimentally determined ^{13}C isotropic chemical shifts with secondary structure in proteins, both in liquids[118, 119] and solids[120-123] and have been reproduced in theoretical calculations[96, 124-126]. These correlations have then been used to calculate chemical shift surfaces from the backbone dihedral angles, φ and ψ, and where applicable, the side chain angles, χ_1 and χ_2. In conjunction with experimentally determined chemical shifts, these *ab initio* chemical shift surfaces can be used to refine solution structures[127-129] and to determine probability-based predictions of dihedral angles[50, 128, 130].

In this chapter, a technique is presented, which determines dihedral angles by correlating experimentally determined chemical shift tensors with *ab initio* chemical shift computations that were calculated as a function of the backbone dihedral angles, φ and ψ, and where applicable, the side chain angles, χ_1 and χ_2. Previously, this technique, also known as the CSA/Z method, was applied to determine the dihedral angles of alanine in several small, powdered crystalline peptides, whose structures had been determined earlier by x-ray crystallography[50]. Here, the CSA/Z method is extended to determine the dihedral angles of alanine, valine and leucine and to show that this approach can be

generalized to other amino acids including those with β-branched and non-β-branched side chains. In Figure (3.1), the general molecular structure of an amino acid is depicted.

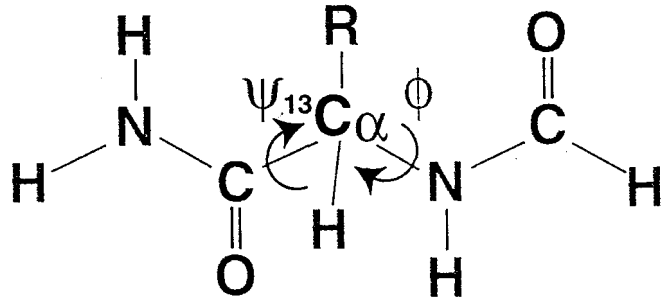

Figure 3.1. The molecular structure of an amino acid with dihedral angles drawn schematically.

Unlike alanine, both valine and leucine necessitate the determination of both the dihedral angles and the side chain angles. The results show that the highest probability solution also predicts the proper side chain angle(s). The advantages of the CSA/Z method are many: First, the method is not experimentally demanding. A series of one-dimensional slow-spinning cross-polarization magic angle spinning (CPMAS) experiments are required to determine the chemical shift tensors. Second, by virtue of the fact that this method exploits all three CSA tensor values, only one label is necessary where, in the past, two or three isotropic chemical shifts were needed to predict the dihedral angles[128]. Third, the method can also predict the side chain angle by selection of the highest probable solution. Fourth, the need for only one ^{13}C α-carbon label allows for the simultaneous determination of numerous dihedral angle pairs since this labeling requirement minimizes spectral overlap. The overlap of the spinning sidebands can be avoided by careful selection of the rotor spinning speed or by implementing one of many two-dimensional experiments[53-58, 131-135].

3.2 Experimental

All of the solid-state NMR experiments described in this chapter involve the measurement of $^{13}C\alpha$ chemical shift tensors in small peptides containing alanine, leucine, and valine residues. In all, six peptides were synthesized: A*AA and G*AV, which were done previously[50], and L*LVY-OMe, LL*VY-OMe, Boc-V*AL-Aib-*VAL-OMe, and Boc-VA*L-Aib-VAL-OMe. The asterik placed before an amino acid indicates that the α-carbon in this amino acid is ^{13}C labeled. The "Aib" in the Boc peptides refers to aminoisobutyric acid. Of the six peptides, two could be crystallized in multiple conformations based on the crystallization solvent used. The different peptides used, along with the references that describe their x-ray crystal structures, are listed in Table (3.1). Below is a brief description of their synthesis, characterization, and crystallization.

Compound	Reference
GAV	[97]
AAA I[a]	[98, 99]
AAA II[a]	[98, 99]
Boc-VAL-Aib-VAL-OMe I[b]	[100]
Boc-VAL-Aib-VAL-OMe II[b]	[101]
L*LVY-OMe	[102]

[a]AAA I refers to the crystal form grown from 60% *N,N'*-dimethylformamide:water, whereas AAA II refers to AAA-hemihydrate crystals grown from 20% DMF:water.

[b]Boc-VAL-Aib-VAL-OMe I refers to the crystal form grown from 50% methanol:water, whereas Boc-VAL-Aib-VAL-OMe II refers to crystals grown from 50% isopropanol:water.

Table 3.1. Crystal structure references for the peptides discussed in this chapter.

3.2.1 - Fmoc Protection of ^{13}C Labeled Amino Acids

All $^{13}C_{\alpha}$-labeled amino acids (Cambridge Isotope Laboratories, Andover, MA; Isotec, Miamisburg, OH) were Fmoc-protected in a manner similar to one previously described[136]. To 3.75 mmol of the amino acid dissolved in H_2O (60 mL), 0.945 g (11.25 mmol) of sodium bicarbonate ($NaHCO_3$) was added. After dissolving 1.265 g (3.75 mmol) of N-(9-fluorenylmethoxycarbonyloxy) succinimide (Fmoc-O-Suc) in acetone (60 mL), the mixtures were combined. The cloudy mixture became clear after stirring for 24 hours, at which point the acetone was removed by rotary evaporation. Citric acid (1 M) was used to precipitate the Fmoc- amino acids from the aqueous solution. Ethyl acetate (EtOAc) (150 mL) was added to redissolve the precipitate. The mixture was transferred to a separatory funnel and the layers were separated. The aqueous layer was washed with EtOAc (100 mL). The combined organic layers were then washed with H_2O (2×100 mL) and saturated NaCl (2×100 mL). The organic layers were dried over magnesium sulfate and the solvent was removed by rotary evaporation. The product was used for solid-phase peptide synthesis without further purification.

3.2.2 - Peptide Synthesis

G*AV, A*AA, L*LVY-OMe, and LL*VY-OMe were synthesized using N-Fmoc protected amino acids on an Applied Biosystems 431A (Perkin Elmer-Perceptive Biosystems, Foster City, CA) peptide synthesizer. The peptides were cleaved from the resin and deprotected by stirring for 3 hours in a 95% (v/v) trifluoroacetic acid (TFA)/H_2O solution. The mixture was filtered to remove the resin. TFA was removed

by rotary evaporation, followed by lyophilization. The cleaved A*AA was then redissolved in H_2O and purified by reversed-phase HPLC on a Vydac C-18 column. Purity and identity of all these samples were checked by electrospray-ionization mass spectrometry (Hewlett-Packard 5989A).

Boc-V*AL-Aib-*VAL-OMe and Boc-VA*L-Aib-VAL-OMe were synthesized using optimized Fmoc chemistry[137] on an Applied Biosystems 433 peptide synthesizer. Fmoc amino acid derivatives were pre-activated by reaction with 2-(1H-benzotriazol-1-yl)-1,1,3,3-tetramethyluronium hexafluorophosphate (HBTU) and diisopropylethylamine (DIEA). After the coupling of each amino acid a capping step was performed using N-(2-chlorobenzyloxycarbonyloxy) succinimide (Novabiochem, La Jolla, CA)[138]. Labeled residues were coupled manually using a 1.5 fold excess of amino acid and coupling efficiency monitored using the quantitative ninhydrin test[139]. The last residue was coupled as the Boc derivatized amino acid. Peptides were cleaved from the resin with 1% TFA in dichloromethane (CH_2Cl_2), and the cleaved peptide solution was collected in a round-bottomed flask containing pyridine. The peptidyl-resin was treated with additional aliquots of cleavage mixture and the filtrates were combined. CH_2Cl_2 was eliminated using a rotary evaporator and the residue taken up in 20% acetic acid. The crude peptides were purified by reversed-phase HPLC on a Rainin (Emeryville, CA) liquid chromatography system using a Vydac C-18 semi-preparative column (250 x 10 mm). The identity of the purified peptides was confirmed by electrospray mass spectrometry using a Perkin Elmer-Sciex API-300 instrument.

3.2.3 - Crystallization

Peptides were crystallized following the protocols from the references listed in Table (3.1), with slight modifications made in order to crystallize larger quantities. In all cases, small crystal clusters were obtained; large single crystals are not necessary in this approach. GAV[97] was dissolved in a minimal volume of warm water and the solution was placed in a Petri dish. The dish was then placed into a sealed container over a reservoir of methanol. Due to vapor diffusion, small crystals formed quickly and crystallization was complete within a day. AAA was crystallized in two crystal forms. The first crystal form of AAA (hence referred to as AAA I) was formed by dissolving the tripeptide in a solution of 60% (v/v) *N,N'*-dimethylformamide (DMF) in water and placing the solution in a glass Petri dish. The solvent was allowed to evaporate slowly. The second crystal form, AAA-hemihydrate (hence referred to as AAA II) was formed by a similar procedure, except that the concentration of DMF was 20% (v/v). The two crystal forms could be distinguished visually, with AAA I forming plates and AAA II forming needles.

Boc-VAL-Aib-VAL-OMe crystals were grown in sample vials with a slow flow of nitrogen gas blowing over the solution. As with AAA, the Boc-VAL-Aib-VAL-OMe peptides crystallize in two forms, depending on the solvent. The first crystal form, Boc-VAL-Aib-VAL-OMe I, was obtained through slow evaporation of the peptide from a 50% methanol in water solution. The second crystal form, Boc-VAL-Aib-VAL-OMe II, was obtained through slow evaporation of the peptide from a 50% isopropanol in dimethyl sulfoxide (DMSO). Unfortunately, only the leucine $^{13}C_{\alpha}$-labeled peptide produced useable crystals in the second form, due presumably due to contamination in the alanine/valine labeled Boc compound. Low-angle x-ray powder diffraction profiles using

CuKα radiation were taken to confirm crystallinity (Inel, Inc. CPS120 Powder Diffraction System, Idaho Falls, ID).

The LLVY-OMe peptides were crystallized from water and DMF. The peptides were first suspended in ~200 μL of water. The suspension was then heated in an oil bath to 70°C and DMF was added in 1 μL aliquots until the peptides completely dissolved. Upon slow cooling, small crystals formed. The remaining solution was removed by slow evaporation.

3.2.4 - Solid-State NMR

All GAV and AAA ^{13}C NMR spectra as well as some Boc-VAL-Aib-VAL-OMe ^{13}C NMR spectra were obtained at 7.07 Tesla (corresponding to a ^{13}C Larmor frequency of 75.74 MHz) on a home-built spectrometer based on a Tecmag (Houston, Texas) pulse programmer. A Chemagnetics (Fort Collins, CO) 4-mm double-resonance MAS probe was used for these experiments. Spinning speeds were controlled to ±1 Hz using a home-built spinning-speed controller. The CP contact time was 2.5 ms, the ^{1}H decoupling field strength was 108 kHz, and the recycle delay was 1.5 seconds. The remaining Boc-VAL-Aib-VAL-OMe and the LLVY-OMe ^{13}C NMR spectra were obtained at 11.72 Tesla (corresponding to a ^{13}C Larmor frequency of 125.75 MHz) on a triple-resonance Varian/Chemagnetics (Fort Collins, CO) Infinity spectrometer with a 4-mm T3 triple-resonance MAS probe. Spinning speeds were controlled to within ±3 Hz using a Chemagnetics spinning-speed controller. The CP contact time was 2.0 ms, the ^{1}H decoupling field strength was 104 kHz, and the recycle delay was 2 seconds. The experimental data was fitted using the Herzfeld-Berger method[51]. An average of the

CSA values derived from each spinning speed was taken and used to compare with theoretically calculated values. Isotropic shift values were measured relative to the carbonyl carbon of glycine at 176.04 ppm.

3.2.5 - Theoretical Calculations

The alanine shielding calculations were performed using the TEXAS-90 program[103], which utilizes the gauge-including-atomic-orbital (GIAO) method[104, 105]. The leucine and valine calculations were performed using the GIAO package in Gaussian-98 (Gaussian, Inc., Carnegie, PA). All calculations were done on N-formyl-L-[amino acid] amide fragments extensively minimized at the helical geometry. A "locally-dense" basis set was employed consisting of 6-311++G(2d,2p) basis functions on the central residue and 6-31G basis functions on the formyl and amide groups. Computations were performed on IBM RISC/6000 workstations (Models 340, 350, and 360; IBM Corporation, Austin, TX) and on a cluster of SGI Origin-200 workstations (Silicon Graphics Inc., Mountainview, CA). The alanine shielding surfaces were constructed by choosing 358 ϕ/ψ points in Ramachandran space, with a more dense placement of points in the allowed regions. The valine and leucine surfaces were created using a strategic placement of 100 ϕ/ψ points in Ramachandran space. Z-surfaces for the chemical shift tensors were created using a Gaussian equation:

$$Z_{\delta_{nn}}(\phi,\psi) = \exp\left[-\frac{\left(\delta_{nn}^{ecs} - \delta_{nn}(\phi,\psi)\right)}{\omega^2}\right] \tag{3.1}$$

where δ_{nn}^{ecs} is the experimental chemical shift tensor, $\delta_{nn}(\phi,\psi)$ is the chemical shift tensor surface, and ω is the root-mean-square deviation between experimentally measured and predicted chemical shift tensors (for all Z-surfaces in this chapter, ω=2.42 ppm).

3.3 Results and Discussion

The $^{13}C_\alpha$ chemical shift tensors for nine crystal forms of the six peptides listed in Table (3.1) were determined by CPMAS NMR. For each crystal, one high spinning speed ^{13}C CPMAS experiment and a series of slow-spinning CPMAS experiments were conducted. Shown in Figure (3.2) are the ^{13}C CPMAS spectra of Boc-V-*A-L-Aib-*V-A-L-OMe, crystallized from methanol:water, at rotor spinning speeds of 1000 Hz (A), 1100 Hz (B), 1200 Hz (C), 1300 Hz (D), 1500 Hz (E), and 10 kHz (F). The spinning sidebands of the valine and alanine α-carbons are well resolved and do not overlap with each other, and therefore both sets of CSA principal values could be readily determined. Similar data were collected for the other valine and leucine labeled crystals, but are not shown. The crystallography data indicate two conformations per unit cell for the Boc peptides when crystallized from methanol/water. However, due to limitations in resolution in our experiments, only one isotropic chemical shift was seen for each labeled carbon in both the leucine labeled and the valine/alanine labeled crystals, as shown in Figure (3.2F). Hence, our experimental resolution was not high enough to differentiate between the two conformers. In the case of $^{13}C_\alpha$ labeled alanine in the Boc compound, the difference between the two conformers was 3° in both φ and ψ, and so average values were used in the calculations. For the leucine labeled α-carbon, the

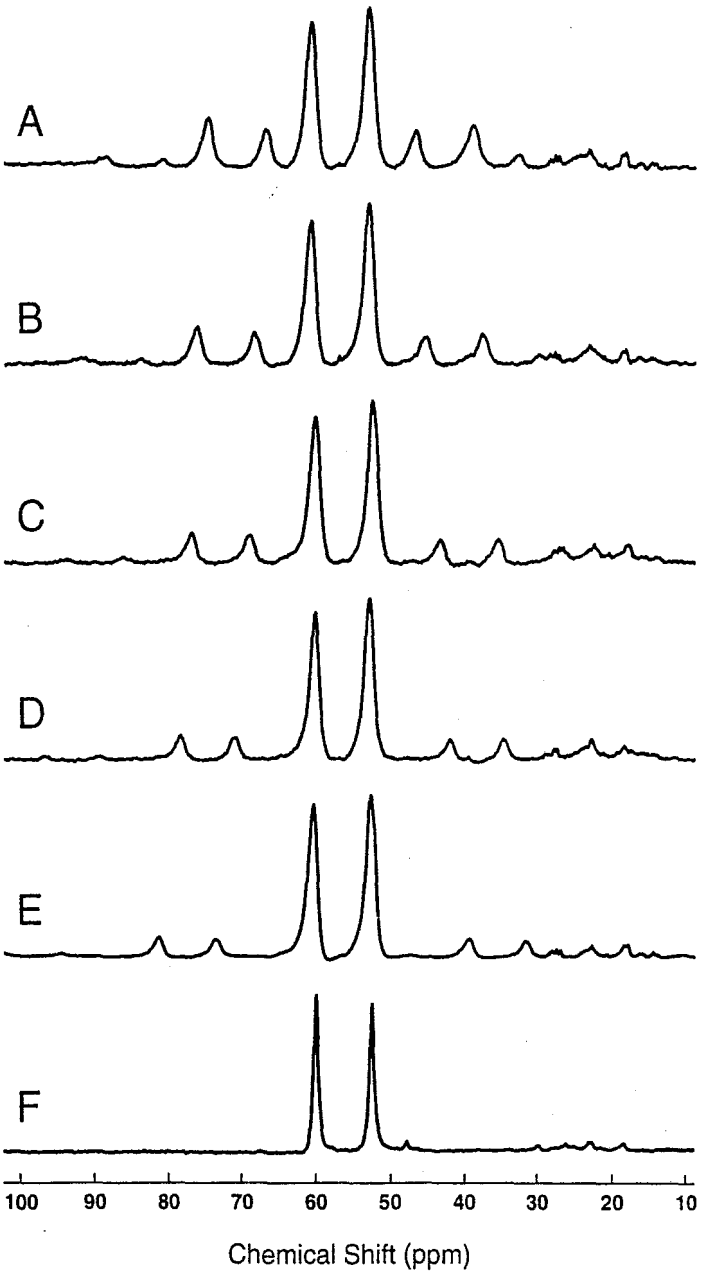

Figure 3.2. ^{13}C CPMAS NMR spectra of Boc-V-*A-L-Aib-*V-A-L-OMe, crystallized from methanol:water, at rotor spinning speeds of 1000 Hz (A), 1100 Hz (B), 1200 Hz (C), 1300 Hz (D), 1500 Hz (E), and 10 kHz (F).

different conformers had similar χ_1 and χ_2 values and a difference of 3° in φ and ψ. Since the two conformers had similar side chain angles, average values of the two conformers and the same Z-surfaces were used. For the $^{13}C_\alpha$ valine label, the crystals grown give two conformations per unit cell, but again the difference was small and an average value of the two conformers was used in the calculations. Similarily, two molecules with slightly different conformations exist in the unit cells of both forms of A*AA. However, the resolution of our experiments was also not high enough to differentiate between them, and as a result, only one line was observed.

Fast CPMAS spectra ($\omega_r \geq 10$ kHz) were collected to determine the isotropic chemical shifts and were referenced to the carbonyl carbon of glycine ($\delta_{iso} = 176.04$ ppm). The Herzfeld-Berger method was used to determine the chemical shift tensors from each of the slow spinning CPMAS spectra and the average tensor values are tabulated in Table (3.2). This method does not account for the presence of a directly bonded ^{14}N nucleus to the α-carbon and thus it does not incorporate couplings between these two nuclei. To investigate the effects of this coupling on the CSA values, a non-linear least-square fitting program, which accounts for the ^{14}N-^{13}C coupling, was also used to determine the CSA values. The two fits were in good agreement and support the notion that the ^{14}N-^{13}C coupling does not significantly alter the α-carbon CSA principal values, as has been shown previously[50]. The values obtained by the Herzfeld-Berger approach gave a correlation line with a lower rmsd (see Chapter 2), and thus were used to determine the dihedral angles.

Residue	Compound	δ_{11}	δ_{22}	δ_{33}
Alanine	G*AV	76.7	54.1	27.1
	A*AA I[a]	70.4	53.0	27.2
	A*AA II[a]	69.7	52.4	26.7
	Boc-V*AL-Aib-VAL-OMe I[b]	72.5	54.5	31.3
Leucine	Boc-VA*L-Aib-VAL-OMe I[b]	73.4	57.5	35.5
	Boc-VA*L-Aib-VAL-OMe II[b]	71.6	58.0	36
	L*LVY-OMe	69.3	52.3	32.2
Valine	Boc-VAL-Aib-*VAL-OMe I[b]	79.1	64.0	37.0
	LL*VY-OMe	77.4	58.0	40.7

[a]A*AA I refers to the crystal form grown from 60% *N,N'*-dimethylformamide:water, whereas A*AA II refers to crystals grown from 20% DMF:water.

[b]Boc-V*AL-Aib-VAL-OMe I refers to the crystal form grown from methanol:water, whereas Boc-V*AL-Aib-VAL-OMe II refers to crystals grown from isopropanol:water.

Table 3.2. Tabulated are the chemical shift tensor values measured by CPMAS NMR and determined by the Herzfeld-Berger method[51].

Using theoretical chemical shift tensor surfaces that describe the behavior of the three principal values of the CSA (δ_{11}, δ_{22}, and δ_{33}) as a function of ϕ and ψ, theoretical chemical shifts were determined for each peptide sample based on the dihedral angles provided in the crystal structure references listed in Table (3.1). Chemical shift tensor surfaces for alanine are shown in Figure (3.3). For leucine and valine, which both possess multiple rotomer conformations, multiple chemical shift tensor surfaces exist to account for each of the allowed backbone rotomers. These correspond to $\chi_1 = 180°$, –60° and +60° for valine and $\chi_1 = 180°$, $\chi_2 = -60°$ and $\chi_1 = 180°$, $\chi_2 = +60°$ for leucine.

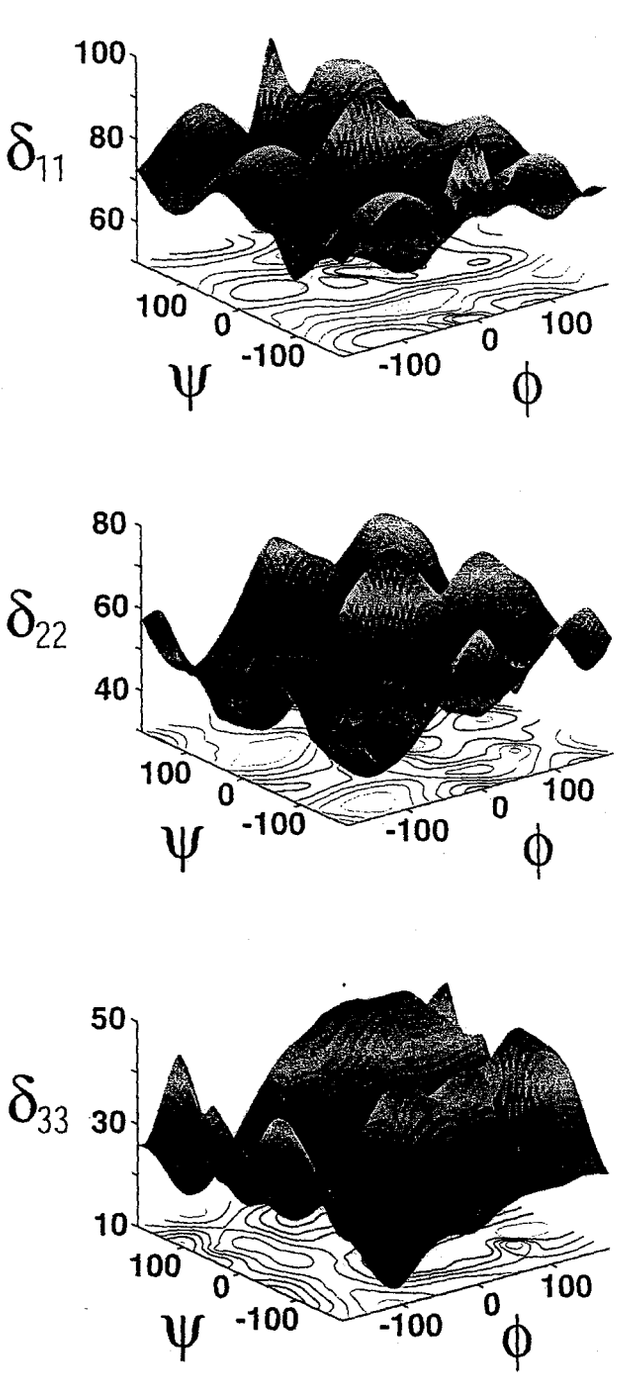

Figure 3.3. The alanine Ramachandran chemical shift surfaces for C_α sites in N-formyl-L-alanine amide. The surfaces, which are calculated based on the dihedral angles, were approximated using 358 points spread over φ/ψ space with a more dense placement of points in the allowed regions.

The CSA/Z method was then used to determine the dihedral angles for alanine, valine, and leucine. As described previously[50], a ^{1}Z probability surface is created for each of the CSA tensor values using the formula in Equation (3.1). The experimental chemical shift tensor value is compared to every point on the corresponding chemical shift tensor surface to determine which φ/ψ combinations produce a chemical shift close to the experimental value. A Gaussian is used to define the probability that a given φ/ψ conformation is correct. As can be seen in the tensor surfaces shown in Figure (3.3) an infinite number of φ/ψ conformations correspond to most measured chemical shifts, making a ^{1}Z-surface incapable of predicting structure on its own. To illustrate this point, Figure (3.4A-C) shows a series of ^{1}Z-surfaces for three experimental chemical shift values. Clearly, many solutions exist. However, a unique solution can be obtained by taking the product of n ^{1}Z-surfaces to create an ^{n}Z-surface.

The Z-surface approach was first used to predict local conformations of proteins in solution based on $C\alpha$, $C\beta$, and $H\alpha$ isotropic chemical shifts[128]. In solution, all three chemical shifts are required in order to create a ^{3}Z-surface capable of predicting a unique ϕ/ψ conformation. In solids, additional experiments to determine the $C\beta$ and $H\alpha$ isotropic shifts are not needed, since the three components of the chemical shift anisotropy, δ_{11}, δ_{22}, and δ_{33}, provide the three independent parameters necessary. Figure (3.4) shows a series of Z-surfaces for Boc-VA*L-Aib-VAL-OMe I. Figures (3.4A-C) show the ^{1}Z-surfaces that correspond to δ_{11}, δ_{22}, and δ_{33}, and Figure (3.4D) shows the ^{3}Z-surface that is a product of the three ^{1}Z-surfaces in Figure (3.4A-C). As can be seen in Figure (3.4D), the ^{3}Z-surface predicts multiple high-probability ϕ/ψ conformations.

However, some of these conformations can be eliminated from consideration because they lie in regions of Ramachandran space that are conformationally unallowed. In Figure (3.4E), this is accomplished by zeroing the probability in all unallowed regions of ϕ/ψ space. Figure (3.4F) shows an expansion of the highest probability region of Figure (3.4D-E). In this case, the CSA/Z method predicts dihedral angles of $\varphi = -74°$, which is within 3° of the x-ray results, and $\psi = -35°$, which is the same value for ψ reported in the reference in Table (3.1). In Table (3.3), the predicted leucine dihedral angles for Boc-VA*L-Aib-VAL-OMe I as well as the dihedral angles for the other peptides are compared to values taken from their x-ray structures. Dihedral angles for A*AA I and A*AA II could not be predicted because the measured chemical shift tensors resulted from an average of two structures present in the AAA unit cell. Although an average theoretical chemical shift tensor can be predicted from two structures, a structure cannot be predicted from an average of two chemical shift tensors if the difference in their structures is significantly large.

For the ^{3}Z-surfaces obtained for Boc-V*AL-Aib-VAL-OMe I, Boc-VA*L-Aib-VAL-OMe II, and L*LVY-OMe, two solutions were found that were very close to each other (within ±30° in both ϕ and ψ). In each case, it was noticed that the correct ϕ/ψ conformation was between the two nearby-local-maximum solutions (Figure 3.5). By using an average of the ϕ and ψ angles for each solution (weighted by the probabilities of each solution) a more accurate conformational prediction was made for each of the three peptides. Although this averaging of conformations is unnecessary (the highest-probability solution is still close to the actual conformation), given the repeated success

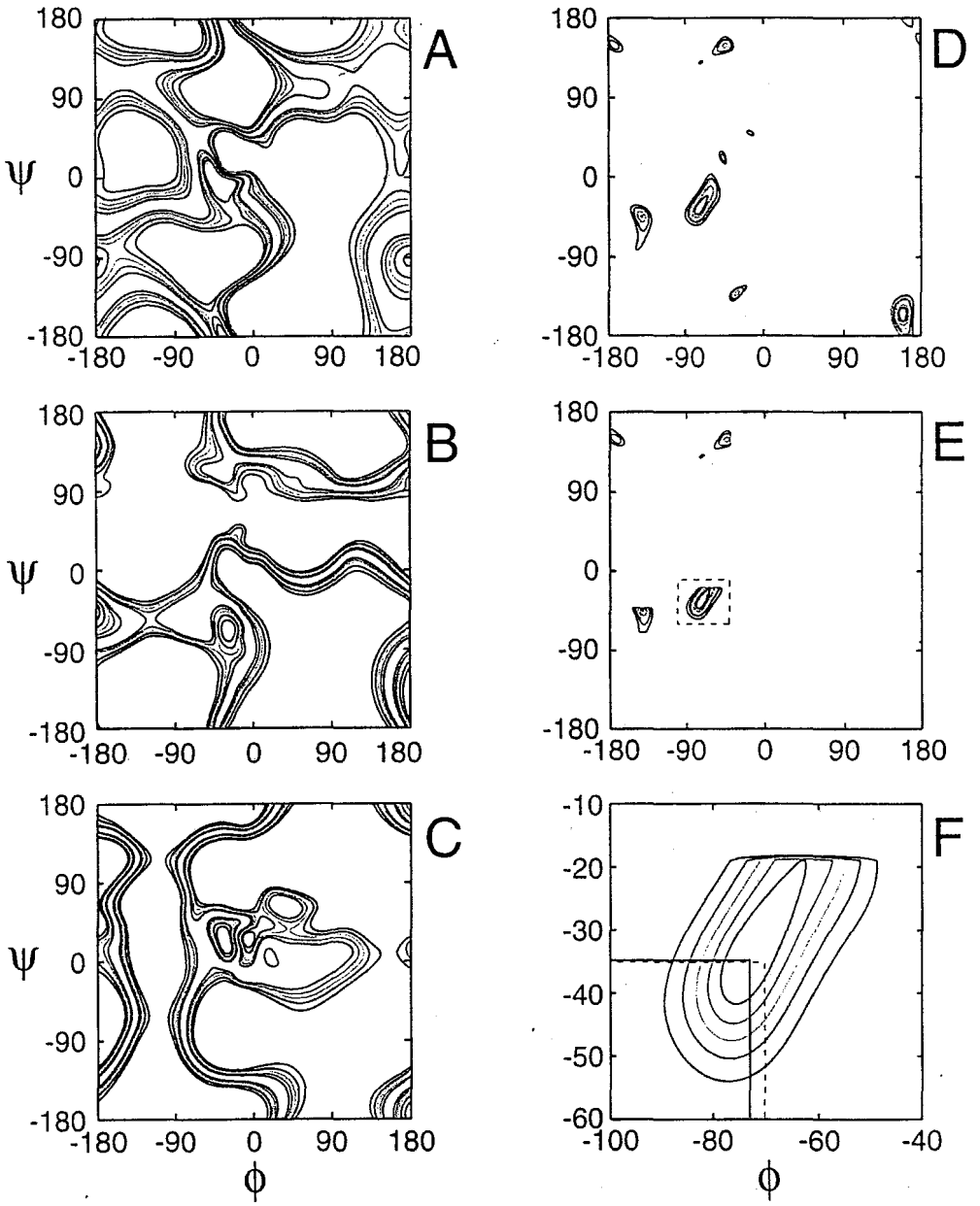

Figure 3.4. (A-C) Z-surfaces calculated from the experimentally determined chemical shift anisotropy for the C_α leucine in Boc-V-A-*L-Aib-V-A-L-OMe and theoretical chemical shift surfaces scaled by the correlation determined in Chapter 2. The three ^{1}Z-surfaces for δ_{11}(A), δ_{22}(B), and δ_{33}(C). (D) ^{3}Z-surface showing the intersection of the surfaces in (A), (B), and (C). (E) ^{3}Z-surface with solutions in unallowed regions of Ramachandran space removed. (F) The dihedral angles as determined by measurement of the CSA tensor (solid lines) are φ=-74° and ψ=-35°, while those determined by x-ray crystallography (dashed lines) are φ=-71° and ψ=-35°. In all cases, contours are plotted at 10%, 30%, 50%, 70%, and 90% of the maximum intensity.

of the weighted average, it seems to be a reasonable procedure to use when two high-probability solutions are in close proximity to each other.

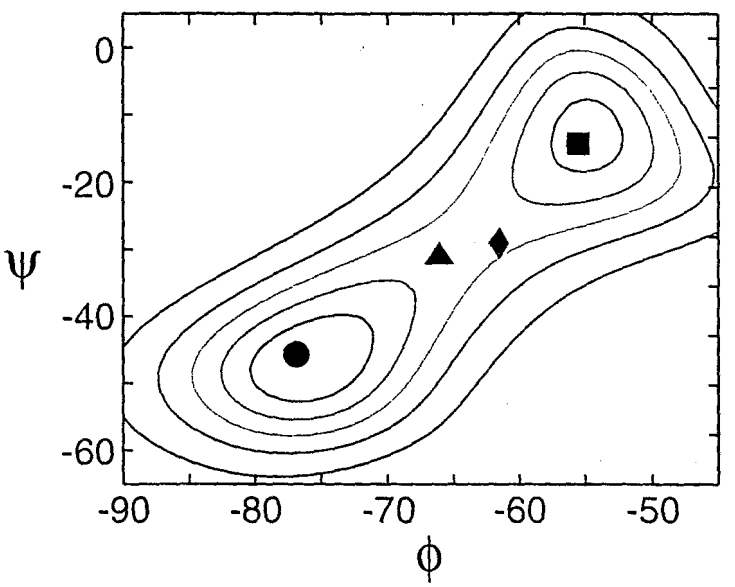

Figure 3.5. A close-up of the two nearby-maximum-solutions of Boc-VA*L-Aib-VAL-OMe II as determined by measurement of the CSA tensor. The two local maxima, marked by a circle and a square, lie within 30° of each other for both angles. By taking a weighted average, the predicted angles are φ=-67° and ψ=-31° (shown by a diamond), which are within 5° and 2° in φ and ψ, respectively, of the x-ray results (shown by the triangle).

Table (3.3) clearly demonstrates the capabilities of the CSA/Z method to determine the torsion angles of alanine and leucine residues in solid-state peptides. Overall, predictions of ϕ were accurate to within ±9° and predictions of ψ were accurate to within ±8°. It should be noted that for leucine, the CSA/Z method was able to predict not just ϕ and ψ, but also the side chain angle χ_2. Attempted predictions of ϕ and ψ using the leucine chemical shift tensor surfaces that corresponded to incorrect χ_2 values (according to the x-ray structures) gave lower probability solutions than predictions using

the correct χ_2 surface. This suggests that δ_{11}, δ_{22}, and δ_{33} might also be sufficient to predict χ_2 as well as dihedral angles. It is not surprising that the principal values would be so sensitive to χ_2, since for certain χ_2 conformations, the α-carbon and the γ-carbon in leucine are in close proximity (the γ-gauche effect).

Compound	X-ray		CSA/Z	
	ϕ	ψ	ϕ	ψ
G*AV	-69	-38	-69	-27
Boc-V*AL-Aib-VAL-OMe I[a]	-61	-45	-52	-31
Boc-VA*L-Aib-VAL-OMe I[b]	-71	-35	-74	-35
Boc-VA*L-Aib-VAL-OMe II[a,b]	-62	-29	-67	-31
L*LVY-OMe[a,b]	-129	124	-100	111
Boc-VAL-Aib-*VAL-OMe I[c]	-87	-11	-78	149
LL*VY-OMe	-124	120	-152	113

[a]The listed ϕ/ψ solution is the result of a weighted average of two nearby high-probability solution.

[b]In addition to predicting ϕ and ψ, the correct χ_2 rotomer was also predicted based on comparisons of the highest probability solutions for each rotomer ^{3}Z surface.

[c]In addition to predicting ϕ and ψ, the correct χ_1 rotomer was also predicted based on comparisons of the highest probability solutions for each rotomer ^{3}Z surface.

Table 3.3. A comparison of the angles predicted by the CSA/Z surface method and by x-ray crystallography.

Dihedral angle predictions for valine residues were not as successful as those for alanine and leucine. For Boc-VAL-Aib-*VAL-OMe I, an incorrect solution was predicted, and for LL*VY-OMe, the highest probability solution was obtained using the wrong χ_1 conformation (although the prediction using the correct χ_1 surface was close to

the actual conformation). It is unclear at this point why the valine predictions are not as accurate as those for alanine and leucine. One possibility is that an α-carbon CSA is not sufficient to predict ϕ, ψ, and χ_1, in which case using ^{1}Z-surfaces for the three $^{13}C\beta$ chemical shift tensor elements to determine a ^{1}Z-surface should vastly improve dihedral angle predictions in valine. Currently, $^{13}C\beta$ chemical shift surfaces exist for a variety of amino acids.

3.4 Conclusion

In this chapter, a method was presented that determines the dihedral angles of alanine, valine, and leucine by correlating experimental chemical shift tensor values with *ab initio* chemical shift calculations. The chemical shift anisotropies (CSAs) of alanine, valine, and leucine α-carbon nuclei from six peptides were measured by cross-polarization magic angle spinning. In conjunction with *ab initio* scaled chemical shift calculations, the experimental CSA values were then used to determine the dihedral angles ϕ/ψ and where applicable, χ_1 and χ_2. Moreover, our predictions of the side chain angle of leucine (χ_2) also agreed with the x-ray crystallographic data. These results show that this method can be generalized to determine dihedral angles in β-branched and non-β-branched amino acids in peptides as well as proteins.

Chapter Four

Structural Studies of the Prion Protein via Solid-State NMR

4.1 Introduction

In this chapter, the strong dependence of chemical shifts on local structure is again utilized to investigate the structure of various fragments of the prion protein, a protein believed to cause fatal diseases. The corresponding prion diseases are neurodegenerative disorders that are caused by a novel mechanism. The diseases appear to be contracted by pathogens that contain proteins, but not nucleic acids, and may result from genetic, infectious, or sporadic modifications to the prion protein[140]. Examples of prion diseases include bovine spongiform encephalopathy (BSE) also known as mad cow's disease, Creutzfeldt-Jakob disease (CJD) in humans, and scrapie in sheep. All forms are characterized by astrocytic gliosis and spongiform (the soft tissue of the brain) degeneration; however, the extent of degeneration varies greatly[140]. Symptoms specific to certain diseases include, for CJD, progressive dementia, and for BSE or scrapie, general ataxia, which is characterized by an inability to coordinate voluntary muscular movements[141].

Although the first prion disease (scrapie) was characterized in the 1930s, it is only recently that this subset of diseases has become a prominent topic of debate both in politics and medicine. Since 1985 when the first case of BSE was reported in Britain, roughly a quarter million cattle have been slaughtered because of fears of a BSE epidemic. What caught the world's attention was that young British persons, who under normal circumstances stood little to no chance of having CJD, were contracting the disease at a far higher rate. It is believed that these new cases were caused by the ingestion of BSE infected beef. Evidence suggests that a change in the processing of cow

feed made of sheep offal may have resulted in these cows becoming infected with BSE. Although this processing change was undertaken around 1980, the severity of the epidemic remains difficult to assess due to a lag time of 5-10 years between infection and expression, caused by the species barrier. As of now, far less than 100 cases of CJD have been reported[108]. In fact, all human prion diseases combined occur in only 1 in roughly 100,000 people.

The manner in which prion diseases are contracted varies. For example, CJD may result in one of three ways: an inherited genetic mutation[142], a sporadic event usually late in life[143], or a transmission via injection of brain tissue[144]. On the other hand, Kuru, which was discovered in the 1960s among the Fore tribe living in Papua-New Guinea, is an infectious disease. It was spread among tribesmen through ritualistic cannibalism, and fortunately, the rampant occurrence of the disease ceased when this ritual was ended. Two other examples of human prion diseases are Gerstmann-Straussler-Scheinker (GSS) disease and Fatal Familial Insomnia (FFI), which are both inherited. Table (4.1) lists the various prion diseases that are currently known in animals and humans[108].

The novel aspect of prion diseases is their cause, which challenges two pillars of modern medicine and biochemistry. Unlike most diseases, which are due to alterations in the nucleic acid either by genetic mutation or viral infection, a large body of data suggests that the prion *protein* (PrP) itself causes the diseases. Although this remains unproven, the only infectious component known to date is the PrP protein. Equally unprecedented is that the disease is correlated with a structural refolding of the prion protein from its normal state, PrP^{C}, to an infectious form, PrP^{Sc}. This surprising fact

contradicts one of the fundamental principles of structural biology that each primary sequence corresponds to only one general fold. Thus, knowing the structure of both PrP^{C} and PrP^{Sc} is vital to understanding and curing these novel, and fatal diseases.

Animal Diseases	*Host*
Scrapie	Sheep
Bovine Spongiform Encephalopathy	Cattle
Transmissible Mink Encephalopathy	Mink
Chronic Wasting Disease	Mule Deers and Elk
Feline Spongiform Encephalopathy	Cats
Exotic Ungulate Encephalopathy	Nyalas
Human Diseases	*Contraction*
Kuru	Infectious
Creutzfeldt-Jakob Disease	Sporadic, Inherited, Infectious
Gerstmann-Straussler-Scheinker Syndrome	Inherited
Fatal Familial Insomnia	Inherited

Table 4.1. Tabulated are the animal and human prion diseases currently known. (Table is adapted with permission from reference [108].)

However, little is currently known about the lethal form of the protein, PrP^{Sc}. Although it is known that PrP^{Sc} aggregates to form insoluble and non-crystalline fibrils or plaques, the specific structure of these plaques and their mechanism of formation are not

fully understood. One reason why the structure of PrP^{Sc} has remained a conundrum is that conventional techniques for structure determination, such as x-ray crystallography and liquid-state NMR, are not amenable to studying such amorphous and insoluble systems. However, solid-state NMR is well suited to studying such systems due to the recent development of solid-state NMR techniques that enable the determination of molecular structures, as described in Chapter 1.

This chapter will provide an overview of prion biology, and an analysis of solid-state NMR investigations of prion protein fragments. In particular, studies will be presented that focus on determining the structural differences between the normal and scrapie forms of two prion protein fragments, Syrian hamster (SHa) PrP 89-143 and mouse PrP 89-143. The two forms of SHaPrP89-143 studied were the wild type and 3AV mutant, and the two forms of MoPrP89-143 were the wild type and P101L mutant.

4.2 – Overview of Prion Biology

4.2.1 – The Protein Only Hypothesis

In the 1960s, Tikvah Alper's seminal work on the scrapie pathogen indicated that prion diseases are not caused by nucleic-acid-containing pathogens[145-147]. Specifically, Alper found the pathogen to be resistant to UV and ionizing radiation, which are methods that typically cause inactivation of nucleic-acid-containing pathogens, such as viruses. Later, similar results were observed for the CJD agent[148]. These data suggested that the scrapie and CJD pathogens were either devoid of nucleic acid or that their nucleic acid was well-protected by some sort of protein layer.

In 1982, Prusiner and co-workers discovered that the scrapie pathogen, when purified, contained a protein. This purified protein consisted of a protease resistant core, named PrP 27-30 (since it had a molecular weight of 27-30 kDa), which was comprised of the last 142 residues of the entire prion protein (the whole protein has 231 amino acids)[149]. Its small size strongly suggested that the infectious particle was not a virus since most viruses are much larger. Furthermore, they showed that PrP 27-30 was specific to prion disease and that it formed the major constituent of the infectious agent[150, 151]. Appropriately, Prusiner coined the name *prion* for *pro*teinaceous *in*fectious particle[149].

However, the notion that a protein could be an infectious particle was extremely controversial, and so Prusiner and co-workers performed numerous tests to show that the infectious particles did not contain nucleic acids. They found the infectious particle to be resistant to numerous nucleases, which are enzymes that degrade nucleic acid chains like RNA and DNA, and to be inactive to UV and ionizing radiation, which confirmed the work of Alper[152-154]. In contrast, they found that prions could be inactivated by procedures that modify or hydrolyze proteins[155-157].

In summary, our current understanding is that prions are proteinaceous infectious particles that lack nucleic acid. Purified pathogens were found to contain mostly protein. Inactivation of the infectious agent occurs when procedures are used that hydrolyze or modify proteins, whereas procedures that alter nucleic acids do not inactivate the infectious particle. Furthermore, the small size of PrP 27-30 does not support the virus hypothesis, since viruses tend to be much larger. Therefore, evidence suggests that prions are comprised of proteins and do not contain nucleic acids.

4.2.2 – The Differences between PrP^C and PrP^{Sc}

PrP^C and PrP^{Sc} differ in many ways, including location and structure. PrP^C is found at the cell surface where its C-terminus is bound. It is easily degraded or digested by proteases[158], and most importantly, it is not infectious. In contrast, PrP^{Sc} is infectious, is only found in the cytoplasm of the cell and has a protease resistant core PrP27-30.

There are over twenty known point mutations that can cause inherited prion diseases. All mutations, which have a biological impact, are close to or within areas of PrP that have secondary structure. This suggests that the point mutations may be destabilizing the structure of PrP^C[159-161]. In Table (4.2), a list of the most commonly found point mutations is given. Included is the P101L point mutation, which when part of a 55-residue peptide (P101L PrP89-143) has been shown to accelerate or possibly initiate prion diseases[162].

Point Mutations Known to Cause Prion Diseases		
P101L	T182A	D178N
P104L	F197S	V179I
A116V	E199K	V209I
M128V	R207H	Q216R

Table 4.2. Tabulated are the point mutations known to cause prion diseases. Those listed in the left column all occur in the key region 90-145.

Structurally, FTIR and CD studies have shown that PrP^C is composed of roughly 40% α-helix and only 3% β-sheet[163]. The liquid state NMR structure of recombinant PrP^C (PrP90-231) was determined recently[161, 164, 165]. The structure contains three α-helices; 144-157, 172-193, and 200-227 and two β-sheets; 129-134 and 159-165. A

ribbon diagram of PrP^C is shown in Figure (4.1B) and a graphical representation of key secondary structure regions is denoted in Figure (4.1A).

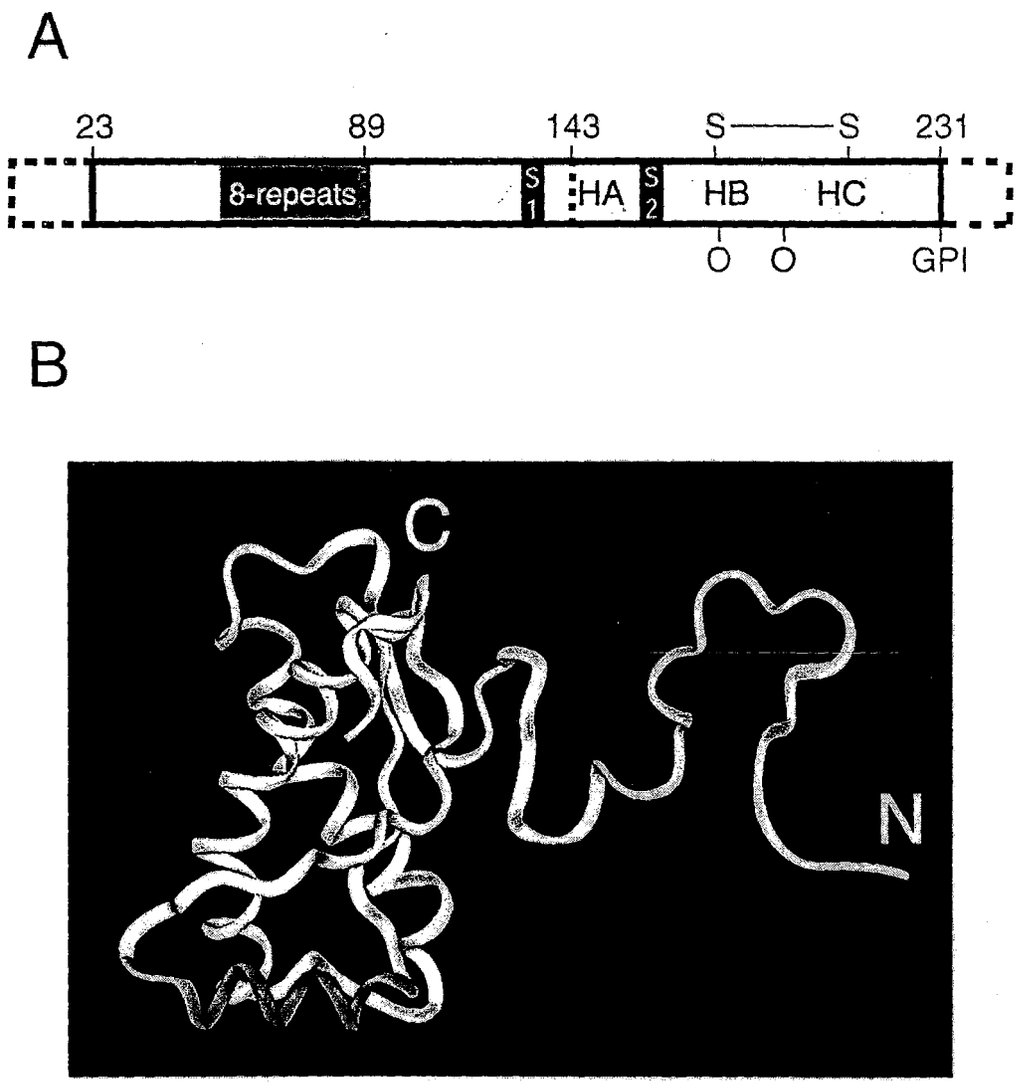

Figure 4.1. (A) A graphical representation of the prion protein with regions that have secondary structure denoted. The region from residue 89-143 is presumed to play a crucial role in the conversion process. (B) A ribbon diagram of the structure of PrP^C, which was determined by liquid-state NMR[161, 166, 167]. The structure contains three α-helices, two β-strands, and a disulfide bridge.

Although the structure of PrP^{Sc} is not known, data suggest that it is β-sheet rich. FTIR and CD studies have shown that PrP^{Sc} contains 30% α-helix and 43% β-sheet[163]. The macroscopic structure was characterized by staining PrP 27-30 gels after SDS/PAGE, a process which separates by weight and purifies the sample. Rod-shaped

particles were observed by electron micrograph, which were indistinguishable from purified amyloids[168]. Huang and co-workers have suggested a possible structure of PrP^{Sc} based on molecular modeling studies[169]. They predict four β-sheets; 108-113, 116-122, 128-135, and 138-144 in the purported critical region.

4.2.3 – Keys Regions of PrP for Functionality and Conversion

After post-translational modifications, the prion protein is composed of 231 amino acids (the first 22 and last 23 residues are cleaved in post-translational modifications). In mammals, the primary sequence of the PrP protein is highly conserved across species with sequence homologies of over 90%[170, 171]. Laying further credence to the protein-only hypothesis, Edman sequencing and mass spectrometry studies show that the two structural forms of the prion protein, PrP^{C} and PrP^{Sc}, have identical sequences and post-translational modifications[172].

Generally, when primary sequence homologies are highly conserved, then the protein serves a vital biological function. However, this is not the case for the prion protein. In fact, Bueler and co-workers have shown that when the gene coding for PrP is deleted from a mouse's DNA, the mouse functions and lives normally[173]. Even though it appears that the prion protein's function is not vital, recent evidence suggests that PrP, when present, acts as a copper binding agent[174].

The N-terminal region, which spans residues 23-90, appears to be the region where the copper binds. Liquid-state NMR data suggest that the region is generally a random coil in the absence of copper, however when copper binds, this region appears more structured[174]. The region has several Gly-Pro rich octarepeats and most differences

in the sequences between species occur in the N-terminal region. In addition, deletion of the N-terminal residues 23-90 does not prevent PrP^{Sc} formation. Therefore, although copper appears to bind to this region, other evidence suggests that this region does not play a crucial role in the structural rearrangement process[175].

Region 90-145 however appears to be of critical importance to infection and the conversion process. Molecular modeling of PrP^{Sc} has indicated that the refolding process to the scrapie form involves conversion of this region into β-sheets[169]. A patient with an amber mutation at residue 145, which is a point mutation replacing an encoding amino acid with a stop codon, died of prion disease[176]. Despite missing the last 87 residues of PrP, this subject still contracted a prion disease, suggesting that the first 145 residues are sufficient for PrP^{Sc} formation. In contrast, deletion of residues 90-145 has been shown to prevent PrP^{Sc} formation[175]. Furthermore, experimental and molecular modeling results indicate that the primary conformational change occurs in residues 90-112[177].

4.2.4 – The Conversion Mechanism from PrP^{C} to PrP^{Sc}

Currently, the most widely accepted cause of prion diseases is the structural rearrangement of PrP. The transformation may result from genetic, infectious or sporadic modifications to the protein that manifest themselves in its tertiary structure. This suggests that the prion disease is both a familial as well as a sporadic disease. As explained previously, the normal form of the prion protein adopts a generally α-helical and coil-like structure that is soluble. For reasons still unknown, PrP^{C} can undergo a structural rearrangement to the scrapie form, which is believed to be a β-sheet rich structure. This sheet structure is thought to serve as a template to convert other PrP^{C}

through a process aided by another protein. Although this protein has not been identified, protein X is believed to play a facilitating role by binding to an intermediary in the conversion process[178].

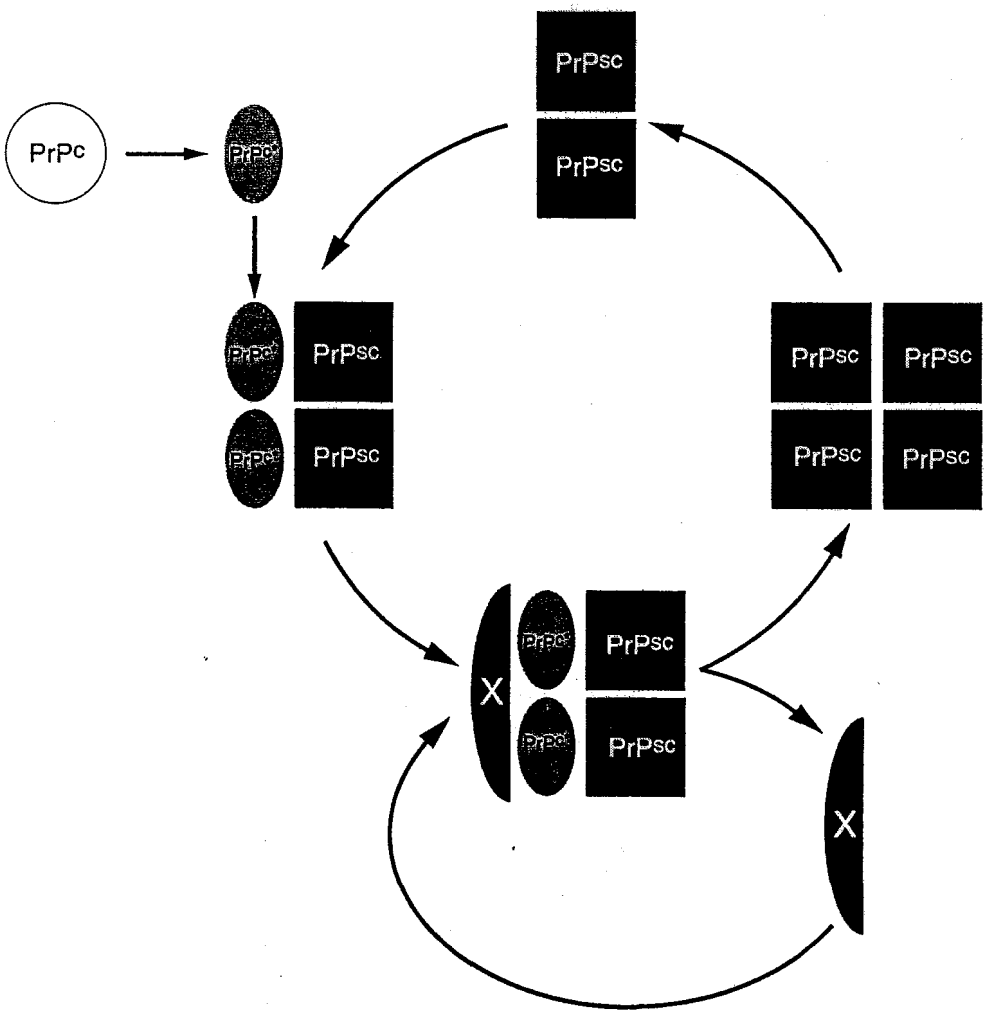

Figure 4.2. The proposed model for the conversion of PrP^{C} to PrP^{Sc} by Prusiner and co-workers[160]. PrP^{C} transforms into an intermediate state, PrP^{C*}. Then, the intermediate state can bind to PrP^{Sc} and the complex can form a dimer with another PrP^{C*}-PrP^{Sc}. An unspecified protein, denoted protein X, then binds to the dimer complex and PrP^{C*} is converted to PrP^{Sc}. (Figure is adapted with permission from reference [108]).

A few mechanisms have been proposed to explain the refolding process[178-180]. As shown in Figure (4.2), Prusiner and co-workers[160, 169] have suggested that PrP^{C} transforms into an activated state, PrP^{C*}, and then forms a complex with another PrP^{C*} and two other converted PrP^{Sc}. Acting as a molecular chaperone, protein X binds to the complex and

aids in the structural rearrangement of the activated state proteins[181, 182]. The process can then be repeated with an exponential increase in rate.

4.2.5 – Summary

Clearly, structural biology and in particular solid-state NMR can play a significant role in answering the many questions that remain regarding the prion protein and its associated diseases. By studying and ultimately determining the structure of PrP^{Sc}, the refolding mechanism may be understood and new drugs can then be designed that would inhibit the conversion process. Furthermore, the debate of whether the infectious particle is a protein can finally be resolved. Finally, the knowledge attained through the study of prions also has broad implications to other diseases, like Alzheimer's disease, which may also be caused by structural rearrangements of proteins.

4.3 - Structural Studies of Syrian Hamster and Mouse PrP 89-143 via Solid-State NMR

4.3.1 – Introduction

Overwhelming evidence indicates that prion diseases are caused by a proteinaceous infectious particle that undergoes a conversion from the normal form (PrP^{C}) to the disease-causing form (PrP^{Sc})[140, 149]. Even though the two forms of the prion protein, the predominantly α-helical PrP^{C} and the β-sheet rich PrP^{Sc}, have identical amino acid sequences and a common disulfide bridge, the two isoforms have profoundly different secondary and tertiary structures as observed by CD, FTIR, and NMR spectroscopies[161, 163, 166, 167, 183]. The current model for the conversion process identifies PrP^{C}

as a kinetically trapped intermediate along the protein-folding pathway that forms PrP^{Sc}. This model, proposed by Cohen and Prusiner[184], is based on their observations that the scrapie isoform is exceedingly stable, while the normal form is only marginally stable, as well as a variety of transgenetic and cellular transfection studies. The kinetic barrier, which is high enough to prevent the wild type from converting the vast majority of the time, can be reduced by the introduction of a scrapie template that acts as a catalyst, or a mutation of the endogenous gene (Prnp) that encodes the prion protein, or stochastic processes that result in infectious, inherited or sporadic prion diseases[162]. It remains unknown which regions of the protein play a significant role in the structural rearrangement and how do mutations known to cause prion diseases lower the kinetic barrier to increase the chances of PrP converting to the scrapie form.

Two studies suggest that the boundaries of the key region in the conversion process are residues 90 and 145. The N-terminus has been localized by studies on the protease resistant core of PrP^{Sc}, PrP 27-30, which found that residue 90 is the approximate start of the infectious domain[185]. The C-terminus has been localized by the fact that a Japanese male with an amber mutation at residue 145 died of prion disease, thereby indicating that the deleted residues were not crucial for the contraction of the disease[176]. Moreover, numerous structural studies of various fragments in this region have supported these findings[123, 160, 182, 186-190]. Certain fragments within residues 90-145 have been found to fold into α-helical as well as β-sheet conformations when characterized under different conditions[160]. Additionally, other peptide fragments, which were converted into a β-rich form, were shown to catalyze the conversion of peptide fragments with distinct structures into the β-rich form. Thus, this evidence suggests that

residues 90-145 show considerable conformational plasticity and play a key role in the conversion process.

The role of mutations that are known to cause prion diseases has also been studied by modeling GSS in two kinds of mice in the presence and absence of the endogenous Prnp gene by injecting a mouse transgene P101L into mice[142, 191]. Transgenic 227 (Tg227) mice expressed high levels of the transgene, developed spontaneous prion disease, and died quickly within ~100 days. In contrast, another mouse type, transgenic 196 (Tg196) mice, expressed substantially lower levels and showed signs of neurodegeneration much less frequently. These mice died in ~260 days, however, when they were inoculated with prions of older Tg196 mice that were clinically asymptomatic of prion disease. These studies suggest that Tg196 mice carry low levels of the transgene that are insufficient to cause clinical or neuropathological disease, but are high enough for transmission of the disease upon inoculation of the recipient mice. Thus, Tg196 mice provide an excellent platform to study the effects of injection of a mutant scrapie template on neurodegeneration[162].

Recently, Kaneko and co-workers[162] tested the effects of injecting Tg196 mice with a prion protein fragment, PrP 89-143 with a P101L point mutation. In humans, the substitution of a leucine for a proline at position 102 in human PrP is known to cause GSS. Kaneko and co-workers[162] modeled this inherited human prion disease in transgenic (Tg) mice by replacing a proline with a leucine at residue 101 in mouse (Mo)PrP. They observed that the MoPrP89-143(P101L) fragment refolded in at least two distinct conformations: an α-helix rich form, which may have the structure of PrP^{C}, and a β-sheet rich form, which may have the structure of PrP^{Sc}. When 20 mice were injected

intracerebrally with the β-rich form of MoPrP89-143(P101L), all of the mice developed signs of dysfunction of the central nervous system (CNS) after ~360 days. In contrast, in the control experiment where 8 mice received the α-rich form of MoPrP89-143(P101L), only a few mice showed signs of CNS deterioration after more than 600 days[162]. These results indicate that this prion disease strain overcomes the species barrier, from humans to Tg mice, and accelerates or possibly initiates prion disease. Work is currently underway to determine the effect of the species barrier on the incubation time. Preliminary results show that when a second set of Tg mice was inoculated intracerebrally with the β-rich form of MoPrP89-143(P101L) that was extracted from infected Tg mice, these mice also died of neurological diseases in ~360 days[192]. Thus, the chemically synthesized 55-residue PrP fragment presents an exciting opportunity to understand more about the infection mechanism and the key structural rearrangements that occur in the conversion process.

As of yet, however, a high-resolution structure of the 55-residue fragment in the β-rich form has not been determined by NMR or x-ray crystallography. As was noted in section 4.1, this is because the scrapie form of the prion protein is particularly difficult to study by conventional structural determination techniques since it is insoluble and lacks long-range order[187]. Solid-state NMR, on the other hand, is capable of answering many structural questions in immobile states, such as membrane proteins and aggregated peptides, through the use of chemical shift information and the determination of internuclear distances.

In this section, solid-state NMR structural investigations of various prion protein fragments are presented. These fragments correspond to the wild type and 3AV mutant

(A112V, A114V, and A117V) of Syrian hamster PrP 89-143 (henceforth referred to as SHaPrP89-143,WT and SHaPrP89-143,3AV) and the wild type and P101L mutant of mouse PrP 89-143 (henceforth referred to as MoPrP89-143,WT and MoPrP89-143,P101L). For both mutants, the non-converted and converted forms were studied and compared to the wild type. Cross-polarization magic angle spinning (CPMAS) was used to determine the ^{13}C isotropic chemical shifts of the selectively labeled PrP 89-143 fragments. As was noted in Chapters 2-3, the ^{13}C chemical shifts are highly correlated with local secondary structure both in solids[50, 120-122, 130, 193] and liquids and have been reproduced in theoretical calculations[96, 126]. For example, the isotropic chemical shifts of an α-carbon in an α-helix versus a β-sheet can differ by as much as 8 ppm. Thus, ^{13}C chemical shifts can provide insight into the local secondary structure, and in this case, can be used to gain insight into the overall secondary structure of the prion protein fragments.

4.3.2 – Experimental

Each prion protein fragment was selectively ^{13}C labeled, such that the isotropic chemical shifts of the labeled carbon nuclei did not overlap and their positions were spaced along the entire length of the fragment. Figure (4.3) shows a graphical representation of the fragments studied with the amino acids underlined that were selectively labeled.

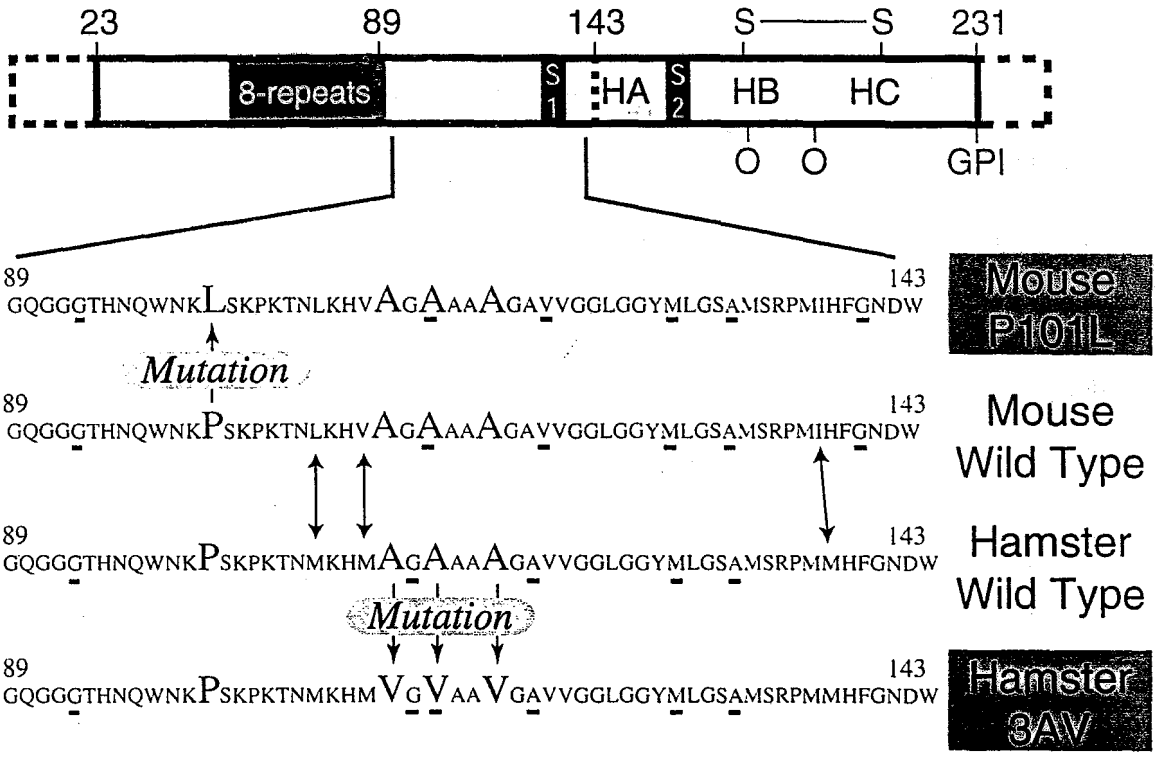

Figure 4.3. A graphical representation of the prion protein with an open reading frame of the mouse and Syrian hamster peptide fragments that were studied via solid-state NMR. The labeled amino acids are underlined and the mutations are also shown.

SHa PrP 89-143		Mo PrP 89-143	
Label	Shift Range (ppm)[a]	Label	Shift Range (ppm)[a]
G93 C_α	43 – 44	G93 C_α	43 – 44
G113 C_0	168 – 172	A114 C_α	46 – 54
V114 C_α	56 – 66	V120 C_α	56 – 66
A119 C_α	46 – 54	M128 C_0	170 – 176
M128 C_0	170 – 176	A132 C_β	14 – 22
A132 C_β	14 – 22	G141 C_0	168 – 172

[a] The shift ranges are based on the data from Refs. [118, 120-122].

Table 4.3. A list of the ^{13}C labels in the SHaPrP89-143 and MoPrP89-143 fragments studied and their corresponding chemical shift ranges.

In Table (4.3), a list of the labels used and their corresponding chemical shift ranges is given.

4.3.2.1 - Fmoc Protection of ^{13}C Labeled Amino Acids

All $^{13}C_{\alpha}$-labeled amino acids (Cambridge Isotope Laboratories, Andover, MA; Isotec, Miamisburg, OH) were Fmoc-protected in a manner similar to one previously described[136]. To 3.75 mmol of the amino acid dissolved in H_2O (60 mL), 0.945 g (11.25 mmol) of sodium bicarbonate ($NaHCO_3$) was added. After dissolving 1.265 g (3.75 mmol) of N-(9-fluorenylmethoxycarbonyloxy) succinimide (Fmoc-O-Suc) in acetone (60 mL), the mixtures were combined. The cloudy mixture became clear after stirring for 24 hours, at which point the acetone was removed by rotary evaporation. Citric acid (1 M) was used to precipitate the Fmoc- amino acids from the aqueous solution. Ethyl acetate (EtOAc) (150 mL) was added to redissolve the precipitate. The mixture was transferred to a separatory funnel and the layers were separated. The aqueous layer was washed with EtOAc (100 mL). The combined organic layers were then washed with H_2O (2×100 mL) and saturated NaCl (2×100 mL). The organic layers were dried over magnesium sulfate and the solvent was removed by rotary evaporation. The product was used for solid-phase peptide synthesis without further purification.

4.3.2.2 - Peptide Synthesis

As described elsewhere[162], the 55-residue peptides were synthesized using optimized Fmoc chemistry[137] on an Applied Biosystems (div. Perkin Elmer, Foster City, CA) 433 peptide synthesizer (with Rink amide MBHA resin). The side chain protecting

groups were Fmoc-L-Asp(OtBu), Fmoc-L-Arg(Pmc), Fmoc-L-Asn(Trt), Fmoc-L-His(Trt), Fmoc-L-Lys(2-ClZ), Fmoc-L-Gln(Trt), Fmoc-L-Tyr(tBu), Fmoc-L-Thr(tBu), Fmoc-L-Trp(Boc), and Fmoc-L-Ser(tBu). Fmoc amino acid derivatives were pre-activated by reaction with 2-(^{1}H-benzotriazol-1-yl)-1,1,3,3-tetramethyluronium hexafluorophosphate (HBTU) and diisopropylethylamine (DIEA). After the coupling of each amino acid a capping step was performed using N-(2-chlorobenzyloxycarbonyloxy) succinimide (Novabiochem, La Jolla, CA)[138]. Labeled residues were coupled manually using a 1.5 fold excess of amino acid and coupling efficiency was monitored using the quantitative ninhydrin test[139]. The peptide was deprotected and cleaved from the resin in 1:2:2:35 ethanedithiol-thiophenol-thioanisole-95% trifluoroacetic acid after removal of the N-terminal Fmoc group. The crude peptide was precipitated with diethyl ether and dissolved in 8 M guanidine hydrochloride prior to purification by semi-preparative C_4 reversed-phase HPLC at 50°C on a Rainin (Emeryville, CA) liquid chromatography system. The identity of the purified peptides was confirmed by electrospray mass spectrometry using a Perkin Elmer-Sciex API-300 instrument.

4.3.2.3 – Sample Preparation

The purified and non-converted peptides were dissolved in an acetate buffered saline solution (100 mM NaCl, 20 mM NaOAc, and pH=5.0) and left to dry for ~1 week. A white powder formed and solid-state NMR experiments were conducted on the samples.

The 3AV and P101L peptides were then converted to the β-rich form. This was achieved by dissolving the samples in 50:50 (v/v) mixture of acetonitrile and the same

acetate buffered saline solution. The suspended sample was then left undisturbed for ~3 weeks. After 2 weeks, the solution grew cloudy as insoluble aggregates began to form. After ~3 weeks, the aggregate suspension was spun down in an ultracentrifuge to separate the aggregates from the supernatant. The aggregates, which consisted of white, gelatinous pellets, were dried overnight.

4.3.2.4 – Solid-State NMR

All ^{13}C NMR spectra were obtained either at 7.07 Tesla (corresponding to a ^{13}C Larmor frequency of 75.74 MHz) on a home-built spectrometer based on a Tecmag (Houston, Texas) pulse programmer with a Chemagnetics (Fort Collins, CO) 4-mm double-resonance MAS probe, or at 11.72 Tesla (corresponding to a ^{13}C Larmor frequency of 125.75 MHz) on a triple-resonance Varian/Chemagnetics Infinity spectrometer with a 4-mm T3 triple-resonance MAS probe. For spectra obtained at 7.07 Tesla, the CP contact time was 2.0 ms, the ^{1}H decoupling field strength was 91 kHz, and the recycle delay was 1.0 second. For spectra obtained at 11.72 Tesla, the CP contact time was 2.0 ms, the ^{1}H decoupling field strength was 114 kHz, and the recycle delay was 1.0 second. Isotropic shift values were measured relative to the carbonyl carbon of glycine at 176.04 ppm.

4.3.3 – Results and Discussion

To determine the degree to which the fragments adopted a particular secondary structure, all spectra were analyzed in a similar fashion to Wishart and Sykes[119], where a secondary structure index, X_{ss}, is defined that is a measure of the degree to which a given ^{13}C chemical shift agrees with literature values for either α-helix or β-sheet:

$$X_{SS} = 2\left(\frac{\delta_{\exp} - \overline{\delta}_{lit}}{\Delta\delta_{lit}}\right), \tag{4.1}$$

where $\delta_{\exp}$ is the experimental ^{13}C chemical shift, $\overline{\delta}_{lit}$ is the average of the literature values for a given carbon in an α-helix or a β-sheet (e.g. from Table 4.4, the alanine α-carbon ^{13}C chemical shifts are 52.5 ppm in an α-helix and 48.7 ppm in a β-sheet, and thus $\overline{\delta}_{lit} = 50.6\,\text{ppm}$), and $\Delta\delta_{lit} \equiv \overline{\delta}_{\beta} - \overline{\delta}_{\alpha}$. As a result, X_{ss} has a value of +1 if the experimental chemical shift is in exact agreement with the literature values for a β–sheet conformation and X_{ss} has a value of –1 if the experimental chemical shift is in exact agreement with the literature values for an α–helix.

4.3.3.1 – SHa PrP 89-143 Studies

^{13}C CPMAS spectra of the SHaPrP89-143(WT) and the non-converted and converted forms of the SHaPrP89-143(3AV) were acquired, as shown in Figure (4.4A-C). The wild type peptide did not undergo a conversion when placed in the acetonitrile/saline solution. The resonance assignments were made based on the chemical shifts previously published[120-122]. In Table (4.4), the isotropic ^{13}C chemical

shifts for the wild type and the converted 3AV form are listed, along with the literature values and X_{ss}.

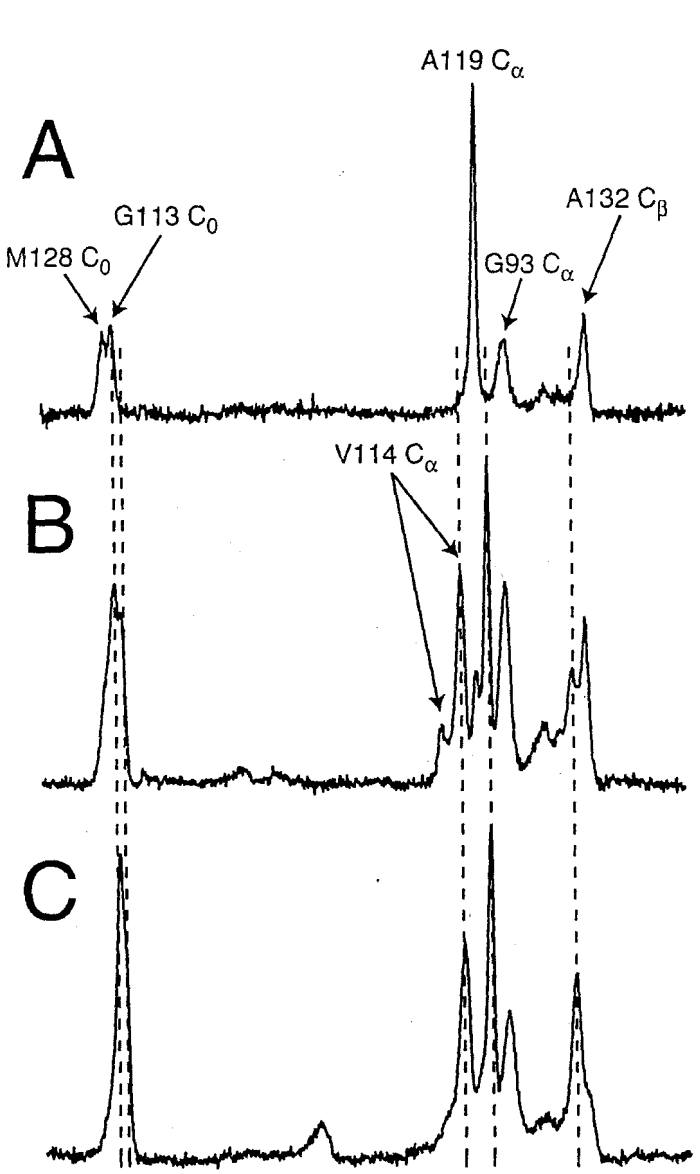

Figure 4.4. Solid-state NMR ^{13}C CPMAS spectra of SHa PrP 89-143 peptides. (A) ^{13}C NMR spectrum of the wild type SHaPrP89-143 peptide with resonance assignments based on the chemical shift ranges shown in Table (4.3). (B) ^{13}C NMR spectrum of the non-converted form of the 3AV mutant of SHaPrP89-143. The sample was dried from a acetate buffered saline solution. (C) ^{13}C NMR spectrum of the converted form of the 3AV mutant of SHaPrP89-143. The dashed lines denote the chemical shifts corresponding to a β-sheet conformation. The chemical shifts for the spectra in (A) and (C) are listed in Table (4.4).

Label	Expected Chemical Shifts[a]		Wild Type		3AV (converted)	
	α-Helix	β-Sheet	Expt. Chem. Shift	X_{ss}	Expt. Chem. Shift	X_{ss}
G93 C_α	Unknown	43.2	43.0	N/A	42.8	N/A
G113 C_0	171.8	168.5	172.6	-1.5	169.5	0.4
V114 C_α	65.5	58.3	N/A	N/A	57.6	1.2
A119 C_α	52.5	48.7	52.9	-1.2	49.2	0.7
M128 C_0	175.1	170.6	175.6	-1.2	170.8	0.9
A132 C_β	15.1	20.1	16.2	-0.6	20.6	1.2

[a]Values taken from reference [120].

Table 4.4. A comparison of measured chemical shifts in SHaPrP89-143 with typical α-helical and β-sheet chemical shifts in solid-state peptides. All chemical shifts are reported in ppm and are referenced to TMS via the $^{13}C_0$ resonance in glycine (176.04 ppm). The values for X_{ss} for the wild type are all negative and thus suggest that the wild type is generally α-helical. The values for X_{ss} for the converted 3AV mutant are all positive and thus suggest that the 3AV when converted assumes a β-sheet secondary structure.

Figure (4.4A) shows the wild type spectrum in which the ^{13}C chemical shifts are consistent with an α-helical conformation. This is confirmed in Table (4.4) by the fact that all values for X_{ss} are negative for the wild type. Since it is rare that the wild type form of the protein converts to the aggregate state, it is not surprising that the wild type form did not form aggregates when placed in the acetonitrile/saline solution. Moreover, the α-helical secondary structure of the wild type may be an indicator of its stability with regards to conversion to the β-rich aggregate state.

Figure (4.4B-C) shows spectra of the SHaPrP89-143(3AV) before conversion (B) and after conversion (C). In contrast to the wild type, the non-converted SHaPrP89-143(3AV) adopts two distinct conformations, where one isoform is α-helical and the other has a β-sheet conformation. Thus, it appears that the 3AV mutant has a certain

propensity to adopt a β-sheet conformation, which the wild type lacks. These observations agree with the fact that the 3AV mutation is known to convert to the β-rich form. In Figure (4.4C), the chemical shifts corresponding to an α-helical structure, which were present in Figure (4.4C), are no longer present, while those chemical shifts that are indicative of a β-sheet conformation remain. Table (4.4) clearly demonstrates that the aggregated 3AV mutant peptide has ^{13}C chemical shifts that are indicative of a β-sheet secondary structure.

4.3.3.2 – Mo PrP 89-143 Studies

The ^{13}C labels in the MoPrP89-143 samples differed slightly from those in the hamster peptides. The valine $^{13}C_{\alpha}$ label was changed to residue 120 so that this label would appear in both the wild type and P101L peptides. In addition, the $^{13}C_{0}$ label at G113 in SHaPrP89-143 was moved to G141 in MoPrP89-143.

Figure (4.5A) shows the ^{13}C NMR spectrum of the wild type MoPrP89-143(WT). Somewhat puzzling is the observation that the wild type spectra (Figure 4.4A and Figure 4.5A) differ since the sequences are nearly identical. Nevertheless, the MoPrP89-143(WT) adopts a partial α-helical and partial β-sheet structure, similar to the non-converted forms of the mutant peptides (Figures 4.4B and 4.5B). The non-converted P101L mutant spectrum (Figure 4.5B) is similar to the MoPrP89-143(WT) spectrum (Figure 4.5A) and shows that the peptide adopts two conformations, one that is α-helical

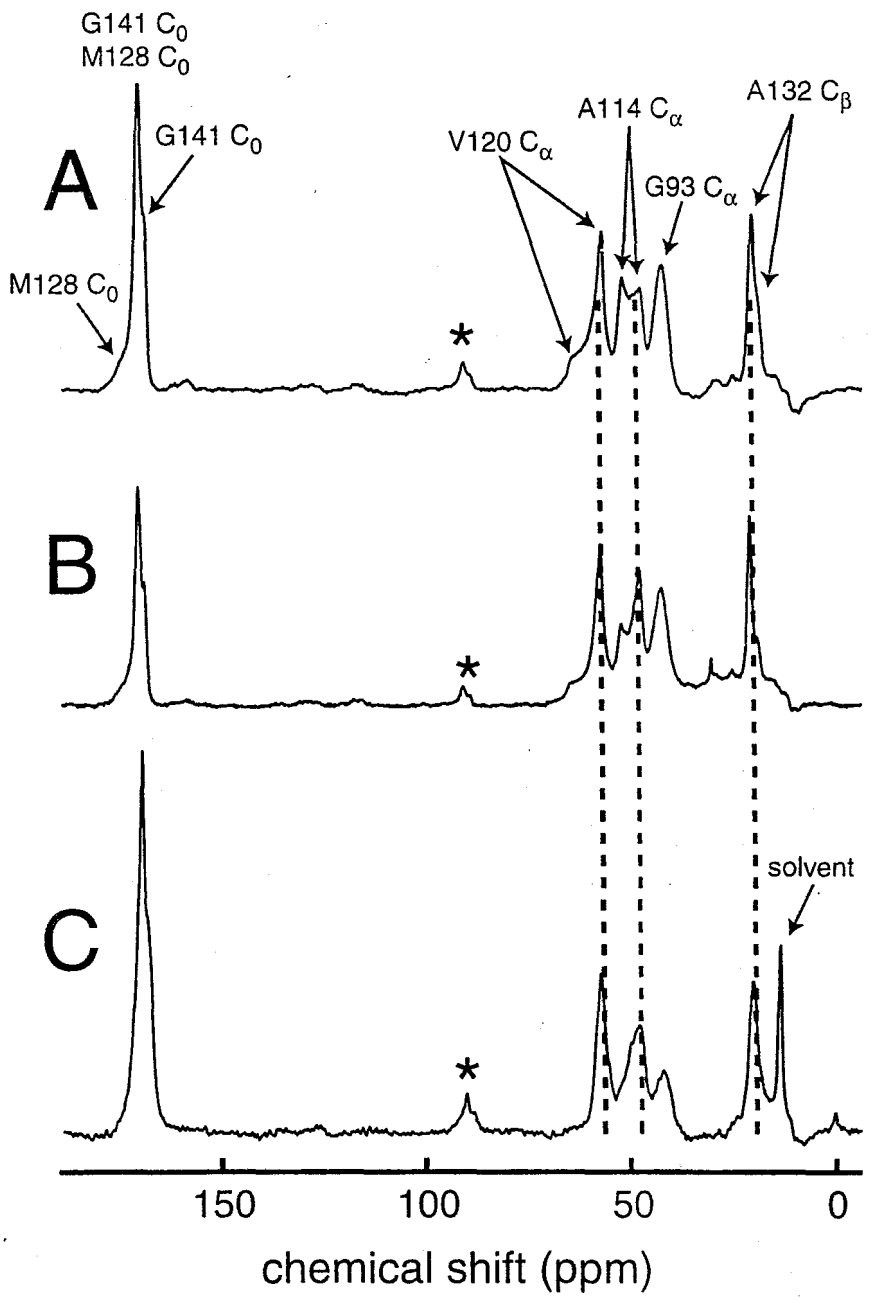

Figure 4.5. Solid-state NMR ^{13}C CPMAS spectra of Mo PrP 89-143 peptides. (A) ^{13}C NMR spectrum of the wild type MoPrP89-143 peptide with resonance assignments based on the chemical shift ranges shown in Table (4.3). (B) ^{13}C NMR spectrum of the non-converted form of the P101L mutant of MoPrP89-143. The sample was dried from an acetate buffered saline solution. (C) ^{13}C NMR spectrum of the converted form of the P101L mutant of MoPrP89-143. The dashed lines denote the chemical shifts corresponding to a β-sheet conformation. The chemical shifts for the spectra in (A) and (C) are listed in Table (4.5). The asterik (*) denotes a spinning sideband.

and the other that has a β-sheet conformation. However, the intensities of the α-helical resonances in the non-converted P101L spectrum are roughly half that of the wild type, suggesting that the P101L may have a propensity to adopt a β-sheet structure albeit not as much so as the 3AV mutant form of SHaPrP89-143. After conversion of MoPrP89-143(P101L) to form aggregates, only chemical shifts corresponding to a β-sheet conformation remain, as evidenced in Figure (4.5C) and Table (4.5).

Label	Expected Chemical Shifts[a]		Wild Type (I)[b]		Wild Type (II)[b]		P101L (converted)	
	α-Helix	β-Sheet	Expt. Chem. Shift	X_{ss}	Expt. Chem. Shift	X_{ss}	Expt. Chem. Shift	X_{ss}
G93 C_α	Unknown	43.2	42.8	N/A	42.8	N/A	42.3	N/A
A114 C_α	52.5	48.7	52.6	-1.1	48.3	1.2	48.4	1.2
V120 C_α	65.5	58.3	64.1	-0.6	57.8	1.1	58.1	1.1
M128 C_0	175.1	170.6	174.9	-0.9	170.6[c]	1.0	170.4	1.1
A132 C_β	15.1	20.1	15.1	-1.0	209	1.3	20.6	1.2
G141 C_0	171.8	168.5	170.6[c]	-0.3	169.3	0.5	168.9	0.8

[a] Chemical shift values are taken from reference [120].
[b] Two conformations were present in the wild type peptide. Wild type (I) represents the set of shifts from one conformation, whereas wild type (II) lists the chemical shifts from the other conformation.
[c] The M128 C_0 sheet chemical shift overlaps with the G141 C_0 helix chemical shift, and so the two are indistinguishable.

Table 4.5. A comparison of measured chemical shifts in MoPrP89-143 with typical α-helical and β-sheet chemical shifts in solid-state peptides. All chemical shifts are reported in ppm and are referenced to TMS via the $^{13}C_0$ resonance in glycine (176.04 ppm). Since the wild type had two conformations, two sets of values for X_{ss} are given. The values for X_{ss} for the converted P101L mutant are all positive and thus suggest that the P101L when converted assumes a β-sheet secondary structure.

It is also important to note that the linewidths in the converted P101L mutant spectrum (Figure 4.5C) are broader than in the non-converted spectrum (Figure 4.5B). Although it is not completely clear why this so, one possible explanation may be that there is conformational heterogeneity in the β-rich form. Some of the aggregates may be in fibrils while others have a β-sheet secondary structure, but are not part of a fibril. Indeed, an electron micrograph of the converted P101L mutant found some fibril formation, but also a significant portion of converted protein not in fibrillar form. The two shoulders found on the A114 C_α and G93 C_α peaks support this possibility, since both A114 C_α and both G93 C_α chemical shifts are within ~1 ppm of each other and so correspond to a β-sheet conformation. Thus, it seems that there is still some conformational heterogeneity in the converted P101L peptide even though all isoforms appear to have β-sheet secondary structure.

4.3.4 – Conclusion

The secondary structures of two prion protein fragments, Syrian hamster PrP 89-143 and mouse PrP 89-143, were studied via solid-state NMR. ^{13}C chemical shifts were measured by CPMAS to determine the secondary structure of the fragments. Both mutant forms studied, SHaPrP89-143(3AV) and MoPrP89-143(P101L), showed a propensity to form an α-helical isoform as well as a β-sheet isoform in their non-converted states. After conversion into an aggregated state, both mutants adopted an exclusively β-sheet conformation. In contrast, the wild type of the Syrian hamster peptide assumed an α-helical conformation while the mouse peptide adopted partial α-helical and partial β-sheet character. Both wild type forms of the peptides did not

convert to form aggregates. These findings support the idea that mutations aid in the conversion process by increasing the propensity of the protein to adopt a β-sheet conformation. It remains unclear however, how the converted peptides form fibrils or whether they form a regular structure in the aggregated form. If such a regular fibrillar structure does indeed exist, future solid-state NMR studies using heteronuclear and homonuclear dipolar recoupling to measure internuclear distances (see Chapter 1) and the CSA/Z method to measure dihedral angles (see Chapters 2 and 3) should provide enough structural constraints to determine the structure of MoPrP89-143(P101L).

Chapter Five

Ultra low-field Magnetic Resonance Imaging using Laser-Polarized ^{129}Xe and a High-T_c dc Superconducting Quantum Interference Device as a Detector

5.1 Introduction

Thus far, this thesis has focused on solid-state NMR techniques and applications, including a method to determine backbone torsion angles in peptides and structural studies of a prion protein fragment. In the final chapter, another area of magnetic resonance will be discussed, namely magnetic resonance imaging (MRI) at ultra-low magnetic fields using laser-polarized ^{129}Xe gas and a high transition temperature (high-T_c) direct current (dc) superconducting quantum interference device (SQUID) for detection. There are numerous advantages to performing MRI at low fields. Effects such as magnetic susceptibilities and chemical shift artifacts, are minimized since they scale with the magnetic field. Thus, at low fields, the unique possibility exists of studying many heterogeneous materials with paramagnetic sites or with large solid-gas magnetic susceptibilities as well as other systems where these effects play a major role. Furthermore, not only is the production of high-field magnets expensive and cumbersome, but it remains difficult to design these magnets with high homogeneity in field. In contrast, low-field MRI systems can be easily designed with high homogeneity, do not require large bulky magnets, and can be used as a compact and portable imaging device. Additionally, low-field gas MRI can be used to image void spaces in electrical conductors due to the increased probing-depth that low frequency RF pulses have into such metallic materials. However, despite these exciting possibilities, it would seem that low-field gas MRI is prohibitively difficult since both the sensitivity of conventional Faraday coil detectors and the polarization of nuclear spins are exceedingly low at these fields.

To overcome the low signal-to-noise ratio (SNR) of Faraday coil detectors at low fields, one possible alternative is using a dc SQUID since this device has higher SNR at these frequencies because it measures the magnetic flux directly and has extremely low noise. In fact, numerous NMR and nuclear quadrupole resonance (NQR) studies using low-T_c SQUIDs for detection have been performed to investigate, for example, the structure of materials and the rates of proton tunneling in methyl groups[194-201]. Additionally, the use of a low-T_c dc SQUID as a detector in low-field MRI has also been demonstrated[202, 203]. However, low-T_c dc SQUIDs have been limited by earlier double dewar designs, which required the sample to be at liquid-helium temperatures. These dewar designs severely restricted the number of interesting systems one could study since most systems including biological molecules are of interest at much higher temperatures than 4 °K. Currently, a new dewar design is being built that would allow the study of room temperature samples with a low-T_c SQUID[204]. Fortunately, these obstacles can also be overcome by using high-T_c SQUIDs, which have a much simpler dewar design. As a result, these SQUIDs are capable of detecting NMR signals from room temperature samples, while maintaining the high SNR that are characteristic of SQUIDs[205].

Recently, high-T_c SQUIDs have been used to detect laser-polarized ^{129}Xe signals at 1.26 mT and protons signals at fields ranging from that of the earth's (0.059 mT) to 2 mT[206, 207]. In addition, a two-dimensional proton image of a phantom filled with mineral oil has also been reported[208]. Such MRI experiments however, remain time consuming due to the exceedingly low equilibrium polarization ($P \sim 10^{-8}$-10^{-9}) of nuclear spins at low fields. In MRI experiment where gases are detected, this is further

exacerbated since the spin densities of gases are significantly smaller (~ 4 orders of magnitude).

One way to reduce experimental times is to greatly enhance the spin polarization by some non-equilibrium means. One such method uses lasers to polarize ^{129}Xe gas and has the advantage that the polarization is independent of magnetic field strength[209-211]. Laser-polarization of ^{129}Xe gas has yielded enormous polarizations of up to 70%[212, 213] and has been used in numerous applications, including the imaging of human lungs at low fields with a conventional Faraday detector[214], and of gas flows at high fields by way of a circular flow system that constantly replenishes the polarized gas[215].

Thus, in contrast to high-field MRI ($B_0 > 1$T), which has increasingly been used in the medical community and elsewhere[216, 217], MRI at low-fields is only now emerging with the recent developments of highly sensitive high-T_c SQUIDs capable of detecting room temperature samples and a circular flow laser-polarized ^{129}Xe gas apparatus as a means of increasing polarizations. In the ensuing sections, two-dimensional millimeter resolution images of the sample cell and of aerogels using laser-polarized ^{129}Xe gas and a high-T_c dc SQUID for detection will be presented. To acquire these images, a home-built three-axis gradient coil system was integrated into our apparatus and the MRI signal of the optically pumped ^{129}Xe gas was detected. The development of such a technique should enable the imaging of gas flows, characterization of microporous and metallic materials as well as many biomedical applications.

5.2 Background

Before discussing the low-field MRI results, a review of some the basic principles underlying SQUIDs (section 5.2) and optical pumping of noble gases (section 5.3) will be presented. More specifically, section 5.2 outlines how a dc SQUID can be used as a detector in magnetic resonance experiments. A short description of key concepts including flux quantization, flux trapping, and Josephson tunneling (a more thorough description is given elsewhere[218-221]), followed by a discussion on how a SQUID serves as a magnetic flux to voltage transformer.

5.2.1 - SQUID Fundamentals

Superconducting Quantum Interference Devices (SQUIDs) are the most sensitive detectors of magnetic flux available today. They have been used in a wide variety of applications in the field of MRI, low field NMR of solids and liquids, and NQR as well as applications outside the field of magnetic resonance[222, 223]. In comparison to conventional NMR detectors, namely Faraday coils, SQUIDs are particularly well suited for the detection of low-field NMR signals[224] (For simplicity, I will confine the discussion to an idealized comparison of the sensitivity between a Faraday coil and a SQUID.) Faraday detectors measure the voltage induced in a coil as a function of the change in magnetic flux $\left(d\Phi/dt\right)$ of the precessing nuclear spins[225]. Moreover, the polarization of the nuclear spins is proportional to the magnetic field, as described by the Boltzmann distribution. As a result, the sensitivity of Faraday detectors varies greatly with the external magnetic field strength and is proportional to B_0^2 [71]. In contrast,

SQUIDs measure the magnetic flux *directly*[223], and so their response scales as B_0, making them an ideal detector of NMR signals at low external magnetic fields $(B_0 < 0.1\,\mathrm{T})$, as shown illustratively, and not quantitatively, in Figure (5.1).

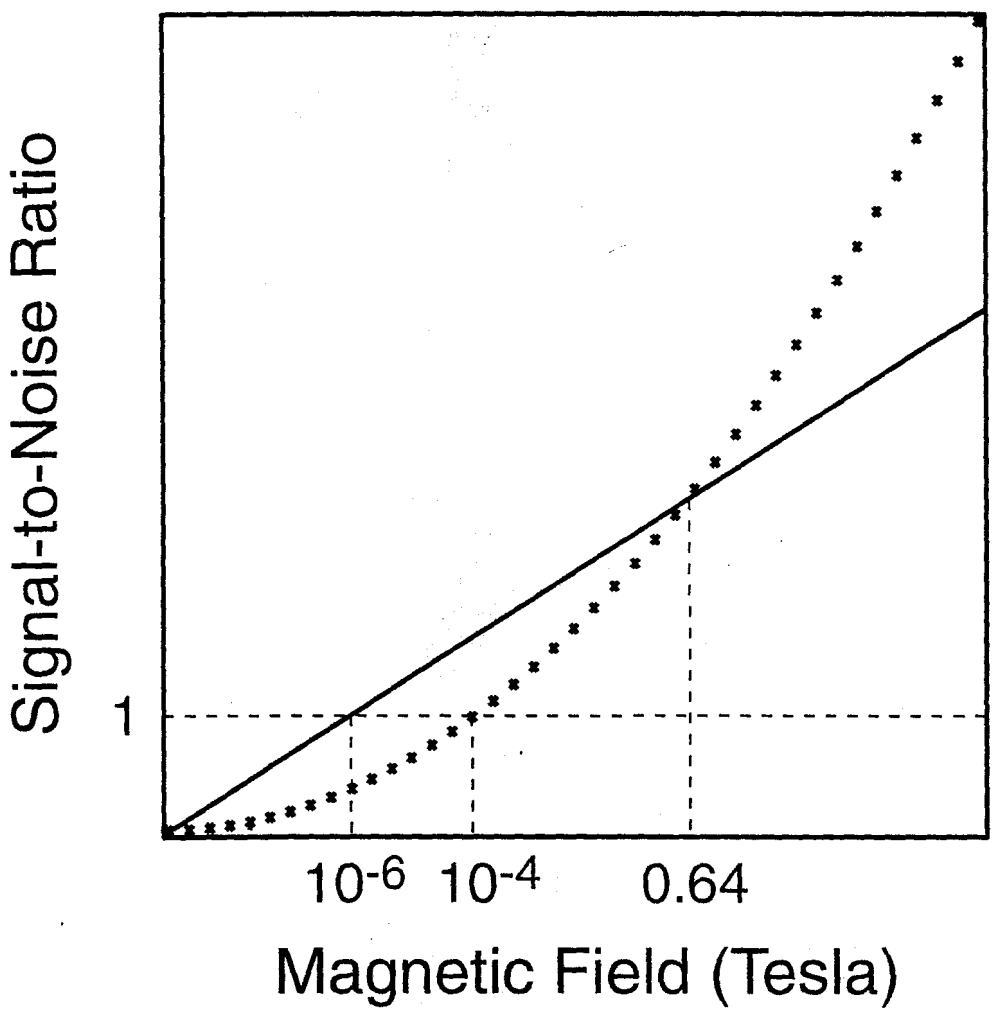

Figure 5.1. In this illustrative example, the sensitivity of a conventional Faraday coil detector (denoted by 'x') is compared to a SQUID detector (solid line) as a function of the external magnetic field strength. At low fields, the SQUID detector has a higher sensitivity due to its linear dependence on field strength and its low inherent noise of ~30-150 $\mathrm{fT/Hz^{1/2}}$ in our systems.

SQUIDs are based on two physical phenomena: the quantization and trapping of flux[105] and Josephson tunneling[226]. Flux quantization refers to the fact that the flux

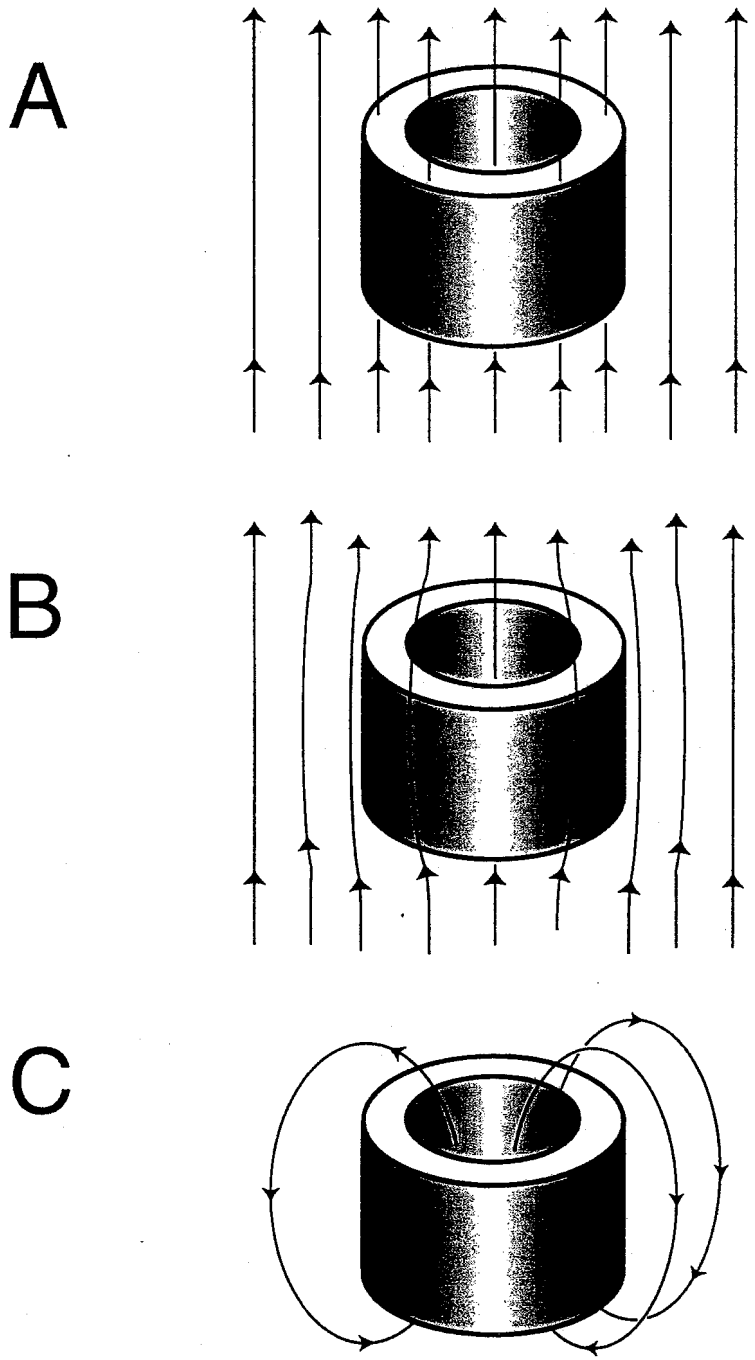

Figure 5.2. (A) A loop of wire is placed in a magnetic field at room temperature. The magnetic field lines run through the ring. (B) When the temperature is brought below the critical temperature, the ring becomes superconducting, thereby repelling the magnetic field. (C) After the external magnetic field is removed, current continues to flow in the superconductor since the resistance is zero. As a result, magnetic flux is trapped. (Figure is adapted from reference [221].)

through a superconducting loop of wire is quantized in units of $\Phi_0 = h/2e = 2.07x10^7 \mathrm{G}\cdot\mathrm{cm}^2$. Flux trapping occurs through a three-step process[221]. First, a loop of wire above its critical temperature (T_c) is placed in a magnetic field, as shown in Figure (5.2A). Second, the temperature is decreased to below the critical temperature of the wire so that it becomes superconducting. This causes the applied magnetic field to be forced outside of the material by the flow of current at the ring's surface. This effect is known as the Meisner Effect and is shown in Figure (5.2B)[227]. Third, when the external magnetic field is then removed, current flow around the surface of the loop persists since in a superconductor the resistance is zero. As a result of the current flow, there is a constant magnetic flux that is *trapped* in the loop[105].

Josephson tunneling occurs at a Josephson junction[105, 226, 228-231], which is a thin insulator that separates two superconductors *A* and *B*, as shown in Figure (5.3). In superconductor *A*, the Cooper pairs of electrons[232] are described by the wavefunction Ψ_A, and in superconductor B, the Cooper pairs are described by the wavefunction Ψ_B. Cooper pairs can tunnel through the junction as long as the wavefunctions (Ψ_A and Ψ_B) have a finite probability in both superconductors, i.e. for a Cooper pair in *A* to tunnel to *B*, $|\Psi_A|^2 \neq 0$ in *B*. This tunneling of Cooper pairs through a Josephson junction is termed Josephson tunneling.

However, there is one more important aspect to Josephson tunneling. The supercurrent, J_s, which is comprised of the flowing Cooper pairs, acquires a shift in its phase when tunneling through the junction. This phase shift is related to the current by:

$$J_S = J_0 \sin(\delta), \tag{5.1}$$

where J_0 is the maximum current, which is a characteristic of the junction, and the angle δ is the shift in phase the supercurrent acquires when it flows from A to B. As will be shown below, it is this phase shift that is related to the magnetic flux threading the loop of wire and leads to the SQUID's ability to transform magnetic flux into voltages.

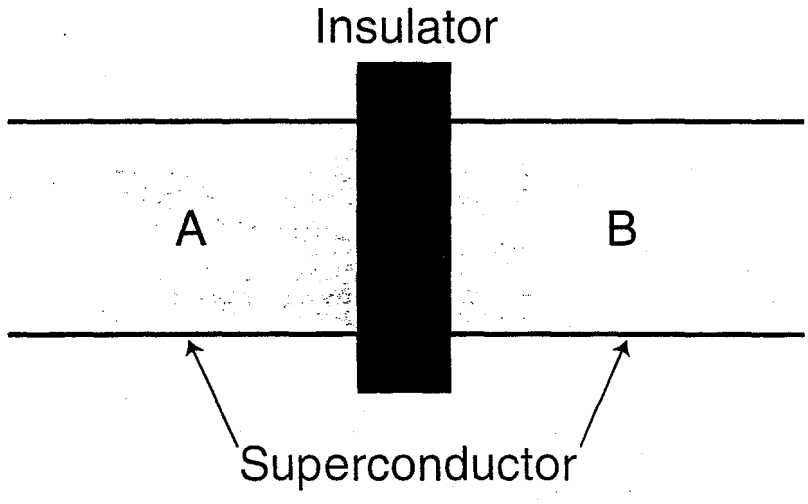

Figure 5.3. A schematic of a Josephson junction. Two superconductors, A and B, are separated by an insulator to form a Josephson junction.

5.2.2 - dc SQUID

A dc SQUID has two Josephson junctions in parallel, as shown in Figure (5.4). There are two possible paths that a Cooper pair of electrons may take to flow from point P to Q, namely paths A or B. If the flow of supercurrent from point P to Q is through the Josephson junction A, then the current will be:

(5.2) $$J_S^{(A)} = J_0^{(A)} \sin(\delta_A),$$

where $J_0^{(A)}$ is the maximum current and δ_A is the phase shift acquired by tunneling through junction A. Both quantities are characteristic of junction A. Similarily, supercurrent flowing through junction B acquires a phase shift:

$$J_S^{(B)} = J_0^{(B)} \sin(\delta_B), \tag{5.3}$$

where $J_0^{(B)}$ is the maximum current and δ_B is the phase shift acquired by tunneling through junction B. Both are characteristic of junction B.

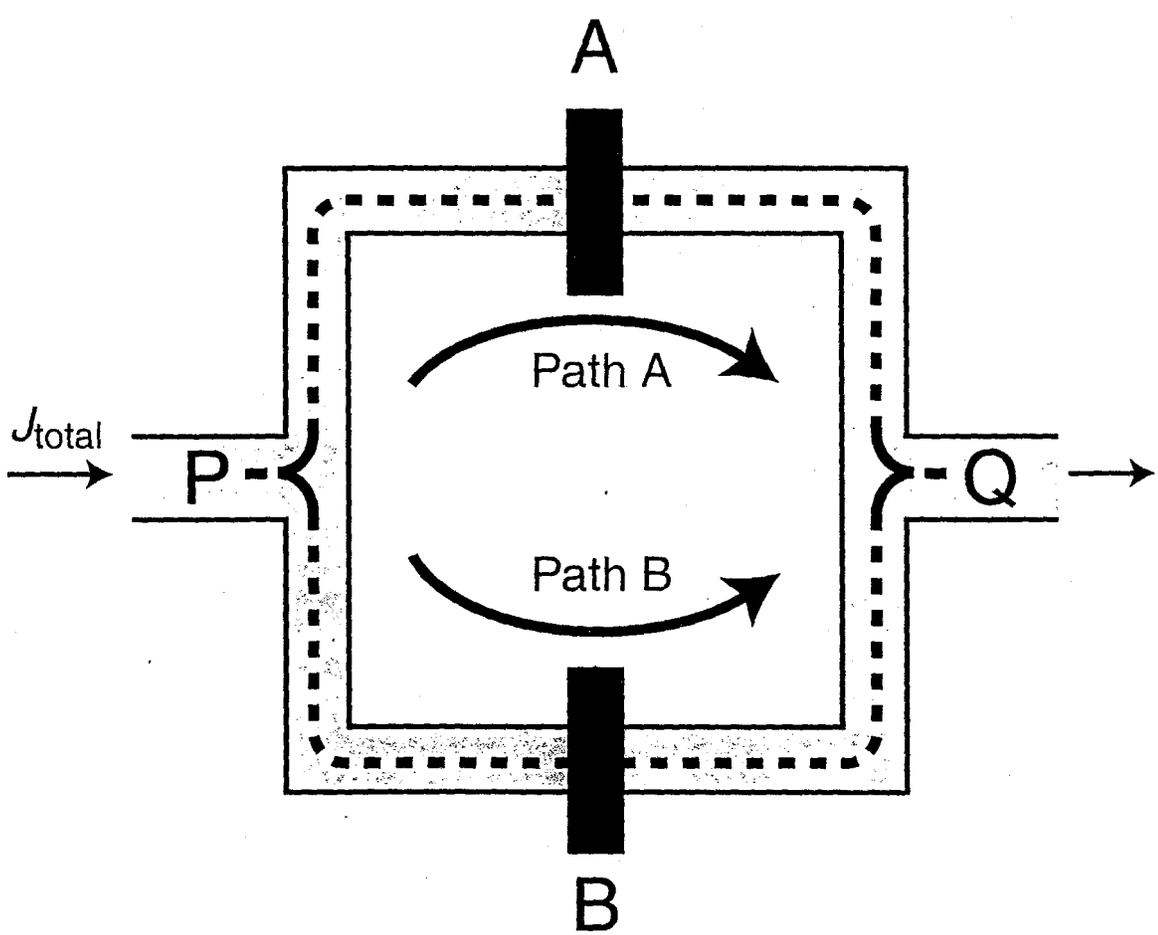

Figure 5.4. A schematic diagram of a dc SQUID, where the two Josephson junctions are in parallel.

If the characteristic current, J_0, is assumed to be the same for both junctions, then the total supercurrent flow from point P to point Q is:

(5.4) $$J_{total} = J_0 \sin(\delta_A) + J_0 \sin(\delta_B).$$

Equation (5.4) shows that the supercurrent flow from point P to Q oscillates. The maximum total supercurrent, $2J_0$, occurs when $\delta_A - \delta_B = (2n)\pi$ (where $n = 1,2,3,...$), since in such instances, the two currents ($J_S^{(A)}$ and $J_S^{(B)}$) constructively interfere with each other. On the other hand, if $\delta_A - \delta_B = (2n+1)\pi$, then the total supercurrent is zero since the two currents destructively interfere. Hence, the difference in phase shifts acquired by the Cooper pairs tunneling through the Josephson junctions gives rise to the interference of the currents from the two junctions.

The interference of the currents depends on the magnetic flux threading the superconducting loop of wire. The phase difference is equal to the sum of the phase shift across the Josephson junction and the line integral of the vector potential along the path[221]:

(5.5) $$\Delta Phase_{P\to Q} = \delta(t) + \frac{2q_e}{\hbar}\int_{path} \vec{A}\cdot ds,$$

where $\vec{A}$ is the magnetic field vector along the chosen path from P to Q and $\delta(t)$ is the phase shift through the Josephson junction. Thus, depending on the path, either through junction *A* or *B*, the two expressions for the phase difference are:

(5.6) $$\Delta Phase^{(A)}_{P\to Q} = \delta^{(A)}(t) + \frac{2q_e}{\hbar}\int_{path\ A} \vec{A}\cdot ds$$

and

(5.7) $$\Delta Phase^{(B)}_{P\to Q} = \delta^{(B)}(t) + \frac{2q_e}{\hbar}\int_{path\ B}\vec{A}\cdot ds.$$

Since the current must be single valued, the difference in the phase shifts between paths A and B must be:

(5.8) $$\Delta Phase^{(A)}_{P\to Q} - \Delta Phase^{(B)}_{P\to Q} = 2\pi n = 0 \text{ for } n = 0.$$

By subtracting Equation (5.7) from Equation (5.6) and by using Stokes' Theorem, the phase difference can be related to the magnetic flux:

(5.9) $$\delta^{(A)}(t) - \delta^{(B)}(t) = \frac{2q_e}{\hbar}\oint_{loop}\vec{A}\cdot ds = \frac{2q_e}{\hbar}\Phi_L,$$

where Φ_L is the flux through the superconducting loop of wire. Thus, Equation (5.9) expresses the phase difference between the two Josephson junctions as a function of the magnetic flux. If the two junctions are equivalent, then $\Delta Phase^{(A)}_{P\to Q} = \Delta Phase^{(B)}_{P\to Q} = \delta_0$, where δ_0 is a characteristic of the junctions. From Equations (5.6)-(5.9), the phase difference can be written as:

(5.10) $$\delta^{(A)}(t) = \delta_0 + \frac{q_e}{\hbar}\Phi_L$$

and

(5.11) $$\delta^{(B)}(t) = \delta_0 - \frac{q_e}{\hbar}\Phi_L.$$

With use of trigonometric identities and Equations (5.4), (5.10), and (5.11), we find that:

(5.12) $$J_{total} = J_0\left[\sin\left(\delta_0 - \frac{q_e}{\hbar}\Phi_L\right) + \sin\left(\delta_0 + \frac{q_e}{\hbar}\Phi_L\right)\right] = 2J_0\sin(\delta_0)\cos\left(\frac{q_e}{\hbar}\Phi_L\right).$$

Equation (5.12) shows that the total supercurrent is an oscillatory function of the magnetic flux threading the superconducting loop of wire.

This periodic behavior can be observed via the voltage when a bias current, J_{bias}, is applied across the Josephson junctions, such that $J_{bias} \geq 2J_0$ (the maximum supercurrent across a dc SQUID). The voltage across a dc SQUID is proportional to the difference between the bias current and the supercurrent, and is given by:

$$V_{P\to Q} = R\left(J_{bias} - J_{total}\right) = R\left[J_{bias} - 2J_0 \sin(\delta_0)\cos\left(\frac{q_e}{\hbar}\Phi_L\right)\right]. \tag{5.13}$$

where R is the resistance across one Josephson junction. Since δ_0 oscillates at gigahertz frequencies, only a time average of the voltage is observed by a narrow-band detector (our detector has a bandwidth of 0-1.1 MHz). Moreover, the time-averaged voltage is not simply zero[219]. Following the derivation found elsewhere[218], the time-averaged voltage can be written as:

$$V_{P\to Q} = R\sqrt{J_{bias}^2 - \left[2J_0 \sin(\delta_0)\cos\left(\frac{q_e}{\hbar}\Phi_L\right)\right]^2}\,. \tag{5.14}$$

Thus, the time-averaged voltage is also a function of the magnetic flux threading the superconducting loop of wire, as shown in Figure (5.5).

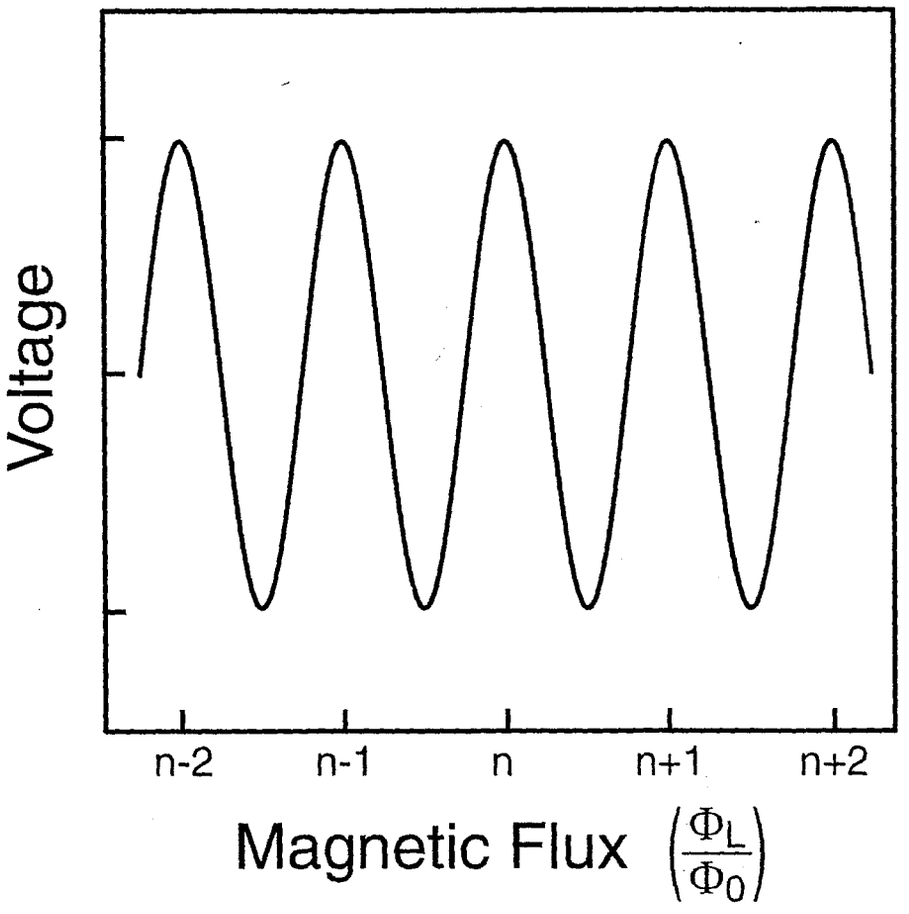

Figure 5.5. A curve of the voltage as a function of the magnetic flux threading the SQUID is shown.

5.2.3 - dc SQUID as a Detector

Although there are three ways in which a SQUID can be used as a magnetic flux to voltage transformer, the most common is to operate the SQUID as a null detector in a feedback circuit[223]. Essentially, the magnetic flux threading the multi-loop magnetometer causes a change in the voltage across the SQUID, as dictated by Equation (5.14). This voltage is amplified, integrated, and fed back to the SQUID as magnetic flux, thereby holding constant (or locking) the flux through the SQUID. The advantages of using this method are that the response of the SQUID is both robust over a large range of magnetic flux (Φ_L), and at the same time, sensitive and linear. Large and small

changes in magnetic flux no longer pose a problem for detection. The only limitation, in principle, is the ability of the electronics to respond quickly enough.

5.3 Optical Pumping of ^{129}Xe

5.3.1 – ^{129}Xe Optical Pumping Theory

One of the fundamental limitations of NMR is its inherent lack of sensitivity. This is due to the small energy difference between "spin up" and "spin down" states, resulting in nearly equal occupation of both energy levels. The polarization, which is the net difference in the number of spins occupying each state, can be written as:

$$P = \tanh\left(\frac{\Delta E}{kT}\right), \tag{5.15}$$

where k is Boltzman's constant. Given the high temperature approximation[73], $\Delta E << kT$ is valid, the polarization is given by:

$$P \approx \frac{\Delta E}{kT}, \tag{5.16}$$

Thus, a collection of nuclear spins at room temperature in a typical NMR magnetic field of a few Tesla has a polarization of only P~10^{-5}–10^{-6}. For example, an ensemble of one million spins under these conditions would have roughly 500,001 spins pointing "up" or parallel with the magnetic field (since this is the lower energy configuration) and 499,999 spins pointing "down" or anti-parallel to B_0.

One way to increase the polarization is to opt for the brute force method; which is to increase the strength of the external magnetic field. Currently, magnetic fields are being designed and built at around 23.5T, which corresponds to a ^{1}H Larmor frequency

of >1 GHz. Yet, it remains an arduous, expensive, and time-consuming enterprise to increase magnetic field strengths.

An alternative approach to achieve higher polarizations is by some non-equilibrium means. Optical pumping has proven to be successful in increasing the nuclear polarizations in noble gases by many orders of magnitude[233, 234]. The technique, which was first developed by Kastler in the 1950's[209-211], has been applied to many materials and molecules[235-237].

The most widely used method for optically pumping of ^{129}Xe is alkali metal spin exchange, where the alkali used is rubidium metal vapor[238]. The process takes advantage of the quantum mechanical selection rules of angular momentum. Shown in Figure (5.6), is a diagram of the process.

In the first step (Figure 5.6A), laser light, tuned to 794.7nm, irradiates the D_1 transition of rubidium. This causes the unpaired electron spins of the rubidium vapor to be excited from the ground state, the $5^{(2)}S_{1/2}$ energy level, to the excited state, the $5^{(2)}P_{1/2}$ energy level. Since the laser light is circularly polarized, only one of the transitions is irradiated. In the example depicted in Figure (5.6A), σ+ circularly polarized light selectively excites the $m_j = -\frac{1}{2}$ ground state to the $m_j = \frac{1}{2}$ excited state. Collisional mixing then occurs, which distributes the excited electrons among both excited sublevels. Relaxation from both excited states occurs to both ground states. However, because the excitation is selective (only from the $m_j = -\frac{1}{2}$ ground state sublevel to the $m_j = \frac{1}{2}$ excited state sublevel), the $m_j = -\frac{1}{2}$ sublevel becomes depleted over time, and subsequently, a non-equilibrium population accumulates in the $m_j = \frac{1}{2}$ ground state.

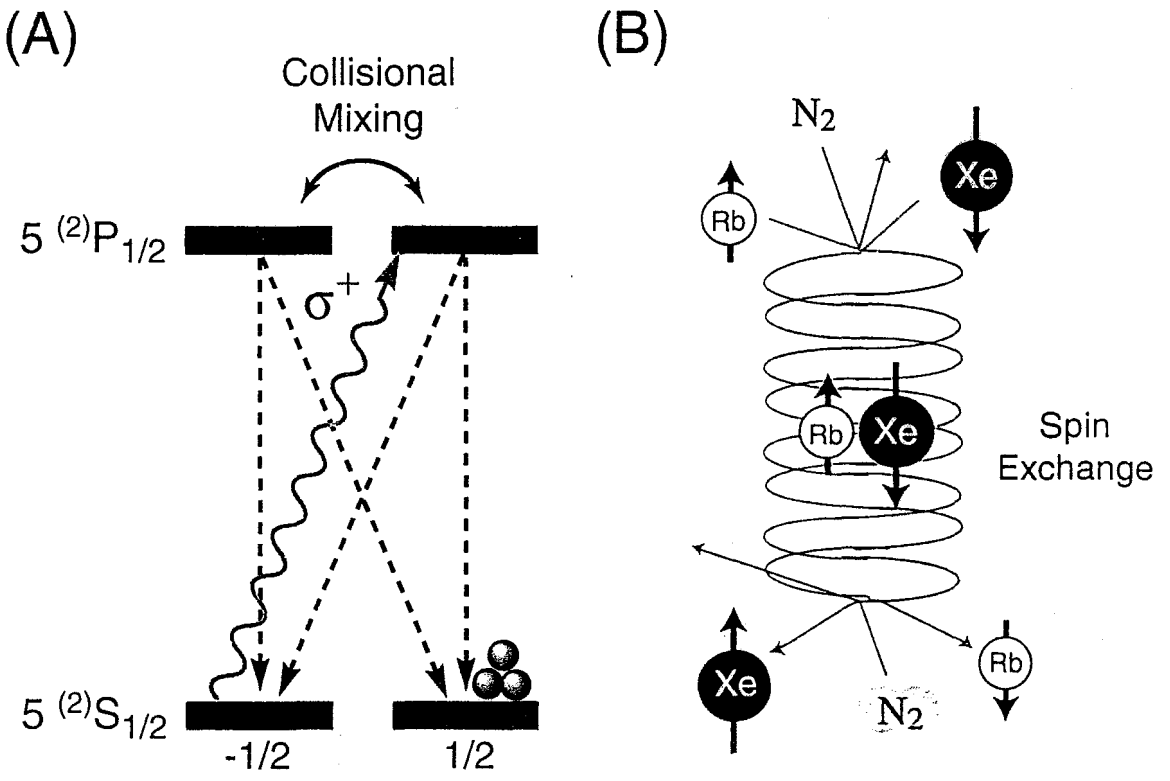

Figure 5.6. (A) A depiction of the optical pumping of rubidium. Even though relaxation occurs from both excited states to both ground states, a non-equilibrium population in the m_j=+1/2 state is formed due to the handedness of the excitation pulse. (B) A schematic of xenon-rubidium collisions and spin exchange processes, where the xenon becomes polarized. (Courtesy of Boyd M. Goodson.)

In the second step (Figure 5.6B), collisions between unpolarized ^{129}Xe atoms and electronically spin polarized rubidium atoms permit spin exchange between the rubidium electron spins and the xenon nuclear spins. The molecules collide and form short lived van-der-Waals complexes during which the exchange occurs. This exchange is mediated by the Fermi-contact hyperfine interaction[235]. The accumulation of xenon nuclear polarization can take anywhere from seconds to hours depending on the experimental conditions and the polarization yield can be as high as 70% percent[212, 213].

5.3.2 – Continuous Flow Apparatus

Two methods have been developed to optically pump xenon gas. The first method, called batch optical pumping, prepares a batch or cell of optically pumped xenon gas. The optical pumping is then ceased and the xenon gas is pump off and placed in an NMR magnet for experimentation. The limitation to this approach is that once the polarization has relaxed back to thermal equilibrium, the process must be started anew. However, the highest polarization has been observed with this method of over 70%[212, 213].

The second approach uses a continuous gas flow apparatus. Developed recently in our lab[215, 239, 240], this approach continuously circulates 5-10 atm of a xenon mixture through an optical pumping cell, into an NMR magnet for experimentation, and back again for laser polarization, as shown in Figure (5.7). In contrast to the batch method, experiments can be conducted for many hours since the supply of laser-polarized xenon is continuously replenished. Polarizations of over 1% have been observed, while 0.1-0.5% has been attained consistently in our set-up.

Similar to the batch method, the rubidium vapor is laser polarized in a pumping cell and collides with the xenon gas flowing through the chamber to transfer its polarization. The rubidium vapor is collected in a distillation column, while the xenon gas flows through the column and into a sample cell placed on top of the SQUID or inside the NMR magnet. During the time the xenon gas mixture is over the SQUID, pulses are applied and the nuclear magnetization of the xenon gas is detected. As the xenon gas returns back to thermal equilibrium it passes through a gas circulating pump and additional tubing on its way back to the pumping cell where the process begins again.

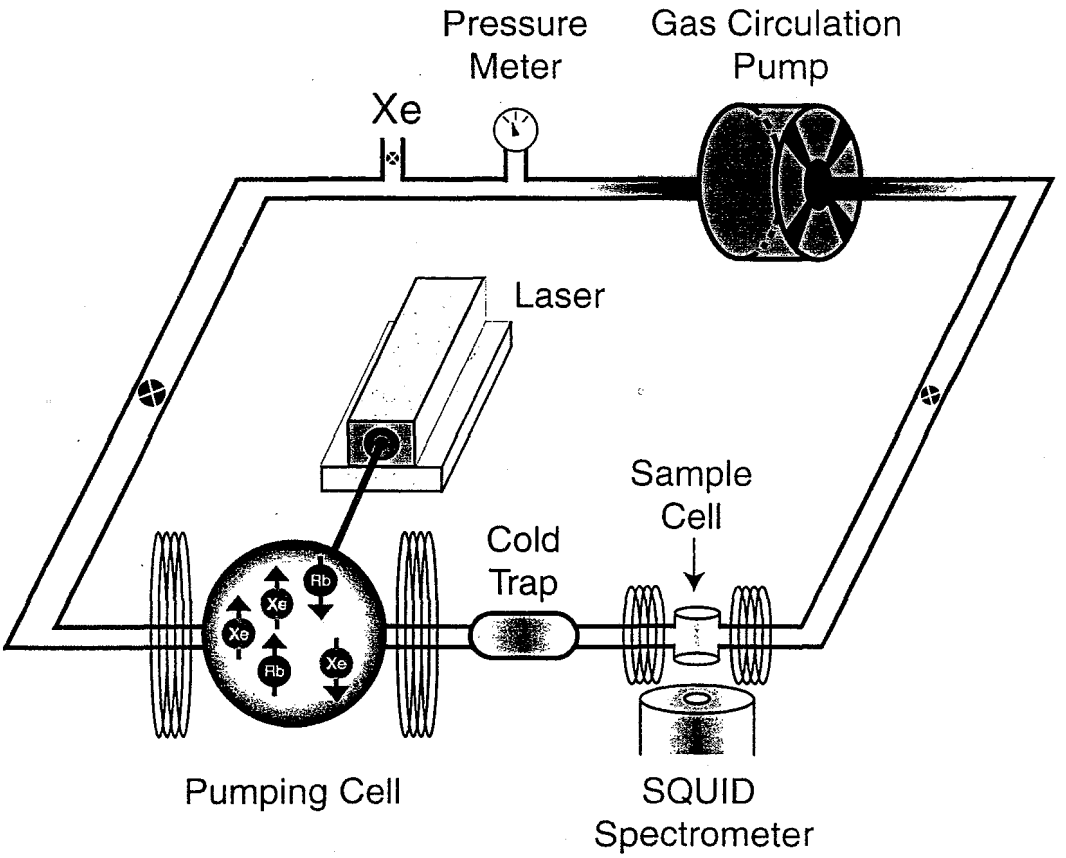

Figure 5.7. A diagram of the circular flow Xe polarization apparatus. The flow of gas is counter-clockwise. First, the xenon molecules are polarized in the pumping cell. As the gas mixture flows through the cold trap, rubidium condenses, while the xenon gas mixture flows through to the sample cell, which is placed on top of the SQUID. While the xenon gas is in the sample cell, pulses are applied and the xenon MRI signal is detected. The gas mixture is then recirculated through the gas circulation pump and back to the pumping cell to be repolarized.

Clearly there are certain considerations that must be monitored for an effective polarization set-up. First, the gas mixture used typically includes xenon, nitrogen, and helium. The ratios and the total pressure of the mixture must be optimized. In our set-up, the gas mixture used was 1 atm xenon, 1 atm nitrogen, and 5 atm helium. Second, the tubing and joints of the apparatus must not contain any relaxing agents, e.g. paramagnetic impurities. Otherwise, the xenon would relax to thermal equilibrium

before reaching the experimentation area. Third, the flow of the gas must be closely monitored to insure that the flow rate is synchronized with the pulse sequence and repetition rate of the experiment. Too high a flow rate would result in pulses being applied to xenon molecules that would already have left the experimental tube before detection. Too slow a flow rate would result in pulsing on the same set of xenon molecules more than once without them being recirculated and repolarized.

5.4 Ultra Low-Field MRI

5.4.1 - Introduction

In this section[241], two-dimensional low-field magnetic resonance images using optically pumped ^{129}Xe gas and a high-T_c dc SQUID detector are presented. Phantom images of the sample cell and of a triangular shaped piece of aerogel were taken by detecting the ^{129}Xe MRI signal. The non-equilibrium ^{129}Xe polarization was achieved with a circulating flow system, which continuously replenished polarized ^{129}Xe gas. The sample cell was placed on top of a 1 cm^2 SQUID, which acted as a surface detector. A home-built three-axis gradient coil was used to apply pulsed-field gradients of 0.04 G/cm in the z-direction and 0.12 G/cm in the x-direction. The images, which were taken with a static field strength of 22.6 G or less than 50 times the Earth's field, have 0.6 mm resolution in the z-direction and 1.4 mm resolution in the x-direction. These results demonstrate the technique's applicability to the characterization of many heterogenous materials.

5.4.2 - Experimental

To calibrate the xenon polarization obtained with our circular flow system, NMR spectra of ^{129}Xe and ^{1}H were acquired at magnetic fields of 22.6 G and 6.2 G, respectively. These fields correspond to a ^{129}Xe Larmor frequency of 26.5 kHz and a ^{1}H Larmor frequency of 26.3 kHz. The static magnetic field was applied by supplying a constant dc current across a home-built Helmholtz pair of coils. The coils have an outer diameter of 12.6 cm, are comprised of 159 turns of wire, and have a field homogeneity of >1%. Perpendicular to B_0 was the irradiation field, B_1, which was a Helmholtz coil pair tuned to the Larmor frequency of the nucleus to be studied. The B_1 coil had a diameter of 8.2 cm, 26 turns of wire, and a field homogeneity of >1%. To acquire the xenon and proton spectra, one-pulse experiments were used. For the xenon experiment, the $\pi/2$ pulse width was 250 μs and had an amplitude of 0.7 G. Before detection, a dead time of 400 μs was included to prevent coil ringing from saturating the SQUID's integrator.

Signals were detected using a high-T_c dc SQUID functioning as a flux-locked loop, where the sensor is a multiloop integrated magnetometer[242]. A schematic diagram of the SQUID spectrometer is shown in Figure (5.8). The magnetometer is not tuned, allowing broadband detection (DC-1.1 MHz) as well as multinuclear detection. The voltage across the SQUID is amplified, integrated, and simultaneously fed back to the SQUID by a single loop of copper wire that is inductively coupled to the SQUID as well as filtered, amplified (Rockland filter model 442), and stored in the spectrometer (Tecmag-ORION).

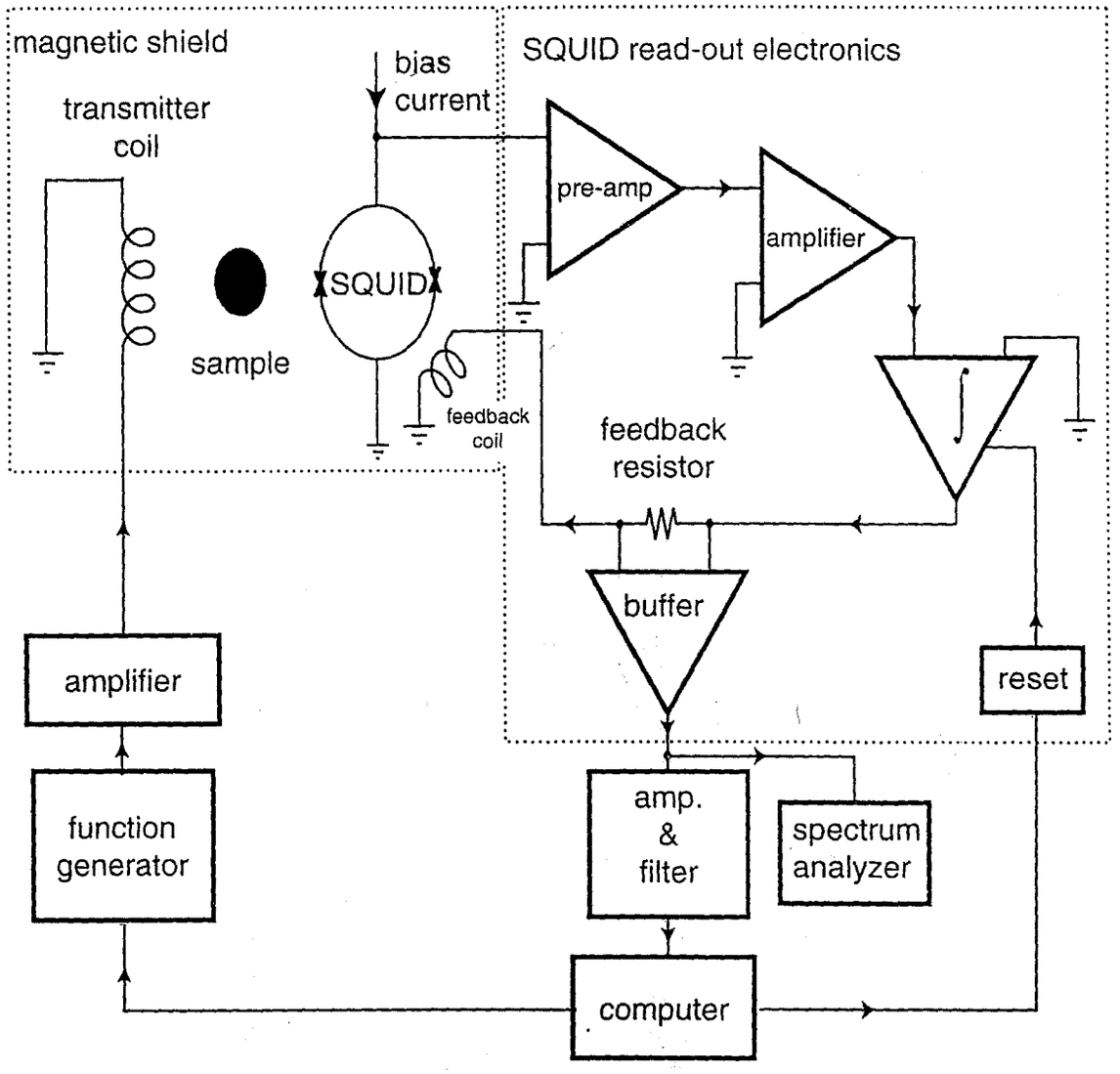

Figure 5.8. A schematic of the SQUID spectrometer. Inside the mu-metal shield are the SQUID, sample, transmitter coils that produce the af pulses, and the feedback coil. The SQUID read-out electronics then process the signal from the SQUID and send it to the computer for data acquisition and processing. The dewar system and the gradient and static field coils are not shown.

The spectrometer controls the gating of audio frequency pulses, gradient pulses, and data acquisition. For the non-gradient pulses, the spectrometer gates a function generator (Hewlett Packard 3314A), which produces *af*-pulses that are amplified (Krohn-Hite model 3322 filter) and sent to the coils. Shaped amplitude modulated gradient pulses were programmed into the pulse sequence for the imaging experiments. The

spectrometer gates a function wave form generator (Tecmag Gradient Controller), which is then amplified by Tecron 7700 amplifiers and fed through the gradient coils. To avoid saturation of the integrator, the spectrometer shorts the integrator during irradiation of *af* and gradient pulses.

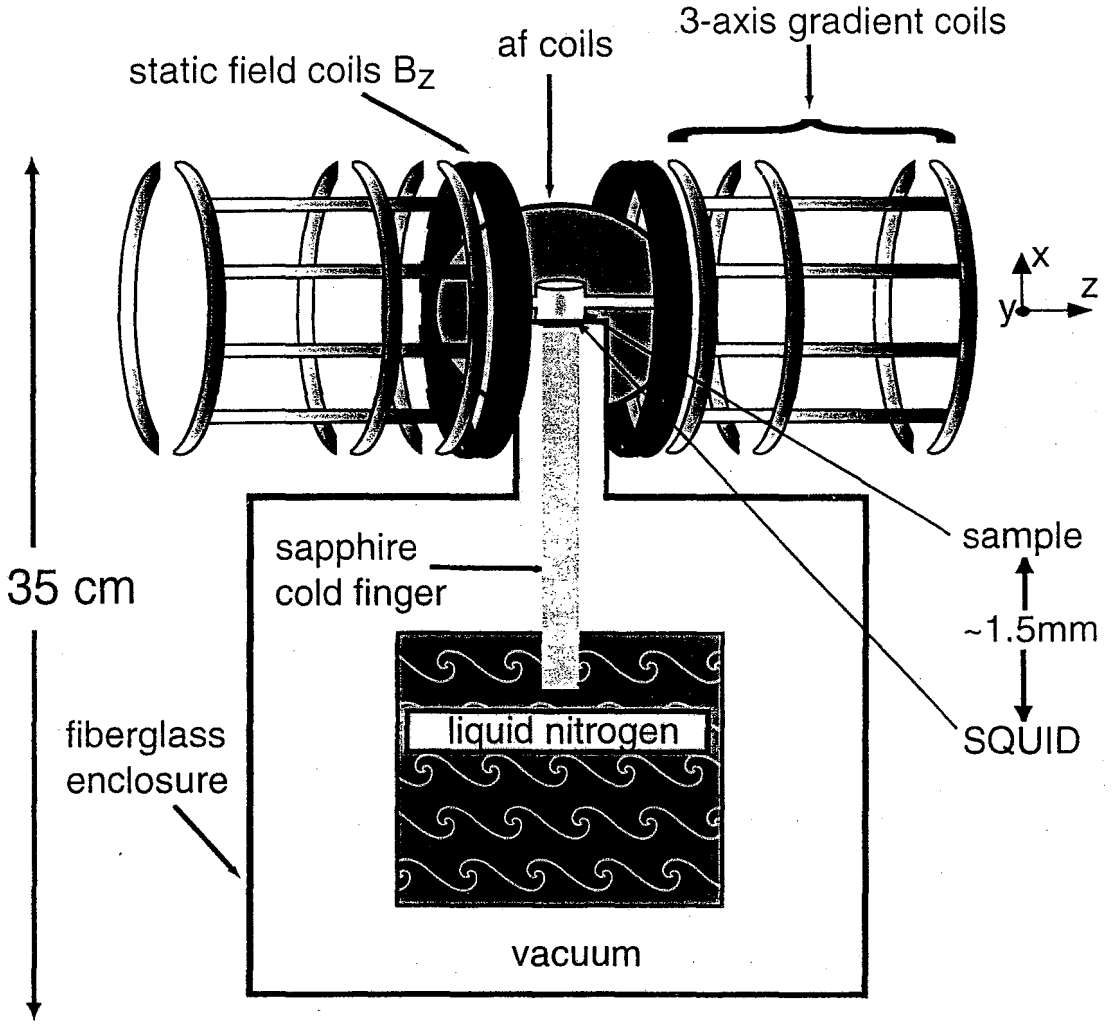

Figure 5.9. A cartoon of the SQUID dewar and coils. Sitting on top of the SQUID and separated by ~1.5 mm is the sample cell. The af coils pulse along the y-axis. The SQUID is thermally coupled via a sapphire cold finger to the liquid nitrogen bath. The liquid nitrogen is housed inside a fiberglass enclosure that is vacuum sealed. The entire dewar and coil apparatus is 35 cm tall.

The SQUID magnetometer is a Yttrium, Barium, Copper, Oxide or YBCO superconductor patterned onto a strontium titanate substrate. Its critical temperature is just above the boiling point of nitrogen (77 K). The magnetometer sits on a 0.1 m long sapphire cold finger that extends into a liquid nitrogen bath, as shown in Figure (5.9). The cold finger thermally couples the SQUID and the liquid nitrogen bath to insure that the SQUID is below its critical temperature. The magnetometer and cold finger are housed in a vacuum dewar[243], which typically must be filled twice daily to maintain liquid nitrogen temperatures. Samples are placed on top of a <1 mm thick sapphire window that is above the SQUID. The distance between the sample and SQUID is 1.5 mm. The entire SQUID dewar apparatus is enclosed by a three-layer mu-metal shield, which attenuates external fields by a factor of 1,430 at zero frequency[206].

The same detector and spectrometer were used in the imaging experiments. Additionally, a home-built three-axis gradient coil, wound onto a plexiglass frame, was incorporated into the system (Figure 5.9). The z-gradient was oriented along B_0, while the x-gradient was oriented perpendicular to the plane of the SQUID. Both gradients had a diameter of 12.6 cm.

The pulse sequence employed in the imaging experiments is shown in Figure (5.10). After a $\pi/2$ pulse, a fixed negative x-gradient and a variable z-gradient was applied for 24 ms in the sample cell image and 42 ms for the aerogel images. The z-gradient was incremented for each image slice in steps of 0.02 G/cm ranging from 32 G/cm to –32 G/cm for the phantom image of the sample cell. For the two aerogel images, the increment step was 0.04 G/cm, ranging from 64 G/cm to –64 G/cm. After a time Δ□of 20 μs, the MRI ^{129}Xe signal was acquired while a positive x-gradient was

applied. A two-dimensional Fourier transform of the data was then performed for processing.

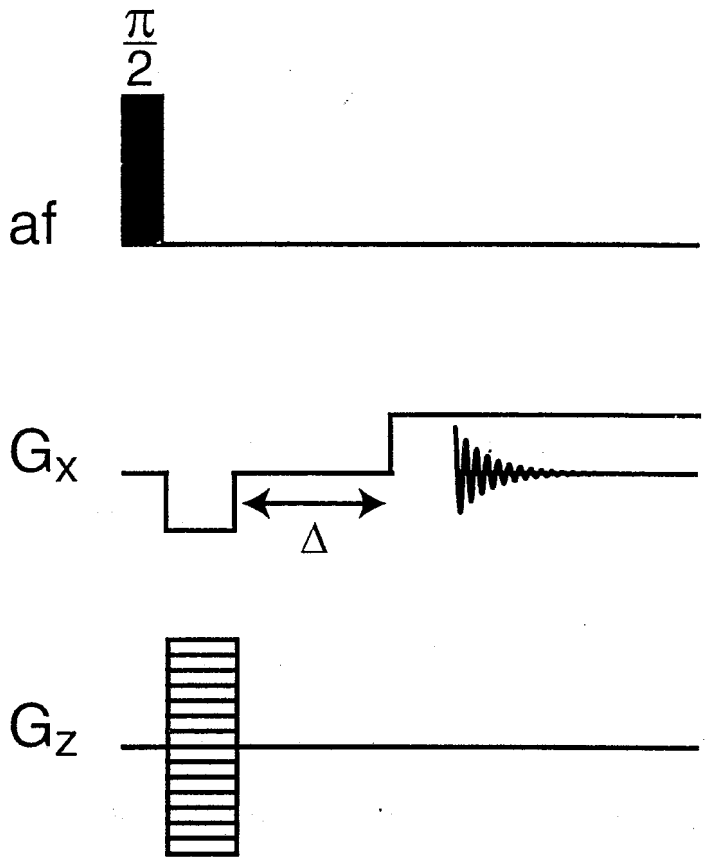

Figure 5.10. Pulse sequence used for the imaging experiments. After excitation of the xenon by a 90° pulse, the spins are spatially phase encoded by G_z. The z-dimension is stroboscopically detected, while the x-dimension is detected directly with an echo.

5.4.3 - Results and Discussion

5.4.3.1 - Spectroscopic Experiments

All ^{129}Xe experiments were conducted with a static magnetic field strength of 22.6 G, corresponding to a ^{129}Xe Larmor frequency of 26.5 kHz. As mentioned above, the ^{129}Xe gas was polarized with a continuous flow system. The ^{129}Xe gas mixture was composed of 1 atm of ^{129}Xe gas, 1 atm of nitrogen, and 5 atm of helium. Such a mixture

facilitates the polarization of the ^{129}Xe gas by pressure broadening the rubidium absorption line. The ratio was optimized to give the maximum signal-to-noise ratio (SNR). Two sample tubes were used-one with an inner diameter (I.D.) of 0.7 cm and the other with an I.D. of 1 cm. Figure (5.11A) shows a spectrum of laser polarized ^{129}Xe gas. The pulse sequence used was a simple "$\pi/2$ pulse and acquire". After only 40 scans or less than $1\frac{1}{2}$ minutes of experiment time, a SNR of 23:1 was observed, demonstrating the high polarizations obtainable by the continuous flow technique and its feasibility for use in SQUID MRI.

As a point of comparison, a spectrum of thermally polarized protons in mineral oil was taken at 6.2 G, corresponding to a ^{1}H Larmor frequency of 26.3 kHz. The proton spectrum of mineral oil was acquired using the same "$\pi/2$ pulse and detect" (Figure 5.11B). Signal averaging of 80,000 scans or over 8 hours gave a SNR of 5:1. At these fields and room temperature, the proton polarization is $P \sim 10^{-9}$. By comparing the SNRs of the two spectra in Figure (5.11), the polarization of the ^{129}Xe gas is calculated to be $\sim 10^{-2}$, which is an improvement of seven orders of magnitude.

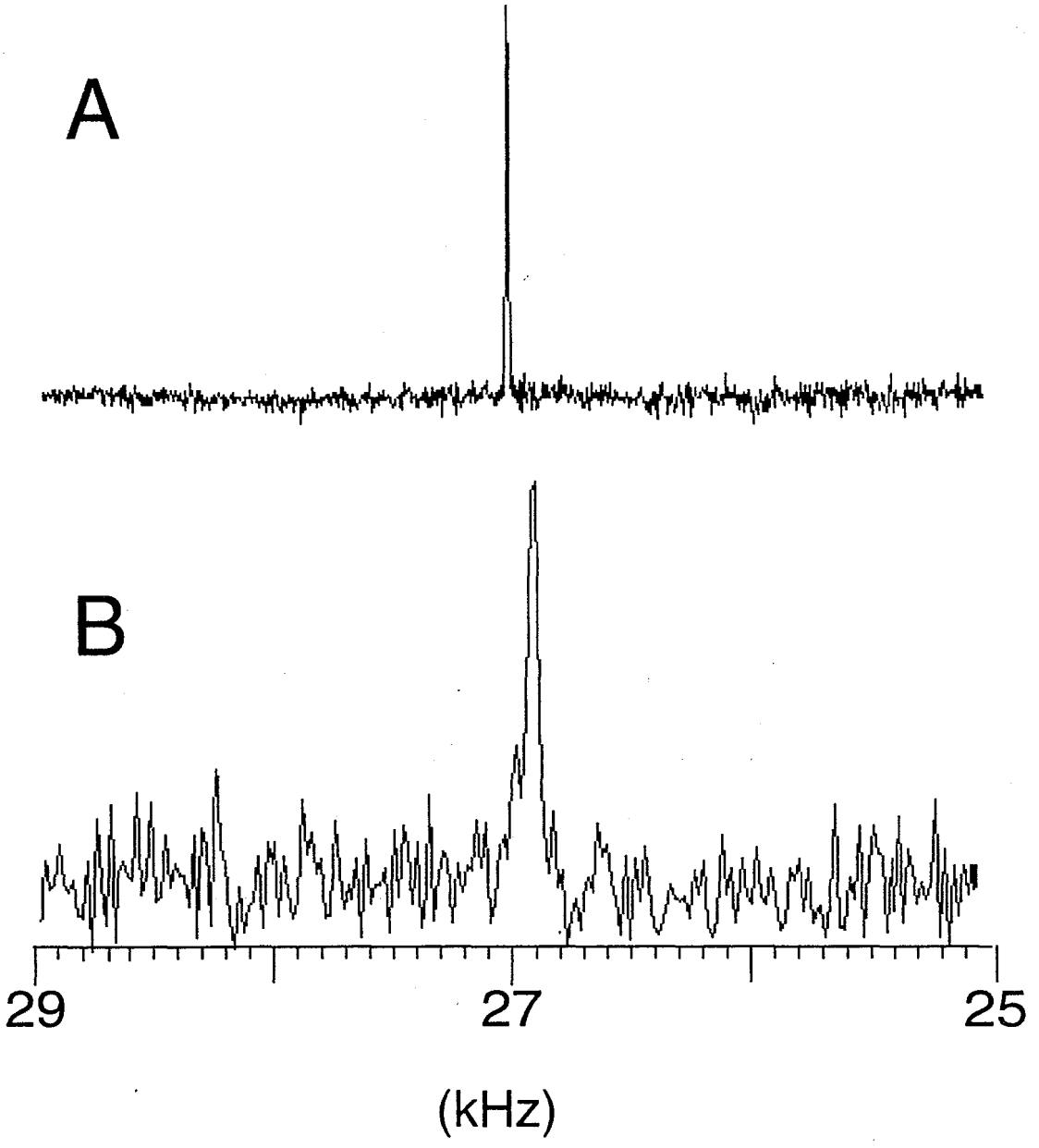

Figure 5.11. (A) Laser-polarized ^{129}Xe NMR spectrum at 22.6 G. After 40 scans, the signal-to-noise ratio (SNR) is 23:1. (B) ^{1}H NMR spectrum of mineral oil at 6.2 G. After 80,000 scans, the SNR is approximately 5:1.

5.4.3.2 - Imaging Experiments

In imaging experiments one must take into account that a SQUID acts as a surface coil detector[244]. As a result, the signal intensity of a given part of the sample depends on how far it is away from the SQUID. Thus, imaging pulse sequences must encode both the frequency as well as the position[207]. Previously by Schlenga and co-workers[208], this was accomplished by using an image-reconstruction technique, which involved a single gradient and sequential rotations of the sample. With the use of pulsed-field gradients, a *k*-space imaging technique was employed in these experiments. The time domain signal is given by[217]:

$$S(t) = \int\int\int \rho(\vec{r}) \exp\left[i\gamma \vec{G} \cdot \vec{r} t\right] d\vec{r}\,, \tag{5.17}$$

where $\rho(\vec{r})$ is the local spin density at position $\vec{r}$ in the sample, $\vec{G}$ is the gradient vector, and $d\vec{r}$ represents volume integration. Physically, the time-domain signal depends on the number of spins occupying a given volume element (dV). This number is represented by the local spin density ($\rho(\vec{r})$) and its frequency and position is encoded by the exponential term ($\exp\left[i\gamma \vec{G} \cdot \vec{r} t\right]$) in Equation (5.17). As first introduced by Mansfield[216, 245-248], Equation (5.17) can be rewritten in terms of a reciprocal space vector, $\boldsymbol{k}$, which is given by:

$$\vec{k} = (2\pi)^{-1} \gamma \vec{G} t\,, \tag{5.18}$$

such that the $\boldsymbol{k}$-vector is dependent on the gradient vector $\vec{G}$ and the time t. Then the signal as a function of the $\boldsymbol{k}$-vector becomes:

$$S(\vec{k}) = \int\int\int \rho(\vec{r}) \exp\left[i 2\pi \vec{k} \cdot \vec{r}\right] d\vec{r}\,. \tag{5.19}$$

Equation (5.19) has the form of a Fourier transformation, whose conjugate is given by:

(5.20) $$\rho(\vec{r}) = \int\int\int S(\vec{k}) \exp\left[i 2\pi \vec{k} \cdot \vec{r}\right] d\vec{r} .$$

Thus, the Fourier transform of the time domain signal gives a Cartesian raster that describes the local spin density as a function of position and frequency[217, 249]. Since our experiments were two-dimensional, we considered only the integration in the *x*-*z* plane in Equations (5.17-5.20), i.e. we project the three-dimensional spin density onto the *x*-*z* plane.

To determine the gradient strengths needed, two factors must be considered. First, it is impossible to have a higher resolution than the intrinsic xenon linewidth when no gradients are applied, which in the set-up used corresponded to 8 Hz. Second, the desired spatial resolution also dictates the strength of the gradient field. Thus, for a typical gradient of 0.1 G/cm and a sweep width of 80 kHz digitized by 8192 points, a spatial resolution of 0.8 mm is obtained, since:

(5.21) $$\text{Spatial Resolution} = \left(\frac{22.6G}{26.5kHz}\right)\left(\frac{cm}{0.1G}\right)\left(\frac{80kHz}{8192pt}\right)\left(\frac{10mm}{cm}\right) = 0.8\,mm/pt .$$

In our experiments, three phantom images were obtained, one of the sample cell, one of a non-descript piece of aerogel, and one of a triangular shaped piece of aerogel. In all cases, the xenon gas mixture (1 atm ^{129}Xe, 1 atm N_2, and 5 atm He) and the static field (22.6 G) were the same as for the NMR experiments. The phantom image (Figure 5.12) of the sample cell with an inner diameter of 0.7 cm was acquired at a gas flow rate of 3.9 mL/s, a gradient strength in the *x*-direction of 0.09 G/cm and 0.04 G/cm in the *z*-direction. These gradients correspond to a spatial resolution of 0.9 mm in the x-direction and 2 mm in the z-direction. The image shows that xenon fully occupies the sample cell as it flows through and it appears to exhibit laminar flow since no spiral pockets were

observed. The image of the non-descript piece of aerogel (Figure 5.13), placed inside of a sample cell with an inner diameter of 1 cm, was taken with a flow rate of 2 mL/s, a gradient strength in the *x*-direction of 0.12 G/cm and 0.04 G/cm in the *z*-direction, corresponding to a spatial resolution of 1.4 mm in the x-direction and 0.6 mm in the z-direction. The phantom of the triangular shaped piece of aerogel was taken under the same experimental conditions as Figure (5.13) and is shown in Figure (5.14). Two of the three sides of the triangle can be discerned, although none of the edges are sharp. The cause is most likely a lack of resolution due to insufficiently strong gradients. Difficulties with the locking of the SQUID were encountered when z-gradients of over 1.0 G/cm were applied. Regardless, Figures (5.12-5.14) do demonstrate the capability of ultra low-field MRI with millimeter resolution. Furthermore, Figures (5.13-5.14) demonstrate how laser-polarized ^{129}Xe can be used to unambiguously differentiate between ^{129}Xe inside and outside aerogels. This should prove useful in the characterization of porous media.

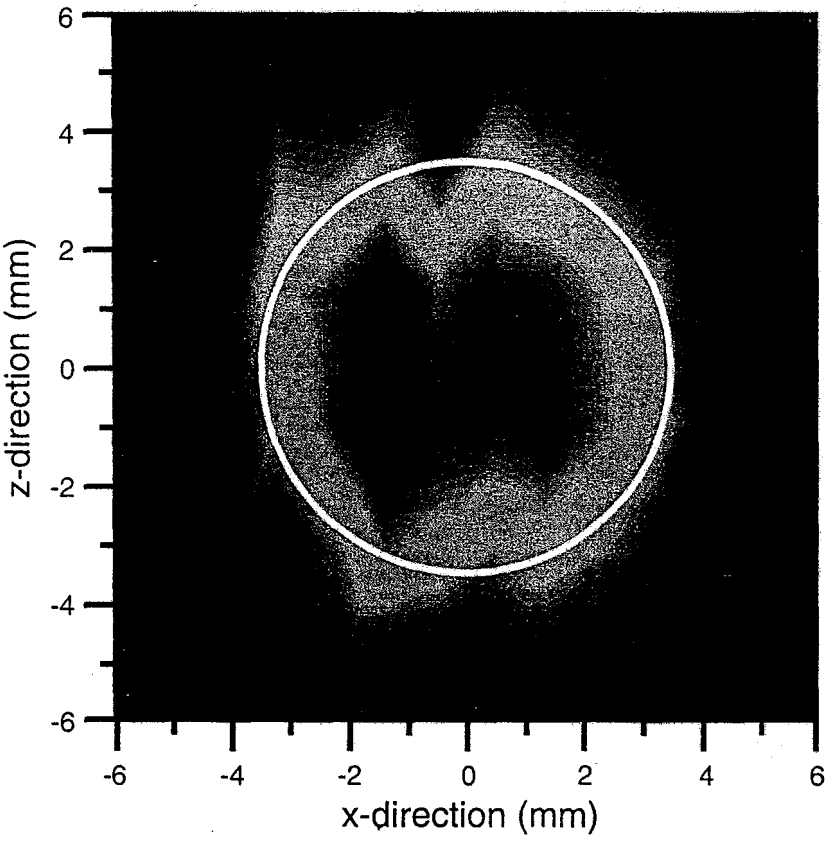

Figure 5.12. A phantom image of the sample cell with laser-polarized ^{129}Xe gas. The image was acquired in 32 slices in increments of 0.04 G/cm in the z-direction. The white circle shows the outline of the sample tube. The xenon pressure was 1 atm and the flow rate was 3.9 mL/s. Static field strength was 22.6 G. Resolution in the x-direction is 0.9 mm and 2 mm in the z-direction.

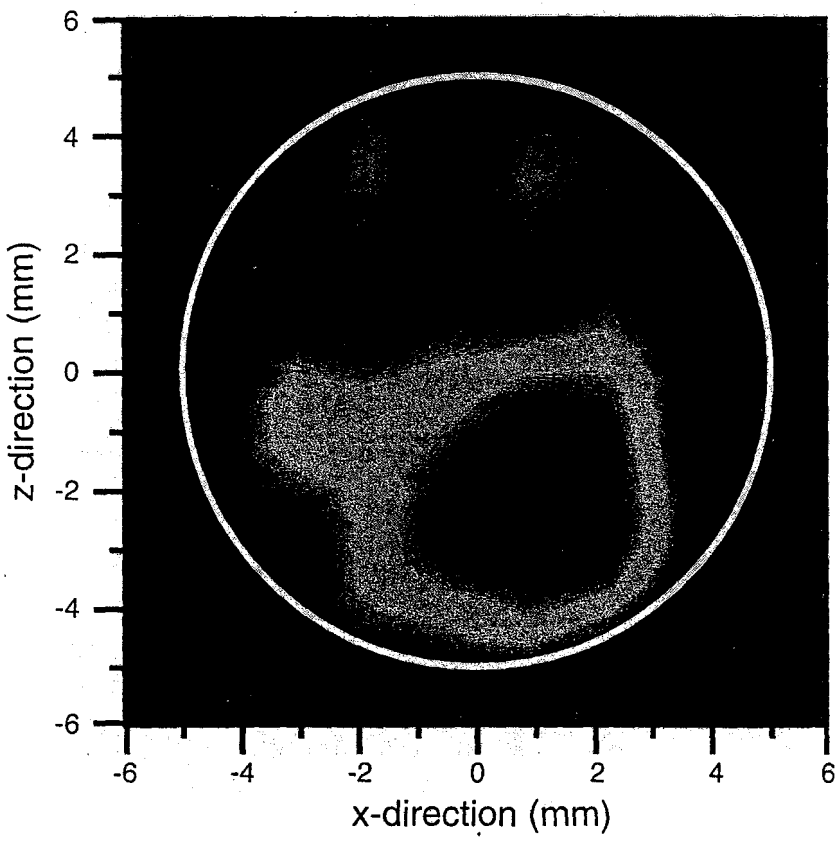

Figure 5.13. A phantom image of a non-descript piece of aerogel using laser-polarized ^{129}Xe gas. The image was acquired in 32 slices in increments of 0.04 G/cm in the z-direction. The white circle shows the outline of the sample tube. The xenon pressure was 1 atm and the flow rate was 2.0 mL/s. Static field strength was 22.6 G. Resolution in the x-direction is 1.4 mm and 0.6 mm in the z-direction.

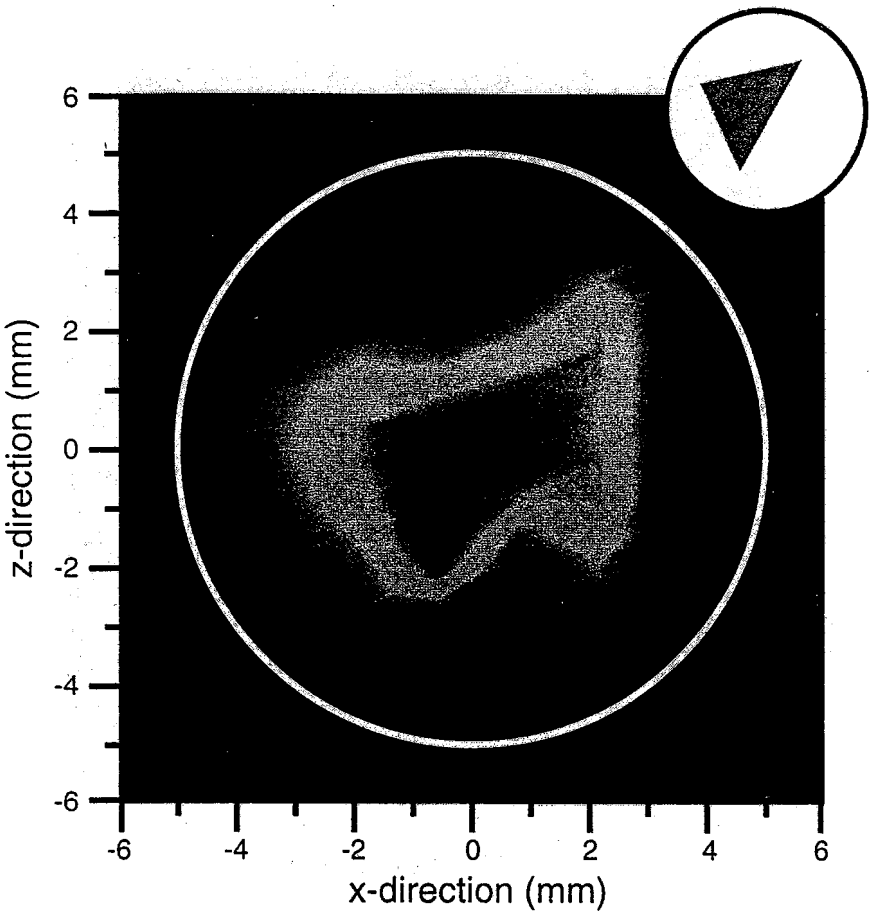

Figure 5.14. A phantom image of a triangular piece of aerogel with laser-polarized ^{129}Xe gas. The experimental parameters and resolution were identical to the image in Figure (5.13). In the upper right hand corner of the image is a schematic of the aerogel piece in the 1 cm sample cell.

5.4.4 - Conclusions and Future Work

In this section ultra low-field magnetic resonance imaging of void spaces and aerogels has been demonstrated. The imaging set-up takes advantage of the high polarizations attainable through the continuous flow of laser-polarized ^{129}Xe gas and the high sensitivity of a high-T_c dc SQUID detector. Furthermore, the successful incorporation of a three-axis pulsed field gradient coil has allowed for more efficient and quicker imaging. The ability of this technique to distinguish between xenon gas in a material and in the gas phase has been shown. With the development of this technique, there now exists the potential of millimeter resolution gas MRI at less than 50 times the Earths' field. Such images will be highly applicable to the characterization of many heterogeneous materials, including porous and granular media.

[1] T. Gullion, J. Schaefer, *J. Magn. Reson.* **1989**, *81*, 196.

[2] T. Gullion, J. Schaefer, *Advances in Magnetic Resonance* **1989**, *13*, 55.

[3] D. P. Raleigh, M. H. Levitt, R. G. Griffin, *Chem. Phys. Lett.* **1988**, *146*. 71.

[4] G. E. Pake, *Journal of Chemical Physics* **1948**, *16*, 327.

[5] F. Bloch, *Physical Review* **1956**, *102*, 104.

[6] F. Bloch, *Physical Review* **1958**, *111*, 841.

[7] M. Mehring, *High Resolution NMR in Solids*, Springer-Verlag, New York, **1983**.

[8] E. R. Andrew, A. Bradbury, R. G. Eades, *Nature* **1958**, *182*, 1659.

[9] I. J. Lowe, *Physical Review Letters* **1959**, *2*, 285.

[10] M. M. Maricq, J. S. Waugh, *Journal of Chemical Physics* **1979**, *70*, 3300.

[11] A. Pines, M. G. Gibby, J. S. Waugh, *Journal of Chemical Physics* **1973**, *59*, 569.

[12] N. F. Ramsey, R. V. Pound, *Physical Review* **1951**, *81*, 278.

[13] S. R. Hartmann**, E. L. Hahn, *Physical Review* **1962**, *128*, 2042.

[14] K. Schmidt-Rohr, H. W. Spiess, *Multidimensional solid-state NMR and polymers*, Academic Press, San Diego, **1994**.

[15] R. R. Ernst, G. Bodenhausen, A. Wokaun, *Principles of Nuclear Magnetic Resonance in One and Two Dimensions*, Clarendon Press, Oxford, **1987**.

[16] L. Emsley, D. D. Laws, A. Pines., in *Proc. S.I.F., Vol. CXXIX*, North-Holland, Amsterdam, **1999**, pp. 45.

[17] K. Schmidt-Rohr, J. Clauss, H. W. Spiess, *Macromolecules* **1992**, *25*, 3273.

[18] J. S. Waugh, L. M. Huber, U. Haeberlen, *Physical Review Letters* **1968**, *20*, 180.

[19] P. Mansfield, *Phys. Lett. A* **1970**, *32*, 485.

[20] P. Mansfield, *J. Phys. C* **1971**, *4*, 1444.

[21] U. Haeberlen, J. S. Waugh, *Physical Review* **1968**, *175*, 453.

[22] W. K. Rhim, D. D. Elleman, R. W. Vaughan, *Journal of Chemical Physics* **1972**, *58*, 1772.

[23] D. P. Burum, M. Linder, R. R. Ernst, *Journal of Magnetic Resonance* **1981**, *44*, 173.

[24] D. P. Burum, W. K. Rhim, *Journal of Chemical Physics* **1979**, *71*, 944.

[25] B.-J. van Rossum, H. Förster, H. J. M. de Groot, *Journal of Magnetic Resonance* **1997**, *124*, 516.

[26] A. Bielecki, A. C. Kolbert, H. J. M. de Groot, R. G. Griffin, M. H. Levitt, *Advances in Magnetic Resonance* **1990**, *14*, 111.

[27] A. Bielecki, A. C. Kolbert, M. H. Levitt, *Chemical Physics Letters* **1989**, *155*, 341.

[28] P. Caravatti, G. Bodenhausen, R. R. Ernst, *Chemical Physics Letters* **1982**, *89*, 363.

[29] P. Caravatti, L. Braunschweiler, R. R. Ernst, *Chemical Physics Letters* **1983**, *100*, 305.

[30] A. J. Shaka, J. Keeler, R. Freeman, *Journal of Magnetic Resonance* **1983**, *53*, 313.

[31] D. Suter, A. Pines, J. H. Lee, G. Drobny, *Chem. Phys. Lett.* **1988**, *144*, 324.

[32] M. H. Levitt, R. Freeman, T. Frenkiel, *Journal of Magnetic Resonance* **1982**, *47*, 328.

[33] A. E. Bennett, C. M. Rienstra, M. Auger, K. V. Lakshmi, R. G. Griffin, *Journal of Chemical Physics* **1995**, *103*, 6951.

[34] M. Ernst, H. Zimmerman, B. H. Meier, *Chemical Physics Letters* **2000**, *317*, 581.

[35] R. C. Zeigler, R. A. Wind, G. E. Maciel, *J. Mag. Res.* **1988**, *79*, 299.

[36] R. Tycko, G. Dabbagh, *Chem. Phys. Lett.* **1990**, *173*, 461.

[37] B.-Q. Sun, P. R. Costa, D. Kocisko, P. T. Lansbury, R. G. Griffin, *J. Chem. Phys.* **1995**, *102*, 702.

[38] R. G. S. Spencer, K. J. Halverson, M. Auger, A. McDermott, R. G. Griffin, *Biochemistry* **1991**, *30*, 10382.

[39] N. C. Nielsen, H. Bildsoe, H. J. Jakobsen, M. H. Levitt, *Journal of Chemical Physics* **1994**, *101*, 1805.

[40] S. Kiihne, M. A. Mehta, S. J.A., D. M. Gregory, J. C. Shiels, G. P. Drobny, *J. Phys. Chem.* **1998**, *102*, 2274.

[41] A. E. Bennett, L. R. Becerra, R. G. Griffin, *J. Chem. Phys.* **1994**, *100*, 812.

[42] M. Hohwy, H. J. Jakobsen, M. Edén, M. H. Levitt, N. C. Nielsen, *J. Chem. Phys.* **1998**, *108*, 2686.

[43] M. Baldus, D. G. Geurts, B. H. Meier, *Solid State NMR* **1998**, *11*, 157.

[44] M. Baldus, D. G. Geurts, S. Hediger, B. H. Meier, *J. Magn. Reson. A* **1996**, *118*, 140.

[49] R. H. Havlin, H. Le, D. D. Laws, A. C. deDios, E. Oldfield, *J. Am. Chem. Soc.* **1997**, *119*, 11951.

[50] J. Heller, D. D. Laws, M. Tomaselli, D. S. King, D. E. Wemmer, A. Pines, R. H. Havlin, E. Oldfield, *J. Am. Chem. Soc.* **1997**, *119*, 7827.

[51] J. Herzfeld, A. E. Berger, *Journal of Chemical Physics* **1980**, *73*, 6021.

[52] M. Alla, E. I. Kundla, E. Lippmaa, *JETP Lett.* **1978**, *27*, 194.

[53] R. Tycko, G. Dabbagh, P. A. Mirau, *J. Magn. Reson.* **1989**, *85*, 265.

[54] A. Bax, N. M. Szeverenyi, G. E. Maciel, *J. Magn. Reson.* **1983**, *52*, 147.

[55] A. Bax, N. M. Szeverenyi, G. E. Maciel, *J. Magn. Reson.* **1983**, *51*, 400.

[56] A. Bax, N. M. Szeverenyi, G. E. Maciel, *J. Magn. Reson.* **1983**, *55*, 494.

[57] J. Z. Hu, D. W. Alderman, C. Ye, R. J. Pugmire, D. M. Grant, *Journal of Magnetic Resonance, Series A* **1993**, *105*, 82.

[58] J. Z. Hu, A. M. Orendt, D. W. Alderman, R. J. Pugmire, C. Ye, D. M. Grant, *Solid State NMR* **1994**, *3*, 181.

[59] L. Frydman, G. C. Chingas, Y. K. Lee, P. J. Grandinetti, M. A. Eastman, G. A. Barrall, A. Pines, *Journal of Chemical Physics* **1992**, *97*, 4800.

[60] A. Lesage, C. Auger, S. Caldarelli, L. Emsley, *J. Am. Chem. Soc.* **1997**, *119*, 7867.

[61] in *Quadrupolar nuclei located withing a cubic crystal will not experience a quadrupolar coupling due to the symmetry of the lattice. This is evidenced by the very narrow 14N lineshape in NH4Cl or the narrow 23Na lineshape in NaCl.*

[62] H. H. Mantsch, H. Saitó, I. C. P. Smith, *Progress in NMR Spectroscopy* **1977**, *11*, 211.

[59] L. Frydman, G. C. Chingas, Y. K. Lee, P. J. Grandinetti, M. A. Eastman, G. A. Barrall, A. Pines, *Journal of Chemical Physics* **1992**, *97*, 4800.

[60] A. Lesage, C. Auger, S. Caldarelli, L. Emsley, *J. Am. Chem. Soc.* **1997**, *119*, 7867.

[61] in *Quadrupolar nuclei located withing a cubic crystal will not experience a quadrupolar coupling due to the symmetry of the lattice. This is evidenced by the very narrow 14N lineshape in NH4Cl or the narrow 23Na lineshape in NaCl.*

[62] H. H. Mantsch, H. Saitó, I. C. P. Smith, *Progress in NMR Spectroscopy* **1977**, *11*, 211.

[63] L. W. Jelinski, *Annual Review of Materials Science* **1985**, *15*, 359.

[64] N. Chandrakumar, *Spin-1 NMR, Vol. 34*, Springer-Verlag, Berlin, **1996**.

[65] D. J. Siminovich, *Biochemistry and Cell Biology* **1998**, *76*, 411.

[66] R. L. Smith, E. Oldfield, *Science* **1984**, *225*, 280.

[67] J. Ackerman, R. Eckman, A. Pines, *Chemical Physics* **1979**, *42*, 423.

[68] P. Diehl, H. Bösiger, H. Zimmerman, *Journal of Magnetic Resonance* **1979**, *33*, 113.

[69] Z. Luz, in *Nuclear Magnetic Resonance of Liquid Crystals, Vol. 141* (Ed.: J. W. Emsley), D. Reidel Publishing Company, Dordrecht, **1983**, pp. 315.

[70] J. W. Emsley,,, Reidel, Dordrecht, **1985**.

[71] A. Abragam, *The Principles of Nuclear Magnetism*, Oxford University Press, Oxford, **1961**.

[72] A. Samoson, E. Lippmaa, A. Pines, *Molecular Physics* **1988**, *65*, 1013.

[73] C. P. Slichter, *Principles of Nuclear Magnetic Resonance*, 3rd ed., Springer-Verlag, New York, **1990**.

[74] A. Samoson, A. Pines, *Review of Scientific Instruments* **1989**, *60*, 3239.

[75] B. Q. Sun, J. H. Baltisberger, Y. Wu, A. Samoson, A. Pines, *Solid State Nuclear Magnetic Resonance* **1992**, *1*, 267.

[76] K. T. Mueller, T. P. Jarvie, D. J. Aurentz, B. W. Roberts, *Chem. Phys. Lett.* **1995**, *242*, 535.

[77] J. H. Baltisberger, S. L. Gann, E. W. Wooten, T. H. Chang, K. T. Mueller, A. Pines, *Journal of the American Chemical Society* **1992**, *114*, 7489.

[78] A. Medek, J. S. Harwood, L. Frydman, *J. Am. Chem. Soc.* **1995**, *117*, 12779.

[79] L. Frydman, J. S. Harwood, *J. Am. Chem. Soc.* **1995**, *117*, 5367.

[80] P. K. Madhu, A. Goldbourt, L. Frydman, S. Vega, *Journal of Chemical Physics* **2000**, *112*, 2377.

[81] N. C. Nielsen, H. Bildsoe, H. J. Jakobsen, *Chemical Physics Letters* **1992**, *191*, 205.

[82] N. C. Nielsen, F. Creuzet, R. G. Griffin, M. H. Levitt, *Journal of Chemical Physics* **1992**, *96*, 5668.

[83] S. Spera, A. Bax, *J. Am. Chem. Soc.* **1991**, *113*, 5490.

[84] D. S. Wishart, B. D. Sykes, *J. Biomolecular NMR* **1994**, *4*, 171.

[85] A. C. de Dios, J. G. Pearson, E. Oldfield, *Science* **1993**, *260*, 1491.

[86] D. D. Laws, A. C. de Dios, E. Oldfield, *J. Biomolecular NMR* **1993**, *3*, 607.

[87] N. Tjandra, A. Bax, *Journal of the American Chemical Society* **1997**, *119*, 9576.

[88] A. Bax, N. M. Szeverenyi, G. Maciel, *Journal of Magnetic Resonance* **1983**, *52*, 147.

[89] R. Tycko, G. Dabbagh, P. A. Mirau, *Journal of Magnetic Resonance* **1989**, *85*, 265.

[90] H. Le, J. G. Pearson, A. C. de Dios, E. Oldfield, *J. Am. Chem. Soc.* **1995**, *117*, 3800.

[91] J. G. Pearson, J. F. Wang, J. L. Markley, H. Le, E. Oldfield, *J. Am. Chem. Soc.* **1995**, *117*, 8823.

[92] D. D. Laws, H. Le, A. C. de Dios, R. H. Havlin, E. Oldfield, *J. Am. Chem. Soc.* **1995**, *117*, 9542.

[93] J. G. Pearson, H. Le, L. K. Sanders, N. Godbout, E. Oldfield, *J. Am. Chem. Soc.* **1997**, *119*, 11941.

[94] J. Wang, A. P. Hinck, S. N. Loh, M. LeMaster, J. L. Markley, *Biochemistry* **1992**, *31*, 921.

[95] M. Ikura, L. E. Kay, A. Bax, *Biochemistry* **1990**, *29*, 4659.

[96] D. D. Laws, A. C. de Dios, E. Oldfield, *J. Biomol. NMR* **1993**, *3*, 607.

[97] S. Chaturvedi, G. Kuantee, R. Parthasarathy, *Biopolymers* **1991**, *31*, 397.

[98] J. K. Fawcett, N. Camerman, A. Camerman, *Acta Crytallographica B* **1975**, *31*, 658.

[99] A. Hempel, N. Camerman, A. Camerman, *Biopolymers* **1991**, *31*, 187.

[100] I. L. Karle, J. L. Flippen-Anderson, K. Uma, P. Balaram, *Prot. Struc. Funct. Gen.* **1990**, *7*, 62.

[101] I. L. Karle, J. L. Flippen-Anderson, K. Uma, P. Balaram, *Biopolymers* **1993**, *33*, 827.

[102] G. Precigoux, C. Courseille, S. Geoffre, F. Leroy, *J. Am. Chem. Soc.* **1987**, *109*, 7463.

[103] K. Wolinski, J. F. Hinton, P. Pulay, *J. Am. Chem. Soc.* **1990**, *112*, 8251.

[104] R. Ditchfield, *J. Chem. Phys.* **1972**, *56*, 5688.

[105] F. London, in *Superfluids, Vol. 1*, John Wiley and Sons, New York, **1950**.

[106] M. Ikura, L. E. Kay, A. Bax, *Biochemistry* **1990**, *29*, 4659.

[107] J. Wang, A. P. Hinck, S. N. Loh, M. LeMaster, J. L. Markley, *Biochemistry* **1992**, *31*, 921.

[108] J. Heller, University of California (Berkeley), **1997**.

[109] A. Lesage, M. Bardet, L. Emsley, *J. Am. Chem. Soc.* **1999**, *121*, 10987.

[110] A. Lesage, D. Sakellariou, S. Steuernagel, L. Emsley, *J. Am. Chem. Soc.* **1998**, *120*, 13194.

[111] Y. Tomita, E. J. O'Connor, A. McDermott, *J. Am. Chem. Soc.* **1994**, *116*, 8766.

[112] R. Tycko, D. P. Weliky, A. E. Berger, *J. Chem. Phys.* **1996**, *105*, 7915.

[113] M. Hong, J. D. Gross, R. G. Griffin, *J. Phys. Chem. B* **1997**, *101*, 5869.

[114] M. Hong, J. D. Gross, W. Hu, R. G. Griffin, *J. Mag. Res.* **1998**, *135*, 169.

[115] P. R. Costa, J. D. Gross, M. Hong, R. G. Griffin, *Chem. Phys. Lett.* **1997**, *280*, 95.

[116] X. Feng, Y. K. Lee, D. Sandstrom, M. Eden, H. Maisel, A. Sebald, M. H. Levitt, *Chem. Phys. Lett.* **1996**, *257*, 314.

[117] R. Tycko, *J. Biomol. NMR* **1996**, *8*, 239.

[118] S. Spera, A. Bax, *J. Am. Chem. Soc.* **1991**, *113*, 5490.

[119] D. S. Wishart, B. D. Sykes, *J. Biomolecular NMR* **1994**, *4*, 171.

[120] H. Saito, *Reson. in Chemistry* **1986**, *24*, 835.

[121] H. Saito, I. Ando, *Annu. Rep. NMR Spectrosc.* **1989**, *21*, 209.

[122] H. Saito, R. Tabeta, A. Shojoi, T. Ozaki, *Macromolecules* **1983**, *16*, 1050.

[123] J. Heller, A. C. Kolbert, R. Larsen, M. Ernst, T. Bekker, M. Baldwin, S. B. Prusiner, A. Pines, D. E. Wemmer, *Protein Science* **1996**, *5*, 1655.

[124] A. C. de Dios, J. G. Pearson, E. Oldfield, *J. Am. Chem. Soc.* **1993**, *115*, 9768.

[125] A. C. de Dios, J. G. Pearson, E. Oldfield, *Science* **1993**, *260*, 1491.

[126] D. D. Laws, H.-M. L. Bitter, L. K. Sanders, J. Grimley, E. Oldfield, D. E. Wemmer, A. Pines, in *J. Magn. Reson.*, **2000**.

[127] P. Luginbühl, T. Szyperski, K. Wüthrich, *J. Mag. Res. B* **1995**, *109*, 229.

[128] H. Le, J. G. Pearson, A. C. de Dios, E. Oldfield, *J. Am. Chem. Soc.* **1995**, *117*, 3800.

[129] J. G. Pearson, J. F. Wang, J. L. Markley, H. Le, E. Oldfield, *J. Am. Chem. Soc.* **1995**, *117*, 8823.

[130] H.-M. L. Bitter, D. D. Laws, H. L. Ball, D. S. King, R. H. Havlin, L. K. Sanders, J. Grimley, S. B. Prusiner, E. Oldfield, D. Wemmer, A. Pines, in *J. Am. Chem. Soc.*, **2000**.

[131] T. Nakai, J. Ashida, T. Terao, *J. Chem. Phys.* **1988**, *88*, 6049.

[132] J. Schaefer, E. O. Stejskal, *J. Am. Chem. Soc.* **1976**, *98*, 1031.

[133] Z. Gan, *J. Am. Chem. Soc.* **1992**, *114*, 8307.

[134] E. Lipmaa, M. Alla, T. Turherm, in *Proceedings of the XIXth Congress Ampere*, Heidelberg, **1976**, p. 241.

[135] Y. Yarim-Agaev, P. N. Tutunjian, J. S. Waugh, *J. Magn. Reson.* **1982**, *47*, 51.

[136] P. B. W. Ten Kortenaar, B. G. Van Dijk, J. M. Peeters, B. J. Raaben. P. J. H. M. Adam, G. I. Tesser, *Int. J. Peptide Protein Res.* **1986**, *27*, 398.

[137] C. G. Fields, D. H. Lloyd, R. L. MacDonald, K. M. Otteson, R. L. Noble, *Peptide Res.* **1991**, *4*, 95.

[138] H. L. Ball, P. Mascagni, *Lett. Peptide. Sci.* **1995**, *2*, 49.

[139] V. K. Sarin, S. B. H. Kent, J. P. Tam, R. B. Merrifield, *Anal. Biochem.* **1981**, *117*, 147.

[140] S. B. Prusiner, *Proc. Natl. Acad. Sci. USA* **1998**, *95*, 13363.

[141] L. Stryer, *Biochemistry*, 4 ed., W.H. Freeman and Company, New York, **1995**.

[142] K. Hsiao, S. B. Prusiner, *Neurology* **1990**, *40*, 1820.

[143] C. L. Masters, D. C. Gadjusek, C. J. Gibbs, *Brain* **1981**, *104*, 559.

[144] J. E. Fradkin, L. B. Schonberger, J. L. Mills, W. J. Gunn, J. M. Piper, D. K. Wysowski, R. Thomson, S. Durako, P. Brown, *J. Am. Med. Assoc.* **1991**, *265*.

[145] T. Alper, D. A. Haig, M. C. Clarke, *Biochim. Biophys. Res. Commun.* **1966**, *22*, 278.

[146] T. Alper, W. A. Cramp, D. A. Haig, M. C. Clarke, *Nature (London)* **1967**, *214*, 764.

[147] R. Latarjet, B. Muel, D. A. Haig, M. C. Clarke, T. Alper, *Nature (London)* **1970**, *227*, 1341.

[148] C. J. Gibbs, D. C. Gajdusek, R. Latarjet, *Proc. Natl. Acad. Sci. USA* **1978**, *75*, 6268.

[149] S. B. Prusiner, *Science* **1982**, *216*, 136.

[150] D. C. Bolton, M. P. McKinley, S. B. Prusiner, *Science* **1982**, *218*, 1309.

[151] S. B. Prusiner, D. C. Bolton, D. Groth, K. A. Bowman, S. P. Cochran, M. P. McKinley, *Biochemistry* **1982**, *21*, 6942.

[152] C. Bellinger-Kawahara, J. E. Cleaver, T. O. Diener, S. B. Prusiner, *J. Virol.* **1987**, *61*.

[153] C. Bellinger-Kawahara, T. O. Diener, M. P. McKinley, D. Groth, D. R. Smith, S. B. Prusiner, *Virology* **1987**, *160*, 271.

[154] C. Bellinger-Kawahara, E. Kempner, D. Groth, R. Gabizon, S. B. Prusiner, *Virology* **1988**, *164*, 537.

[155] G. C. Millson, G. D. Hunter, R. H. Kimberlin, in *Slow Virus Diseases of Animals and Man* (Ed.: R. H. Kimberlin), American Elsevier, New York, **1976**, pp. 243.

[156] S. B. Prusiner, D. Groth, A. Serban, D. Stahl, *Proc. Natl. Acad. Sci. USA* **1993**, *90*, 2793.

[157] S. B. Prusiner, D. Groth, M. P. McKinley, *Proc. Natl. Acad. Sci. USA* **1981**, *78*, 4606.

[158] D. R. Borchelt, M. Scott, A. Taraboulos, N. Stahl, S. B. Prusiner, *J. Cell Biol.* **1990**, *110*, 743.

[159] Z. Huang, J.-M. Gabriel, M. Baldwin, R. Fletterick, S. B. Prusiner, F. E. Cohen, *Proc. Natl. Acad. Sci. USA* **1994**, *91*, 7139.

[160] H. Zhang, K. Kaneko, J. Nguyen, T. L. Livshits, M. Baldwin, F. E. Cohen, T. L. James, S. B. Prusiner, *J. Mol. Biol.* **1995**, *250*, 514.

[161] R. Riek, S. Hornemann, G. Wider, M. Billeter, R. Glockshuber, K. Wütrich, *Nature (London)* **1996**, *382*, 180.

[162] K. Kaneko, H. L. Ball, H. Wille, H. Zhang, D. Groth, M. Torchia, P. Tremblay, J. Safar, S. B. Prusiner, S. J. De Armond, M. A. Baldwin, F. E. Cohen, *J. Mol. Biol.* **2000**, *295*, 997.

[163] K.-M. Pan, M. Baldwin, J. Nguyen, M. Gasset, A. Serban, D. Groth, I. Mehlhorn, Z. Huang, R. Fletterick, F. E. Cohen, S. B. Prusiner, *Proc. Natl. Acad. Sci. USA* **1993**, *90*, 10962.

[164] M. Billeter, R. Riek, G. Wider, S. Hornemann, K. Wüthrich, *Proc. Natl. Acad. Sci. USA* **1997**, *94*, 7281.

[165] K. Kaneko, L. Zulianello, M. Scott, C. M. Cooper, A. C. Wallace, T. L. James, F. E. Cohen, S. B. Prusiner, *Proc. Natl. Acad. Sci. USA* **1997**, *94*, 10069.

[166] R. Riek, S. Hornemann, G. Wider, R. Glockshuber, K. Wütrich, *FEBS Lett.* **1997**, *413*, 282.

[167] T. L. James, H. Liu, N. B. Ulyanov, S. Farr-Jones, H. Zhang, D. G. Donne, K. Kaneko, D. Groth, I. Mehlhorn, S. B. Prusiner, F. E. Cohen, *Proc. Natl. Acad. Sci. USA* **1997**, *94*, 10086.

[168] S. B. Prusiner, M. P. McKinley, K. A. Bowman, D. C. Bolton, P. E. Bendheim, D. Groth, G. G. Clenner, *Cell* **1983**, *35*, 349.

[169] Z. Huang, S. B. Prusiner, F. E. Cohen, *Fold. Des.* **1996**, *1*, 13.

[170] H. M. Schatzl, M. DaCosta, L. Taylor, F. E. Cohen, S. B. Prusiner, *J. Mol. Biol.* **1995**, *245*, 362.

[171] J.-M. Gabriel, B. Oesch, H. Kretschmar, M. Scott, e. al., *Proc. Natl. Acad. Sci. USA* **1992**, *89*, 9097.

[172] N. Stahl, M. Baldwin, D. B. Teplow, L. E. Hood, B. W. Gibson, A. L. Burlingame, S. B. Prusiner, *Biochemistry* **1993**, *32*, 1991.

[173] H. Bueler, M. Fisher, Y. Lang, H. Bluethmann, H.-P. Lipp, S. J. DeArmond, S. B. Prusiner, M. Aguet, C. Weissmann, *Nature* **1992**, *356*, 577.

[174] J. Stöckel, J. Safar, A. C. Wallace, F. E. Cohen, S. B. Prusiner, *Biochemistry* **1998**, *37*, 7185.

[175] T. Muramoto, M. Scott, F. E. Cohen, S. B. Prusiner, *Proc. Natl. Acad. Sci. USA* **1996**, *93*, 15457.

[176] T. Kitamoto, R. Iizuka, J. Tateishi, *Biochem. Biophys. Res. Commun.* **1993**, *192*, 525.

[177] D. Peretz, R. A. Williamson, Y. Matsunaga, H. Serban, C. Pinilla, R. Bastidas, R. Rozenshteyn, T. L. James, R. A. Houghten, F. E. Cohen, e. al., *J. Mol. Biol.* **1997**, *273*, 614.

[178] I. Mehlhorn, D. Groth, J. Stockel, B. Moffat, D. Reilly, D. Yansura, S. Willet, M. Baldwin, R. Fletterick, F. E. Cohen, R. Vandlen, D. Henner, S. B. Prusiner, *Biochemistry* **1996**, *35*, 5528.

[179] R. A. Bessen, D. Kocisko, G. J. Raymond, S. Nandan, P. T. Lansbury, B. Caughey, *Nature* **1995**, *385*, 698.

[180] P. T. Lansbury, *Chemistry & Biology* **1995**, *2*, 1.

[181] G. C. Telling, M. Scott, J. Mastrianni, R. Gabizon, M. Torchia, F. E. Cohen, S. J. De Armond, S. B. Prusiner, *Cell* **1995**, *83*, 70.

[182] K. Kaneko, H. Wille, I. Mehlhorn, H. Zhang, H. L. Ball, F. E. Cohen, M. Baldwin, S. B. Prusiner, *J. Mol. Biol.* **1997**, *270*, 574.

[183] D. G. Donne, J. H. Viles, D. Groth, I. Mehlhorn, T. L. James, F. E. Cohen, S. B. Prusiner, P. E. Wright, H. J. Dyson, *Proc. Natl. Acad. Sci. USA* **1997**, *94*, 13452.

[184] F. E. Cohen, S. B. Prusiner, *Annu. Rev. Biochem.* **1998**, *67*, 793.

[185] S. B. Prusiner, D. Groth, D. C. Bolton, S. B. H. Kent, L. E. Hood, *Cell* **1984**, *38*, 127.

[186] F. Tagliavini, F. Prelli, L. Verga, G. Giaccone, R. Sarma, P. Gorevic, B. Ghetti, F. Passerinin, E. Ghibaudi, G. Forloni, M. Salmoni, O. Bugiani, B. Frangione, *Proc. Natl. Acad. Sci. USA* **1993**, *90*, 9678.

[187] J. Nguyen, M. Baldwin, F. E. Cohen, S. B. Prusiner, *Biochemistry* **1995**, *34*, 4186.

[188] M. Gasset, M. Baldwin, D. H. Lloyd, J.-M. Gabriel, D. M. Holtzman, F. E. Cohen, R. Fletterick, S. B. Prusiner, *Proc. Natl. Acad. Sci. USA* **1992**, *89*, 10940.

[189] G. Forloni, N. Angeretti, R. Chiesa, E. Monzani, M. Salmoni, O. Bugiani, F. Tagliavini, *Nature* **1993**, *362*, 543.

[190] J. H. Come, P. E. Fraser, P. T. Lansbury, *Proc. Natl. Acad. Sci. USA* **1993**, *90*, 5959.

[191] G. C. Telling, T. Haga, M. Torchia, P. Tremblay, S. J. De Armond, S. B. Prusiner, *Genes Dev.* **1996**, *10*, 1736.

[192] H. L. Ball,, (Ed.: P. Communication), San Francisco, **2000**.

[193] H. R. Kricheldorf, D. Muller, *Macromolecules* **1983**, *16*, 615.

[194] C. Hilbert, J. Clarke, T. Sleator, E. Hahn, *Appl. Phys. Lett.* **1985**, *47*, 637.

[195] N. Q. Fan, J. Clarke, *Rev. Sci. Instrum.* **1991**, *62*, 1453.

[196] H. C. Seton, D. M. Bussell, J. M. S. Hutchison, I. Nicholson, D. J. Lurie, *Phys. Med. Biol.* **1992**, *37*, 2133.

[197] B. Black, G. Majer, A. Pines, *Chem. Phys. Lett.* **1993**, *201*, 550.

[198] S. Kumar, B. D. Thorson, W. F. Avrin, *J. Mag. Res. Series B* **1995**, *107*, 252.

[199] S. Kumar, W. F. Avrin, B. R. Whitecotton, *IEEE Trans. Magnetics* **1996**, *32*, 5261.

[200] D. M. TonThat, J. Clarke, *J. Rev. Sci. Instrum.* **1996**, *67*, 2890.

[201] D. M. TonThat, M. Ziegeweid, Y.-Q. Song, E. J. Munson, S. Appelt, A. Pines, J. Clarke, *J. Chem. Phys. Lett.* **1997**, *272*, 245.

[202] M. P. Augustine, A. Wong-Foy, J. L. Yarger, M. Tomaselli, A. Pines, D. M. TonThat, J. Clarke, *Appl. Phys. Lett.* **1998**, *72*, 1908.

[203] H. C. Seton, J. M. S. Hutchison, D. M. Bussell, *IEEE Trans. on Applied Superconductivity* **1997**, *7*, 3213.

[204] S. Saxena,, (Ed.: P. Communication), **2000**.

[205] S. Kumar, R. Matthews, S. G. Haupt, D. K. Lathrop, M. Takigawa, J. R. Rozen, S. L. Brown, R. H. Koch, *Appl. Phys. Lett.* **1997**, *70*, 1037.

[206] R. E. de Souza, K. Schlenga, A. Wong-Foy, R. McDermott, A. Pines, J. Clarke, *J. Braz. Chem. Soc.* **1999**, *10*, 307.

[207] K. Schlenga, R. McDermott, J. Clarke, R. E. de Souza, A. Wong-Foy, A. Pines, *IEEE Trans. on Applied Superconductivity* **1999**, *9*, 4424.

[208] K. Schlenga, R. McDermott, J. Clarke, R. E. de Souza, A. Wong-Foy, A. Pines, *Appl. Phys. Lett.* **1999**, *75*, 3695.

[209] J. Brossel, A. Kastler, *Compt. Rend.* **1949**, *229*, 1213.

[210] A. Kastler, *J. Phys. Radium* **1950**, *11*, 255.

[211] A. Kastler, *Opt. Soc. Am.* **1957**, *47*, 460.

[212] H. J. Jänsch, T. Hof, U. Ruth, J. Schmidt, D. Stahl, D. Fick, *Chem. Phys. Lett.* **1998**, *296*, 146.

[213] U. Ruth, T. Hof, J. Schmidt, D. Fick, H. J. Jänsch, *Appl. Phys. B* **1999**, *68*, 93.

[214] M. S. Albert, A. Venkatesh, A. Zhang, C.-H. Oh, F. Jolecz, L. Kubatins, in *Experimental NMR Conference*, Asilomar, CA, **2000**, p. 182.

[215] E. Brunner, M. Haake, L. Kaiser, A. Pines, J. A. Reimer, *J. Mag. Res.* **1999**, *138*, 155.

[216] P. Mansfield, P. G. Morris, *NMR Imaging in Bio-Medicine*, Academic Press, New York, **1982**.

[217] P. T. Callaghan, *Principles of Nuclear Magnetic Resonance Microscopy*, Oxford University Press, Oxford, **1991**.

[218] B. Black, Ph.D. thesis, University of California (Berkeley), **1993**.

[219] C. Connor, Ph.D. thesis, University of California (Berkeley), **1989**.

[220] M. Zeigeweid, Ph.D. thesis, University of California (Berkeley), **1995**.

[221] R. P. Feynman, R. B. Leighton, M. Sands, *The Feynman Lectures on Physics: Quantum Mechanics, Vol. 3*, Addison-Wesley Publishing Company, Reading, **1965**.

[232] T. G. Walker, W. Happer, *Rev. Mod. Phys.* **1997**, *60*, 629.

[233] E. Brunner, *Concepts Magn. Res.* **1999**, *11*, 313.

[234] B. M. Goodson, *Conepts Magn. Reson.* **1999**, *11*, 203.

[235] B. M. Goodson, University of California (Berkeley), **1999**.

[236] M. A. Bouchiat, T. R. Carver, C. M. Varnum, *Phys. Rev. Lett.* **1960**, *5*, 373.

[237] M. Haake, A. Pines, J. A. Reimer, R. Seydoux, *J. Am. Chem. Soc.* **1997**, *119*, 11711.

[238] R. Seydoux, M. Haake, A. Pines, J. A. Reimer, *J. Phys. Chem. B* **1999**, *103*, 4629.

[239] A. Wong-Foy, S. Saxena, H.-M. L. Bitter, A. Moule, A. Pines, R. McDermott, J. Clarke, in *Experimental NMR Conference*, Asilomar, CA, **2000**, p. 174.

[240] F. Ludwig, E. Dantsker, R. Kleiner, D. Koelle, J. Clarke, S. Knappe, D. Drung, H. Koch, N. M. Alford, T. W. Button, *Appl. Phys. Lett.* **1995**, *66*, 1418.

[241] T. S. Lee, E. Dantsker, J. Clarke, *J. Rev. Sci. Instrum.* **1996**, *67*, 4208.

[242] M. D. Harten, *Med. Phys.* **1987**, *14*, 616.

[243] P. Mansfield, *J. Phys. E.* **1988**, *21*, 18.

[244] P. Mansfield, *J. Phys. Chem. C* **1973**, *6*, L422.

[245] P. Mansfield, P. K. Grannell, *Phys. Rev.* **1975**, *12*, 3618.

[246] P. Mansfield, *Contemp. Phys.* **1976**, *17*, 553.

[247] P. A. Bottomley, *J. Phys. E: Sci. Inst.* **1981**, *14*, 1081.

[240] R. Seydoux, M. Haake, A. Pines, J. A. Reimer, *J. Phys. Chem. B* **1999**, *103*, 4629.

[241] A. Wong-Foy, S. Saxena, H.-M. L. Bitter, A. Moule, A. Pines, R. McDermott, J. Clarke, in *Experimental NMR Conference*, Asilomar, CA, **2000**, p. 174.

[242] F. Ludwig, E. Dantsker, R. Kleiner, D. Koelle, J. Clarke, S. Knappe, D. Drung, H. Koch, N. M. Alford, T. W. Button, *Appl. Phys. Lett.* **1995**, *66*, 1418.

[243] T. S. Lee, E. Dantsker, J. Clarke, *J. Rev. Sci. Instrum.* **1996**, *67*, 4208.

[244] M. D. Harten, *Med. Phys.* **1987**, *14*, 616.

[245] P. Mansfield, *J. Phys. E.* **1988**, *21*, 18.

[246] P. Mansfield, *J. Phys. Chem. C* **1973**, *6*, L422.

[247] P. Mansfield, P. K. Grannell, *Phys. Rev.* **1975**, *12*, 3618.

[248] P. Mansfield, *Contemp. Phys.* **1976**, *17*, 553.

[249] P. A. Bottomley, *J. Phys. E: Sci. Inst.* **1981**, *14*, 1081.